Titre: Title:	Finite Element Modelling of Shot Peening and Peen Forming Processes and Characterisation of Peened AA2024-T351 Aluminium Alloy
Auteur: Author:	Alexandre Gariépy
Date:	2012
Type:	Mémoire ou thèse / Dissertation or Thesis
Référence: Citation:	Gariépy, A. (2012). Finite Element Modelling of Shot Peening and Peen Forming Processes and Characterisation of Peened AA2024-T351 Aluminium Alloy [Ph.D. thesis, École Polytechnique de Montréal]. PolyPublie. https://publications.polymtl.ca/954/

UNIVERSITÉ DE MONTRÉAL

FINITE ELEMENT MODELLING OF SHOT PEENING AND PEEN FORMING PROCESSES AND CHARACTERISATION OF PEENED AA2024-T351 ALUMINIUM ALLOY

ALEXANDRE GARIÉPY
DÉPARTEMENT DE GÉNIE MÉCANIQUE
ÉCOLE POLYTECHNIQUE DE MONTRÉAL

THÈSE PRÉSENTÉE EN VUE DE L'OBTENTION
DU DIPLÔME DE PHILOSOPHIÆ DOCTOR
(GÉNIE MÉCANIQUE)
SEPTEMBRE 2012

UNIVERSITÉ DE MONTRÉAL

ÉCOLE POLYTECHNIQUE DE MONTRÉAL

Cette thèse intitulée :

FINITE ELEMENT MODELLING OF SHOT PEENING AND PEEN FORMING PROCESSES AND CHARACTERISATION OF PEENED AA2024-T351 ALUMINIUM ALLOY

présentée par : GARIÉPY Alexandre
en vue de l'obtention du diplôme de : Philosophiæ Doctor
a été dûment acceptée par le jury d'examen constitué de :

M. GOSSELIN Frédéric, Doct., président
M. LÉVESQUE Martin, Ph.D., membre et directeur de recherche
M. BOCHER Philippe, Ph.D., membre et codirecteur de recherche
M. CHAMPLIAUD Henri, Ph.D., membre
Mme ROUHAUD Emmanuelle, Ph.D., membre

À ma famille

ACKNOWLEDGEMENTS

I would like to first thank Pr. Martin Lévesque and Claude Perron for their guidance and trust throughout this project. Your confidence allowed me to explore hypotheses that made my work interesting, challenging and, I hope, useful. I would also like to thank Pr. Philippe Bocher at École de Technologie Supérieure for welcoming the computer savvy mechanical engineering student I was in his group and introducing me to the fascinating field of materials science.

The time and expertise provided by the National Research Council Canada - Aerospace is also greatly appreciated. I would like to thank Simon Larose for his generous help and advice and well as Christian Corbeil and Xavier Pelletier for their support.

I would like to acknowledge the contributions of Hongyan Miao, Julien Cyr, Derek Berrigan and Dave Demers at École Polytechnique de Montréal as well as Florent Bridier, Vincent Savaria, Majid Hoseini and Jean-Charles Stinville at ÉTS through fruitful discussions during this project. The technical advice and support of Bénédict Besner and Isabelle Nowlan (Polytechnique) as well as Radu Romanica and Jean-Guy Gagnon (ÉTS) is also gratefully acknowledged. The help and explanations of François Ménard and Abel Chouinard at the Laboratoire de Recherche en Fabrication Virtuelle (metrology) were also very useful.

I would like to thank the Natural Sciences and Engineering Research Council of Canada (NSERC), Rio Tinto Alcan and Fondation de Polytechnique for their financial support through scholarships. These scholarships made this project possible.

Finally, I would like to express my gratitude to my family for sticking together throughout the good and bad times of the past four years. I could not have done it without you.

RÉSUMÉ

Le grenaillage est un traitement de surface couramment utilisé pour améliorer la durée de vie en fatigue de différentes pièces métalliques. Un grand nombre de petites particules dures sont projetées sur la surface du composant à haute vitesse. Chaque particle déforme plastiquement le matériau et les impacts répétés produisent un état de contraintes résiduelles compressives bénéfique à la surface. Le grenaillage modifie de plus les propriétés mécaniques locales de même que la microstructure du matériau. Le procédé augmente toutefois la rugosité et peut occasionner des dommages en surface. Son influence sur la vie en fatigue et la limite de fatigue dépend donc d'une combinaison de plusieurs effets.

La mise en forme par grenaillage (MEFG) est une méthode de fabrication dérivée du grenaillage. Le champ de contraintes compressives généré par le grenaillage modifie l'équilibre mécanique de la pièce et est utilisé pour courber des composants minces. Ce procédé est utilisé depuis les années 1950 dans l'industrie aérospatiale pour mettre en forme de grands panneaux requérant des courbures légères, comme des panneaux de voilure et de fusées. La MEFG est une alternative économique aux techniques de mise en forme conventionnelles puisqu'elle ne nécessite pas un ensemble de matrices pour chaque forme à réaliser. De plus, différents contours peuvent être réalisés en modificant simplement les traitements de grenaillage appliqués à différentes régions de la pièce. Cependant, cette flexibilité n'est peut-être pas employée à son plein potentiel puisque les applications actuelles sont généralement basées sur le savoir-faire empirique et une approche par essai-erreur.

Cette thèse visait le développement et la validation d'outils de simulation par éléments finis (ÉF) pour le grenaillage et la mise en forme par grenaillage. L'objectif était d'arriver à des prédictions quantitatives pour ces deux procédés et de démontrer le potentiel de la modélisation ÉF tant pour des études fondamentales que pour des applications industrielles.

Premièrement, un modèle amélioré d'impacts dynamiques prenant en considération la nature aléatoire du grenaillage a été proposé en étudiant avec soin ses dimensions, en introduisant la dispersion des tailles des particules et en réduisant significativement le temps de calcul. De plus, des essais mécaniques cycliques ont été réalisés afin de définir une loi de comportement appropriée pour l'alliage d'aluminium (AA) 2024-T3/T351 soumis au procédé de grenaillage. En combinant un modèle réaliste et une loi de comportement adaptée, de bonnes prédictions ont été obtenues en termes de contraintes résiduelles pour trois ensembles de paramètres de grenaillage.

Deuxièmement, l'état de l'AA2024-T351 grenaillé dans des conditions représentatives des applications d'amélioration de vie en fatigue a été caractérisé expérimentalement et nu-

mériquement. Différentes techniques telles que la micro-indentation, la détermination de contraintes résiduelles et l'imagerie par diffraction des électrons rétrodiffusés ont été combinées afin de mieux comprendre les effects du grenaillage sur le matériau. Les applications potentielles de la simulation ÉF dans le but de complémenter les résultats expérimentaux ont aussi été discutées. L'état hétérogène résultant de la séquence d'impacts aléatoires a été étudié et il a été noté que la modélisation d'impacts pourrait apporter des informations utiles sur cette hétérogénéité.

Troisièmement, une nouvelle méthodologie de simulation de la MEFG a été introduite. La modélisation d'impacts a fourni les données initiales nécessaires dans le cadre d'une approche multiéchelles. Les profils de contraintes induites hors-équilibre prédits numériquement ont été introduits dans des éléments coques et la déformée à l'équilibre a été obtenue par une analyse de retour élastique. De plus, une méthode d'interpolation simplifiée a été proposée pour modéliser la nature incrémentale de la MEFG avec un coût de calcul raisonnable. Le procédé a donc été simulé par une série d'analyses de retour élastique. Cette approche a d'abord été validée à l'aide de données obtenues par des tests à petite échelle.

L'effet possible de l'orthotropie des matériaux laminés a ensuite été étudié numériquement et expérimentalement. Ce facteur pourrait avoir une influence importante pour les applications industrielles puisque plusieurs pièces mises en forme par grenaillage proviennent de feuilles et plaques laminées. Les essais expérimentaux ont montré que l'orientation de la direction de laminage a un effet notable sur les courbures après grenaillage pour de petites plaques d'AA2024-T3. Les propriétés élastiques orthotropiques ainsi que l'état initial de contraintes résiduelles des échantillons ont été introduits dans les simulations de mise en forme et les prédictions concordaient bien avec les données expérimentales pour un des deux ensembles de paramètres de grenaillage à l'étude.

Par la suite, la méthodologie de simulation a été améliorée de manière à tenir compte de la trajectoire de la buse de grenaillage sur la pièce. Ceci a mené à une représentation plus réaliste des procédures de MEFG couramment utilisées pour de grands panneaux, où l'équipement de grenaillage est déplacé sur les surfaces. La trajectoire de grenaillage et les conditions aux frontières utilisées dans les essais à petite échelle ont généré des distributions complexes de rayons de courbure qui ont qualitativement été bien prédites par les simulations de mise en forme.

Finalement, les applications possibles de cette nouvelle stratégie de simulation ont été démontrées en simulant la mise en forme par grenaillage de panneaux de voilure typiques. Les composants modélisés avaient des caractéristiques réalistes, comme des épaisseurs variables et des raidisseurs intégrés, et plusieurs traitements de mise en forme ont été simulés successivement.

La principale contribution de cette thèse est une approche multiéchelle expérimentalement validée pour la simulation de mise en forme par grenaillage. Cette stratégie combine des analyses dynamiques d'impacts et des simulations statiques de retour élastique et prend en considération la nature incrémentale du procédé avec un fondement physique. Les besoins en termes d'étalonnage expérimental ont aussi été réduits par rapport aux méthodes existantes. Des phénomènes complexes reliés à l'orthotropie des plaques et à la trajectoire de grenaillage ont été prédits avec une bonne précision. Bien que la méthodologie n'ait pu être validée pour un composant aéronautique réel de pleine grandeur, ses applications potentielles ont été illustrées. Cette méthode pourrait réduire le temps et les coûts de développement de nouvelles procédures ainsi que limiter le recours aux essais expérimentaux. Finalement, les contributions possibles de la simulation aléatoire pour décrire l'état du matériau après grenaillage ont été étudiées dans le cadre de la caractérisation détaillée de l'AA2024-T351 grenaillé

ABSTRACT

Shot peening is a surface treatment commonly used to improve the fatigue performance of various metallic parts. This process consists of projecting a large number of tiny particles at high velocity onto the surface of a component. Each impact plastically deforms the material and repeated impacts lead to a beneficial compressive residual stress state near the surface. In addition, shot peening alters both the local mechanical properties and microstructure. On the other hand, it also generates increased surface roughness and possible damage. Its influence on fatigue life (or strength) therefore arises from a combination of multiple effects.

Peen forming is a manufacturing method derived from shot peening. The compressive stress field induced by peening alters the mechanical balance and is used to shape thin components. This process has been used in the aerospace industry since the 1950s to contour large panels with gentle curvatures, such as wing skins and rocket panels. It is a cost-effective alternative to conventional forming techniques since it does not require a specific set of dies for each target shape. In addition, peen forming can achieve various target contours by simply altering the shot peening treatments applied on different regions on the parts. This versatility may however not be used to its full potential since current peen forming procedures are commonly developed through empirical knowledge and trial-and-error.

The main purpose of this thesis was to develop and validate finite element (FE) simulation tools for shot peening and peen forming. The specific aim was to achieve quantitatively accurate predictions for both processes and demonstrate the potential of reliable FE modelling for scientific investigation and industrial applications.

First, an improved dynamic impact model that takes into account the stochastic nature of shot peening was proposed by carefully studying its dimensions, introducing a dispersion of shot sizes and significantly reducing its computational cost. In addition, cyclic mechanical testing was conducted to define a suitable material constitutive theory for aluminium alloy (AA) 2024-T3/T351 subjected to shot peening. By combining a realistic shot peening model with an appropriate material law, fairly good residual stress predictions were achieved for three different sets of shot peening parameters.

Second, an experimental and numerical characterization of AA2024-T351 shot peened with parameters representative of fatigue life improvement applications was conducted. Multiple techniques, such as micro-indentation, residual stress determination and electron backscatter diffraction, were combined to gain a better understanding of the influence of shot peening on the material. The potential uses of finite element simulation to complement experimental data were also studied. The material heterogeneity arising from the random impact

sequence was investigated and it was found that the impact modelling methodology could provide useful information on such heterogeneities.

Third, a novel peen forming simulation methodology was introduced. The impact model provided the necessary input data as part of a multiscale approach. Numerically calculated unbalanced induced stress profiles were input into shell elements and the deformed shape after peen forming was computed as a springback analysis. In addition, a simple interpolation method was proposed to model the incremental nature of peen forming in a computationally efficient manner. The process was therefore simulated as a series of springback analyses. This approach was first validated using data from small-scale experimental trials.

The potential effect of sheet orthotropy was then investigated numerically and experimentally. This factor could have a significant influence in industrial applications since peen formed components usually originate from rolled sheets and plates. The orientation of the rolling direction was found to have a significant effect on resulting curvatures for small AA2024-T3 sheets. The experimentally determined orthotropic elastic properties and initial stress state of the samples were input into forming simulations and numerical results correlated well with small-scale experimental data for one of the two sets of peening parameters under study.

The modelling methodology was improved further so as to take into account the trajectory of the peening nozzle. This led to a more realistic representation of actual peen forming procedures used for large components, which require moving peening equipment over the surfaces. The peening trajectory and boundary conditions considered in small-scale tests led to complex distributions of radius of curvature and FE simulations correctly predicted the experimentally observed trends.

Finally, the potential applications of the novel simulation strategy were demonstrated by simulating peen forming of typical wing skin panels. The modelled components had realistic features such as variable thicknesses and integral stiffeners and were subjected to multiple representative peen forming treatments using different shot types.

The main contribution of this work is an experimentally validated multiscale peen forming simulation strategy combining impact simulations with static springback analyses and taking into account the incremental nature of the process with a physical basis. This approach reduced the experimental calibration required and led to good predictions of complex phenomena associated with sheet orthotropy and peening trajectory. Although the methodology could not be validated with large-scale aerospace components, its potential applications for actual parts were illustrated. The proposed methodology could reduce the time and costs associated with process development as well as its dependence on experimental testing. Moreover, the potential contributions of the random impact model to describe the material state after shot peening were investigated through a detailed characterization of shot peened AA2024-T351.

CONDENSÉ

Le grenaillage est un traitement de surface qui consiste à projeter une multitude de petites particules très dures, appelées grenailles, à haute vitesse sur la surface d'un composant métallique. Chaque impact cause des déformations plastiques dans le matériau et le martelage répété tend à compresser la surface. Étant donné que la déformation plastique a lieu à volume constant, ceci amène un étirement dans le plan de la surface. Puisque le matériau sous-jacent n'est pas déformé plastiquement, la compatibilité des déformations génère un état plan de contraintes résiduelles compressives en surface qui est équilibré par des contraintes en tension en profondeur. Ces contraintes résiduelles compressives exercent un effet favorable sur la vie en fatigue en ralentissant ou même en arrêtant la propagation de fissures. Les modifications des propriétés mécaniques et de la microstructure occasionnées par les impacts répétés peuvent aussi avoir un effet bénéfique sur le comportement en fatigue. Cependant, le procédé augmente la rugosité et peut causer des dommages en surface, ce qui peut dégrader la vie en fatigue ou la limite de fatigue. L'amélioration possible de la tenue en fatigue par le grenaillage provient donc d'une combinaison de plusieurs effets concurrents. Ce procédé est couramment employé pour des composants fortement chargés tels que des engrenages, notamment dans les industries automobile et aéronautique, mais ses effets ne sont pas encore parfaitement compris et quantifiés d'un point de vue théorique.

La mise en forme par grenaillage est un procédé de fabrication qui utilise le champ de contraintes compressives généré par le grenaillage pour créer des courbures relativement faibles dans des composants minces. L'effet de mise en forme a pour origine le déséquilibre des contraintes induites compressives introduites en surface par le grenaillage. Celles-ci tendent à allonger et à faire fléchir la pièce afin de rétablir un état de contraintes résiduelles correspondant à un nouvel équilibre. Ce procédé a été développé dans les années 1950 pour mettre en forme des panneaux d'ailes monolithiques (*i.e.* à raidisseurs intégrés) et est maintenant couramment employé dans l'industrie aérospatiale pour générer les contours de grandes pièces minces telles que des panneaux de voilure, de fuselage et de fusées. En plus de permettre d'obtenir des formes tridimensionnelles à partir d'une pièce plane, la mise en forme par grenaillage peut aussi servir à corriger des distorsions, c'est-à-dire rétablir une forme cible à partir d'une pièce déjà courbée. La mise en forme par grenaillage présente plusieurs avantages par rapport aux méthodes de mise en forme conventionnelles puisque :

- Elle ne nécessite pas de grandes presses et matrices pour chaque contour ;
- Elle permet d'obtenir des contours différents en altérant les traitements de grenaillage ainsi que les régions où ils sont appliqués ;

– Elle laisse un état de contraintes résiduelles compressives en surface bénéfique pour la tenue en fatigue.

Cependant, les procédures de mise en forme sont souvent développées par essai-erreur à l'aide du savoir-faire empirique acquis par l'expérience. Cette approche ne permet peut-être pas d'exploiter le plein potentiel de ce procédé de fabrication économique et avantageux.

Il existe des opportunités intéressantes pour la simulation numérique dans les domaines du grenaillage et de la mise en forme par grenaillage. En ce qui concerne le grenaillage, une revue de la littérature a montré que la simulation d'impacts aléatoires représente de façon réaliste le déroulement réel du procédé et que des lois de comportement tenant compte de la plasticité cyclique et de l'influence de la vitesse de déformation permettent de bien prédire quantitativement l'état de contraintes résiduelles après grenaillage. La combinaison de ces deux ingrédients pourrait mener à des prédictions plus précises qui pourraient éventuellement servir de données d'entrée dans des modèles de tenue en fatigue. De plus, beaucoup d'études se sont intéressées à l'état du matériau après grenaillage mais peu ont offert une vision complète et globale tenant compte des hétérogénéités découlant des impacts aléatoires. Des simulations numériques précises et fiables pourraient être un complément très révélateur aux observations expérimentales. Dans le domaine de la mise en forme par grenaillage, différents travaux expérimentaux ont bien caractérisé les phénomènes complexes qui peuvent avoir une influence notable dans le cadre d'applications industrielles. Plusieurs études numériques ont été publiées mais ne sont pas encore arrivées à bien prédire ces comportements. Ces études ont toutefois introduit des éléments essentiels à la simulation de la mise en forme, tels que l'usage de chargements équivalents et d'éléments coques pour réduire le temps de calcul, la répétition de chargements pour simuler le caractère incrémental du procédé et l'emploi de résultats de simulations d'impacts comme données d'entrée. Une nouvelle approche fondée sur des principes physiques pourrait réduire l'écart entre les capacités de modélisation et les procédures industrielles.

Les objectifs visés par cette thèse étaient donc :

1. Améliorer la méthodologie de simulation d'impacts aléatoires
   Pour ce faire, un modèle existant a premièrement été étudié en détails de manière à définir des dimensions appropriées, tenir compte de la dispersion des tailles de grenailles et réduire significativement le temps de calcul. Le temps de calcul est en effet un facteur déterminant pour l'emploi de la simulation numérique dans l'industrie. De plus, des essais mécaniques cycliques ont été réalisés sur l'alliage d'aluminium (AA) 2024-T351 et une loi de comportement relativement simple à écrouissage isotrope et cinématique a été choisie.
2. Caractériser l'état hétérogène du matériau après grenaillage

Cette étude a combiné des outils expérimentaux et numériques afin de décrire l'état de l'AA2024-T351 grenaillé avec des paramètres typiques de l'amélioration de la tenue en fatigue.

3. Développer et valider une nouvelle approche de simulation de la mise en forme par grenaillage

   Il s'agit de l'objectif principal de ce travail. Une nouvelle méthodologie de simulation incrémentale basée sur des comportements observés numériquement a d'abord été proposée. Cette approche a ensuite été améliorée et appliquée à la modélisation de deux phénomènes plus complexes, soit l'orthotropie résultant du laminage et la trajectoire de grenaillage. Ceux-ci pourraient avoir une influence importante pour la mise en forme de composants industriels. Finalement, les applications potentielles de cette stratégie ont été illustrées en simulant la mise en forme de pièces aéronautiques représentatives.

Les travaux réalisés afin d'atteindre ces objectifs ont fait l'objet de cinq articles qui sont présentés dans cette thèse.

Dans un premier temps, une étude détaillée de la simulation d'impacts aléatoires a été faite. Un modèle existant, où les positions des impacts étaient définis aléatoirement, a été amélioré en analysant l'influence de chacune de ses dimensions, en introduisant une distribution de tailles de grenailles représentative du procédé réel et en corrélant les résultats numériques et expérimentaux sur la base de la masse des grenailles. Il a été conclu qu'un modèle de petites dimensions, avec une surface soumise aux impacts de l'ordre d'une dizaine de fois la superficie d'un cratère d'impact, représentait bien le comportement du matériau grenaillé à plus grande échelle avec un coût de calcul significativement moindre. Le temps de calcul a aussi été réduit par un facteur de ≈ 10 en réorganisant la séquence d'impacts : la durée entre chaque impact a été réduite tout en maintenant un amortissement suffisant de la solution et l'état de contraintes résiduelles a été extrait après chaque impact. De plus, en considérant les déformations alternées causées par le grenaillage, des essais mécaniques cycliques uniaxiaux ont été réalisés sur des échantillons d'AA2024-T351 jusqu'à une amplitude de déformation de $\pm 3\%$. Ceux-ci ont permis de déterminer les paramètres d'une loi de comportement à écrouissage isotrope et cinématique qui a mené à des prédictions prometteuses en termes de contraintes résiduelles pour deux ensembles de paramètres de grenaillage. Une nouvelle approche de simulation de la mise en forme par grenaillage a aussi été introduite en se basant sur des résultats d'analyses d'impacts. Ces résultats ont suggéré que le profil de contraintes initial avait peu d'effet sur les contraintes induites par le grenaillage en surface. Au contraire, les impacts simulés affectaient peu l'état de contraintes initial en profondeur. Ces observations ont été utilisées comme fondement pour simuler la nature incrémentale de la mise en forme avec une base physique. Des profils de contraintes induites déséquilibrés

ont été imposés à travers l'épaisseur d'éléments coques à plusieurs reprises et le retour à l'équilibre a été calculé à chaque étape à l'aide du logiciel commercial ABAQUS. Une formulation mathématique simple visant à combiner le profil de contraintes induites prédit pour l'état de contraintes initial avec le profil de contraintes existant dans le matériau juste avant le grenaillage a été suggérée. L'efficacité de cette méthode provient de l'usage des profils de contraintes induites prédits pour un état de contraintes initial donné tout au long des analyses de mise en forme. Cette approche a été validée expérimentalement pour le cas de bandes d'AA2024-T3 de 76 mm $\times$19 mm et de 1.6 mm d'épaisseur grenaillées dans un support Almen. Après étalonnage de la relation entre le nombre d'étapes de calcul et le temps d'exposition expérimental, les simulations ont bien prédit l'évolution des flèches en fonction du temps d'exposition pour trois ensembles de paramètres de grenaillage de même que le développement des flexions contraintes et de courbures complexes en raison des contraintes imposées à l'échantillon pendant le grenaillage. Une contribution importante de ce travail était une stratégie permettant de calculer simultanément les profils de contraintes résiduelles (ou induites) et les flèches résultant de la mise en forme par grenaillage avec une bonne précision.

Une étude détaillée de l'état de l'AA2024-T351 grenaillé avec un ensemble de paramètres représentatifs de l'amélioration de la vie en fatigue a ensuite été réalisée. Des méthodes de diffraction des rayons X, de micro-indentation, de profilométrie 2D et 3D, de microscopie optique et électronique ainsi que d'imagerie par diffraction des électrons rétrodiffusés ont été employées pour évaluer les profils de contraintes résiduelles, l'état d'écrouissage, la rugosité, l'endommagement et les modifications microstructurales après grenaillage. Une attention particulière a été portée aux hétérogénéités occasionnées par la séquence d'impacts aléatoires, un facteur possiblement important qui est cependant négligé dans la plupart des modèles prédictifs de tenue en fatigue. Des simulations d'impacts aléatoires ont de plus été menées afin de complémenter les données expérimentales. La simulation numérique présente des avantages notables comme la capacité de dissocier des phénomènes couplés dans les mesures physiques. Par exemple, l'état d'écrouissage et le champ de contraintes résiduelles affectent tous deux les mesures de dureté et sont difficilement dissociables dans le cas du grenaillage ; au contraire, la simulation offre de l'information spécifique à chacun. Les analyses d'impact ont relativement bien prédit les profils de contraintes résiduelles déterminés expérimentalement et ont aussi permis d'estimer la dispersion spatiale des contraintes résiduelles à une échelle plus petite que celle possible par la diffraction des rayons X. Pour ce matériau et ces paramètres spécifiques, le grenaillage a produit des dommages restreints en surface, des modifications microstructurales importantes sur une profondeur de 75 μm, une couche écrouie de 175 à 200 μm et des contraintes résiduelles compressives sur 350 à 400 μm. Ces informations et surtout la

méthodologie de caractérisation développée pourraient s'avérer utiles dans des études futures sur la tenue en fatigue.

Le développement de l'approche de simulation de mise en forme par grenaillage a été poursuivi en étudiant expérimentalement et numériquement l'influence de l'orthotropie associée au laminage sur les courbures. Ce comportement pourrait avoir un effet notable dans les applications industrielles puisque plusieurs composants mis en forme par grenaillage proviennent de plaques laminées et usinées, mais n'avait pas été modélisé auparavant. Les variations de courbures occasionnées par l'orthotropie élastique, l'anisotropie plastique et les contraintes initiales ont d'abord été discutées. Des échantillons d'AA2024-T3 de 76 mm $\times$19 mm et de 1.6 mm d'épaisseur ont été découpés selon les directions de laminage et transverse de la plaque puis grenaillés avec deux ensembles de paramètres. Une influence de l'orientation de la direction de laminage sur les échantillons jusqu'à 10% a été notée en termes de rayons de courbure. Les propriétés élastiques orthotropes et les profils de contraintes résiduelles non-équibiaxiaux déterminés expérimentalement ont été introduits dans les simulations de mise en forme. Les prédictions concordaient bien avec les résultats des tests pour un des deux ensembles de paramètres à l'étude. Pour le second ensemble, l'influence de l'orientation de la direction de laminage était significativement sous-estimé, ce qui suggère que l'anisotropie plastique devrait être considérée dans le but d'arriver à des prédictions plus précises. Cette étude a aussi montré l'intérêt d'évaluer les rayons de courbure, plus sensibles et directionnels, plutôt que les flèches maximales.

La méthodologie a ensuite été améliorée afin de prendre en considération l'effet de la trajectoire suivie par l'équipement de grenaillage. La plupart des composants mis en forme par grenaillage sont de grandes dimensions, ce qui fait que l'équipement de grenaillage doit être déplacé en suivant un tracé prédéfini sur les surfaces. Des échantillons d'AA2024-T3 de 1.6 mm d'épaisseur avec des dimensions de 76 mm $\times$19 mm et de 76 mm $\times$76 mm ont été grenaillés en une passe lente, au lieu des multiples passes rapides employées dans les expériences précédentes. L'effet de l'orientation de la direction de laminage a aussi été considéré dans cette étude. Une distribution complexe de rayons de courbures a été déterminée expérimentalement. Une nouvelle méthode de simulation de l'avance de l'équipement de grenaillage a été suggérée en utilisant le cadre mathématique développé précédemment. Le jet de billes et sa trajectoire ont été modélisés en adoptant certaines hypothèses simplificatrices. Le jet de billes ainsi que le tracé grenaillé ont été divisés en cases dans lesquelles de nouvelles contraintes induites déséquilibrées étaient imposées un certain nombre de fois. Ce nombre de répétition a été étalonné avec comme référence les flèches des échantillons de 76 mm $\times$19 mm grenaillés. La méthode étalonnée a ensuite été appliquée aux échantillons de 76 mm $\times$76 mm. Les simulations ont pu prédire qualitativement les contours complexes reliés aux conditions

aux frontières. L'asymétrie des rayons de courbures, qui serait le résultat de la trajectoire de grenaillage, a aussi été prédite et une explication a été proposée en se basant sur les résultats de simulation. De plus, cette étude a aussi montré l'importance de tenir compte des non-linéarités géométriques dans les analyses de mise en forme.

Les applications potentielles de la modélisation multiéchelles de mise en forme par grenaillage dans un contexte industriel ont enfin été illustrées à l'aide de simulations utilisant des composants et des traitements de grenaillage représentatifs. Les modèles d'impact et de mise en forme ont été ajustés pour les énergies d'impact plus élevées nécessaires pour la mise en forme par grenaillage. Un système graphique a été développé pour faciliter la mise en place d'analyses complexes à l'aide de l'interface visuelle d'`ABAQUS`. Une hypothèse a aussi été proposée pour simuler des traitements de grenaillage successifs sur une même région. Des simulations par éléments finis ont d'abord été réalisées pour construire des bases de données reliant l'épaisseur du matériau et les paramètres de grenaillage aux courbures résultantes. La mise en forme de panneaux d'ailes typiques incluant des épaisseurs variables et des raidisseurs intégrés a ensuite été modélisée en utilisant les bases de données obtenues numériquement. Des techniques de grenaillage couramment employées pour générer des contours complexes, telles que le grenaillage de bandes parallèles étroites, l'élongation des raidisseurs intégrés et l'élongation des bords par grenaillage à haute énergie, ont aussi été simulées afin d'évaluer les capacités de modélisation. L'effet attendu des deux premières a bien été prédit, mais l'influence de l'élongation des bords n'a pas été correctement prédite. Finalement, l'utilité de prédire l'élongation et la déformation angulaire des composants a été discutée. Cette étude a permis de mieux cerner les capacités prédictives de la modélisation, d'évaluer sommairement la nécessité d'un compromis entre le réalisme de la simulation et le temps de calcul et d'identifier les éléments qui requièrent une étude plus poussée.

Finalement, les phénomènes complexes intervenant pendant le grenaillage, tels que les déformations cycliques tridimensionnelles à haute vitesse de déformation, les pressions hydrostatiques élevées et l'anisotropie plastique, ont été discutés. Les aspects de modélisation et de caractérisation expérimentale ainsi que les défis associés ont été abordés sommairement. Sur le sujet de la mise en forme, une explication sommaire et partielle visant à comprendre le faible effet des contraintes initiales sur le développement de contraintes induites a été suggérée en se basant sur la variation de la pression hydrostatique sous l'impact en fonction des contraintes initiales. Les avantages et inconvénients de la simulation basée sur les contraintes ont été analysés, notamment en ce qui concerne l'usage de contraintes induites prédites numériquement et l'étalonnage expérimental. L'évaluation de recherches expérimentales et de procédures industrielles publiées a aussi permis d'identifier des opportunités d'amélioration de la méthode proposée.

En résumé, ce travail a mené au développement et à la validation d'outils de simulation par éléments finis statiques et dynamiques pour le grenaillage et la mise en forme par grenaillage. Premièrement, les analyses d'impact ont permis de prédire avec une bonne précision l'état de contraintes résiduelles après grenaillage et pourraient s'avérer très utiles dans l'étude de l'hétérogénéité du matériau grenaillé. Deuxièmement, une méthodologie de simulation de la mise en forme par grenaillage utilisant les résultats de simulations d'impacts et fondée sur des phénomènes physiques a été introduite. Cette méthodologie a permis de prédire l'influence de phénomènes complexes et possiblement importants dans le cadre d'applications industrielles, soit les conditions aux frontières, l'orthotropie des matériaux laminés et la trajectoire de grenaillage. De plus, une attention particulière a été portée à la réduction du coût de calcul. Ce projet a donc établi une base de travail prometteuse pour la modélisation de la mise en forme par grenaillage et mené à une meilleure compréhension du procédé.

Plusieurs questions de recherches pertinentes ont été soulevées au cours de ces travaux quant à la modélisation du grenaillage et de la mise en forme par grenaillage.

Premièrement, en ce qui concerne le grenaillage, les travaux futurs devront étudier plus en détails la loi de comportement choisie. Celle-ci est en effet certainement incomplète et doit être améliorée pour inclure les effets de mémoire de déformation et de sensibilité à la vitesse de déformation. De plus, il serait nécessaire d'introduire les effets thermiques et possiblement de pression hydrostatique dans les simulations. L'influence de l'anisotropie plastique devrait aussi être quantifiée et, si nécessaire, modélisée. Il serait souhaitable de réaliser des expériences d'indentation instrumentée sur le matériau grenaillé. Cette méthode permet d'estimer les propriétés mécaniques locales : ces résultats pourraient donc être employés pour valider l'évolution prédite de l'état du matériau pendant le grenaillage. Un défi à relever sera dans ce cas l'influence combinée des contraintes résiduelles et de l'écrouissage sur les mesures d'indentation. Une autre option intéressante à considérer serait la simulation basée sur la microstructure et les mécanismes physiques de déformation. Bien que plus complexe, celle-ci permettrait de mieux comprendre le comportement du matériau sous impact et, ensuite, sa réponse aux chargements cycliques de fatigue.

Des résultats préliminaires ont montré que le modèle d'impacts actuel ne permet pas encore de bien prédire l'évolution de la rugosité et du recouvrement. Cette lacune doit être résolue en vue d'applications scientifiques et industrielles puisque la rugosité est un facteur important gouvernant la tenue en fatigue et puisque le recouvrement est une mesure omniprésente dans l'industrie.

Lorsqu'une loi de comportement et un modèle d'impacts améliorés auront été établis et validés, la simulation numérique du grenaillage pourrait contribuer à l'étude quantitative des hétérogénéités dues au grenaillage et à leur introduction dans des modèles prédictifs de tenue

en fatigue. L'amélioration des simulations d'impacts sera aussi bénéfique pour les simulations de mise en forme, en fournissant des données d'entrées plus fiables.

Deuxièmement, sur le sujet de la mise en forme par grenaillage, des expériences contrôlées devront être réalisées pour évaluer, comprendre et modéliser l'influence du rapport de forme et de l'épaisseur relative des échantillons sur le développement de contours complexes tels que des cylindres. La méthode de simulation actuelle ne permet en effet pas de prédire de tels comportements. Des hypothèses possibles à étudier seraient les chargements dus au poids du composant, la flexion associée aux forces d'impacts ou les vibrations du composant causées par les chargements dynamiques. Il serait aussi souhaitable de mener ces expériences sur des échantillons non contraints, une méthode de support plus représentative des usages industriels du procédé (à l'exception de la mise en forme avec précontraintes).

Dans la perspective d'arriver à des prédictions utiles en milieu industriel, plusieurs hypothèses simplificatrices employées dans le présent travail doivent être révisées. D'abord, le poids des composants a été négligé. Pour de longues pièces minces, celui-ci pourrait causer une flexion importante. Ensuite, l'interaction entre des traitements de grenaillage appliqués successivement n'a été considérée que sommairement et doit être mieux comprise. De plus, les prédictions de contraintes induites pour de faibles taux de recouvrement n'ont pas été validées. Finalement, une validation expérimentale avec des pièces de pleine grandeur demeure nécessaire pour évaluer les capacités prédictives de la méthodologie proposée et identifier au besoin les points à améliorer.

Finalement, il serait pertinent de s'intéresser à la mise en forme concave (à haute énergie d'impact) et à la mise en forme par grenaillage avec précontrainte. Il s'agit de deux variations couramment utilisées de la mise en forme par grenaillage. La validité de la méthode proposée devrait être étudiée et les simulations d'impacts et de mise en forme devraient être améliorées pour tenir compte des phénomènes intervenant dans ces deux cas.

TABLE OF CONTENTS

LIST OF TABLES

LIST OF FIGURES

LIST OF SYMBOLS AND ABBREVIATIONS

a	Affected depth
	Advance length
a_h	Almen arc height
$a_h^{N_p}$	Almen arc height after N_p passes
a_h^S	Almen intensity
a_{ij}	Partial cross-sectional area
A	Fitting parameter
$A_{influence}$	Area affected by impact
$A_{intersection}$	Part of area affected by impact belonging to representative region
A_{CS}	Cross-section area
A_{target}	Area subjected to shot peening
b_i	Material parameter
B	Fitting parameter
c_i	Material parameter
$c(t)$	Coverage as a function of exposure time
$c(z_i)$	Average depth of element layer i
C	Hardening parameter in kinematic hardening law
	Chord length
	Fitting parameter
C_e	End fixity coefficient
d	Interplanar spacing
D	Fitting parameter
D_{shot}	Shot diameter
DS	Directional scatter
E	Young's elastic modulus (isotropic)
E_r	Young's modulus along rolling direction
E_t	Young's modulus along transverse direction
E_{tangent}	Tangent modulus in the plastic regime
f_I^k	Influence factor for shot k
F	Force
F^{con}	Constraining force
ΔG_0	Activation enthalpy
h	Sheet/plate thickness

h_{fine}	Thickness of refined mesh volume
h_{p}	Depth of plastic strain
h_{total}	Total thickness of impact model
	Total deflection
h_{X}	Deflection along X
h_{Y}	Deflection along Y
H	Linear strain-hardening coefficient
I	Width of the impacted area
$\mathbf{I}$	Identity matrix
I_D	Impact density
I_k	Impact density at increment k
I_{min}	Minimum moment of inertia
k	Increment number
	Boltzmann constant
k_0	Initial athermal flow stress
k_1	Variable related to Poisson's ratio
K	Evolutional athermal part of the flow stress
K_t	Stress concentration factor
$l_{\{x,y\}}$	Distance from edge along X or Y
L	Length of the shot stream along the travel direction
L_c	Column length
L_{min}	Minimum element dimension
$L^k_{\{X,Y\}}$	Impact location along X or Y for the k^{th} modelled shot
$L_{\{X,Y\}}$	Sample dimensions
L_p	Effective length of robot travel
$\dot{m}$	Mass flow rate
m	Material parameter, Eq. (1.9)
m_e	Effective mass of impacting shot
M	Bending moment
M^{con}	Constraining moment
M_e	Cumulated effective mass of impacting shots
$M_e^{N_p}$	Cumulated effective mass of impacting shots after N_p passes
M_e^S	Cumulated effective mass of impacting shots at saturation
M_i	Impacting mass increment per simulation step
M_t	Total impacting mass
n	Simulation step number

	Material parameter, Eq. (1.9)
	Constant, Eq. (5.2)
n_p	Pass number
n_s	Number of passes at saturation
N_i	Number of simulated increments
N_p	Total number of passes
N_t	Effective number of adjacent peening lines
p	Section point number
$\dot{q}$	Rate of evolution of the radius of the inelastic strain yield surface
P	Hydrostatic pressure
$P^{\text{far field}}$	Hydrostatic pressure far from the surface
Q	Asymptotic value of K for a given strain amplitude
Q_0	Material parameter
$Q_{\max}$	Material parameter
r	Radial distance between shot and peening axis at stand-off plane
	Radius of curvature of notch, Eq. (5.2)
R	Width of the representative area
R_a	Average roughness over evaluation length
R_{ai}	Average roughness over sampling length i
R_c	Radius of curvature (isotropic curvature case)
R_t	Maximum peak-to-valley height over evaluation length
R_{ti}	Maximum peak-to-valley height over sampling length i
$R_{\{X,Y\}}$	Radius of curvature along direction X or Y
s	Number of narrow peened strips
$\mathbf{s}$	Deviatoric stress tensor
$S_{\bar{a}_h}$	Results scatter in terms of arc height
S_{cr}	Critical buckling stress
S_m	Mean spacing between profile peaks over evaluation length
S_{mi}	Mean spacing between profile peaks over sampling length i
S_p	Superposition/interpolation function
t	Exposure time
t_{ext}	Width of unimpacted coarse mesh region
t_{int}	Width of unimpacted refined mesh region
t_{sat}	Exposure time at saturation
$t(z_i)$	Deformed thickness of element layer i
Δt	Time increment

$u_{\{x,y,z\}}$	Displacement along X, Y or Z
T	Temperature
v_r	Robot travel velocity
v_{shot}	Impact velocity
x	2D height between shot projection and peening axis at stand-off plane
z	Depth
z_i	Discrete depth increments in impact model
z_{indent}	Local depth
$z_{\text{indent}}^{\text{affected}}$	Affected depth in terms of hardness values
$z_{\text{FWHM}}^{\text{affected}}$	Affected depth in terms of FWHM values
z_{RS}	Global depth
$z_{\text{RS}}^{\text{affected}}$	Affected depth in terms of residual stress
z_s	Depth in impact model

Greek symbols

α	Coefficient of thermal expansion
α_R	Mass-proportional Rayleigh damping coefficient
β	Material parameter
β_R	Stiffness-proportional Rayleigh damping coefficient
γ	Recall parameter in kinematic hardening law
$\varepsilon^{\max}$	Maximum nominal strain
$\varepsilon^{\min}$	Minimum nominal strain
$\dot{\varepsilon}$	Strain-rate
$\dot{\varepsilon}_0$	Reference strain-rate
ε_e	Elongation
$\dot{\boldsymbol{\varepsilon}}_p$	Plastic strain rate tensor
$\bar{\varepsilon}_p$	Equivalent plastic strain
$\dot{\bar{\varepsilon}}_p$	Equivalent plastic strain rate
$\dot{\bar{\varepsilon}}_p^*$	Normalized equivalent plastic strain rate
ε_t	Thermal strain
$\Delta\varepsilon$	Nominal strain range in cyclic tests
η	Material parameter
θ	Diffraction angle
μ	Friction coefficient
	Material parameter, Eq. (1.11)
ν	Poisson's ratio (isotropic)

ν_{mn}	Orthotropic Poisson's ratio when material is stressed along direction m
ξ	Ratio of mass flow rate to shot velocity
$\boldsymbol{\xi}$	Back-stress tensor
ρ	Material density
$\rho_{\min}$	Minimum radius of gyration of a cross-section
ρ_t	Target material density
ρ_s	Shot density
σ	Stress component
$\boldsymbol{\sigma}$	Stress tensor
$\bar{\sigma}$	Average stress
σ_0	Initial monotonic yield stress
σ^*	Thermal part of the flow stress
σ_0^*	Material parameter
σ_{axial}	Stress profile associated with elongation to equilibrate part
σ_{bend}	Stress profile associated with bending to equilibrate part
σ^{induced} or σ_{ind}	Unbalanced induced stress
σ^{initial}	Initial stress
σ^{last}	Previous balanced residual stress
$\sigma_{\max}$	Maximum compressive stress after shot peening
σ^{new} or $\sigma^{\text{unbalanced}}$	User-defined unbalanced induced stress
$\sigma^{peening}$	Stress profile induced by peening near the surface
σ^{pressure}	Normal pressure during impact
σ^{residual} or σ_{res}	Balanced residual stress
σ_{surface}	Surface stress after shot peening
σ_{VM}	von Mises equivalent stress
$\sigma_{\text{VM}}^{\text{far field}}$	von Mises equivalent stress far from the surface
$\Delta\sigma^{\text{final}}$	Variation of residual stress as a function of the initial stress
$\Delta\sigma^{\text{reaction}}$	In-plane reaction stress during impact
τ	Shear stress
ψ	Tilt angle

Abbreviations

DOF	Degrees of freedom
EBSD	Electron backscatter diffraction
FE	Finite element
FWHM	Full width at half maximum

GOS	Grain orientation spread
HCF	High cycle fatigue
HK	Knoop hardness
HV	Vickers hardness
LCF	Low cycle fatigue
NCI	Normalized confidence interval
ND	Normal direction
PEEQ	Equivalent plastic strain
RD	Rolling direction
RVE	Representative volume element
SEM	Scanning electron microscope
TD	Transverse direction
TEM	Transmission electron microscope
XRD	X-ray diffraction

INTRODUCTION

Shot peening is a surface treatment commonly used to improve fatigue life in different fields such as the aerospace, automotive, biomedical, and power industries. Repeated impacts of small particles, called shots, at high velocity on a metallic part generate plastic strains near the surface. This induces a compressive residual stress state near the surface that inhibits crack propagation. Shot peening also leads to strain-hardening and increased surface roughness, which affect fatigue properties. This process has been used since the 1930s.

In the 1950s, Lockheed Martin needed to shape integrally-stiffened wing panels for the Constellation aircraft. Shot peening was then studied as a means to correct detrimental tensile surface residual stresses left by conventional cold forming. During the trials, its was found that shot peening itself allowed shaping useful curvatures and the wing panels were finally formed using this technique, known as peen forming. This manufacturing method uses the unbalanced stress state induced by peening to shape large and thin components with relatively small curvatures (*i.e.* large radii). It is now used in the aerospace industry to shape wing and fuselage skins, as well as rocket panels. Peen forming also has applications for distortion correction. The process is most commonly used for aluminium alloy components, but can be applied to other metallic materials such as steel and titanium alloys.

Shot peen forming is a versatile and cost-effective method for shaping large and thin components with integral stiffeners and variable thicknesses since complex contours can be obtained by carefully choosing the peening parameters applied on different areas of the part. The process is generally performed at room temperature and can be considered as dieless since it does not require forming dies. Jigs are however typically necessary to check the dimensional accuracy of the components. In addition, peen forming parameters can be easily modified, which reduces costs associated with design changes and can prove very useful for distortion correction. It should be noted that stress peen forming, a variation of peen forming in which the component is elastically prestressed to achieve more complex curvatures, requires jigs to preload the component during peen forming and is therefore more costly.

The versatility of the peen forming process also makes it difficult to comprehend and harvesting its full potential is still a challenge. Definition of processing procedures is generally based on empirical relationships and knowledge, geometrical methods and trial-and-error with prototype parts. While knowledge acquired from previous, similar parts can provide a good starting point for developing a procedure for a new part, introducing new contours and materials can be challenging. This leads to large development time and cost, as well as an inherent risk when introducing new geometries.

Since the 1980s, there have been many experimental studies and patents which related peen forming parameters and resulting curvatures. These studies revealed a number of significant phenomena that have an effect on the development of curvature. However, researchers took interest in combinations of peening parameters typical of specific applications and their conclusions often described behaviours qualitatively rather than provide detailed explanations that could be generalized to other situations. In the 1990s, analytical and numerical (finite element) research on shot peening and peen forming became more prominent and provided a better understanding of the mechanics of peen forming. These studies also introduced simulation and optimization methods for the process. The fundamental behaviours observed experimentally were modelled successfully for simple cases, but the more complex and potentially significant phenomena have not been investigated yet.

The purpose of this work was to develop predictive tools for shot peening and peen forming. This study relied on finite element simulation to reduce the dependence of peen forming process development on physical testing and had two main themes:

- Improve a random impact model for shot peening and investigate its possible uses;
- Develop a new peen forming modelling approach capable of simulating complex behaviours and parameters.

These models were validated with data acquired from the literature and from controlled shot peening and peen forming experiments.

This thesis is organized as follows. Chapter 1 presents a literature review on the shot peening and peen forming processes. Chapter 2 introduces the objectives of the project with respect to the findings of Chapter 1. Chapter 3 describes the relationship between the research objectives and the publication strategy. The five articles resulting from this work are included in Chapters 4 to 8. Chapter 4 presents the principles of the methodology developed in the project and its initial validation. Chapter 5 studies experimentally and numerically the effects of shot peening on an aerospace aluminium alloy. Chapters 6 and 7 describe the application of the forming simulation methodology to more complex peen forming studies involving material anisotropy and peening patterns. Chapter 8 investigates the potential use of finite element simulation for industrial peen forming applications. Chapter 9 discusses the relationships between the articles as well as complementary work performed during this project. The contributions from this thesis are finally summarized and topics for future studies are recommended.

CHAPTER 1

LITERATURE REVIEW

This section first introduces the principles of shot peening and peen forming. A review of experimental and finite element (FE) modelling works is then presented. Finally, information on the industrial applications of the peen forming process is provided.

1.1 Concepts and definitions

1.1.1 Shot peening

The main purpose of shot peening is to improve fatigue properties by inducing compressive residual stresses σ^{residual} near the surface. This is done by impacting a ductile metallic component repeatedly with small and hard shots at high velocity. During each impact, shot deformation remains mostly elastic while plastic strains occur in the target material. Impacts tend to compress the surface which, due to constant-volume plastic flow, leads to in-plane plastic stretching near the surface. Since the underlying material is not permanently deformed, it opposes this stretching. A typical residual stress profile after shot peening $\sigma^{\text{residual}}(z)$ is illustrated in Figure 1.1: compatibility of strains leads to in-plane compressive residual stresses near the surface, which are balanced by tensile residual stresses in the core of the component. Shot peening also results in strain-hardening near the surface as well as increased surface roughness and local damage: fatigue life and strength improvements depend on the combination of these effects and the applied loading (Lillamand *et al.*, 2001; Curtis *et al.*, 2003; Fathallah *et al.*, 2003, 2004; Guechichi and Castex, 2006; Luong and Hill, 2010; Zupanc and Grum, 2011). For aluminium alloys, shot peening also inhibits stress corrosion cracking (Kulkarni *et al.*, 1981).

The effect of shot peening in terms of residual stresses, strain-hardening, roughness and damage depends on many process parameters that can be divided into three categories (Kyriacou, 1996):

Shot: Size, shape, density, hardness, etc.

Flow: Mass flow, shot velocity, angle of impingment, exposure time, etc.

Target: Material behaviour, *e.g.* hardness, yield stress, Young's elastic modulus, work hardening, cyclic hardening or softening, strain-rate sensitivity, etc.

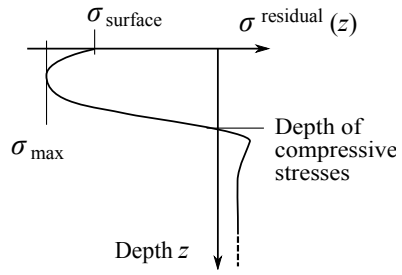

Figure 1.1 Typical residual stress profile $\sigma^{\text{residual}}(z)$ after shot peening.

Shot peening is typically performed with rounded cast steel, cut steel wire (usually conditioned), ceramic or glass particles (SAE Standard AMS2431, 2010) and with impact velocities ranging between 40 and 70 m/s (Meguid *et al.*, 1999). Shots and flow parameters generally need to be tailored to the target material. In some cases, two or more peening treatments can be applied successively to further improve fatigue properties (Benedetti *et al.*, 2009).

Shot peening metrics

In practical shot peening applications, it is not convenient to monitor accurately all shot and flow parameters in real time. Instead, processing is characterised in terms of Almen intensity and coverage. The Almen intensity of a given treatment is determined by peening multiple standardized SAE 1070 steel strips held in standardized Almen holders at different exposure times (Figure 1.2(a)). After peening, each strip is removed from its holder and its free deflection is measured using an Almen gauge (Figure 1.2(b)). This is a dedicated instrument that measures the deflection of the strip over a 31.75×15.88 mm area, also known as Almen arc height a_h. Finally, the arc height of each strip is plotted as a function of its exposure time t to obtain the saturation curve (Figure 1.2(c)). The saturation point is defined as the exposure time t_{sat} for which doubling the exposure time increases the arc height by 10%. The Almen intensity a_h^S of a treatment is the arc height at time t_{sat}. Three strip types are available to determine the intensity across a wide range of peening treatments (SAE Standard J443, 2010):

– "N" strip, 0.79 mm thickness, for peening intensities below 0.10mmA;
– "A" strip, 1.30 mm thickness, for peening intensities between 0.10mmA and 0.60mmA;
– "C" strip, 2.39 mm thickness, for peening intensities above 0.60mmA.

In the metric system, intensities are evaluated in mm$X$, where X is the strip type used (N, A or C); in the imperial system, intensities are quoted as, for instance, 18C, where 18 indicates the arc height at saturation in thousandths of an inch and C is the strip type. The intensity assesses the kinetic energy available in the shot stream and transferred to the strip. Different

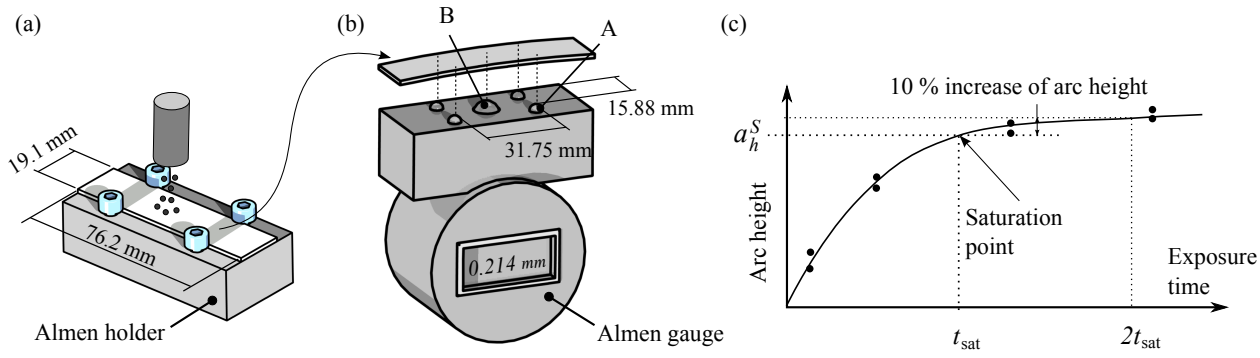

Figure 1.2 Determination of the Almen intensity. (a) Almen strip held on an Almen holder subjected to peening at a given exposure time. (b) The Almen arc height of the strip is then measured with an Almen gauge. (c) The saturation curve is built by peening multiple strips at different exposure times.

combinations of shot and flow parameters can yield the same intensity (Herzog *et al.*, 1996). Generally speaking, increasing the intensity (or energy) can be achieved with either heavier (larger and/or denser) shots or higher impact velocities.

The second measurand, coverage, evaluates the progress of peening (Figure 1.3). Coverage $c(t)$ at exposure time t is determined by dividing the area covered by impact dimples by the total area of the specimen and is generally expressed as a percentage (SAE Standard J2277, 2009). Full coverage is defined as indents covering 98% of the surface. For values greater than 100%, the percentage indicates the peening exposure time with respect to the time required for full coverage: for instance, 200% corresponds to peening at twice the exposure time required for full coverage. Coverage is easier to determine than exposure time, especially for complex components, since it is defined from the final surface state rather than from the processing procedure. It should be noted that the evaluation of coverage is somewhat subjective since the extent of the "impact dimple" is not always clearly defined.

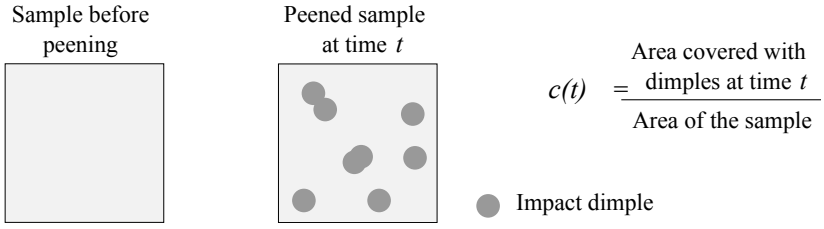

Figure 1.3 Definition of coverage $c(t)$

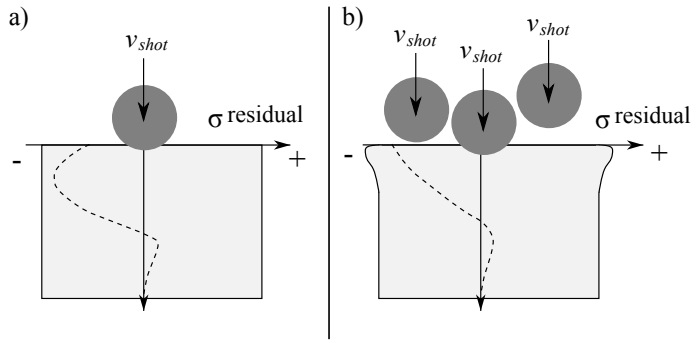

Figure 1.4 Origin of residual stresses after shot peening (Wolfhart, 1984).

Brief explanation of shot peening mechanics

To explain the different shapes of residual stress profiles $\sigma^{\text{residual}}(z)$ depending on shot, process and target parameters, Wolfhart (1984) described two different mechanisms leading to compressive residual stresses. First, Hertz's theory indicates that when a spherical indenter is pressed statically into a material, the maximum shear stress is located underneath the surface. As a result, the maximum plastic strains and residual stress are also observed below the surface (Figure 1.4(a)). The second phenomenon involves hammering of the surface by multiple indenters. In this case, in-plane stretching and residual stress amplitude are larger at the surface (Figure 1.4(b)). The residual stress profile after shot peening arises from a combination of these two mechanisms (Ebenau *et al.*, 1987).

1.1.2 Peen forming

The principle of peen forming can be explained as illustrated in Figure 1.5. Consider a flat component that is fully constrained and that cannot bend and elongate during peen forming. The stress profile in such a situation is labelled as induced stress $\sigma^{\text{induced}}(z)$ (VanLuchene *et al.*, 1995). Constraining forces F^{con} and moments M^{con} can be calculated from the induced stress profile as:

$$M^{\text{con}} = \int_0^h \sigma^{\text{induced}}(z) \left(z - \frac{h}{2} \right) \mathrm{d}z \tag{1.1a}$$

$$F^{\text{con}} = \int_0^h \sigma^{\text{induced}}(z) \, \mathrm{d}z \tag{1.1b}$$

where h is the thickness (Guagliano, 2001). It should be noted that F^{con} and M^{con} are calculated per unit width of the sheet. Releasing the constraints corresponds to applying opposite forces and moments. While the generation of induced stresses is clearly a plasticity-driven phenomenon, the response of the component following the release of the constraints is

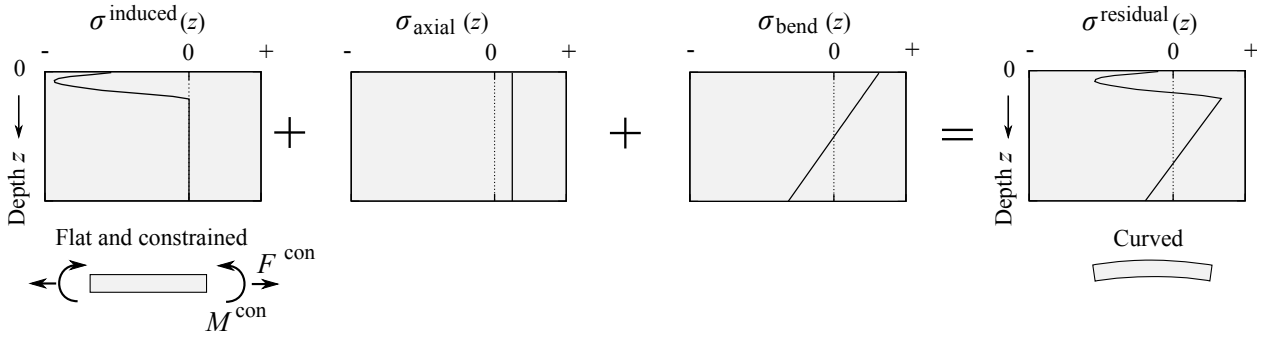

Figure 1.5 Relationship between induced stress σ^{induced} and residual stress σ^{residual} profiles.

usually elastic (Homer and VanLuchene, 1991), which allows using the superposition principle to calculate the stress profiles $\sigma_{\text{axial}}(z)$ and $\sigma^{\text{bend}}(z)$ associated with elongation and bending of the component, respectively (Guagliano, 2001):

$$\sigma_{\text{axial}}(z) = -\frac{F^{\text{con}}}{h} \tag{1.2a}$$

$$\sigma_{\text{bend}}(z) = -\frac{12M^{\text{con}}\left(z - \frac{h}{2}\right)}{h^3} \tag{1.2b}$$

and the residual stress profile $\sigma^{\text{residual}}(z)$ is determined as:

$$\sigma^{\text{residual}}(z) = \sigma^{\text{induced}}(z) + \sigma_{\text{axial}}(z) + \sigma_{\text{bend}}(z) \tag{1.3}$$

Assuming that deflections remain small and considering that shot peening an isotropic material typically introduces an equibiaxial stress field, the curvature $1/R$ of the component, where R is the radius of curvature, and in-plane elongation ε_e can be calculated as:

$$\frac{1}{R} = -\frac{12(1-\nu)M^{\text{con}}}{Eh^3} \tag{1.4a}$$

$$\varepsilon_e = -\frac{(1-\nu)F^{\text{con}}}{Eh} \tag{1.4b}$$

where ν is the Poisson's ratio and E is the Young's elastic modulus.

It should be noted that peen forming can also be performed at very high intensities, as shown in Figure 1.6(b) (Kondo *et al.*, 1979; Kopp and Schulz, 2002). In this case, plastic strains are present in the whole cross-section and are more important at the surface opposite to the impacted side. This leads to concave forming (*i.e.* the components bends away from the shot stream). When compared to convex peen forming, concave forming also results in larger elongations. In the present work, only convex forming is investigated.

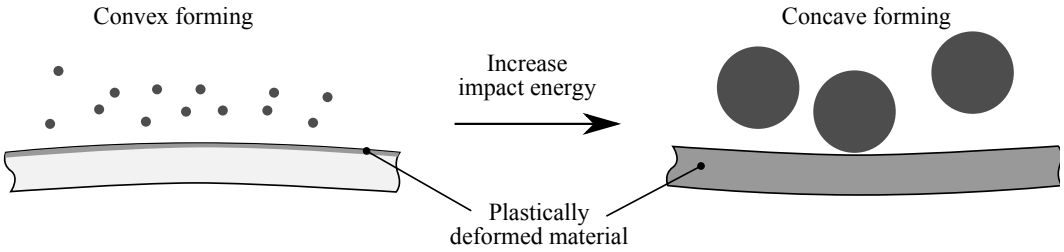

Figure 1.6 Difference between convex and concave forming.

1.2 Experimental studies on shot peening

The purpose of this section is to present a brief summary highlighting the various methods that have been used to characterize the process.

1.2.1 Residual stresses

The effects of different process parameters on the resulting residual stress profile $\sigma^{\text{residual}}(z)$ have been the subject of numerous experimental studies (Wolfhart, 1984; Ebenau *et al.*, 1987; Herzog *et al.*, 1996; Wang *et al.*, 1998; Lillamand *et al.*, 2001; Pariente and Guagliano, 2009; Zimmermann *et al.*, 2010; Miao *et al.*, 2010; Child *et al.*, 2011). Measurements have also been performed within the context of fatigue life, crack propagation or stress relaxation studies (Peyre *et al.*, 1996; Fathallah *et al.*, 2003; Kumar, 2006; Benedetti *et al.*, 2009; Luong and Hill, 2010). Residual stresses are often determined using the X-ray diffraction (XRD) technique and in-depth profiles are obtained by incremental electropolishing (Prevey, 1991). Some studies have also used the hole-drilling technique (Romero, 2002; Rodopoulos *et al.*, 2004; Sidhom *et al.*, 2005; Zupanc and Grum, 2011), which relies on relaxation of strains due to material removal. It should however be noted that this method may not be accurate when the residual stress amplitude is larger than 60% of the yield stress (ASTM Standard E837, 2008). Finally, some researchers have also determined residual stress profiles using the slitting method, which relies on distortion generated by cutting a part subjected to residual stress (Luong and Hill, 2010), or from indentation testing (Arun Prakash *et al.*, 2010).

1.2.2 Strain-hardening

Micro-indentation (or hardness) testing has often been used to quantify the depth affected by peening as well as strain-hardening in the thin layer of material experiencing large plastic strains during peening (Vöhringer, 1987; Peyre *et al.*, 1996; Ferreira *et al.*, 1996; Rodopoulos *et al.*, 2004; Benedetti *et al.*, 2009; Pariente and Guagliano, 2009; Kang *et al.*, 2010; Arun Prakash *et al.*, 2010; Zaroog *et al.*, 2011b; Zupanc and Grum, 2011; Mylonas and Labeas,

2011; Child *et al.*, 2011). One challenge with indentation testing is that, in addition to material hardening, the compressive residual stress state also contributes to higher measured hardness values near the surface (Vöhringer, 1987; Child *et al.*, 2011). Other works have used the width of the X-ray diffraction peak, generally the full width at half maximum (FWHM), to evaluate the dislocation density and micro-residual stresses and assess the degree of strain-hardening (Vöhringer, 1987; Ebenau *et al.*, 1987; Fathallah *et al.*, 2003, 2004; Guechichi and Castex, 2006; Pariente and Guagliano, 2009; Turski *et al.*, 2010; Zaroog *et al.*, 2011b). More recently, Child *et al.* (2011) used crystallographic orientation data acquired with electron backscatter diffraction (EBSD) mapping to evaluate the average orientation spread within each grain as an indicator of strain-hardening.

Mylonas and Labeas (2011) noted that knowledge of the degree of cold work is important since the work-hardened material may exhibit different properties than the base material. It should be noted that work-softening effects have also been observed after shot peening for some materials (Vöhringer, 1987).

1.2.3 Microstructure

Considering that large plastic strains can lead to grain refinement (Wu *et al.*, 2002; Arun Prakash *et al.*, 2010), the microstructure of various materials after shot peening has also been studied. For instance, grain refinement has been observed after peening in stainless steel and a nickel alloy (Turski *et al.*, 2010; Child *et al.*, 2011). Child *et al.* (2011) also reported high dislocation densities near the surface of nickel superalloy Udimet 720Li peened with a high intensity (8-10A) using ion beam induced secondary electron imaging. In addition, complex phenomena can occur in some material types. For instance, shot peening of steel with specific composition and heat treatments can lead to phase transformation of austenite into martensite (Vöhringer, 1987; Turski *et al.*, 2010). (Vöhringer, 1987) and Ebenau *et al.* (1987) also studied the crystallographic texture of Ck 45 steel before and after shot peening. It was found that peening significantly altered the texture near the surface by aligning the slip planes with the surface.

For aluminium alloys, optical micrographs taken after etching suggested that peening does not affect the microstructure significantly (Benedetti *et al.*, 2009; Zaroog *et al.*, 2011a). On the other hand, de los Rios *et al.* (2000) reported a significant local decrease of the average grain size along the direction perpendicular to the peened surface. Zupanc and Grum (2011) also noted that the orientation of second-phase particles in AA7075-T651, originally aligned with the rolling direction, changed after peening. Moreover, transmission electron microscopy (TEM) of aluminium samples peened with high intensity and coverage have shown the development of complex dislocation tangles, microbands, cell blocks, and submicron grain

structures depending on the extent of plastic straining (Wu *et al.*, 2002; Arun Prakash *et al.*, 2010). The choice of the observation method is therefore very important to properly evaluate the material state after peening.

1.2.4 Surface topography

In terms of surface state, two aspects at different length scales have been considered.

First, surface roughness over distances much larger than the indent diameter has been studied by many researchers (Li *et al.*, 1992; Ferreira *et al.*, 1996; Clausen and Stangenberg, 1999; Fathallah *et al.*, 2003; Rodopoulos *et al.*, 2004; Benedetti *et al.*, 2009; Miao *et al.*, 2010; Luong and Hill, 2010; Zupanc and Grum, 2011) in order to determine stress concentration factors. Roughness can be determined from 2D or 3D data acquired using contact or non-contact methods.

Secondly, local defects at smaller scale such as sharp microcracks (surface and sub-surface), scaling, overlaps and embedded shots have been investigated as crack nucleation sites (Fathallah *et al.*, 2003, 2004; Sidhom *et al.*, 2005; Luong and Hill, 2010; Zupanc and Grum, 2011). Due to their small size, these defects are typically characterized using scanning electron microscopy.

1.2.5 Process heterogeneity

Most studies have investigated the average effect of shot peening on the material. However, the stochastic nature of the process leads to a spatially heterogeneous material state. Vöhringer (1987) investigated this dispersion by performing XRD and indentation measurements. The surface residual stress was determined at different locations using a X-ray beam of dimension similar to a single impact dimple and considerable differences were observed. On the other hand, the strain-hardening state was found to be relatively homogeneous. In addition, roughness after shot peening and the resulting stress concentration factors can exhibit a significant scatter (Clausen and Stangenberg, 1999; Miao *et al.*, 2010). Surface defects are also by nature a local, non-uniform phenomenon: for instance, Fathallah *et al.* (2004) noted that their density increased when increasing coverage.

Characterizing the average effect allows comparing different sets of peening parameters. However, fatigue phenomena, especially in the high cycle fatigue (HCF) regime, are often driven by the most unfavourable regions in a material. Knowledge of the dispersion of residual stresses, strain-hardening, roughness and local damage would be useful in the context of probabilistic fatigue life or strength predictions (Bouraoui *et al.*, 2009).

1.3 Experimental studies on peen forming

Since peen forming applications were initially based upon empirical knowledge, extensive experimental testing has been performed by manufacturers to relate process parameters to the resulting deformed shapes, as well as to explore the mechanics of the process (Harburn and Miller, 1982; Kopp and Ball, 1987; VanLuchene *et al.*, 1995). However, most of these results were most likely not published.

Early studies by Kondo *et al.* (1979, 1981); Kondo (1984) presented results on the effects of process parameters, constraints and prestressing on the resulting contours of small samples.

Kulkarni *et al.* (1981) investigated the effects of multiple shot, flow and target parameters in an industrial context by peen forming samples made of two aluminium alloys (AA2024-T3 and AA7075-T6) with different thicknesses using a wide range of representative shot diameters, impact velocities, and impact densities. The typical specimen size was 152 × 610 mm. The influences of feed direction and the orientation of the rolling direction with respect to the sample were also evaluated. Their conclusions included:

- Rectangular samples (with an aspect ratio of 4 or 1/4) exhibited similar curvatures along orthogonal directions. On the other hand, square samples developed cylindrical curvatures influenced by secondary effects such as the anisotropy and residual stresses generated by rolling;
- Sample thickness relative to its in-plane dimensions affected the development of curvature;

The latter was also noted by Cochennec *et al.* (2009) in their study of completely and partially peened 300 × 200 mm AA2024-T3 sheets with thicknesses of 2 and 5 mm.

Cao *et al.* (1995) studied the evolution of radii of curvature for Almen strips during the Almen test (see Figure 1.2). Radii were determined for strips constrained in the Almen holder and after removing the holder bolts. Results showed that significant curvatures developed while the strips were still held in the holder. An analytical method was also introduced to model this phenomenon. For simplification purposes, it was assumed that peening always restores the same "saturation" induced stress profile in the affected depth. This hypothesis relied on the experimental observation that residual stresses tended to stabilize as the exposure time increased.

It should be noted that stress peen forming has also been investigated (Li, 1981; Miao *et al.*, 2010). This variation of peen forming is however beyond the scope of this project and is not reviewed herein.

1.4 Shot peening modelling

Finite element simulation of shot peening typically uses an explicit scheme such as the central difference rule with a diagonal mass matrix. This scheme advances the solution with a large number of small time increments and is well suited for analyzing a dynamic response over a short time period. Simulations typically consist of projecting one or many particles towards the target surface with a given initial velocity and determining the response of the material during and after the impact(s). It should be noted that some authors adopted a Newmark implicit time-integration scheme (Meguid *et al.*, 1999; Schiffner and Droste gen. Helling, 1999) or equivalent static loading (Frija *et al.*, 2006).

For an isotropic material, the minimum stable time increment Δt depends on the mesh size and material properties and can be evaluated as:

$$\Delta t = k_1 \times L_{\min} \sqrt{\frac{\rho}{E}} \tag{1.5}$$

where $L_{\min}$ is the minimum dimension in the FE mesh, ρ is the density of the material and k_1 is a variable depending on the Poisson's ratio of the material.

1.4.1 Model types

Early shot peening simulations involved a single impact and were used to study the effect of shot, flow and target parameters (Grasty and Andrew, 1996; Schiffner and Droste gen. Helling, 1999; Meguid *et al.*, 1999; Han *et al.*, 2000a; Meo and Vignjevic, 2003; ElTobgy *et al.*, 2004; Hirai *et al.*, 2005; Hong *et al.*, 2008b). Analysis variables such as the friction coefficient μ and the contact algorithm were also investigated. Meguid *et al.* (1999) also simulated two adjacent impacts (co-indentation model) to determine the effect of the separation distance between shots. This parameter has a significant influence on the resulting stress field. Han *et al.* (2002) discussed the advantages of a discrete representation of shots with rigid surfaces. On a similar topic, ElTobgy *et al.* (2004) noted that the choice of modelling shots as rigid, elastic or elasto-plastic also has a significant effect on the resulting stress state. Obviously, an appropriate model for the shots depends on the relationship between the target and shot material properties (stiffness, hardness, etc.).

Symmetry cells were introduced to take into account the effect of a larger number of impacts on the residual stress state while keeping a low computational cost (Schiffner and Droste gen. Helling, 1999; Meguid *et al.*, 2002; Frija *et al.*, 2006; Meguid *et al.*, 2007; Kim *et al.*, 2010). Multiple impact models with predefined patterns of indents and limited or no symmetry boundary conditions were also widely studied (Grasty and Andrew, 1996; Guagliano,

2001; Han *et al.*, 2002; Schwarzer *et al.*, 2002; Klemenz *et al.*, 2009; Kang *et al.*, 2010). Multiple impact models allowed studying the effects of coverage as well as the dispersion and biaxiality of the calculated residual stress fields (Meguid *et al.*, 2002; Majzoobi *et al.*, 2005; Klemenz *et al.*, 2006; Meguid *et al.*, 2007; Kang *et al.*, 2010; Kim *et al.*, 2010).

Finally, random impact models were proposed to take into account the stochastic nature of shot peening. Wang *et al.* (2002) mentioned a model involving 1000 randomly positioned shots on a rather coarsely discretized model and discussed the prediction of coverage. It was noted that plastic coverage, evaluated from the accumulated plastic strain in each element, did not correlate well with visual coverage. Dai and Shaw (2007) used an impact model with random impact locations in their study of shot peening and severe plastic deformation processing. Miao *et al.* (2009) presented a smaller and more refined model with random impact coordinates. The potential of such a model to predict residual stresses, saturation curves, coverage and surface roughness was discussed. Since the impact sequence was random, multiple analyses were run for each number of impacts studied to determine the average values as well as their distribution. Zimmermann *et al.* (2010) compared ordered and random impact sequences and studied the resulting residual stress distributions. They observed that the calculated average residual stress profile was sensitive to the impact sequence and that a random model required a greater number of impacts to reach a given coverage when compared to an ordered model, which increased the calculated accumulated plastic strains. It was noted that while both random and ordered impacts led to good predictions in terms of residual stresses (for 100% coverage), the random model yielded a more realistic surface topography.

For multiple impact simulations, different approaches have been proposed to determine the average residual stress profiles in the material. Area averaging methods were introduced by Han *et al.* (2002) and Schwarzer *et al.* (2002) to account for the heterogeneity of the residual stresses at the scale of the dimple size. Meguid *et al.* (2007) suggested an averaging method based on a regular grid in their symmetry cell and briefly discussed the issue of the definition of the peened surface ($z = 0$).

One challenge with dynamic simulations is oscillation of the response. To determine the stable residual stress state, some artificial damping can be introduced throughout the analysis Schiffner and Droste gen. Helling (1999); Han *et al.* (2000b); Meguid *et al.* (2002); Meo and Vignjevic (2003); ElTobgy *et al.* (2004); Kim *et al.* (2010). Another method consists of adding a static stabilization step periodically during the impact analyses (Kang *et al.*, 2010; Bhuvaraghan *et al.*, 2010). Models without symmetries can include infinite elements at their boundaries to minimize energy reflection into the mesh (Schwarzer *et al.*, 2002; Klemenz *et al.*, 2009; Zimmermann *et al.*, 2010; Bagherifard *et al.*, 2010; Bhuvaraghan *et al.*, 2010).

1.4.2 Material constitutive theory

Shot peening creates large plastic strains and high strain-rate loading with strain-rates up to 10^6 s^{-1} (Meguid *et al.*, 2007). In addition, as coverage increases, the material is subjected to reversed cyclic strain due to repeated impact: the Bauschinger effect and kinematic hardening may be significant in determining the material response (Al-Hassani, 1984). Finally, the loading history varies from one point to another in the target. This makes the material constitutive theory a key element for shot peening simulations.

Strain-rate sensitivity

Table 1.1 summarizes simulation works that have considered the influence of strain-rate sensitivity. Evans (2002) measured dynamic stress-strain curves for three different materials up to 10 s^{-1} and extrapolated values for larger strain-rates. Good agreement was observed between an experimental residual stress profile and the numerically predicted profile for the titanium alloy. Meguid *et al.* (2002) noted that adding the strain-rate dependency in the material law for AISI 4340 steel increased the predicted residual stress amplitude. Schwarzer *et al.* (2002) used a constitutive law that took into account the effects of temperature and strain-rate on the flow stress based on thermally activated dislocation slip. The model significantly overestimated the residual stress amplitude measured in AISI 4140 steel. ElTobgy *et al.* (2004) used the Johnson-Cook model, including thermal and failure effects, to simulate shot peening of AISI 4340 steel and the calculated residual stress profiles were in fairly good agreement with experimental data for two different impact velocities. For a single impact, thermal effects were found to be negligible. Including strain-rate effects decreased the calculated residual stress amplitude, an observation contrary to that of Meguid *et al.* (2002). In Majzoobi *et al.* (2005), modelling the behaviour of two types of steel at high strain-rates using the Johnson-Cook and Cowper-Symonds model correctly predicted indent shapes and one residual stress profile.

Cyclic properties and kinematic hardening

Other studies have modelled kinematic hardening of the material subjected to multiple impacts (Table 1.2). Guagliano (2001) considered the stabilized cyclic properties of two types of steel and a kinematic work hardening rule to calculate the residual stress field under a single impact surrounded with other indents. This corresponded to simulating impacts on a material that had previously been subjected to multiple impacts. The model correctly predicted the surface and maximum compressive stresses but underestimated the depth of compressive residual stresses. Bagherifard *et al.* (2010) modelled the cyclic behaviour of 39NiCrMo3

Table 1.1 Numerical studies taking into account strain-rate sensitivity.

Study	**Characterisation**	**Material**	**Model type**
Evans (2002)	Up to 10 s^{-1}	AA5052 316 stainless steel Ti-6Al-4V	Ordered impacts
Meguid *et al.* (2002)	Up to 10^5 s^{-1}	AISI 4340 steel	Symmetry cell
Schwarzer *et al.* (2002)	- -	AISI 4140 steel	Ordered impacts No symmetry
ElTobgy *et al.* (2004)	-	AISI 4340 steel	Single impact
Majzoobi *et al.* (2005)	Up to $\approx 10^2$ s^{-1}	AISI 4340 steel	Symmetry cell
Meguid *et al.* (2007)	Up to 10^3 s^{-1}	Ti-6Al-4V	Symmetry cell
Bhuvaraghan *et al.* (2010)	-	IN718 (nickel alloy)	Single impact

Table 1.2 Numerical studies taking into account cyclic behaviour.

Study	**Characterisation**	**Material**	**Model type**
Guagliano (2001)	Stabilized cyclic properties	SAE 1070 39NiCrMo3 steel	Ordered impacts
Lillamand *et al.* (2001)	Transient and stabilized cyclic properties	Ti-6Al-4V	Analytical impacts
Bagherifard *et al.* (2010)	Stabilized cyclic properties properties, strain amplitudes up to $\pm 1.6\%$	39NiCrMo3 steel	Random impacts

steel, which exhibited cyclic softening, with the non-linear kinematic Chaboche hardening model. Predictions of surface and maximum compressive residual stresses correlated well with experimental measurements. The authors also noted that the Johnson-Cook model (strain-rate dependent with isotropic hardening) overestimated the residual stress amplitude.

Material laws with kinematic hardening and strain-rate sensitivity

Recent studies have proposed more detailed consitutive theories combining strain-rate sensitivity and isotropic-kinematic hardening (Table 1.3). Klemenz *et al.* (2009) performed tensile tests at varying temperatures and strain-rates as well as push-pull tests (at a strain-rate of 10^{-4} s^{-1}) on quenched and tempered AISI 4140 steel. A viscoplastic model taking into account strain-rate and thermal effects with isotropic-kinematic hardening was developed and programmed with a user subroutine in `ABAQUS`. This constitutive theory used a flow condition

expressed as:

$$F = \sqrt{\frac{3}{2}(\mathbf{s} - \boldsymbol{\xi}) : (\mathbf{s} - \boldsymbol{\xi})} - \sigma^* - k_0 - K \leq 0 \tag{1.6}$$

where $\mathbf{s}$ is the deviatoric stress tensor, k_0 is a material parameter defining the initial athermal flow stress and the other terms are described below. The law considered the following behaviours:

- Kinematic hardening, meaning that the yield surface moves when yielding occurs. This models the Bauschinger effect. The kinematic component was expressed as the sum of two back-stress tensors $\boldsymbol{\xi}_1$ and $\boldsymbol{\xi}_2$ defining the center of the flow surface:

$$\dot{\boldsymbol{\xi}}_i = c_i \dot{\boldsymbol{\varepsilon}}_p - b_i \boldsymbol{\xi}_i \dot{\bar{\varepsilon}}_p \tag{1.7}$$

  with

$$\dot{\bar{\varepsilon}}_p = \sqrt{\frac{2}{3}(\dot{\boldsymbol{\varepsilon}}_p : \dot{\boldsymbol{\varepsilon}}_p)} \tag{1.8}$$

  where $i = [1, 2]$, c_i and b_i are material parameters, $\dot{\boldsymbol{\varepsilon}}_p$ is the plastic strain rate tensor and $\dot{\bar{\varepsilon}}_p$ is the equivalent plastic strain rate.
- The effect of temperature and strain-rate on the flow stress σ^*, with:

$$\sigma^* = \sigma_0^* \left[1 - \left(\frac{kT \ln(\dot{\varepsilon}_0/\dot{\varepsilon})}{\Delta G_0}\right)^n\right]^m \tag{1.9}$$

  where T is the temperature (in K), k is the Boltzmann constant and σ_0^*, $\dot{\varepsilon}_0$, ΔG_0, n and m are material parameters. The evolution of temperature was calculated adiabatically for each element.
- The athermal evolution K of the flow stress as a function of the accumulated plastic strain was modelled as:

$$\dot{K} = -\beta(Q + K)\dot{\bar{\varepsilon}}_p \tag{1.10}$$

  where Q is the asymptotic value for K for a given strain amplitude and is defined as:

$$\dot{Q} = 2\mu\eta(Q_{\max} - Q)\dot{q} \tag{1.11}$$

  with the initial value Q_0, $Q_{\max}$, β, μ and η being material parameters. This strain memory term required an internal variable $\dot{q}$ to account for the maximum plastic strain experienced by each element, which results in cyclic hardening or, as observed for AISI 4140, cyclic softening.

Residual stress predictions were in good agreement with experimental data for different peening parameters (shot size and impact velocity). When simulating push-pull tests, it was

not possible to model accurately both initial loading and cyclic behaviour: a compromise was required when optimizing material parameters.

Zimmermann *et al.* (2010) took into account strain-rate dependency and cyclic behaviour in their study of shot peening of IN718 nickel alloy. Their formulation for strain-rate dependency and isotropic hardening was however different from that by Klemenz *et al.* (2009) and is not presented here. Calculated residual stress profiles and depths of strain-hardening were in good agreement with experimental data. Simulations also correctly predicted the increase of the depth subjected to compressive residual stresses with increasing coverage.

Mylonas and Labeas (2011) modelled kinematic hardening and strain-rate sensitivity for aluminium alloy AA7449-T7651 subjected to shot peening. The kinematic hardening behaviour was determined based on Bauschinger tests in which samples were first stretched to a predefined strain and then compressed until buckling occurred. A multi-linear kinematic law without an isotropic hardening component was used. The stabilized cyclic behaviour of the material was therefore not taken into account. The high strain-rate behaviour of the alloy was characterized using a split Hopkinson pressure bar setup and modelled with the Cowper-Symonds equation.

It is interesting to note that Fribourg (2009) developed a microstructure-based model to describe the behaviour of age-hardenable AA7449-T7651 subjected to different thermomechanical treatments, including shot peening. This model included isotropic and kinematic hardening as well as strain-rate effects and took into account physical work hardening mechanisms such as precipitates, forest dislocations and Orowan loops.

Table 1.3 Numerical studies taking into account kinematic hardening and strain-rate sensitivity.

Study	**Characterisation**	**Material**	**Model type**
Klemenz *et al.* (2009) Klemenz *et al.* (2007) Klemenz *et al.* (2006)	Strain-rate 10^{-4}-10^{-3} s^{-1} Temperature 100 - 573 K Strain amplitude ±1% - 9%	AISI 4140	Ordered impacts no symmetry
Zimmermann *et al.* (2010) Zimmermann *et al.* (2009)	Strain-rate 10^{-3}-10^{4} s^{-1} Strain amplitude up to ±6%	IN718	Ordered and random impacts
Mylonas and Labeas (2011)	Linear kinematic hardening, strain-rate up to 8×10^{3} s^{-1}	aluminium alloy 7449-T7651	Random impacts

1.4.3 Surface damage

Lillamand *et al.* (2001) and Frija *et al.* (2006) also proposed methods to predict the occurence of damage. Their law was based on the accumulated plastic strain, the hydrostatic pressure and the Von Mises equivalent stress in each element. Simulation results by Frija *et al.* (2006) suggested that damage would reduce the residual stress amplitude near the surface. Correlating such predicted damage with actual scaling or microcracks however remains a complicated task.

1.4.4 Analytical modelling

Analytical models have also been proposed to predict the residual stress state after shot peening (Fathallah *et al.*, 1996; Franchim *et al.*, 2009; Miao *et al.*, 2011). Although their capabilities remain somewhat limited when compared to numerical models with respect to the phenomena that could be taken into account, these developments can provide approximate solutions quickly and lead to a better understanding of the process. It should be noted that this project does not investigate analytical approaches.

1.4.5 Input parameters

It is worth noting that there is a distinction between the terminology of experimental and numerical studies. Experimental works typically describe peening treatments in terms of intensity (for a given shot type and size) and coverage since they are easier to measure. However, these parameters cannot be used directly as input data in analytical or finite element models. In addition to shot type and size, modelling requires physical parameters such as impact velocity and an evaluation of peening progress such as the impacting mass on the target. It should be noted that, while some studies directly measured shot velocities (Cao *et al.*, 1995; Zimmermann *et al.*, 2010), others determined it from empirical and/or numerical relationships (Wang *et al.*, 2002; Kim *et al.*, 2010).

1.5 Peen forming modelling

One possible method for simulating the peen forming process consists of "direct simulation" of every impact on the component to be shaped (Han *et al.*, 2002). This approach was studied by Grasty and Andrew (1996), Wang *et al.* (2002) and Kang *et al.* (2010) by combining dynamic impact simulations with static springback analyses. Their models however remained very small (20×20 mm) due to the high computational cost of impact simulations.

Alternate "equivalent loading" methods are therefore required to reduce calculation time

(Grasty and Andrew, 1996; Han *et al.*, 2002). These are based on the assumption that induced stresses and strains are distributed uniformly over the peened surface and vary only depending upon depth z (Han *et al.*, 2002). A much coarser mesh can then be used in the plane of the surface for forming simulations when compared to impact analyses. This hypothesis is well supported by the research of Grasty and Andrew (1996), Wang *et al.* (2002) and Kang *et al.* (2010) and is only true at a scale much greater than that of a single indent, as discussed in Section 1.4.1. It should be noted that its validity at very low coverage levels, where each indent is well separated from its neighbours, has not been fully studied yet. Forming simulation methods can be categorized into three groups based on the methodology used to model the process:

1. Thermal equivalent loading;
2. Pressure equivalent loading;
3. Induced stresses.

1.5.1 Thermal equivalent loading

The possibility of using thermal equivalent loading to model peen forming was mentioned by Homer and VanLuchene (1991), but very little information was provided. Simple temperature gradients were used to simulate the equivalent bending and stretching effects of peen forming. Loads were determined from empirical relationships.

Levers and Prior (1998) presented a thermal loading method in which temperature distributions $\Delta T(z)$ were used in combination with the coefficient of thermal expansion α to input unbalanced initial stress states in shell elements, as illustrated in Figure 1.7. By varying the imposed temperature T at each section point, a distribution of thermal strains corresponding to the experimentally measured induced stress profile was obtained. It was mentioned that impact simulations could also provide the induced stress profiles. Multi-layer shell elements were defined with a higher density of section points (through-thickness integration points) near the surfaces to capture the large gradients of the stress profiles generated by peening. The equilibrium configuration was calculated as a springback analysis by `ABAQUS`. Two suc-

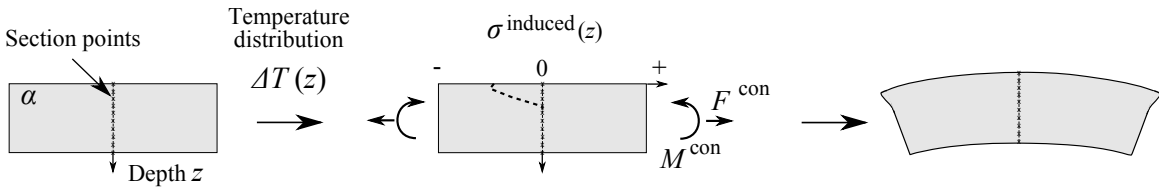

Figure 1.7 Forming simulation method by Levers and Prior (1998).

cessive peen forming treatments were simulated on a representative aerospace component and it was noted that the method could also account for external loads (*e.g.* clamps). Zeng (2002) and Huang *et al.* (2006) discussed a similar approach which relied on empirical relationships instead of measured or predicted induced stress profiles. Finite element models for an integrally-stiffened panel and for forming a saddle shape were briefly presented.

Gardiner and Platts (1999) applied a similar methodology in their study of stress peen forming. Equivalent thermal loading was used to investigate the effect of initial bending on calculated stresses after peening. The main difference was that analyses by Levers and Prior (1998) remained elastic while those by Gardiner and Platts (1999) included plasticity.

Wang *et al.* (2006) relied on thermal loading to create localized plastic strains in multi-layer shell elements. Their equivalent loading cycle consisted of four steps (Figure 1.8):

1. Constrain all degrees of freedom of the shell element;
2. Apply a temperature distribution $\Delta T(z)$ to permanently stretch the peened surface;
3. Restore the initial temperature;
4. Release boundary conditions, except those associated with physical constraints during processing.

This led to a deformed shape equivalent to that generated by peen forming. The loading unit was defined so as to correspond to a plastic coverage of approximately 80%. The depth of plastic strains h_{p} was determined analytically from an equation relating shot and target parameters to the resulting indent size while the thermal strain amplitude ε_t was calibrated to experimental results.

Yamada *et al.* (2002) also used thermal loading to create local plastic strains equivalent to those introduced by shot peening. Their method relied on a distribution of coefficients of thermal expansion $\alpha(z)$ and on a temperature cycle, as shown in Figure 1.9. Plastic strains resulted from the mismatch of expansion between regions with large and small α when increasing temperature from T_0 to T_1. Upon resetting the temperature to its initial value T_0, plastic stretching of the surface led to elongation and bending of the component similar to those associated with shot peening. Little information was provided on the definition of the coefficients of thermal expansion and temperature cycle.

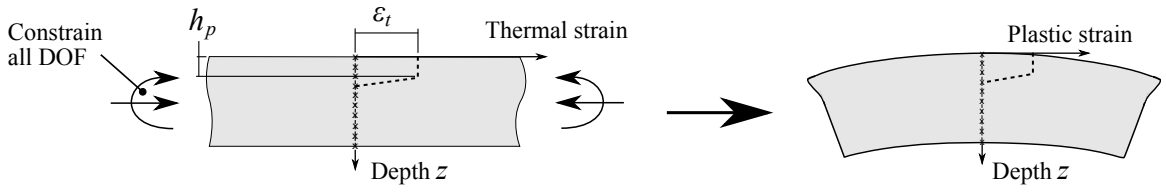

Figure 1.8 Forming simulation method by Wang *et al.* (2006).

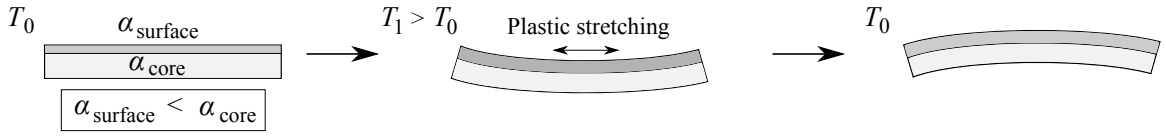

Figure 1.9 Forming simulation method by Yamada *et al.* (2002).

In all cases, it is important to note that temperature and/or coefficients of thermal expansion are numerical tools used to simulate the forming effect and are not physically related to the process mechanics (Wang *et al.*, 2006).

Related method Cochennec *et al.* (2009) presented a method in which a plastic strain gradient was introduced in the model to simulate peen forming. Two methods for experimentally calibrating the gradient were suggested: the first was based on measured residual stress profiles and the second on measured deflections. Although it was not explicitly stated, it seems likely that this approach relied on thermal loading.

1.5.2 Pressure loading

Grasty and Andrew (1996) performed impact simulations and observed build-up of plastic strains as a series a layers. Based on this result, a "squeezed layer" was created by applying pressure to elements near the surface, as shown in Figure 1.10. The first step consisted of subjecting a few layers of continuum elements near the surface to a pressure so that they became permanently stretched parallel to the surface. Normal displacements were blocked for the bottom nodes (opposite to the peened surface) during this step. In the second step, the pressure and the boundary conditions were released and the free deformed shape was calculated. The pressure was calibrated from experimental data. The authors noted that the use of solid elements led to excessive computation time due to the large number of elements.

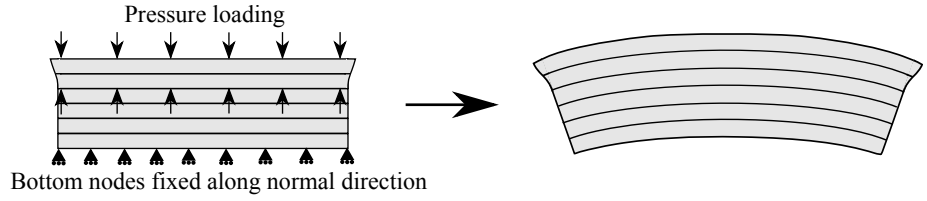

Figure 1.10 Forming simulation method by Grasty and Andrew (1996).

1.5.3 Induced stresses

Han *et al.* (2002) combined dynamic impact analyses with static forming simulations to model peen forming with a multi-scale approach:

1. Shot peening simulations were conducted on a small-scale model and provided numerically calculated induced stress profiles at various stages during processing;
2. These profiles were then input as an initial condition in a larger-scale continuum element-based model to determine the shaping effect by means of a static springback analysis.

One advantage of this approach is that induced stresses can be predicted using the shot peening FE models described in Section 1.4, thus reducing the dependence upon experimental calibration. It was suggested that, in addition to stresses or elastic strains, the plastic strain state should also be transferred from the impact to the forming simulations in order to account for possible yielding during springback. The authors noted that the methodology allowed simulating different induced stress profiles in different regions of a model with varying boundary conditions. Potential convergence issues, such as those arising from large displacements (geometrical non-linearities), were mentioned. It was suggested that gradually releasing boundary conditions or applying the induced stress profiles could lead to better convergence. In their forming simulation of a 150×50 mm, 4 mm-thick AA7050-T7651 sample, no significant difference was found between geometrically linear and non-linear analyses. In addition, gradual load application was not required to achieve convergence.

1.5.4 Modelling the incremental nature of peen forming

The simple formulation presented in Section 1.1.2, although useful to understand the basic principles, neglects a key feature of peen forming: components actually deform continuously throughout processing (Cao *et al.*, 1995). Among the FE simulation methods described above, those of Grasty and Andrew (1996) and Wang *et al.* (2006) have considered the incremental aspect of peen forming.

Grasty and Andrew (1996) first conducted impact simulations with nine impacts and boundary conditions fixing the bottom nodes of the model and tested two analysis sequences:

- Simulate all nine impacts and then release the boundary conditions;
- Simulate the first impact, release the boundary conditions to find the equilibrium configuration, block normal displacements of the bottom nodes on the deformed shape, simulate the second impact, release the boundary conditions, and so on.

They observed that the incremental analysis led to a deflection approximately 30% larger than that for the "one-step" approach. Although these simulations were performed with a very

coarse mesh, they provided useful information on the incremental nature of peen forming. The same principle was applied using the "squeezed layer" approach described in Section 1.5.2. A number of pressure loading cycles were simulated while releasing the constraints between each cycle, until the calculated deflection did not increase significantly (5 cycles). The final deflection was $\approx 30\%$ larger than that predicted after a single loading cycle. The modelling methodology was validated using rectangular 10×50 mm and circular 25 mm-diameter, 0.9 mm-thick annealed AA5251 samples peened near saturation. Specimens were free to bend and elongate during peening. The appropriate squeezing pressure was calibrated from the experimental deflection of the rectangular strip and then applied to the disc model: predicted deflection for the disc was then in good agreement with the experimental result.

In Wang *et al.* (2006), the thermal loading unit, which was defined for a relatively low coverage, was applied repeatedly. Each loading cycle corresponded to a specific peening time: this relationship was also calibrated to experimental data. After calibration, the methodology correctly predicted the evolution of arc height when increasing peening time for 76×19 mm, 3 mm-thick AA5251-H22 samples that were free to bend and elongate during peening. The authors noted that work was underway to study the effects of geometry, fixtures (constraints and prestressing) and sequences, but no result was published.

1.6 Actual peen forming procedures

While shot peening aims to create a uniform compressive stress field near the surface to improve fatigue behaviour, the objective of peen forming is to manufacture a component to prescribed contours as quickly and inexpensively as possible. Due to their respective purposes, there are key differences between the shot peening and peen forming processes. First, when compared to shot peening, peen forming typically requires larger shots and/or velocities to achieve the desired curvatures, especially for thicker components as suggested by Eq. (1.4). Second, peen forming may be performed at low coverage percentages (Baughman, 1984; Ramati *et al.*, 1999) to visually assess the evolution of processing and leave room to increase curvature by increasing exposure time and coverage, if required. Third, peen forming generally does not use the same peening parameters over the whole component.

Actual peen forming applications typically involve complex components and contours. To achieve a good strength-to-weight ratio, aerospace parts are often machined with variable thicknesses and integral stiffeners (Moore, 1982; Homer and VanLuchene, 1991; Yamada *et al.*, 2002). While some applications such as fuselage and rockets panels require relatively simple cylindrical or spherical curvatures (Kopp and Ball, 1987; Friese *et al.*, 2002), wing skin forming aims to obtain complicated aerodynamic profiles with varying curvatures. Even for simple

contours, different peening parameters must be applied in various regions of the component (Friese *et al.*, 2002; Yamada *et al.*, 2002). Furthermore, peening can be performed on both sides of the component to control elongation (stretching) as well as bending (Homer and VanLuchene, 1991; O'Hara, 2002). Peening on both sides of a plate introduces compressive induced stresses near both surfaces: based on Equations (1.1) to (1.4), such an induced stress profile leads to larger elongation and lesser curvature.

For wing skin shaping, operations are often divided into three stages (Moore, 1982; Burmeister, 1984; VanLuchene *et al.*, 1995; Ramati *et al.*, 1999):

Chordwise forming, to shape the aerodynamic chord profile;

Spanwise forming, to shape dihedral or anhedral breaks along the span;

Compression (or saturation) peening on all surfaces, to improve fatigue life.

Each operation calls for different processing parameters, *e.g.* shot size, intensity and coverage. For instance, spanwise forming generally requires large shots (up to 3 mm diameter, intensity 2C-20C) to achieve sufficient elongations while compression peening uses smaller shots ($\approx$ 0.6 mm diameter, intensity 5-8A) at full coverage. In addition, the sequence of operations may not be the same for all applications. Developing peen forming procedures therefore requires a great deal of process knowledge to understand the interactions between all operations.

In addition to the targeted out-of-plane deflections, peen forming generates in-plane displacements in the component (Moore, 1982; Homer and VanLuchene, 1991). For wing skin forming, these are known as growth (elongation) and fanning (angular deformation). While the in-plane displacements may remain relatively small, they must be taken into account in the design since they alter the boundary of the panel as well as the locations of interfaces with other parts.

When conventional peen forming cannot achieve specific shapes such as "saddle back" aerodynamic breaks, parts are mechanically prestressed (below their elastic limit) to alter the forming effect (Moore, 1982; Barrett, 1984; Kopp and Ball, 1987).

A consequence of the complexity of the peen forming process is that procedures are generally developed based on empirical relationships, geometrical methods and trial-and-error (Harburn and Miller, 1982; Burmeister, 1984; Homer and VanLuchene, 1991; VanLuchene *et al.*, 1995). While these methods are successful, they rely on costly and time-consuming physical testing rather than a fundamental understanding of the process. It is however worth noting that this is the publicly available state of the art as found in the literature: it is possible that more advanced methods have been developed but not disclosed by the manufacturers.

There are also many complementary procedures to peen forming. For instance,

– Parts may have to be sanded after peening with large intensities to reduce roughness and yield a suitable aerodynamic finish (VanLuchene *et al.*, 1995; Ramati *et al.*, 1999);
– Peen forming may be combined with other shaping processes such as press bending (Ramati *et al.*, 1999);
– For large parts, dimensional accuracy is typically checked by placing the component on a dedicated fixture. Weights can often be placed on the formed panel to achieve the required tolerances.

CHAPTER 2

OBJECTIVES AND RATIONALE

Based on this literature review, the rationale of the project can be explained as follow:

1. The random impact model proposed by Miao *et al.* (2009) showed great potential for predicting the residual stress state, roughness and coverage after shot peening. However, arbitrary dimensions were used and the methodology was not validated. Further study is required to determine an appropriate representative volume element (RVE) and validate predictions against experimental data.
2. Studies like those of Klemenz *et al.* (2009) and Zimmermann *et al.* (2010) have shown that material constitutive theories including both strain-rate sensitivity and cyclic behaviour led to accurate residual stress predictions for steel and a nickel alloy. No published study had thoroughly investigated the selection of an appropriate material law for an aluminium alloy.
3. Investigations of the material microstructure after shot peening for different materials have led to significantly different conclusions depending on the observation method (Section 1.2). For aluminium alloys, the microstructure after shot peening with typical industrial parameters is not fully understood.
4. Numerical simulations and limited experimental characterization suggest that shot peening does not lead to a uniform material state at the scale of the dimple diameter but this phenomenon has not been studied extensively. Quantification of process heterogeneity would be very useful in probabilistic models for the prediction of fatigue life or strength (Bouraoui *et al.*, 2009).
5. Although many peen forming simulation approaches have been introduced in the literature, few take into account the incremental nature of peen forming. Moreover, these studies have modelled the simple case of unconstrained specimens being formed.

   Considering the experimental results by Kulkarni *et al.* (1981), there is a significant gap between observed behaviours and simulation capabilities. Furthermore, actual applications involve a complex sequence of operations (Section 1.6) and have not been modelled yet. It is believed that accurate numerical simulation could reduce development time and cost in an industrial context.

The general objective of this research was to acquire a better understanding of the shot peening and peen forming processes through finite element modelling and material charac-

terization. This work was divided into three specific objectives:

1. Improvement of a random impact modelling strategy

   As presented in Section 1.4, shot peening simulation has two main themes: model type and material constitutive theory. In order to achieve accurate predictions, it is important to consider both aspects. The first specific objective of this project consisted of improving an existing random impact model and combining it with an appropriate material constitutive theory to accurately predict the material state after shot peening. This model was validated against published experimental data.

2. Metallographic characterization of shot peened specimens

   The second objective of this thesis was to explore experimentally and numerically the material state heterogeneity arising from the stochastic nature of shot peening as well as potential microstructural effects in an aluminium alloy. The possibility of complementing experimental results with accurate and more detailed numerical simulation data was investigated.

3. Development of a new incremental peen forming simulation method

   The third objective and main purpose of this thesis aimed at developing and validating a new forming simulation methodology that combines the advantages of published methods:
   - Incremental modelling to take into account progressive deflection (Cao *et al.*, 1995; Grasty and Andrew, 1996; Wang *et al.*, 2006);
   - Reduced calculation time through the use of shell elements (Levers and Prior, 1998; Wang *et al.*, 2006);
   - Reduced experimental calibration by relying on finite element impact simulations for input data (Han *et al.*, 2002);

   Unlike previous studies that have considered unconstrained peen forming, the methodology was applied to constrained specimens. Cao *et al.* (1995) have shown that an Almen strip peened in an Almen holder develops non-uniform curvatures but this behaviour had not been modelled previously.

   Furthermore, the influences of sheet rolling direction orientation and peening path were investigated numerically. These factors had only been studied experimentally (Kulkarni *et al.*, 1981; Miao *et al.*, 2010) and their modelling led to a better understanding of the process.

   Finally, the potential applications of a finite element predictive methodology for industrial applications were considered by modelling typical aerospace components subjected to representative peen forming treatments.

CHAPTER 3

SCIENTIFIC APPROACH

This thesis is divided into five sections. Each section presents a research article that was prepared during this project in order to complete the objectives stated in Chapter 2. The following describes each article as well as its context with respect to the three specific objectives.

3.1 Article 1: Shot peening and peen forming finite element modelling - Towards a quantitative method

This article introduced novel and experimentally validated shot peening and peen forming models. This article spanned multiple length scales, from the microstructure to the macroscopic behaviour of samples being formed, and aimed for quantitatively accurate predictions for both shot peening and peen forming. Previous studies had rarely investigated shot peening and peen forming modelling simultaneously and validated their residual stress and deformed shape predictions at the same time. In this article, simulation results were compared with experimental data for validation and the influence of constraints on the resulting curvatures was correctly predicted for the first time.

The main contributions of this paper are:

- A stochastic shot peening model that improves on previous work with systematically studied parameters, reduced calculation time, random distribution of shot diameters and a new mass-based method to relate experimental and numerical results (objective 1).
- A relatively simple combined isotropic-kinematic hardening law based on the experimentally observed transient and stabilized cyclic behaviour of AA2024-T3/T351 aluminium alloys (objective 1).
- A preliminary study of the effects of shot peening on the microstructure (objective 2) that justified further study of the topic.
- A novel peen forming simulation approach that takes into account the incremental nature of peen forming (objective 3). The method relies on accurate impact analysis results (objective 1) as input data to simulate the shaping effect of peen forming. Based on numerical observations, an interpolation method is introduced to simulate incremental deflections with a physical basis and a low computational cost.

This article lays the groundwork for studying more complex phenomena and representative forming processes.

This article was published in the "International Journal of Solids and Structures", volume 48, issue 20, pages 2859-2877 in October, 2011. This journal publishes research in the field of the mechanics of solids and structures. This article was written almost entirely by the author of this thesis.

3.2 Article 2: Experimental and numerical investigation of material heterogeneity induced by shot peening in an aluminium alloy AA2024-T351

This paper presented a combined experimental and numerical investigation on the effects of shot peening on aluminium alloy AA2024-T351 (objective 2). Samples were peened using one set of parameters representative of typical fatigue properties improvement applications and then characterized using different techniques at various length scales: residual stress determination, micro-indentation testing, surface topography, damage evaluation and microstructural study with electron backscatter diffraction. Finite element simulations were performed to provide more information on phenomena outside the reach of the selected experimental methods.

The main contributions of this paper within objective 2 are:

- A detailed characterization of AA2024-T351 shot peened with typical aerospace parameters using multiple complementary methods;
- An assessment of the heterogeneous effect of shot peening at the scale of the dimple diameter. This heterogeneity could affect the material behaviour under cyclic loading and its quantification would be very useful in the context of probabilistic fatigue life or strength predictions;
- A discussion on the potential uses of shot peening simulations (objective 1) to complement experimental data;
- A preliminary study of the microstructural modifications generated by shot peening in AA2024-T351.

Few studies had thoroughly investigated the heterogeneous material state after shot peening, especially for aluminium alloys. It is believed that a good knowledge of the material state and its dispersion after shot peening is essential to understand the influences of peening on fatigue life and strength.

This article was submitted to "Surface and Coatings Technology" on July 29, 2012. This journal publishes research on surface engineering and its uses to improve the performance of materials in demanding environments. This article was written almost entirely by the author of this thesis.

3.3 Article 3: On the effect of the orientation of sheet rolling direction in shot peen forming

This article extended the peen forming study presented in the first article by studying the potential anisotropic effects associated with sheet/plate rolling. Theoretical effects were first discussed using a simple analytical approach. The influences of elastic orthotropy and initial stresses in the material were then investigated using finite element simulations. Numerical predictions were validated with experimental results acquired for the purpose of this work.

The main contribution of this paper is an accurate modelling of some of the influences of the rolling direction orientation in peen forming (objective 3), which had not been done before. This is of great interest in the field of peen forming since most formed parts are sheets and plates. Kulkarni *et al.* (1981) had also identified rolling direction effects as a source for the development of cylindrical contours in some situations, which justifies a good understanding of the involved phenomena.

This article was submitted to the "Journal of Materials Processing Technology" on July 9, 2012. This journal broadly examines metal processing and manufacturing techniques. This manuscript was written almost entirely by the author of this thesis.

3.4 Article 4: On the effect of the peening trajectory in shot peen forming

This article presented a modification of the methodology described in the first article and built upon the results of the third article to simulate a peen forming treatment performed as a single pass of the shot stream over a component. The influences of constraints and peening pattern were investigated both numerically and experimentally. The simulated treatment was first calibrated to a simple experiment and then applied to a different and larger specimen. Predictions were compared to experimental results obtained for the purpose of this study.

The main contributions of this paper within objective 3 are:

- A simulation method to model peening treatments conducted in a single pass;
- A first study on the possibility of calibrating the numerical description of the treatment using small-scale tests for forming simulations of large components;
- An investigation on the effect of geometrical non-linearities in peen forming simulations.

The modelling capability developed in this article could prove essential to accurately simulate some forming treatments performed as a single pass of a component in a peening machine (Kulkarni *et al.*, 1981) or by moving a peening nozzle over the part (Friese *et al.*, 2002).

This article was submitted to "Finite Elements in Analysis and Design" on August 7, 2012. This journal aims to advance the current state of the art of metal component manufacturing mechanics, processes and tools. This article was written almost entirely by the author of this thesis.

3.5 Article 5: Potential applications of peen forming finite element modelling

This article discussed the potential uses of the finite element predictive methodology presented in the first article for industrial applications. Accurate peen forming simulations could substantially reduce development time, cost, and risk and could be a part of a wider design toolset that could include other operations. Modelling representative aerospace components and treatments had not previously been studied in details. Aspects that require improvements in order to achieve accurate and useful predictions were also identified.

The main contributions of this paper towards objective 3 are discussions on:

- Using numerical simulations to replace physical testing for building process databases;
- Simulating peen forming of complex components by multiple treatments;
- A first hypothesis to simulate successive treatments in a given area with a low computational cost.

This article was published in "Advances in Engineering Software", volume 52C, pages 60-71 in July, 2012. This journal publishes research on computer-based engineering methods. The work described in the paper was led by the author of this thesis and was performed in part in collaboration with Julien Cyr, who was a bachelor student at that time. The article was written almost entirely by the author of this thesis.

CHAPTER 4

ARTICLE 1: SHOT PEENING AND PEEN FORMING FINITE ELEMENT MODELLING – TOWARDS A QUANTITATIVE METHOD

A. Gariépy, S. Larose, C. Perron, M. Lévesque (2011). *International Journal of Solids and Structures* 48 (20), pp. 2859-2877.

4.1 Abstract

Peen forming is commonly used on aluminium alloys in the aerospace industry for wing skin shaping. Numerous analytical, numerical, and experimental studies have been made to better understand the effects of various peening parameters on the final material state and to predict deformed shapes, but conclusions were often limited to trends. The purpose of this study is therefore to develop and verify experimentally quantitative numerical tools for peen forming applications by studying the simple case of peening an Almen-sized AA-2024 aluminium strip in an Almen holder. The first step consisted in improving an existing random dynamic model by determining optimal dimensions. The AA-2024 target mechanical behaviour was characterized experimentally and a combined isotropic-kinematic hardening law was selected to model the material behaviour. The dynamic impact model and material constitutive law provided good prediction of peening-induced stresses in thick AA-2024 for two shot velocities. The sequence-sensitive aspect of the forming process was also investigated and a new shell-based finite element model was proposed. Numerical and experimental results for three shot velocities were compared to evaluate the validity of this numerical simulation method and promising agreement was observed.

4.2 Introduction

Peen forming is a cold-working method used to modify the shape of thin components. In this process, small particles are propelled towards a metallic surface at high velocities. Each impact creates an indentation in the material, inducing plastic stretching near the surface. Since the underlying material is not plastically deformed, compressive induced stresses are created close to the surface. These induced stresses offset the mechanical equilibrium, leading to bending and/or stretching. Useful shapes with relatively small curvatures (*i.e.* large radii) can be created by carefully controlling the peening parameters. This flexible and cost-effective

method is commonly used in the aerospace industry to shape large parts like wing skins and rocket shells.

Two measurands are commonly used to evaluate the intensity and progress of peening. The first method is the determination of the saturation curve. It is created by measuring the deflections of thin strips subjected to peening to characterize a specific set of process parameters. It involves plotting the arc height of SAE 1070 steel strips (called Almen strips) peened in an Almen holder as a function of peening time. The saturation point is calculated by determining the time t_{sat} for which doubling the peening duration increases arc height by exactly 10%. The measured arc height a_h^S at time t_{sat} is defined as the Almen intensity. Figure 4.1(a) illustrates this technique. The second measurand used is coverage: progress of shot peening is evaluated by determining the proportion of a peened area covered with indentations from impacts. Figure 4.1(b) shows the concept of coverage evaluation.

In shot peening, unbalanced induced stresses create stretching and bending of the part to reach a balanced residual stress state. Unbalanced induced stresses σ_{ind} are those encountered in a fully constrained component that does not allow stretching and/or bending (VanLuchene *et al.*, 1995). Residual stresses σ_{res} are those present in a component after the removal of external constraints and are mechanically balanced. Induced and residual stresses are related through:

$$\sigma_{ind} + \sigma_{axial} + \sigma_{bend} = \sigma_{res} \tag{4.1}$$

where σ_{axial} is the stress field related to stretching and σ_{bend} is the stress field related to bending (Homer and VanLuchene, 1991). For simplification purposes, σ_{axial} will be referred to as "axial stress" and σ_{bend} as "bending stress". Both of these stresses can be calculated from the forces applied by the external constraints in order to maintain the induced stresses. Residual stresses measured in a thick component can be used to estimate induced stresses since a large thickness does not allow significant bending and stretching and therefore $\sigma_{ind} \approx \sigma_{res}$ for a thick part. Figure 4.2 presents graphically the relationship between induced and residual stresses through axial and bending balancing stresses.

Numerous numerical studies of shot peening have already been proposed. Meguid *et al.* (1999) modelled single and twin co-indenting rigid shot impacts on a geometry with two symmetry boundary conditions. Distance between simultaneous impacts was investigated with the twin-shot model and it was shown that this variable had a significant effect on the residual stresses. Guagliano (2001) used cyclic material properties and kinematic work hardening to model multiple load cycles during multiple ordered impacts on a SAE 1070 steel target. Schwarzer *et al.* (2002) suggested a 3D geometry to study the effect of multiple, ordered steel shots impacts on an AISI 4140 steel target. Shots were modelled with rigid surfaces and mass and rotary inertia elements. Their model used infinite element to reduce stress wave energy

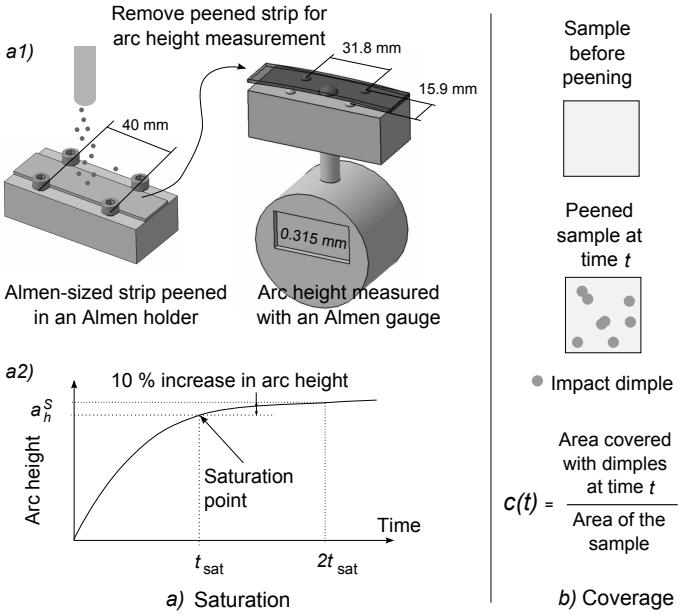

Figure 4.1 Principles of the methods commonly used to characterize peening processes. (a) The saturation curve (a2) is obtained by peening Almen strips in an Almen holder for different peening durations and measuring the Almen arc height with the Almen gauge (a1). Saturation point (t_{sat}, a_h^S) is determined at the time t_{sat} for which doubling the peening time does not increase arc height by more than 10%. a_h^S is then called "intensity". (b) Coverage for a specific peening time t, labelled as $c(t)$, is defined as the ratio of the area covered by indentations at time t to the area of the sample.

reflection into the mesh and residual stresses profiles were averaged over an area covering multiple impacts. Differences between simultaneous and successive adjacent impacts were evaluated. Meguid *et al.* (2002) introduced a symmetry cell representing successive rows of organized steel shots impacting a large AISI 4340 surface at normal incidence. Mass- and stiffness-proportional damping were used. The effect of shot deformation was studied and a rigid representation of the impacting particles was chosen. Friction was also considered and it was concluded that, for $0.25 \leq \mu \leq 0.5$, where μ is the friction coefficient, variations of residual stresses and plastic strains were negligible. Wang *et al.* (2002) suggested using multiple random impacts to take into account the random nature of the impacts. Hong *et al.* (2008a) developed a discrete element model to characterize the shot stream. By taking into account interactions between shots, the effect of process parameters – such as mass flow rate, angle of impact, and shot diameter – on the impact velocity distribution was demonstrated. Klemenz *et al.* (2009) simulated multiple ordered impacts using an isotropic-kinematic hardening law to model the behaviour of AISI 4140 steel. Their constitutive law took into account both strain history and strain rate. Good correlation was observed between experimental data and

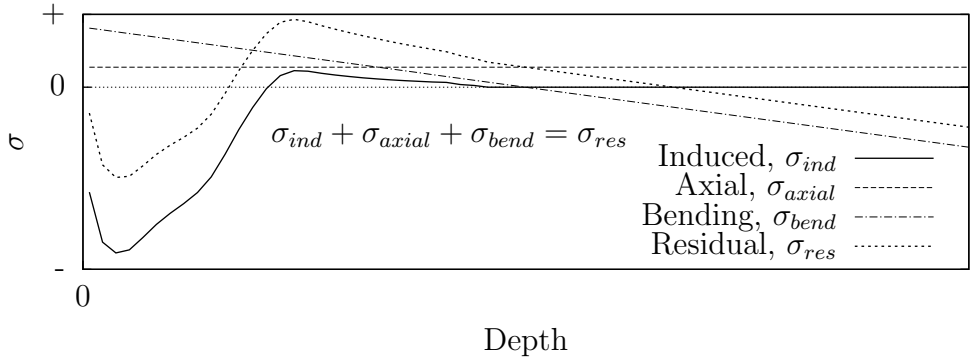

Figure 4.2 Relationship between a typical induced stress profile and the resulting residual stress profile in an unconstrained thin component. In presence of unbalanced induced stresses, axial and bending strains and the associated stresses are generated in order to maintain global part equilibrium (Homer and VanLuchene, 1991).

simulation results for surface deformation and residual stresses. Miao *et al.* (2009) suggested a random finite element model and showed that this type of model could be used to study the influence of peening parameters on residual stresses, saturation, coverage, and surface roughness. Zimmermann *et al.* (2010) compared deterministic and random finite element simulations regarding the development of coverage, residual stresses and surface topography. Using a strain rate sensitive isotropic-kinematic hardening law for nickel-based alloy IN718, good predictions of residual stress profiles were achieved. Using a symmetry cell, Kim *et al.* (2010) showed that averaging calculated stresses over an impacted area provides results closer to experimental XRD measurements of residual stresses than a 4-node average. Kang *et al.* (2010) modelled single and multiple predefined impacts of steel shots on a square AA-2024-T351 target. A springback static analysis was used to stabilize the model. The authors showed that multiple impacts tend to create a uniform state in the peened material and that multiple impact modelling is more appropriate than single-impact models to represent shot peening and peen forming.

Numerical tools have also been developed for forming simulation. These tools use equivalent loading methods to determine deformed shapes of large parts without simulating millions of impacts. Grasty and Andrew (1996) introduced a "squeezed-layer" model: by applying a squeezing pressure causing yielding of surface elements, permanent deformations and a stress distribution were obtained. Successive loading cycles were applied to determine a stabilized deflection. Calibration was however required to find the appropriate squeezing pressure. Levers and Prior (1998) suggested a thermal loading method to simulate peen forming processes. Their method consisted of introducing stress distributions in shell elements by creating

thermal strains. Wang *et al.* (2006) suggested a thermally-applied loading unit to create a plastic layer in shell elements. The case of unconstrained peening, in which the sample is free to bend and elongate, was studied. A numerical arc height vs. peening time curve was obtained by applying multiple loading cycles and, with proper calibration, accurate predictions were obtained. It should be noted that in the models of Levers and Prior (1998) and Wang *et al.* (2006), temperature was used as a numerical tool and was not related to the actual process. Han *et al.* (2002) proposed an equivalent loading scheme that used induced stresses in a solid model to simulate peen forming.

Experimental research on shot peening and peen forming has also been performed. Cao *et al.* (1995) studied the progressive deformation of an Almen strip in an Almen holder during peening in multiple passes. They observed non-uniform curvatures in the constrained and free Almen strip. The authors proposed an analytical model to explain this behaviour. The development of residual stresses after various numbers of passes was also investigated using X-ray diffraction. Miao *et al.* (2010) performed a detailed study on the peening of aluminium strips and plates. They studied the effects of shot velocity on saturation, roughness, and coverage and obtained residual stress profiles in thin and thick peened samples. The authors also measured monotonic mechanical properties of AA-2024 and studied the effect of material anisotropy on the development of arc heights.

Based on this literature survey, the following limitations of current models have been identified:

1. Miao *et al.* (2009) have demonstrated the interest of a multiple-shot random finite element model to represent accurately shot peening but further study was required regarding model dimensions.
2. The random dynamic model of Miao *et al.* (2009) used monotonic mechanical properties and isotropic hardening, which may not be accurate due to reverse yielding during shot peening. Transient and stabilized cyclic properties and kinematic hardening should be used in modelling of shot peening (Guagliano, 2001; Klemenz *et al.*, 2009; Zimmermann *et al.*, 2010).
3. Single- and multiple-shot dynamic impact models are useful to calculate stress distributions in thick components and to study the effects of shot, process, and target material parameters. However, these models alone could not model accurately peening of thin components, due to progressive deformation during processing. To the authors' knowledge, progressive deformation phenomena have not been studied in details with numerical pressure-, temperature- or stress-based forming models. Cao *et al.* (1995) proposed a useful analytical model to explain progressive deformation in the specific case of the Almen strip in an Almen holder but their model lacks the flexibility of

numerical simulation. Although this simple case is commonly encountered in peening applications, it has not been studied in details with numerical forming models.

The first objective of this work is to propose a numerical method for peen forming simulation. The commercial significance and relative simplicity of the Almen test makes it an interesting case study for the development of flexible finite element forming tools. The second objective of this article is to achieve quantitative numerical predictions of stresses in a thick component and deformation of a thin part due to peening, and compare them with experimental results from Miao *et al.* (2010) and with additional results generated for the purpose of this study.

This article is divided into five sections. Section 4.3 presents the experimental results used to develop and evaluate the finite element models. Section 4.4 discusses the dynamic impact model dimensions and parameters, determination of a material constitutive law and a new sequence-sensitive forming simulation tool. Section 4.5 compares experimental and numerical results. Section 4.6 concludes this work and suggests possible improvements and topics for future works.

4.3 Experiments

4.3.1 Peening experiments

Results from Miao *et al.* (2010)

The experimental setup used by Miao *et al.* (2010) consisted of a mobile blasting machine and a manipulator arm. Zirshot Z425 shots (shot density $\rho_s = 3850$ kg/m^3) were fed with a mass flow rate of 0.4 kg/min and the manipulator arm travel velocity was 320 mm/s. Peened samples were $76 \times 19 \times 1.6$ mm sheets of AA-2024-T3 and 12.5 mm thick plates of AA-2024-T351. Three shot velocities v_{shot} were used: 34.6 m/s, 53.7 m/s, and 66.2 m/s. Normal impacts were considered. Peening time was varied by changing the number of passes of the robot over the samples for saturation experiments and by varying the robot travel velocity for residual stress measurement samples. Residual stresses were measured in thick AA-2024-T351 samples at saturation parameters for shot velocities of 34.6 m/s and 66.2 m/s. Measurements were performed using the X-ray diffraction method. This experimental data will be used to validate the impact model and material constitutive law. Saturation behaviour of Almen-sized AA-2024-T3 strips peened in Almen holders was also determined for three different shot velocities. These results will be used as a comparison basis for the development of the forming model.

Additional results generated for the current study

The same peening equipment and parameters as in Miao *et al.* (2010) were used to obtain the additional data required for the current study.

A study of the actual shot distribution within the shot stream was performed. High-speed photography was used to "freeze" shots leaving the nozzle. A peening enclosure was modified to accommodate photographic equipment, as shown in figure 4.3. A DSLR camera with a macro lens and a flash unit were positioned in front of clear windows. Pictures covered an area located at the intersection of the optical, flash, and peening axes (point A). The following exposure parameters were found to provide good results: 1/200 s at $f5.6$, ISO 200, and flash at 1/128 power. This provided a claimed flash duration of 1/38500 s: shots still appeared as bright white lines due to their high velocity. Pictures were made with a shot velocity of 66.2 m/s and a mass flow rate of 0.4 kg/min.

The evolution of constrained deflection was studied by peening four Almen-sized aluminium strips in Almen holders, one pass at a time, with a shot velocity of 66.2 m/s. Maximum deflection of strips screwed onto Almen holders were measured with a digital indicator with a resolution of 0.01 mm after various numbers of passes. Two strips were cut with the rolling direction along the long side and two with the rolling direction parallel to the short side. Only small differences were observed between both cases and deflections were averaged for all samples.

Non-uniform curvature development was also studied by determining radii of curvatures in the long and short directions for two peened strips near the experimental saturation condition, before and after removal from the Almen holder. Radii were averaged for both samples. Radii parallel to the short side were determined from the full width of the strip and radii parallel to the long side were obtained from data points within ±15 mm from the center of the

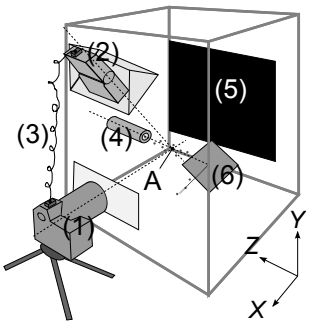

Figure 4.3 Schematic view of the photographic setup used to study the shot stream. The setup consisted of a camera and lens (1), a flash (2), an off-shoe cable (3), the peening equipment (4), a dark background (5), and a deflector (6). Drawing is not to scale.

strip. Both measurement lines intersected in the center of the strip. Measurements and radii determination were made with the method described in Miao *et al.* (2010).

4.3.2 Determination of mechanical properties

In order to develop an appropriate material constitutive law for shot peening, low-cycle, high-strain cyclic mechanical testing of the unpeened material was performed and microstructures of the peened and unpeened material were studied.

Cyclic material behaviour

Cyclic test samples were milled from a 12.7-mm thick plate of AA-2024-T351. Tests were performed on a MTS 810 uniaxial hydraulic system equipped with hydraulic wedge grips at a constant strain rate of 8×10^{-5} s^{-1}. A MTS 632.26C extensometer with a 8-mm gauge length was used. ASTM Standard E9 (2000) was considered to evaluate the critical buckling stress. With a target compressive strain of 5%, it was not possible to follow ASTM Standard E606 (1992) recommendations regarding specimen dimensions. A modified specimen geometry was designed and simulated by finite element analysis in order to verify that the stress field was sufficiently uniform in the 8-mm gauge length. Selected specimen geometry is presented in figure 4.4. The nominal strain range $\Delta\varepsilon$ is defined as $\Delta\varepsilon = \varepsilon^{\max} - \varepsilon^{\min}$, where $\varepsilon^{\max}$ and $\varepsilon^{\min}$ are respectively the maximum and minimum nominal strains reached during the test. Only results for nominal strain ranges $\Delta\varepsilon$ of 2%, 4%, and 6% are presented in this work since buckling occurred for larger values of $\Delta\varepsilon$. This premature buckling was due to the fact that cyclic hardening was not taken into account in buckling calculations.

Monotonic and cyclic yield stresses were determined with the 0.2% strain offset method. The number of cycles to saturation was defined as the number of cycles after which an additional cycle did not increase the maximum tensile stress by more than 1%. In this study, mechanical properties for AA-2024-T3 and AA-2024-T351 were assumed to be identical.

Microstructure characterization

Scanning electron microscopy (SEM) was selected to study the material microstructure. A 1.6-mm thick AA-2024-T3 sheet peened in experimental saturation conditions with a shot velocity of 66.2 m/s was cut through-thickness to provide a sample in the longitudinal direction. The highest shot velocity investigated in this work was selected since it was more likely to induce microstructure modifications. This sample was cold-mounted in epoxy resin and mechanically polished. Keller's reagent was used to show grain boundaries. Images were taken with a JEOL-JSM840 microscope at 15 kV, 1 nA, and a working distance of 25 mm.

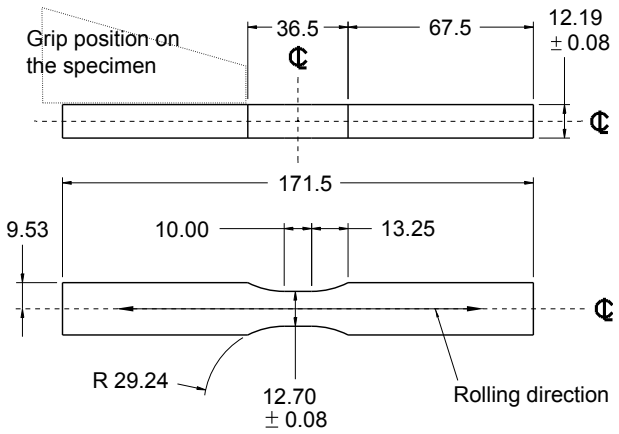

Figure 4.4 AA-2024-T351 cyclic test sample geometry (dimensions in mm). Position of the hydraulic grip on the specimen is also shown.

Grains with clear boundaries were traced and introduced into ImageJ image processing software. Ellipses were fitted to grains and grain size was calculated as the average of all major and minor axes. Since peening only affects a thin surface layer, grain sizes were determined separately for a $\approx$ 150-μm thick surface layer and for depths between $\approx$ 150 and $\approx$ 350 μm. Measurements were made on both the peened and unpeened sides to evaluate possible effects of rolling and heat treatment.

4.4 Modelling approach

The modelling work described in this article had three parts. The first part consisted of improving the random dynamic impact model proposed by Miao *et al.* (2009) by studying the effects of its dimensions and parameters. The second part aimed at evaluating the behaviour of AA-2024 under high-strain cyclic loading encountered in peening. The last part was the development of an induced-stress based, sequence-sensitive forming method capable of representing complex peening conditions.

4.4.1 Dynamic impact model

For the development of the model, material properties for aluminium AA-2024 were $E =$ 71.7 GPa, $\nu = 0.33$, and $\rho_t = 2810$ kg/m^3. Linear isotropic hardening was assumed, based on the work of Miao *et al.* (2009). Isotropic hardening allows an enlargement of the yield surface with increasing plastic strain (ABAQUS Theory Manual, 2008). The initial yield strength σ_0 was set to 379 MPa and the strain-hardening coefficient H to 810 MPa, with a maximum stress of 1189 MPa. All analyses were run with a shot velocity of 66.2 m/s. Initial residual

stresses were assumed to be negligible.

The random FE model proposed by Miao *et al.* (2009) consisted of four square regions in the X-Y plane and two layers stacked in the depth direction, as shown in figure 4.5. The same model structure was investigated in the current study. The model thickness (Z direction) used was 1.6 mm, equal to the thin sample thickness. Table 4.1 lists the meshing parameters. Fine mesh dimension was selected based on the work of Hong *et al.* (2008b). A coarser mesh was used in the 0.85-mm thick lower layer in order to reduce the number of elements in the model. Eight-node reduced-integration brick elements (C3D8R) were selected.

In figure 4.5(a), region 1 is the coarse-mesh outer area in which damping was introduced (see section 4.4.1). Region 2 allows impact indentations to be separated from region 1. Region 3 is the area containing the impact centers. Region 4 is the representative region in which induced stress profiles were calculated. These profiles were determined by averaging stresses in all the elements of the representative volume, by element layer. Average stress profiles $\bar{\sigma}_x(z_i)$ and $\bar{\sigma}_y(z_i)$ were determined in X and Y directions, respectively. For normal impacts, it is expected that $\bar{\sigma}_x(z_i) \approx \bar{\sigma}_y(z_i)$ (Zimmermann *et al.*, 2010). An average stress $\bar{\sigma}(z_i) = (\bar{\sigma}_x(z_i) + \bar{\sigma}_y(z_i))/2$ was therefore used to evaluate induced stress profiles. To take surface deformation into account, stress profiles were determined with deformed depth coordinates. Normal displacements were blocked on surfaces with X and Y normals, creating symmetry boundary conditions on those surfaces. All displacements were constrained on the bottom surface.

ABAQUS/Explicit version 6.5.1 was used to perform random dynamic impact analyses. This commercial software uses a central-difference time integration rule (ABAQUS Analysis User's Manual, 2008). Calculations were run on an IBM P690 Regatta computer at École Polytechnique de Montréal. Analyses were run on 4 to 6 processors: parallelization efficiency was estimated to be around 88%.

Shot stream definition

Studies like that of Meguid *et al.* (1999) have shown that shot size has a significant influence on stress profiles. Shots provided by the manufacturers are not of a constant size. Documentation from St-Gobain ZirPro, the shot manufacturer, showed that the Z425 shots

Table 4.1 Mesh selection

Mesh type	Dimension	Location, X-Y	Location, Z
Coarse	$0.1 \times D_{shot} = 0.05$ mm	Region 1	Lower layer
Fine	$0.05 \times D_{shot} = 0.025$ mm	Regions 2-4	Upper layer

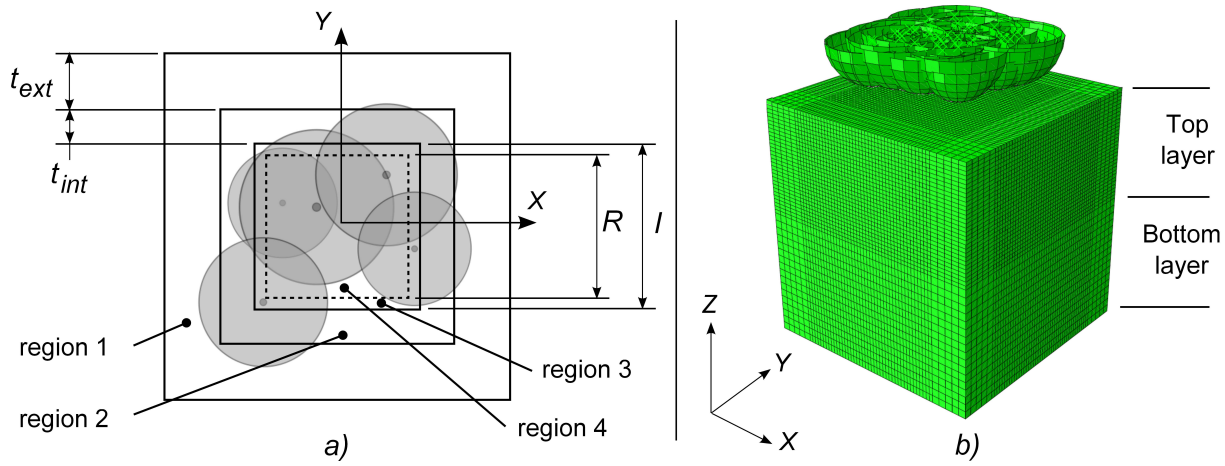

Figure 4.5 (a) Schematic view of the regions defined in the X-Y plane. Dashed lines delimit the representative area and each shot is represented by a circular shadowed area with a dot indicating its center. (b) Isometric view of the model showing the finely-meshed upper layer and the coarsely-meshed lower layer. The compacted shot stream is also shown: shots are accelerated up to the appropriate velocity one at a time so that all impacts occur independently.

have a diametral dimension within the range of 425 to 600 μm (Saint-Gobain, 2003). In the simulations, shot diameters were assumed to be random within the prescribed range according to:

$$D_{shot}^{k} = D_{shot}^{\min} + \text{rand}(0,1) \times (D_{shot}^{\max} - D_{shot}^{\min}) \tag{4.2}$$

where D_{shot}^{k} is the diameter of shot k, $D_{shot}^{\min}$ and $D_{shot}^{\max}$ are respectively the minimum and maximum dimensions indicated by the manufacturer, and $\text{rand}(0,1)$ is a decimal number in the range $[0;1]$ from a uniform random distribution.

Pictures of the shot stream showed that shots were generally well separated in the Y-Z plane: figure 4.6(a) presents a typical case. With the materials properties listed in section 4.4.1, an impact duration of approximately 1 μs was determined by finite element analysis. Two shot impacts did not occur simultaneously if these shots were located more than $\approx$ 0.1 mm apart in the Z direction. Preliminary numerical simulations have also shown that stress profiles are almost the same for two simultaneous and time-separated impacts when the distance between shots centers was more than $\approx 2 \times D_{shot}$. In cases where Y spacing was small, such as group 1 in figure 4.6(a), Z distance was generally sufficient to prevent impacts from occurring simultaneously. When Z distance was small, as with group 2 in figure 4.6(a), the spacing in the X-Y plane was generally large enough to assume independence between shot impacts. There was a minority of cases where shots appeared to be closely grouped,

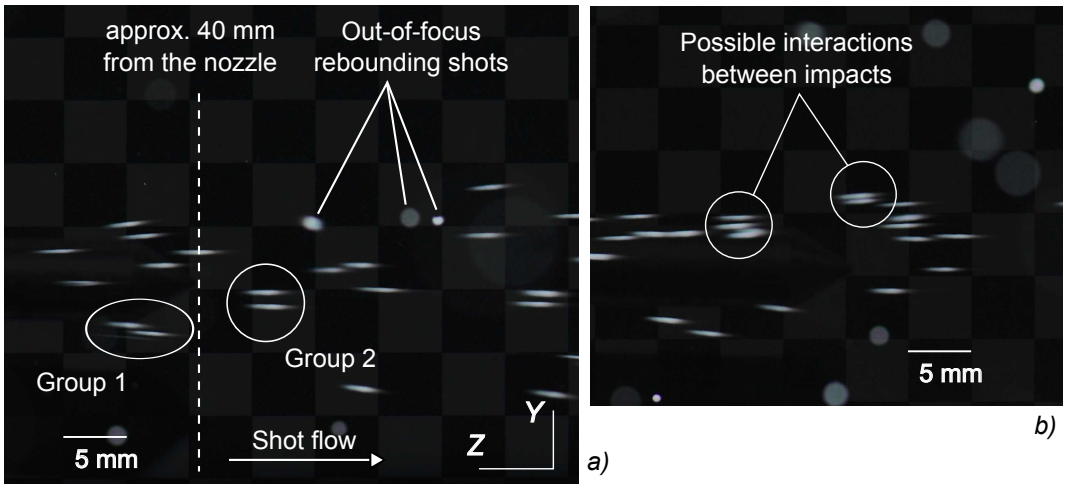

Figure 4.6 Typical pictures of the actual shot stream used to determine modelled stream definition. Shots leaving the nozzle at 66.2 m/s appear as elongated white lines. Bright rounded shapes are created by out-of-focus rebounding shots. (a) Well-separated shots and (b) Examples of closely-grouped shots.

as in figure 4.6(b). However, images in figure 4.6 are projections of shots on the Y-Z plane and therefore provide no information in the X direction. It is likely that X distance was large enough in those cases to consider that impacts were independent. It was therefore assumed realistic to simulate independent impacts. Modelling each shot impact successively and independently during the analysis decreased the computational cost since it decreased the number of contact verifications required at each simulation increment.

The modelled rigid shots were initially positioned at the same distance from the surface, as shown in figure 4.5(b), and were sequentially accelerated up to impact velocity prior to impact. X and Y locations of the shot centers were randomly calculated using:

$$L_i^k = \frac{\text{randint}(-1000, 1000)}{1000} \times \frac{I}{2} \tag{4.3}$$

where $i = \{X, Y\}$, L_X^k and L_Y^k are the X and Y coordinates of the center of shot k, $\text{randint}(-1000, 1000)$ is an integer in the range $[-1000; 1000]$ from a uniform random distribution, and I is the width of region 3 (figure 4.5(a)). Each shot was represented by an analytical half-sphere rigid surface and mass and inertia elements.

Contact properties

A kinematic contact algorithm was selected to model shot-target interactions (ABAQUS Analysis User's Manual, 2008). Regarding frictional behaviour, Meguid *et al.* (2002) and

Meo and Vignjevic (2003) observed that differences in induced stresses were negligible for $0.1 \lesssim \mu \lesssim 0.5$. In Miao *et al.* (2009), a friction coefficient of $\mu = 0.2$ was used: the same value was kept in this work. Hong *et al.* (2008a) defined ξ as the ratio of mass flow rate to shot velocity and showed that collisions between shots were less significant when ξ was low. The experimental peening parameters used by Miao *et al.* (2010) yielded a value of $\xi \approx 0.15$ g/m, which is nearly an order of magnitude smaller than the values studied by the Hong *et al.* (2008a). Collisions between shots were not considered in the current model.

Damping

Studies like that of Meguid *et al.* (2002) have shown that damping is necessary to avoid uncontrolled post-impact oscillations in the model, especially when symmetry boundary conditions are used. Rayleigh damping was introduced in region 1 (figure 4.5(a)) to reduce stress oscillations. Since the damping definition was maintained during the analysis, the selected damping values had to provide efficient stabilization without modifying the impact behaviour. In order to avoid increasing the computational cost, the stiffness-proportional factor β_R had to be of the same order of magnitude as the stable time increment (ABAQUS Analysis User's Manual, 2008). A value of $\beta_R = 0.75$ ns was chosen, which decreased the stable time increment from ≈ 3.2 ns to ≈ 1.9 ns. The stress response was used to study the effect of the mass-proportional factor α_R. Figure 4.7 shows the effect of this parameter on stresses at an element adjacent to the impact centerline in the third element layer, during and following an impact of a 600 μm shot at the corner of region 3. It can be seen that, in the case without damping, oscillations did not decay significantly. In the actual peened material, material damping would reduce these oscillations. Figure 4.7 also shows that stress oscillation amplitude decreased more rapidly with increasing α_R. Based on these results, a value of $\alpha_R = 8.0 \times 10^5$ s^{-1} was arbitrarily selected and a delay of 5 μs was introduced between impacts. The suggested damping parameters did not affect notably the impact behaviour and were able to control stress oscillations after the impact. It should be noted that this damping definition is a numerical tool and does not represent actual material damping.

Model dimensions

The size t_{ext} of region 1 (figure 4.5(a)) was first defined. Analyses were run in which only the overall size of the model was modified. All others parameters remained unchanged: $I = R = 0.75$ mm and $t_{int} = 0.125$ mm. Shot diameters were kept constant at $D_{shot} = 0.5$ mm. Figure 4.8 shows the effect of t_{ext} on the calculated induced stress profiles $\bar{\sigma}(z_i)$ after 48 impacts. The most significant differences of the induced stress profiles appeared at depths

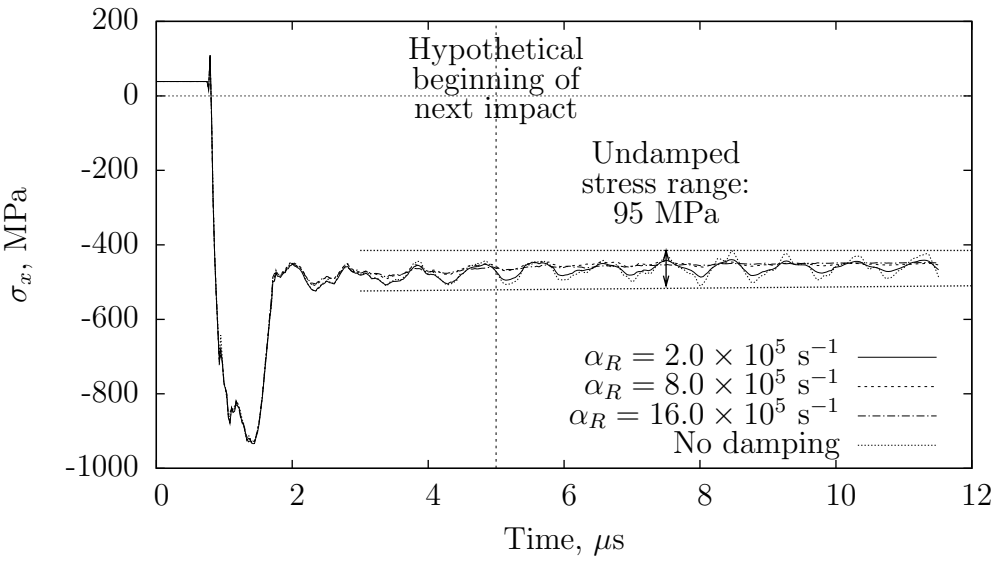

Figure 4.7 Stress response in the X direction of an element adjacent to the centerline of an impact, in the third element layer from the surface. Model dimensions were $I = 0.75$ mm, $t_{int} = 0.15$ mm, and $t_{ext} = 0.25$ mm. Shot diameter was 600 μm and the impact center was located at a corner of region 3. Except for the case without damping, $\beta_R = 0.75 \times 10^{-9}$ s. With $\alpha_R = 8.0 \times 10^5$ s^{-1} and a delay of 5 μs between impacts, stress oscillation amplitude decreased to 25 MPa before the following impact. Stresses in the Z direction exhibited less oscillations.

where stresses were tensile. In order to evaluate the deformation of the impacted area, plastic strains in the X and Y directions were averaged in the same manner as stresses. Average plastic strains in the X-Y plane increased when t_{ext} increased. Larger plastic strains in the impacted area created greater elastic stretching in the material just below the plastically deformed volume, hence the higher stress values at depths larger than 0.3 mm. In other words, when t_{ext} increased, compliance of region 1 increased and allowed more stretching in the impacted area. The decrease of the maximum tensile stress with decreasing t_{ext} also showed that the observed tensile peak was caused at least in part by the presence of unimpacted elements in periphery of the impacted area: when $t_{ext} \to 0$, it would be expected that tensile stresses become negligible. This means that in a large peened plate, these tensile induced stresses would be small.

Considering the symmetry boundary conditions, a small t_{ext} would allow a better representation of a large completely peened plate. Reduction of t_{ext} allows for a greater proportion of the modelled surface to be covered with indentations, as shown in figure 4.9. A compromise was however required since artificial damping was present only in region 1 to stabilize

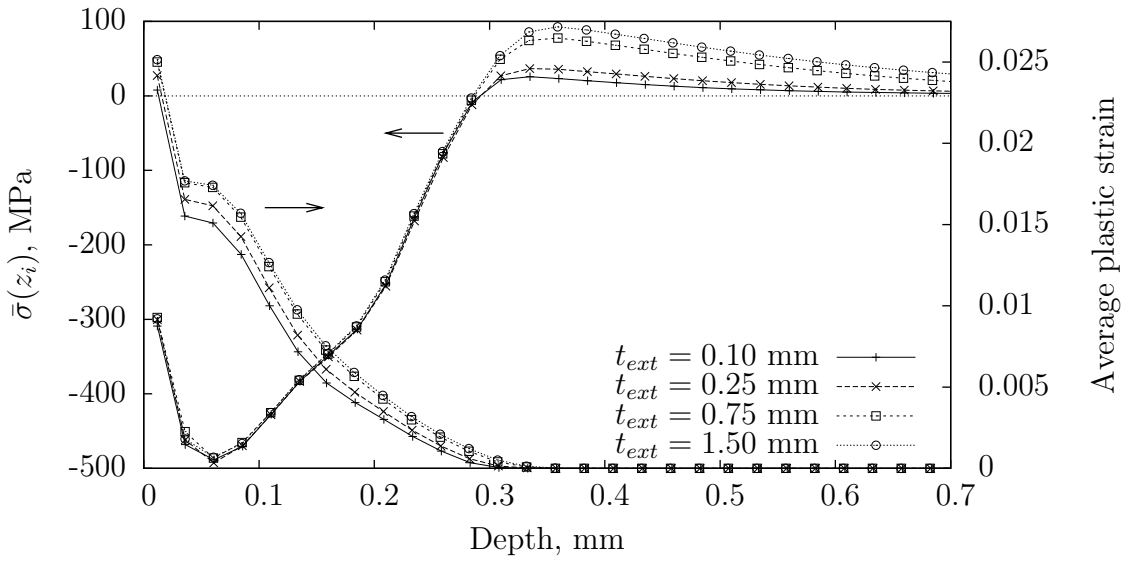

Figure 4.8 Effect of t_{ext} on the induced stress profiles calculated with $\bar{\sigma}(z_i)$ after 48 identical impacts. The surface and maximum compressive stresses remain nearly constant and the most significant influence is observed around the maximum tensile stress. The average plastic strain profiles show that a greater t_{ext} allows more plastic stretching of the impacted surface.

the model response: reducing t_{ext} would require either a longer delay or higher damping parameters to ensure a similar stabilization. Based on the results of figure 4.8, a value of $t_{ext} = 0.25$ mm was chosen.

A study similar to that presented for t_{ext} was performed to define the size t_{int} of region 2 (figure 4.5(a)). The value of t_{int} had an effect similar to that of t_{ext}. Even with a value as low as $t_{int} = 0.05$ mm, induced stress profiles did not differ appreciably. One possible explanation is that averaging the stresses dilutes possible stress differences near region 2 boundary. It was decided to choose t_{int} as to prevent indentations from reaching into region 1. This involved running a preliminary analysis of a single impact with the parameters that would create the largest dimple. The value of t_{int} was then taken to be the radius of the dimple, defined as the number of elements between the impact center and the dimple ridge, plus one. In this study, $t_{int} = 0.15$ mm was used.

Dimensions I and R of the impacted and representative areas (figure 4.5(a)) were then investigated. For three dimensions I of region 3, six analyses were run in which both impact locations and shot diameters were randomly generated. The effect of dimension R of region 4 was studied by averaging results for different representative areas. In the current section, a "case" consists of six analyses using the same combination of I and R and different shot diameters and locations; a total of eight cases were studied.

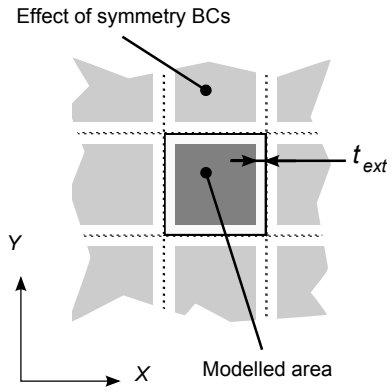

Figure 4.9 Effect of the symmetry boundary conditions on the area covered by indentations. The model is represented by the middle cell and solid lines indicate its symmetry boundary conditions. Impacted areas are represented with gray squares. When the dark gray area approaches the size of the model, *i.e.* t_{ext} becomes small, the model represents a large, completely peened part.

Since shot dimension was random, it was more appropriate to use mass as an indicator of progress, instead of the number of impacts. Moreover, some impacts were not contained completely in the representative region 4. This means that some of the shots kinetic energy was converted to plastic deformations in regions 2 and 3. The influence of impact location with respect to the representative region was considered. Figure 4.10 shows stress and plastic strain fields created by a single impact. Two possibilities were studied: a) the first impact on the unpeened material and b) an impact on a previously impacted material. For possibility (b), an analysis of 20 random impacts on an impacted area with $I = 0.75$ mm was run and the average stress and equivalent plastic strain ($PEEQ$) profiles were calculated and then uniformly applied as an initial state to the model presented in figure 4.10(b) prior to impact simulation. The equivalent plastic strain is a scalar value that provides an indication of the full plasticity history. It was observed that the effect of an impact on the stress field extends further than its effect in terms of plastic strains. The altered diameter was also larger than the dimple diameter (Zimmermann *et al.*, 2010). It can be also seen that in case *b*) material hardening and initial stresses caused a small reduction of the plasticized radius. An approximate area of influence with a diameter of $0.6 \times D_{shot}$ was defined so as to include most of the plasticized material following an impact. This diameter was reduced to $0.5 \times D_{shot}$ for $v_{shot} = 53.7$ m/s and to $0.4 \times D_{shot}$ for $v_{shot} = 34.6$ m/s. The effective mass of the k^{th}

impact m_e^k and cumulated effective mass after k impacts M_e^k were then calculated with:

$$m_e^k = m^k \times f_I^k \tag{4.4a}$$

$$M_e^k = \sum_{l=1}^{k} m_e^l \tag{4.4b}$$

where m^k is the mass of shot k and f_I^k is the influence factor of impact k, determined as illustrated in figure 4.11.

Unlike analyses for t_{ext} and t_{int}, analyses for R and I had numerous random parameters and the impacted area was also a variable. In order to consider an equivalent state for comparisons, it was decided to use arc heights at pseudo-saturation as a comparison basis instead of imposing predetermined masses. Pseudo-saturation curve refers to an arc height a_h versus cumulated effective mass curve defined without considering the progressive aspects of the process. In other words, it is assumed that the sample is fully constrained and does not stretch and bend during peening. This allows simple calculation of arc heights with:

$$M^{\bar{\sigma}(z_i)} = \sum_{z_i=1}^{z_i=30} \left[\bar{\sigma}(z_i) \times t(z_i) \times \left(c(z_i) - \frac{h}{2} \right) \right] \tag{4.5a}$$

$$\frac{1}{R_c^{\bar{\sigma}(z_i)}} = (1-\nu) \times \frac{12 M^{\bar{\sigma}(z_i)}}{Eh} \tag{4.5b}$$

$$a_h^{\bar{\sigma}(z_i)} = \frac{(35.5 \text{ mm})^2}{8 \times R_c^{\bar{\sigma}(z_i)}} = a_h \tag{4.5c}$$

where $M^{\bar{\sigma}(z_i)}$ is the bending moment created by $\bar{\sigma}(z_i)$ induced stresses, R_c is the calculated radius of curvature, $t(z_i)$ is the deformed thickness of element layer i, $c(z_i)$ is the average depth of element layer i (measured from the peened side), h is the thickness of the plate, and E is the elastic modulus. The superscript $\bar{\sigma}(z_i)$ indicates the stress profile used for arc height calculation. Equation (4.5(a)) was used to calculate the bending moment generated by induced stresses. Summation was made over 30 element layers (0.75 mm deep). Calculated stresses became small at greater depths: stress values of 0 were assumed for the remaining thickness. Equation (4.5(b)) used shell theory to calculate the free radius of curvature. In equation (4.5c), the assumptions that the part does not bend during peening and that $\bar{\sigma}_x(z_i) = \bar{\sigma}_y(z_i)$ lead to a spherical cap deformed shape. The deflection could then be calculated from the distance between supports and the radius of curvature. 35.5 mm is the distance between opposite support spheres on an Almen gauge (figure 4.1(a)). This method was based on the work of Guagliano (2001). Total sheet thickness reduction due to peening was neglected and $h = 1.6$ mm.

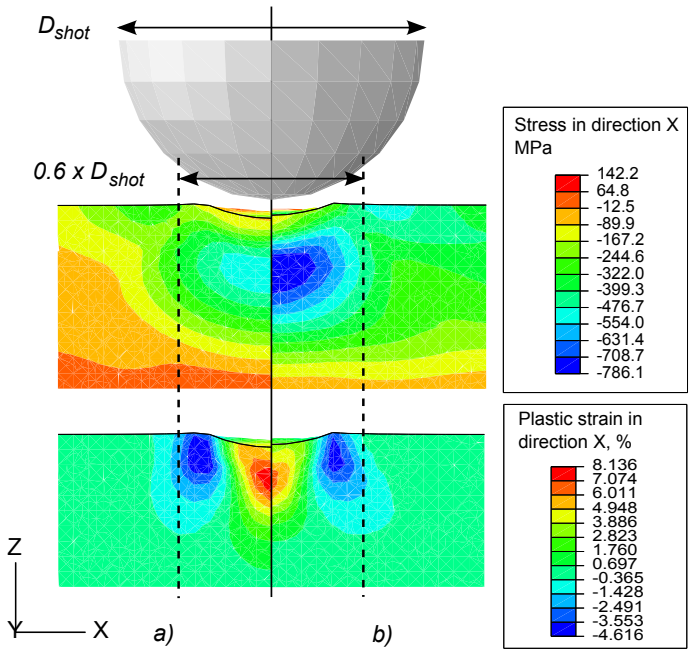

Figure 4.10 Simulation results used to define an approximate area of influence. A single impact of a 500 μm shot at 66.2 m/s was simulated on a) a material with its original properties and b) a material in which stress and equivalent plastic strain ($PEEQ$) states are roughly equivalent to those existing after 20 impacts on an impacted area with $I = 0.75$ mm (based on random FE analysis).

For each analysis, after each impact k, the induced stress state was extracted from the model and used to calculate the arc height a_h^k with equations (4.5a) to (4.5c). For each case presented in table 4.2, six curves of arc height a_h^k versus cumulated effective mass M_e^k were generated (one per analysis). For each case, a curve with equation:

$$a_h^k = \frac{A \times M_e^k}{B + M_e^k} \tag{4.6}$$

was fitted by adjusting parameters A and B. This type of equation was used by Wang *et al.* (2008). The effective mass at pseudo-saturation was then determined by solving for M_e^S:

$$1.1 \times \frac{A \times M_e^S}{B + M_e^S} = \frac{A \times (2 \times M_e^S)}{B + (2 \times M_e^S)} \tag{4.7}$$

which is based on the definition of saturation presented in section 4.2. Equation (4.6) provided an adequate fit below M_e^S but results for larger masses tended to diverge slightly from the best-fit curve.

Once M_e^S was determined, pseudo-saturation points $(M_e^S, a_{h_j}^S)$, where $a_{h_j}^S$ is the arc height

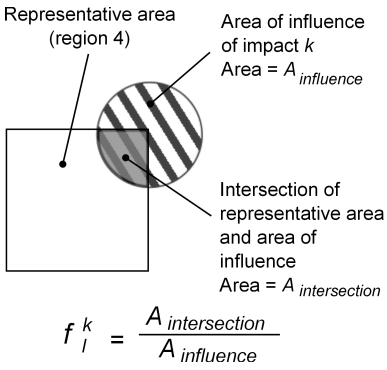

Figure 4.11 Determination of factor f_I^k used to calculate the effective mass m_e^k of the k^{th} impact.

at pseudo-saturation for the j^{th} analysis of a case, were identified for each analysis by selecting the first data point k where $M_e^k \geq M_e^S$. These pseudo-saturation points were then used to compare combinations of I and R with four indicators:

$$\bar{a}_h = \frac{\sum_{j=1}^{6} a_{h_j}^S}{6} \tag{4.8a}$$

$$S_{\bar{a}_h} = \frac{\max_j(a_{h_j}^S) - \min_j(a_{h_j}^S)}{\bar{a}_h} \times 100 \tag{4.8b}$$

$$DS = \frac{\sum_{j=1}^{6} \mid a_{h_j}^{S_x} - a_{h_j}^{S_y} \mid}{6 \times \bar{a}_h} \times 100 \tag{4.8c}$$

$$I_D = \frac{M_e^S}{R^2} \tag{4.8d}$$

where $a_{h_j}^{S_x}$ and $a_{h_j}^{S_y}$ were calculated for a cumulated effective mass of M_e^S using equation (4.5) with $\bar{\sigma}_x(z_i)$ and $\bar{\sigma}_y(z_i)$ respectively. $\bar{a}_h$ was the average arc height at pseudo-saturation for a case. $S_{\bar{a}_h}$ estimated the results scatter for a specific case. DS was used to evaluate the directional scatter of the results by calculating arc heights based on induced stress profiles $\bar{\sigma}_x(z_i)$ and $\bar{\sigma}_y(z_i)$. I_D was the calculated impact density at pseudo-saturation. Interest was also taken in the duration of the analyses since computational cost remained an issue. Table 4.2 shows the results extracted from the analyses. It can be seen that the calculated average arc heights at pseudo-saturation $\bar{a}_h$ were included within a 5% range when considering all cases. As the value of R approached that of I, the results scatter $S_{\bar{a}_h}$ tended to decrease (the exception being case 2). Increasing I also reduced the scatter. For normal shot peening, it would be expected that $DS \approx 0$. The proposed model could correctly represent this behaviour since the directional scatter DS remained small in all cases. It is believed that this model would be appropriate to represent oblique impacts since directional differences

would then be caused by the impact angle and not by stress averaging. Regarding impact density at pseudo-saturation, calculated values differed quite notably: this may indicate that the definition of area of influence presented in figure 4.10 could be improved. It can be observed that higher I values and $R \to I$ tended to reduce $S_{\bar{a}_h}$ and DS. However, $\bar{a}_h$ values did not differ significantly (especially when $R \to I$) and calculation time increased rapidly when increasing I. It was therefore decided to use $I = 0.75$ mm $\approx 1.5 \times D_{shot}$ for the following steps of this work to obtain a calculation time of around 10 hours per analysis.

In table 4.2, results for cases 2 to 5 and 6 to 8 show that $\bar{a}_h$ were slightly lower when $R = I$ than in cases where $R < I$. By studying the stress fields in the representative volume, higher stresses (*i.e.* less compressive) were observed in elements near the boundary of region 3. These higher values tended to decrease the calculated arc height. This behaviour was observed in most analyses and is inherent to the definition of the model. An element near the middle of the model can be affected by impacts all around its location while an element located near the impacted area boundary can only be plasticized by impacts occurring towards the center of the model. This boundary element is therefore likely to exhibit less permanent stretching and higher stresses. It was chosen to use $R = 0.70$ mm $< I$ in order to reduce the effect of this phenomenon.

Table 4.2 Comparison of calculated indicator values for 8 cases of I and R values

Case	**1**	**2**	**3**	**4**	**5**	**6**	**7**	**8**
I, mm	0.5	0.75				1.0		
R, mm	0.5	0.5	0.65	0.70	0.75	0.5	0.75	1.0
$\bar{a}_h$, mm	0.2746	0.2871	0.2753	0.2725	0.2724	0.2833	0.2764	0.2756
$S_{\bar{a}_h}$, %	16.4	9.0	11.4	10.2	7.7	13.4	6.0	4.4
DS, %	3.4	3.8	3.6	3.3	2.7	3.0	2.5	0.9
I_D, mg/mm^2	19.4	25.3	22.0	20.9	20.0	20.8	20.6	18.2
Number of impacts	40	85				135		
Number of elements	83028	127343				181073		
Calculation time for 1 analysis, h	3.3	$\approx 9.0^{(a)}$				25.4		

$^{(a)}$ Simulations for $I = 0.75$ mm were run on two processors rather than four for all other cases. This value is an estimate of the computation time with equal computing power.

Model scaling

To study different peening conditions, it was chosen to use an element size of approximately one tenth of the dimple diameter. The resulting fine mesh dimensions were 0.015 mm for a shot velocity of 34.6 m/s and 0.020 mm for a velocity of 53.7 m/s. Model dimensions were scaled so as to keep the same number of elements in each of the regions of figure 4.5.

4.4.2 Material constitutive law

The high strain rate, high plastic strain, cyclic, and compressive nature of the shot peening process makes determining correct material properties a challenging task. Study of the average equivalent plastic strain ($PEEQ$) profile at pseudo-saturation in the model presented in section 4.4.1 showed that the isotropic hardening law allows $PEEQ$ values as high as 0.5 to build up in the first two element layers. With $\sigma_0 = 379$ MPa and $H = 810$ MPa, this means that the material yield stress increases locally to more than 750 MPa. Kim *et al.* (2003) studied the effects of heat treatment and severe plastic deformation on the mechanical properties of AA-2024: a maximum tensile yield stress of 630 MPa was achieved. This indicates that a yield stress of 750 MPa is not realistic. This observation motivated studies of the microstructure after peening and of the properties of AA-2024 under moderately-high cyclic plastic straining in order to better understand the involved phenomena. In addition, Hospers and Vogelesang (1975) have shown that rolling of aluminium could create significant residual stresses in the material. These initial stresses may have an effect on the development of curvature. It was decided to evaluate the rolling stress profile in the strips used by Miao *et al.* (2010) and input it as an initial state in the impact and forming models.

Mechanical properties

Two aspects of the material constitutive law were investigated. The effect of cyclic plastic straining on the mechanical behaviour of AA-2024 was evaluated and the microstructure of this alloy after shot peening was studied to identify possible microstructure changes due to the process.

Significant differences were observed between the monotonic and cyclic behaviour for AA-2024-T351, as shown in figure 4.12. Monotonic and cyclic yield stresses are presented in table 4.3: yield stress increases by 18% between the monotonic and $\Delta\varepsilon = 6\%$ cases. Considering the high cyclic strains encountered in shot peening, this cyclic hardening behaviour needs to be considered in the material constitutive law. Table 4.3 also presents stabilization data extracted from the cyclic testing. Higher strain amplitudes required more plastic straining to stabilize. Numerical simulations have shown that equivalent plastic strains could reach

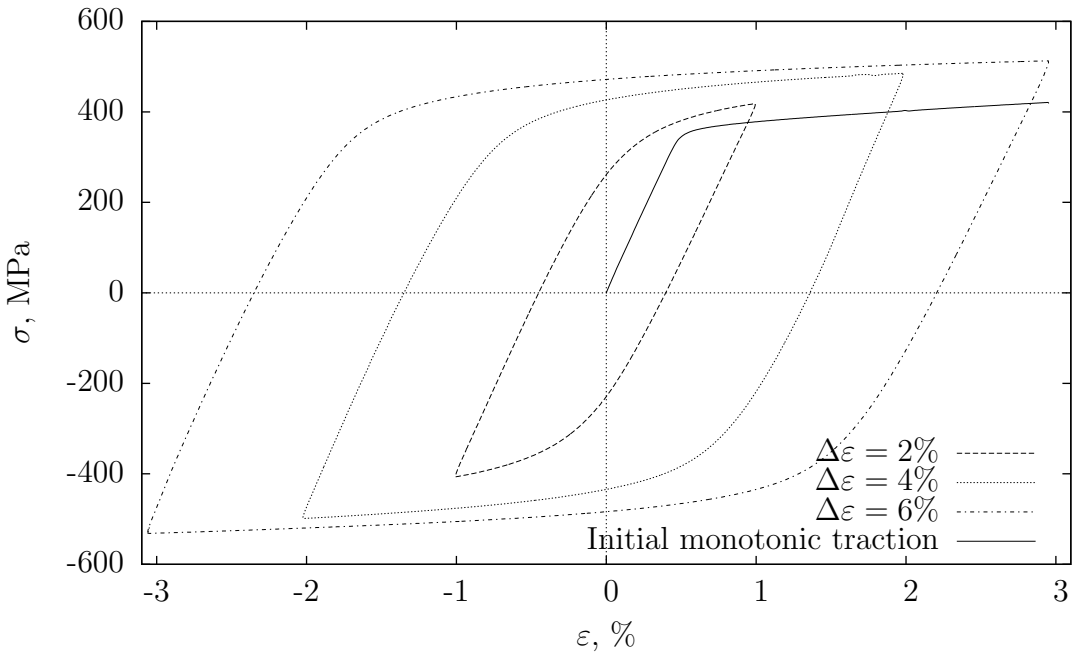

Figure 4.12 Stabilized cyclic σ-ε curves for strain ranges of 2%, 4%, and 6% compared to the initial monotonic traction data from the $\Delta\varepsilon = 6\%$ test. It should be noted that small extensometer slip occurred in early cycles during the $\Delta\varepsilon = 6\%$ test.

20% for an impact with $v_{shot} = 66.2$ m/s. While it was not possible to achieve such high strains in cyclic testing, the mechanical tests performed provided a good approximation of the hardening behaviour of AA-2024 under cyclic loading. Wu *et al.* (2002) used transmission electron microscopy (TEM) to describe the deformation mechanisms leading to nanometer-sized grains in heavily peened AA-7075. The authors observed ultra-fine grain (submicron-order) structures after severe plastic deformation by ultrasonic shot peening. The Hall-Petch equation suggests that such structures would be associated with higher yield stresses. It

Table 4.3 Yield stress and stabilization data for 3 nominal strain amplitudes

Strain amplitude	Yield stress MPa	Plastic strain per cycle %	Cycles to stabilization -	Plastic strain to stabilization %
Monotonic	370	-	-	-
1%	369	1.9	4	7.6
2%	418	5.6	5	28.0
3%	437	9.2	4	36.8

was decided to investigate a possible similar behaviour for the peening conditions used in this work with the methodology described in section 4.3.2. As shown in table 4.4, it was observed that grain size was not significantly affected by shot peening with the parameters presented in section 4.3.1. High standard deviations are due to the elongated structure in the rolling direction and different grain shapes. It should however be noted that SEM does not show dislocations structures: further study with electron backscatter diffraction (EBSD) or TEM would allow more detailed conclusions. Grain size refinement due to shot peening was assumed to be negligible for the peening conditions studied in this work.

A combined isotropic-kinematic law was chosen to represent the material behaviour. The kinematic hardening component was required to model cyclic stabilization. In this model, the yield surface moves and changes dimensions when yielding occurs (ABAQUS Theory Manual, 2008). The kinematic parameters were identified from a monotonic tensile stress-strain curve: $\sigma_0 = 370$ MPa, $C = 4985.5$ MPa, and $\gamma = 32.762$. The cyclic hardening option was used to input the estimated effect of equivalent plastic strain on yield stress. Since cyclic testing did not reach strain amplitudes typical of shot peening, the maximum yield stress and accumulated plastic strain ($PEEQ$) to stabilization for the peened material had to be estimated. Based on the data presented in table 4.3, a maximum yield stress of 460 MPa at $PEEQ = 0.4$ was chosen. This means that for each element, yield stress increases progressively from 370 to 460 MPa when the equivalent plastic strain ($PEEQ$) increases from 0.0 to 0.4. For $PEEQ > 0.4$, yield stress remains constant at 460 MPa. Strain-rate effects and material anisotropy were not modelled.

Initial rolling stresses

Residual stress measurements in a 1.6-mm thick sheet of AA-2024-T3 by Miao *et al.* (2010), shown in figure 4.13(a), were used to evaluate initial stresses. It was observed that stresses in the core of the sample were not consistent with simple bending and stretching of

Table 4.4 Grain size measurements on peened and unpeened sides of the sample

Depth μm		Grain size μm	Number of observations	Standard deviation μm	N.C.I., 95%[(a)] μm
Peened side	< 150	14.3	70	7.3	$\pm$1.73
	$\approx$ 150-350	14.9	47	8.6	$\pm$2.52
Unpeened side	< 150	17.2	32	8.6	$\pm$3.09
	$\approx$ 150-350	17.0	30	9.7	$\pm$3.62

[(a)] Normalized confidence interval, 95% level, assuming a normal distribution.

the sample to achieve equilibrium described in figure 4.2. Shot peening directly affects only a thin layer of material near the surface and could not explain such compressive stresses at mid-thickness. Based on Hospers and Vogelesang (1975), it was assumed that the observed phenomenon was caused by initial residual stresses due to rolling.

Bending stresses σ_{bend} were evaluated and removed as shown in figure 4.13(a). These stresses are caused by bending of the thin aluminium sheet due to unbalanced peening-induced stresses. Assuming that (i) the initial residual stress profile was symmetrical and that (ii) peening had a direct effect only near the peened surface, the stress profile for depths of 0.8 to 1.6 mm was then approximated with a simple trapezoidal model and balanced axially so that the total force created by initial stresses was zero. Figure 4.13(b) shows the results from this calculation. Stress values were consistent with the residual rolling stress profile obtained by Hospers and Vogelesang (1975) for a 3.0-mm thick sheet of AA-2024-T3. This profile was introduced as an initial state in the dynamic impact and forming models presented in this article. It was assumed that residual stresses due to rolling are equal in both the transverse and rolling directions: this hypothesis requires further validation. In the case of thick AA-2024-T351 samples, modelling did not include initial residual stresses since the Tx51 stress relieved state is likely to have reduced residual stresses, as shown by Prime and Hill (2002) for AA-7050.

4.4.3 Sequence-sensitive forming simulation

Shot peening of a thick part does not induce any significant bending, so models like that of section 4.4.1 can be used to adequately calculate the residual stresses in a thick component. However, during an Almen test or peen forming processes, a thin component bends and elongates progressively as it is subjected to an increasing amount of shots. Stresses induced by each impact are therefore constantly redistributed. Since the way the component bends and elongates depends on its shape and boundary conditions, it is not possible to establish a simple universal model for predicting the stress redistribution. Moreover, this redistribution creates complex stress fields that have an effect on the development of new stresses during following impacts. As explained in section 4.2, current peen forming models do not take this phenomenon into account. Modelling this effect will lead to more accurate deformed shape predictions.

One computationally-expensive way of modelling the Almen test, for example, would be to create a 3D solid finite element model of the whole Almen strip and submit it to shot impacts, as for the dynamic model of section 4.4.1. This approach was investigated by Kang *et al.* (2010) on a 20×20 mm target. In section 4.4.1 of the present study, simulating an impacted area of 0.56 mm^2 required approximately 10 hours of computational time: modelling the

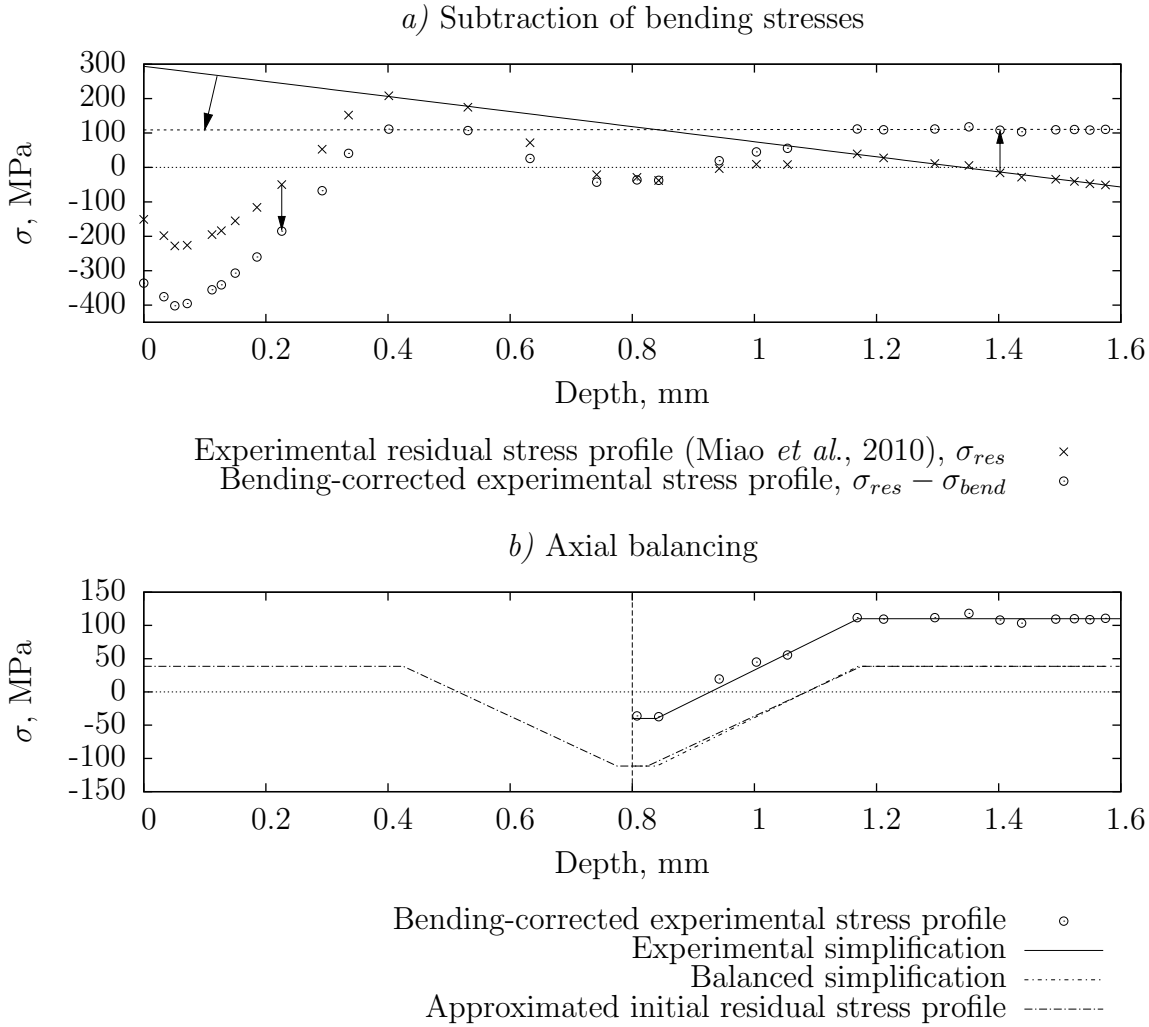

Figure 4.13 Determination of initial rolling stresses. (a) Based on residual stress measurements by Miao *et al.* (2010), bending stresses were approximated (solid line) and subtracted (dashed line). This caused increased compression on the peened side (left) and increased tension on the unpeened side (right). (b) Assuming symmetry, the bending-corrected stress profile was simplified and balanced axially.

Almen strip (1450 mm^2) – or a wing skin – response in such a way is therefore not adequate with current computers. In order to obtain useful and efficient predictions for peen forming processes, simplifications must be introduced.

The newly developed methodology introduced in this paper is based on induced stress profiles, *i.e.* stresses in the non-equilibrium state. The following assumptions and observations were made:

a. In the case of normal shot peening, uniform peening generates at the part scale an induced

stress field dependent only on depth, *i.e.* uniform in the X-Y plane (Kang *et al.*, 2010).

b. Peening of a part with multiple passes is studied in this article. The effect of the shot peening equipment trajectory over the component is neglected. During one pass, the part is uniformly subjected to shot peening so that the same induced stress profile is introduced simultaneously in all elements of the model.

c. The development of induced stresses near the surface is almost insensitive to initial residual stresses. Figure 4.14 illustrates this observation. For two cumulated effective masses M_e, four dynamic analyses were performed with two different initial stress profiles. Cases 1 and 3 use the initial stress profile due to rolling determined in section 4.4.2. In cases 2 and 4, non-equal stress profiles were selected in the X and Y directions based on residual stress profiles calculated after one and eight passes, respectively. It was observed that near-surface induced stresses with different initial stress profiles were nearly the same and could be assumed to be equal. Cao *et al.* (1995) used a similar hypothesis in their work.

d. As can be seen from figure 4.14, induced stresses far away from the surface are not appreciably affected by shot peening and tend to be quite close to the initial residual stresses.

e. Based on the two previous observations, it was assumed that peening-induced stresses near the surface would be those calculated from the dynamic model. Far away from the surface, stress values after peening would be those that existed prior to peening. In order to obtain a systematic procedure, clear definitions for "near the surface" and "far away from the surface" must be supplied.

f. The stress field between "near the surface" and "far away from the surface" after peening is assumed to be an interpolation between the induced stresses calculated with the dynamic model and those existing in the strip prior to peening. A systematic definition of the interpolation procedure must also be introduced.

The proposed methodology relies on the dynamic model presented in section 4.4.1 for computing the shot peening induced stresses and on a shell-based FE model for predicting the deformed shape of the component. The analysis is performed in a number of *steps*. These calculation steps must be related to the actual peening process. For example, steps could be defined as increments of impacting mass M_i on a target up to a total impacting mass of M_t. The methodology is as follows. The dynamic impact model is first used to calculate induced stress profiles up to an effective impacting mass of M_t. The forming model is then used to simulate each step. The initial stress profile in the strip is that generated by previous fabrication processes, like rolling. At the beginning of step 1, the calculated induced stress profile corresponding to an impacting mass of M_i is input uniformly into the shell-based model and the stress field at equilibrium is computed. Step 2 is then initiated. The balanced

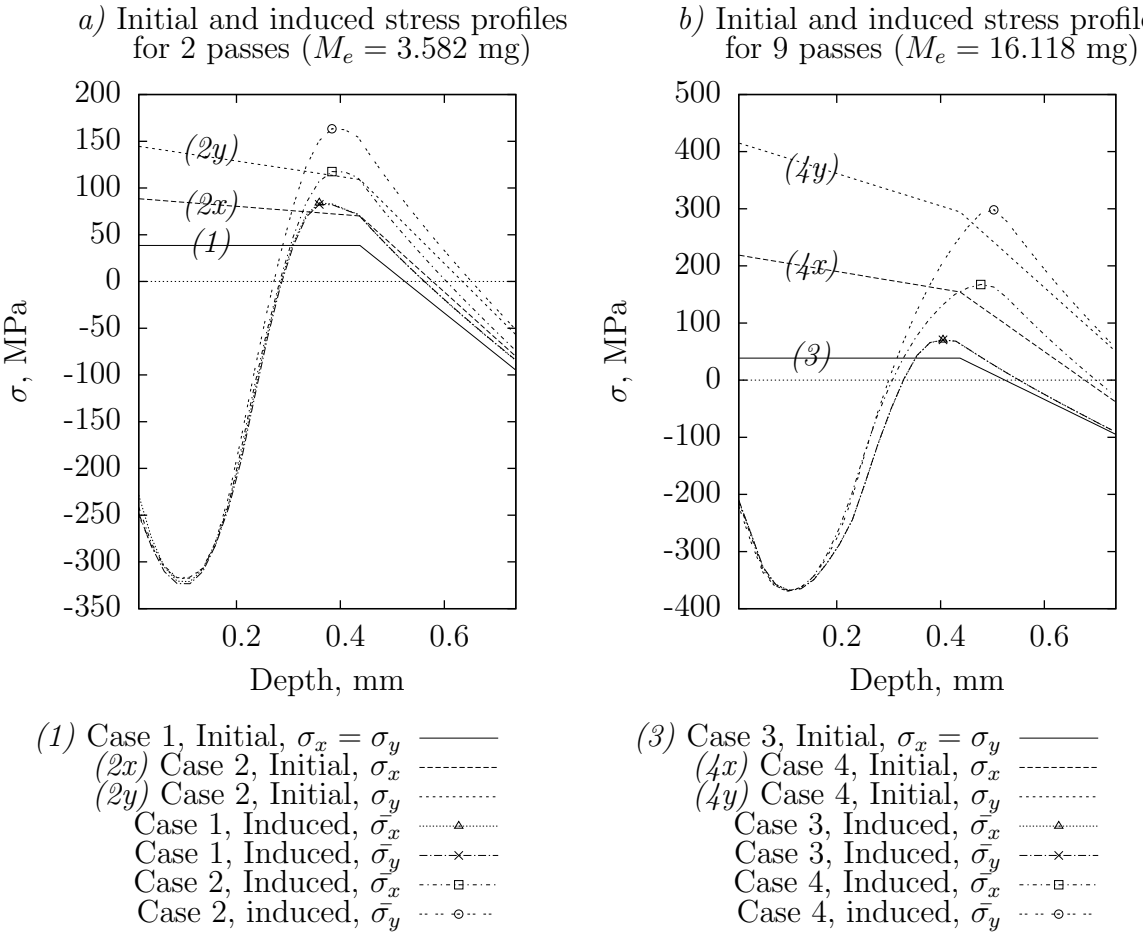

Figure 4.14 Effect of initial residual stresses on induced stress profiles for a shot velocity of 66.2 m/s. (a) Two cases of initial stresses impacted with a cumulated effective mass of 3.582 mg. Case 1 had only rolling residual stresses (figure 4.13) and case 2 had different stress profiles in the X and Y directions. (b) The same methodology was applied for a cumulated effective mass of 16.118 mg.

stress field obtained at the end of step 1 is considered as initial stresses for step 2. Induced stress profiles corresponding to an impacting mass of $2 \times M_i$, computed with the dynamic model, are "added" into the model based on hypotheses (e) and (f). A new stress distribution is computed using the induced stresses from the dynamic model and the stresses at the end of step 1. This new stress distribution is input into the deformed mesh imported from the end of step 1 and the stress field at equilibrium is computed again. This process is repeated, step by step, until the total impacting mass M_t is reached.

The following sections detail the various elements of the procedure and its application to the experimental pseudo-Almen test of Miao *et al.* (2010).

Modelling approach

Figure 4.15 shows the 3-layer structure of the 4-node reduced-integration (S4R) composite shell elements used. Each 0.5-mm thick outer layer could be used to introduce numerically-calculated peening induced stresses at 15 Simpson section integration points while the middle layer allowed variations of the thickness of the simulated plate. This model allowed independent introduction of unbalanced induced stresses in the X and Y directions at section points. Successive equilibrium iterations were performed with ABAQUS/Standard, version 6.8.3, with the nonlinear analysis option.

Assumptions (e) and (f) presented in section 4.4.3 had to be translated into a mathematical form. The following equation was developed to calculate new weighted stresses:

$$\sigma_x^{\text{new}}(p) = S_p \times \sigma_x^{\text{peening}}(p, n) + (1 - S_p) \times \sigma_x^{\text{last}}(p) \tag{4.9}$$

where $\sigma_x^{\text{new}}(p)$ is the stress at section point p of an element in the X direction at the beginning of step n, $\sigma_x^{\text{peening}}(p, n)$ is the induced stress at section point p for the n^{th} modelling step calculated using the random dynamic impact model, $\sigma_x^{\text{last}}(p)$ is the balanced stress at section point p in the X direction extracted from the end of the step $n - 1$, and S_p is the discrete superposition function described below. Stresses at section points $\sigma_x^{\text{peening}}(p, n)$ were interpolated from induced stress profiles obtained with dynamic impact simulations. The same equation was used for stresses in the Y direction. For elements and section points unaffected by peening, stress values were simply transferred from one step to the next. Shear stresses remained unchanged between steps.

Figure 4.16 presents graphically the determination of S_p. Since induced stress profiles varied with cumulated effective mass M_e, it was decided to use the profiles at half the numer-

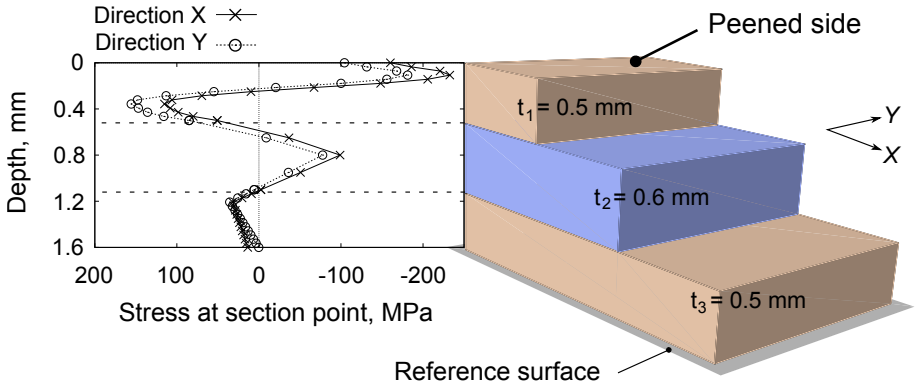

Figure 4.15 Layered structure of shell elements. Each outer layer has 15 section points and the middle one has 5. Stresses could be input for both directions independently.

ical saturation mass in defining S_p. This was a compromise between representing accurately low and high impacting masses. The induced stress values at section points were used to define "near the surface" and "far away from the surface", as shown in figure 4.16. Section points for which induced stress values were more compressive than the surface stress value were defined to be "near-surface" and for these points $S_p = 1$. Section points located deeper than the maximum tensile stress were considered to be "far away from the surface" and for these points $S_p = 0$, so that stress values remained unchanged. It should be noted that this latter approximation is not perfect:

1. Figure 4.14 shows that tensile stresses after shot peening were higher than those of the initial stress profile. However, figure 4.8 shows that this increase was at least partially related to the presence of unimpacted material in the dynamic impact model;
2. In figure 4.14(b), for large tensile initial stresses, the maximum tensile stress depth was shifted slightly to the right.

Despite these drawbacks, it was deemed that the S_p function could be used as a simple method to model sequence-sensitive peen forming. A progressive transition between near- and far-surface was assumed, as shown in figure 4.16. Figure 4.17 shows an example of calculation of new stresses $\sigma^{new}(p)$ with equation (4.9) and the selected definition of S_p. S_p values had to be determined for each velocity since this parameter had a significant effect on the stress profiles: S_p values for the studied shot velocities are presented in table 4.5. It should be noted that this definition of S_p remains empirical and should be subject of further study.

Table 4.5 Superposition functions S_p values

Shot velocity	Section point p									
	1 to 4	5	6	7	8	9	10	11	12	13 to 15
66.2m/s	1.0	1.0	1.0	1.0	0.9	0.7	0.5	0.3	0.1	0
53.7m/s	1.0	1.0	1.0	0.9	0.7	0.3	0.1	0	0	0
34.6m/s	1.0	0.9	0.7	0.3	0.1	0	0	0	0	0

Due to boundary conditions, stress redistributions did not create a uniform stress field in the modelled component. For example, at the beginning of step 2, stress profiles in the part vary from one element to another. Equation (4.9) therefore had to be applied to each element of the FE mesh at each step, using the same S_p functions for all elements. Boundary conditions could be modified in each step of the analysis. Strip bending and vibration due to impact forces were not taken into account in this study.

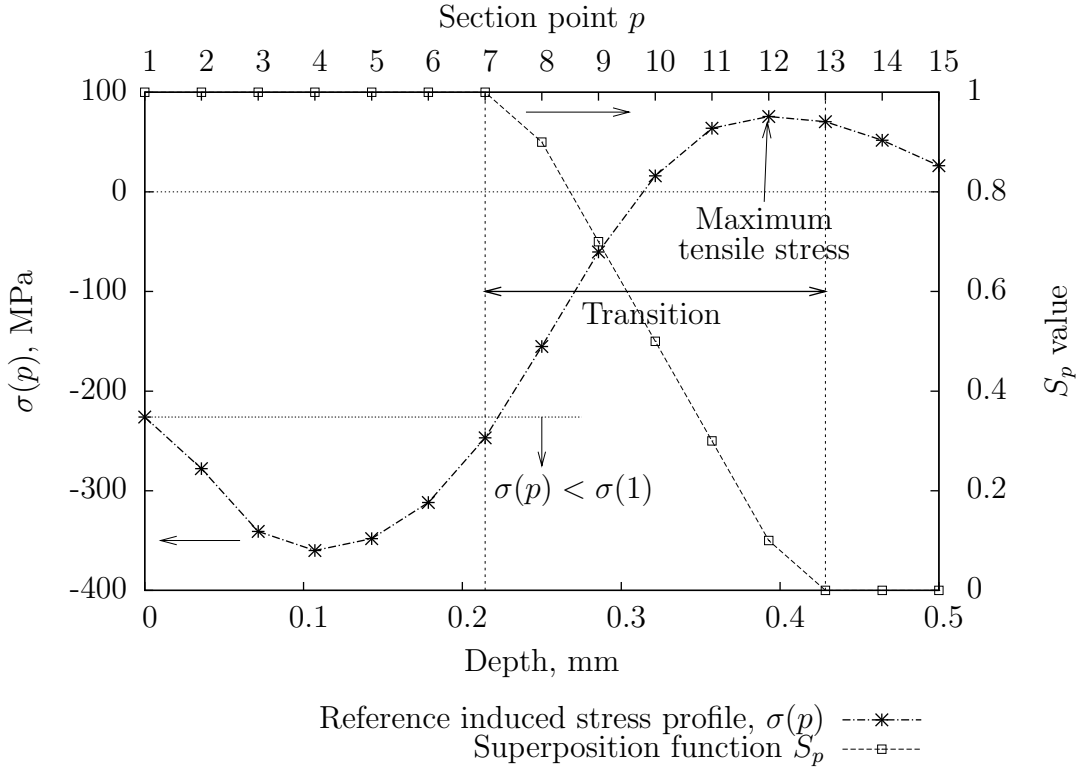

Figure 4.16 Principles of definition of superposition function S_p based on induced stress profile at approximately half the numerical saturation mass. The induced stress profile was first determined numerically with the dynamic impact model and the reference case of initial residual stresses and then interpolated at section points p.

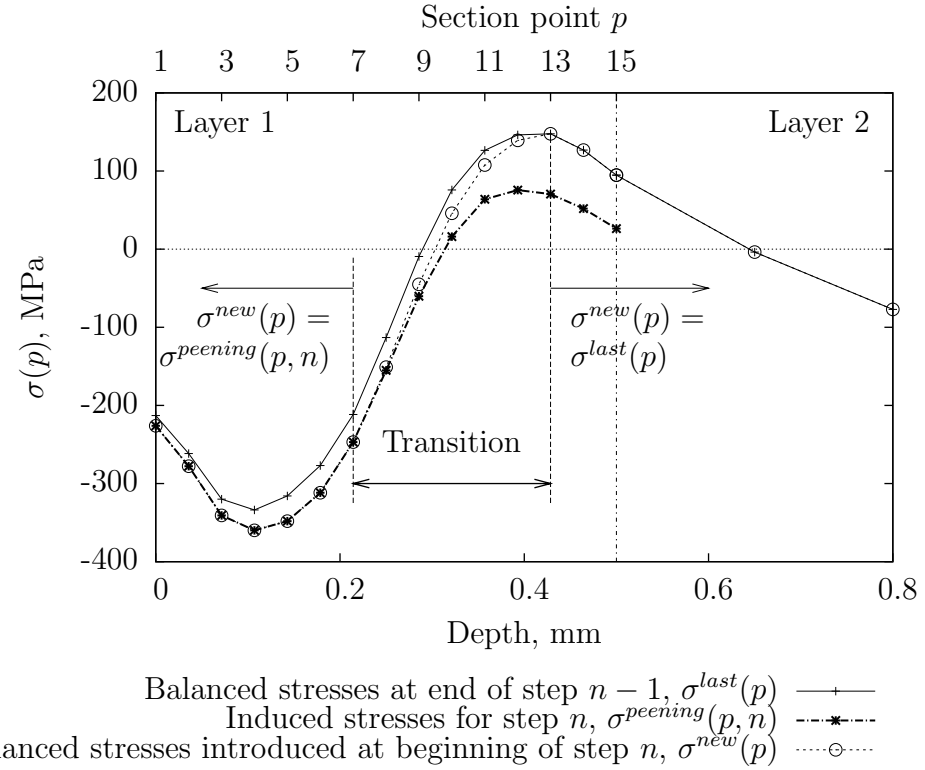

Figure 4.17 Example of calculation of new stresses $\sigma^{new}(p)$ for a step n, based on equation (4.9).

Modelling of the pseudo-Almen test

The sequence-sensitive forming model was set up to study the case of a 1.6-mm thick AA-2024-T3 sample peened in an Almen holder. All nodal displacements were blocked at nodes corresponding to the holder screws, as shown in figure 4.18. Peening stresses were not introduced in the elements covered by screws. Contact between the shell reference surface (figure 4.15) and a fixed rigid plane underneath the deformable shells was modelled to represent the Almen holder.

As explained in section 4.3.1, Miao *et al.* (2010) used number of passes of the robot over the Almen holder as the variable to vary experimental peening time. The robot trajectory for one pass is illustrated in figure 4.19. For the purpose of the present study, it was necessary to evaluate the effective mass associated with one peening pass. Using:

$$I_D^{1\text{pass}} = \frac{\frac{L_p \times N_t \times \dot{m}}{v_r \times 60}}{A_{target}} \tag{4.10}$$

it was estimated that one pass of the robot over the 1.6-mm thick Almen-sized aluminium strip delivered an impact density $I_D^{1\ \text{pass}} = 3.65$ mg of shots per mm^2. In equation (4.10), L_p is the effective length of the robot travel over the Almen-sized strip, N_t is the number of times the robot travels along the length of the strip to cover the full width of the strip, $\dot{m}$ is the mass flow rate in kg/min, v_r is the travel velocity of the manipulator arm in mm/s, and A_{target} is the area of the strip in mm^2. As shown in figure 4.19, L_p was estimated at 80 mm to take the 6-mm nozzle diameter into account and $N_t = 19$ mm/6 mm = 3.167. It was calculated that one pass of the robot was equivalent to a cumulated effective mass M_e of 1.791 mg on the representative area of the dynamic impact model presented in section 4.4.1.

The effect of the number of calculation steps used to represent one peening pass was first investigated. Almen arc height was used as a comparison basis. Figure 4.20 shows results of calculations run for three progression cases for a shot velocity of 66.2 m/s:

1. One calculation step per two experimental passes;
2. One calculation step per experimental pass;
3. Two calculation steps per experimental pass.

Arc heights calculated without considering progressive deformation, *i.e.* by simply introducing the induced stresses corresponding to the number of passes studied in the strip model, are also presented in figure 4.20 (case 4). This latter case corresponds to the pseudo-saturation curve discussed in section 4.4.1. The effect of progressive deformation was not negligible and the number of calculation steps per peening pass had a significant influence. For six passes,

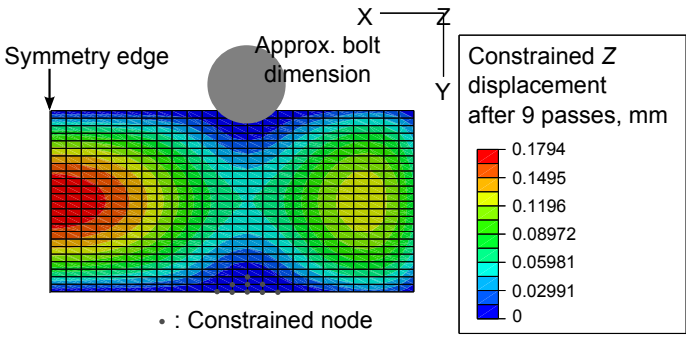

Figure 4.18 Nodal constraints used to represent the holder screws. All displacements and rotations were blocked at nodes covered by screws. Contour shows constrained deflections after nine passes with $v_{shot} = 66.2$ m/s. The full strip was modelled although figures in this article show only half the strip.

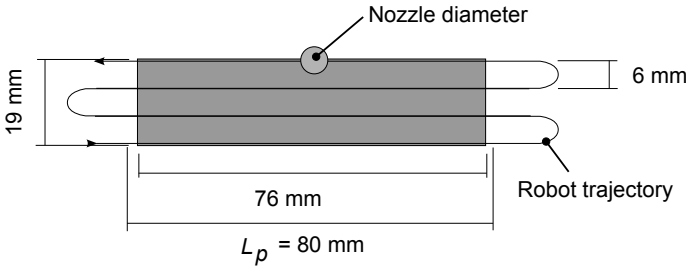

Figure 4.19 Robot trajectory over the Almen-sized aluminium strip. One pass of the robot corresponds to the nozzle following this trajectory once; for multiple passes, the robot goes back to the start of the trajectory and follows the path again.

it was calculated that case 1 yielded an arc height 9.8% lower than case 2 and that case 3 provided an arc height 6.7% higher than case 2. Using more calculation steps for a given number of passes accelerates arc height build-up since each new induced stress calculation with equation (4.9) contributes to progressive deformation by offsetting the previous equilibrium. It was decided to use one forming simulation step for each peening pass (case 2).

To calculate numerical saturation curves, induced stresses were extracted from the impact simulations at integer multiples of the effective mass per pass of 1.791 mg. The sequence-sensitive process simulation for N_p peening passes, requiring $N_p + 1$ steps, was performed as follows:

Step $n = 1$**:** First constrained peening step:

i. Boundary conditions representing the Almen holder were imposed;

ii. The initial stress state in the strip was the rolling stress profile determined in section 4.4.2;

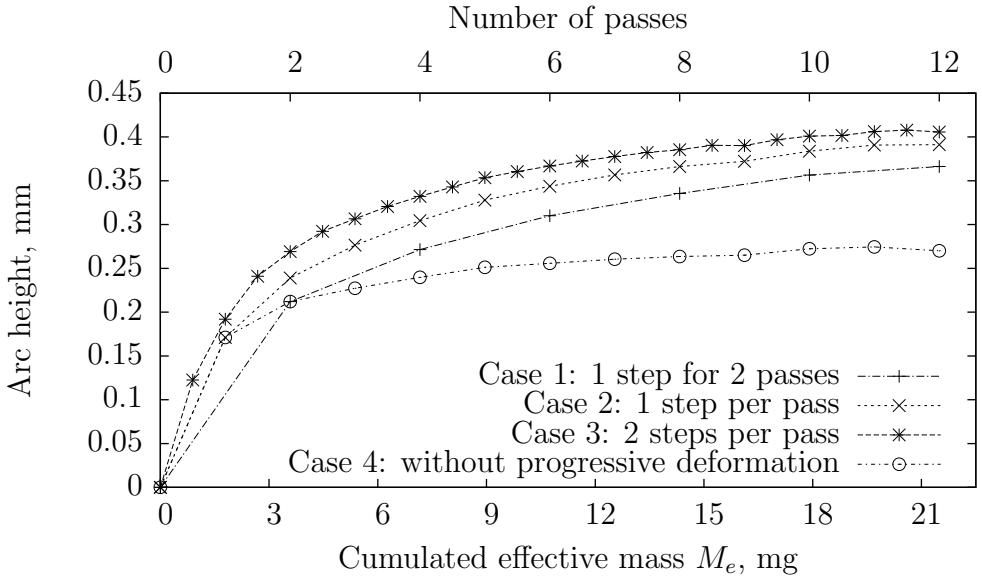

Figure 4.20 Effect of the number of calculation steps per peening pass. Three options were studied: one step per two peening passes (1), one step per pass (2), and two steps per pass (3). Arc heights determined from induced stress profiles without considering progressive deformation are shown as a comparison basis.

iii. Calculated induced stress profiles for $M_e = 1.791$ mg were introduced in all elements except those covered by holder screws;

iv. As shown in figure 4.21, complex stress fields were created after stress redistribution.

Steps $n = 2$ **to** $N_p - 1$ Subsequent constrained peening steps, for $N_p > 2$:

i. Model geometry was imported from step $n - 1$ and boundary conditions were maintained;

ii. Numerically-calculated induced stresses for a cumulated effective mass of $M_e^n = 1.791 \times n$ were used in equation (4.9) to calculate new stresses $\sigma_x^{new}(p)$ and $\sigma_y^{new}(p)$ at each element for section points $p = [0, 15]$;

iii. New balanced stresses were computed.

Step $n = N_p$ Last constrained peening step:

i. Model geometry was imported from step $N_p - 1$ and boundary conditions were maintained;

ii. Induced stresses for $M_e^{N_p} = 1.791 \times N_p$ and equation (4.9) were used to calculate new stresses at each element;

iii. After calculation of the balanced deformed shape by ABAQUS, maximum constrained deflection was extracted for comparison with experimental results.

Step $n = N_p + 1$ Free deformation:

i. Model geometry and stresses were imported from step N_p, screws boundary conditions were removed and minimal boundary conditions were imposed at corner nodes to prevent rigid body motions;

ii. Free deformed shape and final residual stresses were computed;

iii. Free arc height $a_h^{N_p}$ was determined by subtracting the Z displacements of the node corresponding to the Almen gauge probe and a node corresponding to the location of a support sphere (see figure 4.1(a)) These nodes were identified from the undeformed geometry. Displacements in the X-Y plane had a negligible effect on the relative locations of the measured nodes.

For each shot velocity and number of passes N_p studied, $(M_e^{N_p}, a_h^{N_p})$ values were calculated. For instance, for $v_{shot} = 66.2$ m/s, values of N_p were $[1, 2, \ldots, 12]$, which provided 12 results. This simulation data was best-fitted using equation (4.6) and cumulated effective mass at saturation M_e^S was calculated with equation (4.7). Arc heights at saturation a_h^S were determined with:

$$a_h^S = \frac{A \times M_e^S}{B + M_e^S} \tag{4.11}$$

Figure 4.21 shows an example of this sequence-sensitive procedure with nine peening passes and a shot velocity of 66.2 m/s. In figure 4.21(a), initial introduction of peening stresses (except at the elements covered by the screws), stress field at equilibrium at the end of step 1, and the introduction of new weighted stresses at the beginning of step 2 are presented. In figure 4.21(b), constrained and free deformation are presented along with their associated stress profiles. Different stress profiles were obtained in the X and Y directions due to boundary conditions.

As mentioned in section 4.4.3, peening stresses were introduced simultaneously in all elements of the model for each step. The effect of the robot trajectory was neglected in this work but will be investigated in a future study.

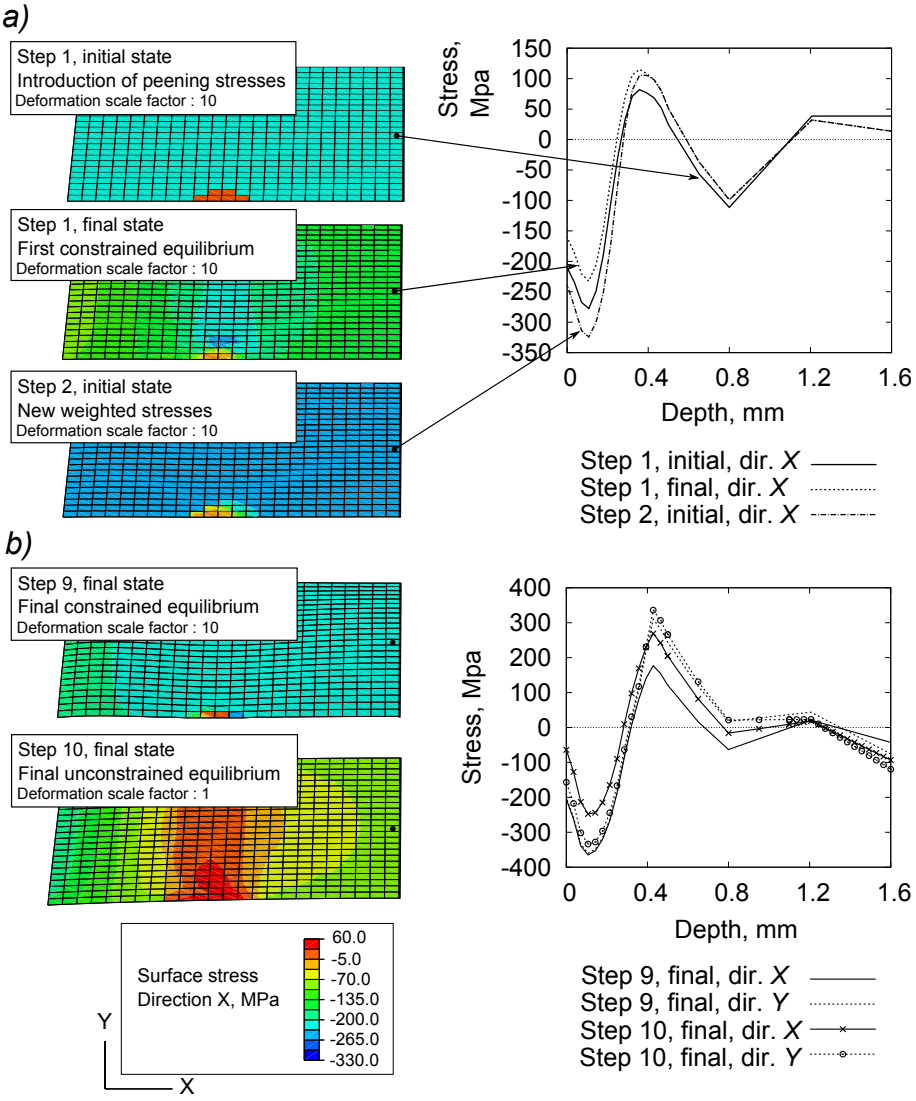

Figure 4.21 Example of the proposed forming simulation method. (a) First introduction of peening stresses in a flat sheet followed by constrained equilibrium state and calculation of new weighted stresses in the peened layer for the 2$^{\text{nd}}$ step. (b) Deformation and stress profiles at the element marked by a dot, in the middle of the model before and after removal of the nodal bolt constraints. Stress profiles in the X and Y directions were not equal after stress redistribution. A non-uniform stress field was created in the strip.

4.5 Results and discussion

The finite element models presented in section 4.4 were used to simulate experiments from Miao *et al.* (2010). Additional experiments were performed to complement these results. Stress profiles in thick samples were first compared to validate the random dynamic impact model and material constitutive law. Saturation experiments were then considered to evaluate the sequence-sensitive forming model. For each velocity, four simulations were run with the dynamic impact model to obtain average induced stress profiles. For forming simulations, $\bar{\sigma}(z_i)$ profiles were used. Having multiple experimental cases to compare allowed verification of the versatility of the proposed numerical simulation approach.

4.5.1 Induced stress profiles

Figure 4.22 shows the average induced stress profiles calculated with a 5-mm thick impact model at the cumulated effective masses at saturation presented in table 4.7. Two shot velocities were studied: 34.6 m/s and 66.2 m/s. The numerical stress profiles were compared to experimental residual stress profiles from Miao *et al.* (2010) for a 12.5-mm thick plate of AA-2024-T351 and experimental saturation parameters. The effect of model thickness on induced stress profiles was evaluated by running two analyses in which only model thickness was different: values of 5 mm and 12.5 mm were selected. Average stress profiles did not vary by more than 3.5 MPa. Since the induced stress profile was fairly insensitive to model thickness, a 5-mm thick model was used instead of a 12.5-mm thick model to reduce calculation time. It was assumed that AA-2024-T3 and AA-2024-T351 properties were the same and that initial stresses in AA-2024-T351 were negligible. Stress profiles in the X and Y directions for four simulations exhibited a relatively small scatter consistent with the results of Zimmermann *et al.* (2010). Selected model dimensions and the definition of the effective mass contributed to reducing the scatter of the results. The proposed model was therefore deemed appropriate to evaluate induced stress profiles from four random analyses.

The isotropic-kinematic material behaviour could represent the increase of compressed depth with increasing velocity. Surface stress and compressed depth were well approximated. Maximum compressive stress prediction could be improved. One possible explanation is that cyclic strain amplitudes in the material vary with depth and shot velocity. Material closer to the surface and/or impacted with a higher shot velocity is subjected to higher strain amplitudes. In section 4.4.2, it was shown that strain amplitudes greatly influence the stabilized yield stress. Since the modelled material behaviour did not consider these variations, the model may have overestimated yield stress at greater depths, causing excessive compressive stresses. The material law could be improved by taking such effects into account, as in Klemenz *et al.* (2009) and Zimmermann *et al.* (2010).

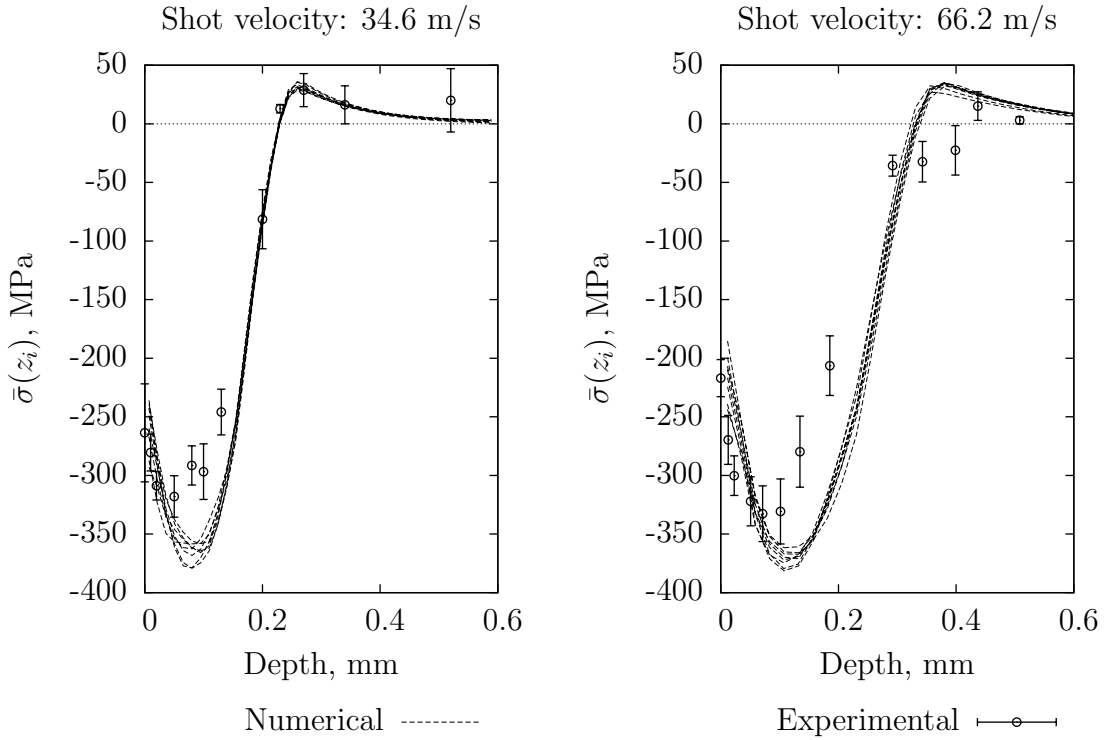

Figure 4.22 Comparison of experimental and numerical stress profiles at saturation conditions in a thick part for two shot velocities. Experimental results were taken from Miao *et al.* (2010). Four numerical simulations were run with random shot locations and diameters for each shot velocity. Induced stress profiles were extracted in the X and Y directions, yielding a total of eight numerical stress profiles for each velocity.

4.5.2 Forming

Figure 4.23 presents the comparison of numerical and experimental results for a shot velocity of 66.2 m/s. Experimental arc height measurements were taken from Miao *et al.* (2010) and constrained deflection curve was measured with the method described in section 4.3.1. Figure 4.23 shows that constrained deflections were not negligible compared to arc heights, as observed by Cao *et al.* (1995). Predicted constrained deflections were within measurement accuracy but free Almen arc heights were slightly underestimated. Some of this difference may be related to peening equipment variability since experimental results of constrained deflections were obtained a year after those of free arc heights. In section 4.5.1, it was shown that the dynamic model overestimated the maximum compressive stress value for a shot velocity of 66.2 m/s (figure 4.22), which would lead to overestimated arc heights. This may indicate that other phenomena, like strip vibration, affect deformation results for high peening energy. The differences between calculated and experimental arc heights values

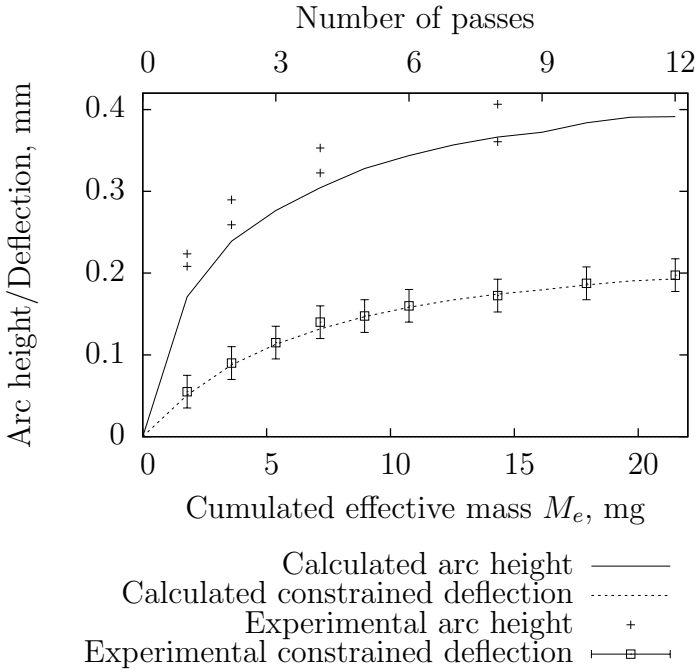

Figure 4.23 Comparaison of calculated and experimentally determined free arc heights and constrained deflections for a shot velocity of 66.2 m/s. Experimental arc heights were taken from Miao *et al.* (2010). Vertical bars for experimental deflections indicate the measurement accuracy.

were larger for low numbers of passes. This can be related to inaccuracies of the proposed forming model in the first calculation steps or to an incorrectly represented transient material behaviour, prior to establishing stabilized properties.

Radii of curvatures in the long (X) and short (Y) directions were measured as indicated in section 4.3.1 for a number of passes slightly higher than the experimental saturation point. Radii were determined from numerical simulations at an equivalent state. Results are presented in table 4.6. Experimental results are consistent with those of Cao *et al.* (1995). The numerical forming model could correctly represent the development of larger curvatures (smaller radii) in the transverse (Y) direction. A significant difference was observed between the measured and numerically-calculated constrained radii along X: in this case, due to the nearly flat profile, the fitting method may have been affected by surface roughness. It should also be noted that samples were maintained in Almen holders for a long time before measurements were made, which may have allowed small sample movement in the Almen holders.

Analyses were run for two other velocities: 34.6 m/s and 53.7 m/s. Figure 4.24 shows a comparison of numerical and experimental saturation curves and presents calculated con-

strained deflections for these cases. Promising agreement was observed between experimental and numerical arc height results for the two lower shot velocities of 34.6 m/s and 53.7 m/s. Considering experimental variations, calculated arc heights for these shot velocities were close to experimental values. It is possible that the proposed material law was more appropriate to represent the behaviour of aluminium peened with lower shot velocities for which the material was subjected lower strain amplitudes and strain rates.

Table 4.7 presents numerically and experimentally determined saturation points for the 3 shot velocities under investigation. Arc heights at saturation were underestimated by a maximum of 5.5% but masses at saturation were considerably overestimated. Numerical determination of the saturation point proves to be challenging since it involves fitting a 2-parameter curve (equation 4.6) over all the data points. Discrepancies between numerical and experimental saturation points can arise from the small differences between numerical and experimental saturation curves noted earlier in this section. For example, the underestimation of experimental arc heights at low number of passes had an effect on the determination of the fitting parameters of equation (4.11) and therefore affected the numerical saturation point.

In summary, the proposed numerical approach provided promising induced stress and saturation results for low shot velocities but differences between numerical and experimental results were larger for a high shot velocity. The non-uniform curvatures were also calculated with fair agreement.

Table 4.6 Experimental and numerical radii of curvature near saturation for a shot velocity of 66.2 m/s

	Constrained radii, mm		Free radii, mm	
	Along X	Along Y	Along X	Along Y
Experimental	2130.9	259.5	507.3	277.1
Numerical	1272.1	261.5	469.5	260.4
Difference (%)	-40.3	0.8	-7.4	-6.0

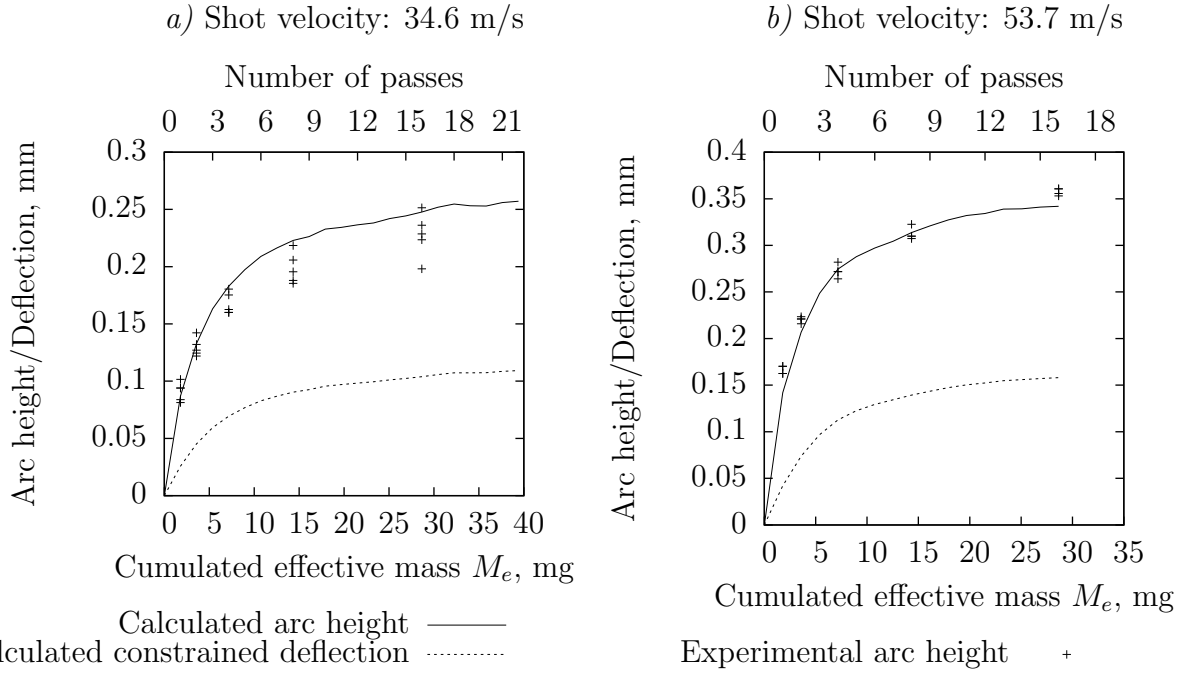

Figure 4.24 Comparaison of calculated and experimentally determined saturation curves for shot velocities of (a) 34.6 m/s and (b) 53.7 m/s. Experimental arc heights were taken from Miao *et al.* (2010).

Table 4.7 Experimental and numerical saturation points for shot velocities under investigation

$v_{shot} = 66.2$ m/s	Arc height, mm	Impact density, mg/mm^2
Numerical	0.3658	29.0
Experimental	0.387	21.5
Difference (%)	−5.5	+34.9

$v_{shot} = 53.7$ m/s	Arc height, mm	Impact density, mg/mm^2
Numerical	0.3102	26.7
Experimental	0.321	25.0
Difference (%)	−3.4	+6.8

$v_{shot} = 34.6$ m/s	Arc height, mm	Impact density, mg/mm^2
Numerical	0.2309	36.1
Experimental	0.224	34.6
Difference (%)	+3.1	+4.4

4.6 Conclusion

The contributions of this study are as follows:

1. The random dynamic impact model proposed by Miao *et al.* (2009) was further studied in order to better understand the effects of its dimensions. Dimensions and parameters were determined to correctly represent the residual stress profile of a large, completely peened plate.
2. An approximate material model for peened AA-2024 was developed by studying cyclic material properties, the effect of peening on the microstructure, and initial residual stresses. An isotropic-kinematic constitutive theory provided a fair prediction of induced stresses for two different shot velocities.
3. A new stress-based forming simulation approach using the commercial finite element software ABAQUS was proposed. The influence of initial stresses on development of peening-induced stresses was investigated in order to take into account the effects of peening sequence. The case of an Almen-sized aluminium strip peened in an Almen holder was studied. Comparison with experimental saturation results showed promising agreement for three sets of peening parameters. To the authors' knowledge, an accurate numerical modelling of the Almen test had not been achieved before.
4. The forming simulation method used induced stresses calculated with a small dynamic impact model to simulate component deformation due to multiple peening passes via a simple superposition function determined from induced stress profiles. This approximate approach is an efficient option for modelling large peened parts like wing skins.

A better understanding of the peened material state and behaviour would be beneficial. The material law used in this article remains an estimate based on limited data and requires improvements. Characterization of the peened material is challenging because only a thin material layer is affected and complex loads are created by the process.

Definition of the superposition function S_p should be studied further. It was also shown that large initial tensile stresses caused shifting of the maximum tensile stress depth: this phenomenon should be taken into account in the simulations.

The experimental case studied in this article remains fairly simple, but provides a starting basis for more complex cases. The main advantage of this numerical tool is its flexibility for modelling complex cases. Future studies could investigate peening in one slow pass instead of multiple passes and peening of a part with different peening patterns. Comparison of numerical and experimental residual stress profiles in a thin part would also be useful to further validate the proposed models.

Acknowledgements

This research was made possible by a Natural Sciences and Engineering Research Council of Canada (NSERC) scholarship to A. Gariépy. The authors would like to thank Bénédict Besner at École Polytechnique de Montréal for setting up the cyclic testing experiments, Dr Hong Yan Miao at École Polytechnique de Montréal for her suggestions in the development of the dynamic impact model, Christian Corbeil at the NRC-AMTC for preparing the stream photography setup, and Xavier Pelletier at the NRC-AMTC for the preparation of microscopy samples.

CHAPTER 5

ARTICLE 2: EXPERIMENTAL AND NUMERICAL INVESTIGATION OF MATERIAL HETEROGENEITY INDUCED BY SHOT PEENING IN ALUMINIUM ALLOY AA2024-T351

A. Gariépy, F. Bridier, M. Hoseini, P. Bocher, C. Perron, M. Lévesque. Submitted to *Surface and Coatings Technology* on July 29, 2012.

5.1 Abstract

Shot peening is a heterogeneous mechanical surface treatment that consists of projecting numerous small particles onto a ductile surface. Repeated and random hammering leads to compressive residual stresses as well as work-hardening near the surface resulting in a potentially significant improvement of the fatigue performance. On the other hand, shot peening also increases surface roughness and can produce surface damage which are detrimental to fatigue properties. Fatigue life prediction models have been proposed to predict the combined influence of these factors. Most of these models assume that shot peening generates a uniform material state parallel to the surface. The current work investigated for the first time the heterogeneities induced in aluminium alloy AA2024-T351 by the random impact sequence in terms of residual stresses, work-hardening, surface roughness, and damage. Experimental and numerical methods were combined to obtain a detailed description of the material state at various length scales. The implications of the heterogeneities in terms of fatigue performance as well as the potential contributions of numerical simulation were also discussed.

5.2 Introduction

Shot peening is a surface treatment commonly used in the aerospace and automotive industries to improve the fatigue properties of metallic components. This process consists of projecting small and hard particles at high velocities onto a ductile surface. Each particle, called shot, plastically deforms the surface. Repeated hammering tends to permanently stretch a thin layer of material parallel to the surface. Constraint from the underlying material results in an in-plane compressive residual stress state near the surface. Surface plastic strains also lead to increased surface roughness and work-hardening of the material. Curtis *et al.* (2003) summarized the effects of shot peening on fatigue life as follows:

1. Surface compressive residual stress and strain-hardening that inhibit crack propagation;
2. Surface roughening that accelerates crack nucleation and early propagation.

Benedetti *et al.* (2009) also noted that shot peening can lead to detrimental material embrittlement for aluminium alloys. Such effects were included in micromechanical predictive models for low cycle fatigue (LCF) and crack propagation and high cycle fatigue (HCF) for aluminium alloys (de los Rios *et al.*, 2000; Curtis *et al.*, 2003; Benedetti *et al.*, 2009). In addition, Fathallah *et al.* (2003, 2004) further studied surface damage and modelled its effects on HCF properties. Interestingly, Guechichi and Castex (2006) reported the influence of strain-hardening on fatigue strength to be more important than that of compressive residual stress for steel. The overall improvement of fatigue properties from shot peening therefore results from a complex combination of multiple factors.

The beneficial and detrimental effects of shot peening are controlled by factors such as the mechanical properties of the target surface, the shot type, the impact velocity and the exposure time. Continuous monitoring of shot velocity and exposure time in an industrial context is quite challenging. For this reason, industrial applications typically rely on two other measurands based on the observable effect of the process to monitor peening treatments. The first is the Almen intensity. This value quantifies the kinetic energy available in a given shot stream and corresponds to the deflection of a standardized spring steel strip subjected to a specific set of peening parameters (SAE Standard J442, 2008). The second is coverage, which indicates the portion of the original surface that is covered with dimples after peening or, for values greater than 100%, the ratio between the peening exposure time and the time required for full (98%) coverage (SAE Standard J2277, 2009).

Many researchers have taken interest in the material state after shot peening for different metals, often in the context of fatigue life or fatigue limit studies. Four main topics can be identified in literature:

1. The stress field after shot peening is arguably the most commonly studied aspect of the process. Residual stress profiles are typically determined with two different methods: incremental hole drilling (Rodopoulos *et al.*, 2004; Sidhom *et al.*, 2005; Zupanc and Grum, 2011), which relies on strain relaxation around a hole drilled in a material subjected to residual stresses (Ruud, 1991; ASTM Standard E837, 2008), and X-ray diffraction (XRD) (Vöhringer, 1987; Benedetti *et al.*, 2009; Luong and Hill, 2010; Miao *et al.*, 2010; Zaroog *et al.*, 2011b), which quantifies the variation of the interplanar spacing of a given set of crystallographic planes in the presence of residual stresses (Prevey, 1991; Withers and Bhadeshia, 2001). Both techniques provide information on the average stress state at a scale much larger than the grain size, labelled as macro-stress or types I stress.

2. Local strain-hardening is often assessed using indentation testing. Due to the relatively thin layer affected by peening (often less than 0.5 mm), Vickers micro-indentation testing at loads around 100 gf is often chosen to determine hardness profiles (Vöhringer, 1987; Rodopoulos *et al.*, 2004; Sidhom *et al.*, 2005; Benedetti *et al.*, 2009; Zaroog *et al.*, 2011b). It should however be noted that indentation results are also affected by residual stresses (Vöhringer, 1987; Tsui *et al.*, 1996; Bolshakov *et al.*, 1996).

   When using the X-ray diffraction method for stress determination, work-hardening of the material widens the observed diffraction peak (Prevey, 1991; Withers and Bhadeshia, 2001). This phenomenon arises from the micro-stresses (or types II and III stresses) developing in the lattice at a scale similar or smaller than the grain size due to strain compatibility between grains and the presence of dislocations. X-ray diffraction peak broadening has therefore also been used as an evaluator of plastic strain (Vöhringer, 1987; Fathallah *et al.*, 2004; Zaroog *et al.*, 2011b).

   In addition, Child *et al.* (2011) suggested using the electron backscatter diffraction (EBSD) technique, which provides local information on lattice orientation, to quantify the depth of strain-hardening. The scatter of crystallographic orientations within each grain, called grain orientation spread, was considered as an evaluator of strain-hardening. The main advantage of the latter two methods is that they do not alter the material state in order to evaluate the degree of strain-hardening (Vöhringer, 1987).

3. The surface topography resulting from shot peening can be characterized at different length scales. First, roughness parameters such as arithmetic average height and maximum peak-to-valley roughness were often determined from 2D profiles at a scale much larger than a single dimple diameter (Li *et al.*, 1992; Clausen and Stangenberg, 1999; Benedetti *et al.*, 2009; Zupanc and Grum, 2011). Clausen and Stangenberg (1999) recommended that each sampling length should include at least 10 ball impacts. Some researchers also determined roughness parameters from a 3D surface (Miao *et al.*, 2010; Child *et al.*, 2011). However, the correlation between roughness parameters calculated with 2D profiles and 3D surfaces has not been investigated yet.

   Roughness parameters have been used to evaluate stress concentration factors for fatigue life prediction models. Based on finite element simulations, Li *et al.* (1992) suggested a relationship between the stress concentration factor K_t and the maximum peak-to-valley height R_t and the mean spacing between profile peaks S_m over an evaluation length as:

$$K_t = 1 + 2.1 \left(\frac{R_t}{S_m} \right) \tag{5.1}$$

   for $R_t/S_m \leq 0.30$. Similarly, Bhuvaraghan *et al.* (2011) related the stress concentration

factor to the arithmetic average height R_a and the indentation root radius r as:

$$K_t = 1 + n\sqrt{\left(\frac{R_a}{r}\right)} \tag{5.2}$$

where n is a constant that depends upon the type of loading. Using the finite element method, Fathallah *et al.* (2004) also quantified the surface stress concentration factor associated with 2D surface roughness on a notched sample.

In addition, surface damage at a scale smaller than an indent has been considered by some researchers (Fathallah *et al.*, 2004). Sidhom *et al.* (2005) observed overlaps, scaling as well as surface and subsurface microcracks in AA5083-H11 peened with a relatively high intensity of 0.41-0.51mmA and 125% coverage. It was noted that such damage can accelerate crack nucleation and this effect was taken into account in HCF modelling through a damage variable. Luong and Hill (2010) reported similar surface overlaps and sharp features for AA7050-T7451 peened with an intensity of 0.40mmA and 200% coverage.

4. The microstructural changes resulting from shot peening have been investigated with different methods. de los Rios *et al.* (2000) reported a 20% reduction of near-surface grain size perpendicular to the surface for a shot peened AA2024-T351 plate. Honda *et al.* (2005) also observed elongated and flattened grains near the peened surface of AA7075-T7351. Zupanc and Grum (2011) noted a variation in the orientation of large particles in AA7075-T651 after peening. A similar observation was made by Lindemann *et al.* (2006) for a lamellar titanium alloy. On the other hand, Benedetti *et al.* (2009) and Zaroog *et al.* (2011a) reported no significant effect of peening on the microstructure of aluminium alloys based on optical micrographs of etched specimens.

   EBSD can provide additional information on the material state as it identifies local crystallographic orientations. Misorientations on local and grain-wide bases as well as grain boundary characteristics are therefore available. In addition, Child *et al.* (2011) used focused ion beam induced secondary electron images to assess dislocation density gradients. An unrecognizable grain structure was noted near the surface of a nickel superalloy sample shot peened with an intensity near 0.25mmA and 200% coverage and was attributed to very fine grains with dimensions of the order of 10-20 nm.

   This grain refinement phenomenon has been a topic of interest through research on surface nanocrystallisation. For instance, Wu *et al.* (2002) performed ultrasonic shot peening for very long exposure times on AA7075 aluminium alloy and investigated the resulting microstructures using transmission electron microscopy (TEM). They ob-

served the development of progressively finer features (dislocation cells, microbands, cell blocks, submicro-sized grains and nanostructures) with increasing plastic strain. It was also concluded that the variable strain paths and high strain-rates found in shot peening promoted subgrain formation and lattice rotation, respectively.

At a larger scale, Ebenau *et al.* (1987) and Vöhringer (1987) also observed a modification of the near-surface crystallographic texture for normalized steel. Shot peening had the effect of aligning the slip planes parallel to the surface.

Due to its random impact sequences, shot peening does not generate a homogeneous material state at the scale of the impact dimple. Vöhringer (1987) used XRD with a beam area comparable to a single dimple area and observed significant spatial variations of the surface residual stress from one location to another for steel peened at 125% coverage. Constrastingly, X-ray peak widths did not vary much from one measurement point to another and it was concluded that shot peening led to a homogeneous strain-hardening state near the surface. Clausen and Stangenberg (1999) also noted a significant dispersion of measured roughness parameters after shot peening.

Few other studies have considered the heterogeneity arising from shot peening in terms of residual stresses, strain-hardening, surface topography and microstructure. Most studies have determined residual stresses averaged over a large area and hardness profiles have often been obtained by averaging 3 to 5 individual values per depth (Benedetti *et al.*, 2009; Zaroog *et al.*, 2011b) instead of considering the variations as intrinsic information about the process.

The principal objective of this work was to perform a detailed experimental characterization of aluminium alloy AA2024-T351 subjected to shot peening as well as to describe process heterogeneity by combining multiple techniques at various scales. In addition, experimental results were complemented with numerical simulations. The observations were also discussed with respect to their potential contributions to existing fatigue prediction models.

This article is divided into four sections. Section 5.3 presents the experimental methods used in this study. Section 5.4 presents and discusses the data acquired and suggests relationships between the different effects of shot peening. Section 5.5 concludes this work and suggests topics for future studies.

5.3 Experimental methods

The material under study is aluminium alloy AA2024-T351, an alloy developed for aerospace applications requiring damage tolerance. Its composition is presented in Table 5.1. The T351 treatment for aluminium alloy indicates that the material was solution heat treated, cold worked, naturally aged and finally stress-relieved by traction. Material was received as

12.9 mm thick plates. Optical micrographs of samples etched using Keller's reagent revealed a grain size gradient through the thickness. Average grains dimensions were approximately 250 μm along the Rolling Direction (RD), 70 μm along the Transverse Direction (TD) and 23 μm along the Normal Direction (ND) near the surface and increased to 640 μm (RD) $\times$ 115 μm (TD) $\times$ 38 μm (ND) deeper into the material. It should be noted that there was a large dispersion of grain sizes and shapes in the RD-TD plane, as shown in Figure 5.1. This alloy also features large constituent particles with dimensions of 5-10 μm dispersed throughout the microstructure. These particles contain aluminium as well as copper, manganese, iron and silicium. Such constituents are typically crack initiation and corrosion sites and accelerate crack propagation (Wang and Starink, 2005).

Two types of samples were prepared from the plate:

1. 22 mm $\times$ 12 mm samples were cut and the as-rolled surface was mechanically polished to a mirror finish with a 0.05 μm colloidal silica solution. These samples were used for indentation testing, microstructure characterization and surface damage study.
2. 22 mm $\times$ 20 mm samples were cut and the as-rolled surface was gently grinded with 1200 grit SiC paper. These samples were used for residual stress determination and surface roughness measurements.

Since XRD measurements are easier to conduct and more accurate for fine-grained materials (Prevey, 1991), care was taken not to excessively remove material during surface preparation before peening to take advantage of smaller grain sizes near the as-rolled surface.

One sample of each type was kept in the as-polished/as-grinded state to characterize the initial material and therefore clearly identify the changes induced by shot peening. The other samples were shot peened using a Baiker air blast peening machine feeding shots to a 6 mm-diameter nozzle fixed on a Motoman manipulator arm (for details on the setup, see Miao *et al.* (2010)). Impact angle was 90° and the stand-off distance between the nozzle and the

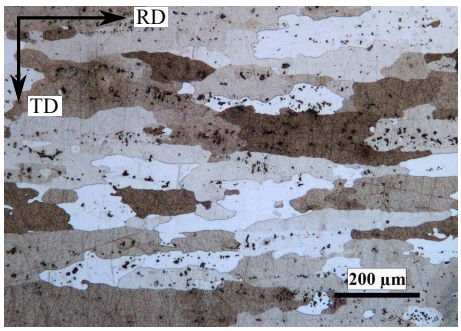

Figure 5.1 Optical micrograph of the surface microstructure in the RD-TD plane before shot peening. Sample was etched with Keller reagent and observed under polarized light.

Table 5.1 Nominal composition of alloy elements in AA2024 (Brown *et al.*, 1996)

Element		Cu	Mg	Mn	Fe	Si	Zn	Ti	Cr
% weight	min.	3.8	1.2	0.3	-	-	-	-	-
	max.	4.9	1.8	0.9	0.5	0.5	0.25	0.15	0.1

sample surface was kept close to 25 mm. The pressure was set to 96.5 kPa to propel Z425 ceramic shots with diameters ranging from 425 to 600 μm at a velocity near 53 m/s with a mass flow rate of 0.4 kg/min. The bead composition is mostly ZrO_2 and SiO_2 (Saint-Gobain, 2003). The robot travel velocity was 24 mm/s. The peening machine was filled with new, unused peening media and shots were not recycled. These peening parameters corresponded to an Almen intensity of 0.189 mmA (7.4A) with full (98%) coverage (Miao *et al.*, 2010), which are typical parameters used in industry for fatigue life improvement.

Samples were ultrasonically cleaned in denatured alcohol before characterization. Cross-sections for micro-indentation and microstructure characterization were prepared by low-speed cutting with a diamond saw, using water lubrication. To preserve the edges without altering the material work-hardening state, samples were cold-mounted in epoxy resin and then mechanically polished to a mirror finish with 0.05 μm colloidal silica solution. The samples were finally removed from the non-conductive mount before scanning electron microscopy observation.

5.3.1 Residual stress determination

Residual stress profiles in the center of as-grinded and shot peened samples were determined using a Proto iXRD system with a chromium (Cr) X-ray tube with a vanadium (V) filter. The diffraction peak corresponded to the aluminium {311} planes with $2\theta = 139.3°$ (Prevey, 1991). Interplanar spacings (d) were determined for 11 different tilt (ψ) values for 2 detectors and residual stresses were computed using the $\sin^2\psi$ method. Due to the large grain size in this alloy, a rectangular 5 mm $\times$ 1 mm slit was selected. In addition, a $\pm 3°$ amplitude angular oscillation was performed with the diffractometer and a 2 mm amplitude lateral movement was applied to the sample during measurement in order to probe a sufficient number of individual grains. The actual irradiated area was therefore 5 mm $\times$ 3 mm and measurements provided the non-uniformly averaged macroscopic stress over this area (Prevey, 1991). It should be noted that the setup calculated small compressive stresses on the order of -10 MPa for a nominally stress-free aluminium powder sample.

In-depth stress profiles were obtained by successive electropolishing using a methanol, water, butoxyethanol, and perchloric acid electrolyte. The electropolished area was a 15 mm

diameter circle. The measurement depth z_{RS} was defined as the distance between the center line of the surrounding shot peened surface and the bottom of the electropolished pocket, based on a 2D profile (Figure 5.2(a)). Corrections for stress gradient were made using the built-in software to account for the penetration of X-rays into the material. Corrections for material removal were performed following the model developed by Savaria *et al.* (2012). Measurements using a profilometer showed that electropolishing led to a curved surface as schematically illustrated in Figure 5.2(b). This increases the uncertainty on depth values and introduces some error since X-ray beam also probes material located closer to the surface.

It should be noted that XRD measurements were performed once at each depth and on only one as-grinded sample and on one as-peened sample. Repeat measurements are required to confirm the observed trends.

5.3.2 Micro-indentation

Indentations were made with a FutureTech FM micro-hardness tester that was verified for a 300 gf load and 300 HV/HK test blocks (ASTM Standard E384, 2011). All indent diagonals and positions were then measured with a Hitachi S-3600N scanning electron microscope (SEM) operated at 15 kV with working distances of 10-15 mm and magnifications between 1500 and 2500.

Micro-indentation testing was first performed to evaluate the hardness and its dispersion in the RD-TD plane. Measurements were performed on initial (as-polished) and peened samples with a Vickers indenter, loads of 300 gf and 100 gf, and a 10 s dwell time. After peening, the rough surface was gently grinded and polished with 1200 grit paper to 0.05 μm colloidal silica solution to obtain a flat surface without altering the material state. The sample was polished until only few impact dimples remained so as to characterize the highly-deformed surface layer. This corresponded to a depth of approximately 20 μm below the original surface. It should be noted that this removal of material subjected to residual

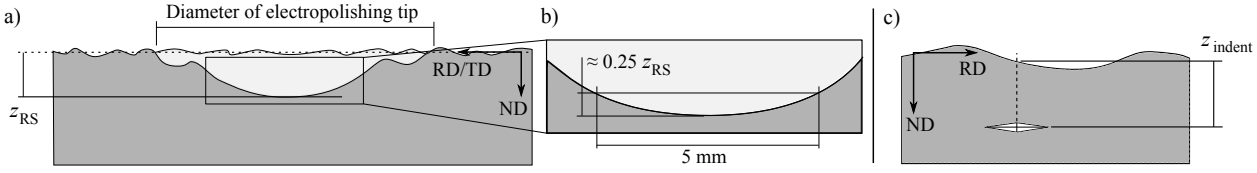

Figure 5.2 (a) Global depth z_{RS} for residual stress profile determination (cut view, not to scale). (b) Schematic illustration of the curvature of the electropolished pocket over the 5 mm width of the irradiated area. (c) Local depth z_{indent} for indentation testing on the RD-ND cross-section.

stresses also altered slightly (less than 10 MPa) the residual stress field in the sample due internal stress redistribution. Five rows of 10 indentations along the transverse direction were made for a total of 50 indentations per sample and per load. Spacing between indentations was 500 μm (RD) $\times$ 250 μm (TD) for the 300 gf load and 300 μm (RD) $\times$ 150 μm (TD) for the 100 gf load.

Using the same apparatus, testing was also conducted with a Knoop pyramid and a 25 gf load to characterize the through-thickness hardness profile along the normal direction in the peened material. Due to its elongated shape, the Knoop indenter is more suitable for evaluating strong hardness gradients such as that obtained after peening (ASTM Standard E384, 2011). Two different RD-ND cross-sections were prepared. Spacing between indentation rows was 200 μm along the rolling direction. In order to determine the hardness profile through thickness, the local distance from the as-peened surface z_{indent} was determined for each indentation as illustrated in Figure 5.2(b).

5.3.3 Surface topography

Surface roughness after shot peening was evaluated over 12.5 mm evaluation lengths encompassing five 2.5 mm sampling lengths (Figure 5.3) with a Mitutoyo SJ-400 contact stylus instrument (Clausen and Stangenberg, 1999). The pitch was set to 2 μm. The non-periodic measured profiles were filtered with a high-pass filter of 5 mm and a low-pass filter of 0.01 mm to remove long-range waviness and excessive short-range oscillations, respectively.

Twelve profiles were acquired along the rolling and transverse directions for a total of 24 evaluations lengths and 120 sampling lengths. Three roughness parameters were evaluated in each sampling length: the arithmetic average height R_{ai}, the maximum peak-to-valley height R_{ti} and the mean spacing between profile peaks S_{mi}. The latter parameter required the definition of a dead zone that determines the minimum height of peaks and valleys that are taken into account when calculating the mean spacing S_{mi} (SURFPAK-SJ help, 2004). The selection of this dead zone had a significant effect on the S_{mi} values. It was chosen to determine S_{mi} for a 0% dead zone since this led to peak-to-peak values consistent with the dimple diameters. For comparison purposes, surface average roughness S_a was also evaluated over a 3 mm $\times$ 3 mm area with a 5 μm pitch using a Micro-Photonics CHR150 non-contact confocal microscope.

One shot peened sample was observed in a Hitachi S-3600N SEM to characterize damage caused by shot peening at a length scale much smaller than the surface roughness. The sample surface was mapped before peening to verify the absence of prior damage as well as to account for the presence of large constituent particles and their potential influence on surface damage.

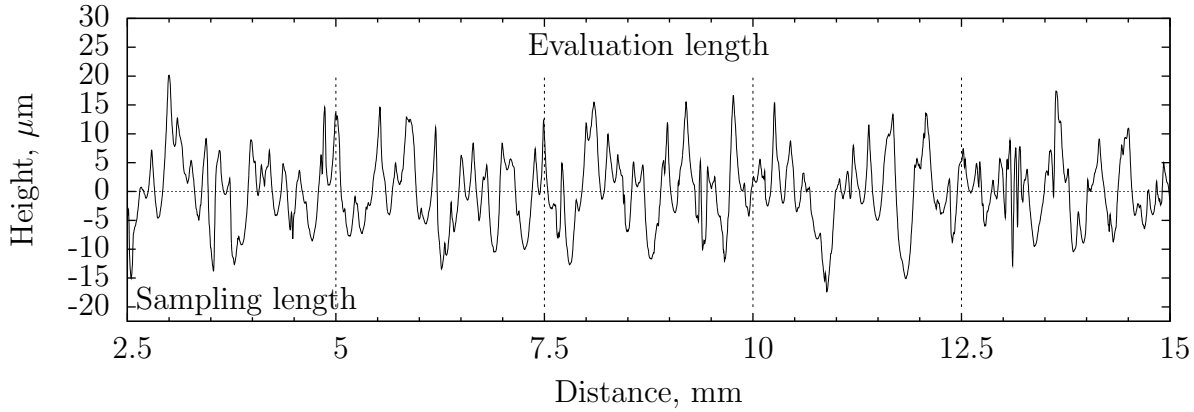

Figure 5.3 Definition of evaluation length and sampling length on a measured and post-processed roughness profile along the transverse direction.

5.3.4 Microstructure characterization

Electron backscatter diffraction (EBSD) maps were acquired before and after shot peening on RD-TD surfaces and RD-ND cross-sections. Characterization was performed on a Hitachi SU-70 FEG-SEM operated at 20 kV and equipped with a Oxford HKL EBSD module. Due to the stochastic nature of shot peening, it was necessary to map sufficiently large regions encompassing multiple grains. The large grain size combined with the small step size required to capture the microstructure evolution led to long acquisition times. As a compromise between map size and acquisition time, step sizes of 1.0 and 0.2 to 0.5 μm were used before and after peening, respectively. Minimal noise reduction was performed on all maps to remove wild spikes and attribute orientations to some unindexed points based on the orientation of their neighbours.

Due to significant roughness and large plastic strains near the surface, EBSD indexation was very low on the as-peened surface. The RD-TD observations after shot peening were therefore conducted at the same depth as the Vickers micro-indentation testing (Section 5.3.2).

5.4 Results and discussion

5.4.1 Residual stress determination

Residual stress profiles were determined along the rolling and transverse directions for as-grinded and shot peened samples. For the specimen in the as-grinded condition, the

surface stress state was affected by the preparation operation. Deeper inside the plate, small compressive residual stresses were still found along both the rolling and transverse direction. This is consistent with the material being stress-relieved. For the shot peened specimen, surface and maximum compressive stresses were similar along both the rolling and transverse directions. Additional measurements were performed at the surface in directions aligned at $\pm 45^{\circ}$ to the rolling direction and showed no significant effect of the measurement direction. The depth subjected to compressive residual stress $z_{\mathrm{RS}}^{\mathrm{affected}}$ was roughly estimated for each direction as the depth where the residual stress profile after peening crossed the stress profile before peening. It can be noted that compressive stresses extend to a slightly greater depth along the TD when compared to the RD. Based on the mechanical testing results by Miao *et al.* (2010) and the trends identified by Vöhringer (1987), this could be related to the smaller yield and tensile strengths of the alloy along the TD direction. To explain the reduced residual stress amplitude at the surface when compared to the maximum compressive stress, Fathallah *et al.* (2003) suggested that local damage (see Section 5.4.3) can contribute to the reduction of the average residual stress values at the surface. The residual stress profiles in the shot peened sample can be fitted with the following equation (de los Rios *et al.*, 2000):

$$\sigma_{\mathrm{residual}}(z_{\mathrm{RS}}) = A \times \exp\left(-2 \times \frac{(z_{\mathrm{RS}} - B)^2}{C^2}\right) + D \tag{5.3}$$

with the fitting parameters specified in Table 5.2.

Table 5.2 Fitting parameters for the residual stress profiles in the shot peened sample.

Parameter	A MPa	B μm	C μm	D MPa
Rolling	-376.5	96.0	265.6	21.1
Long transverse	-362.4	99.1	312.9	14.2

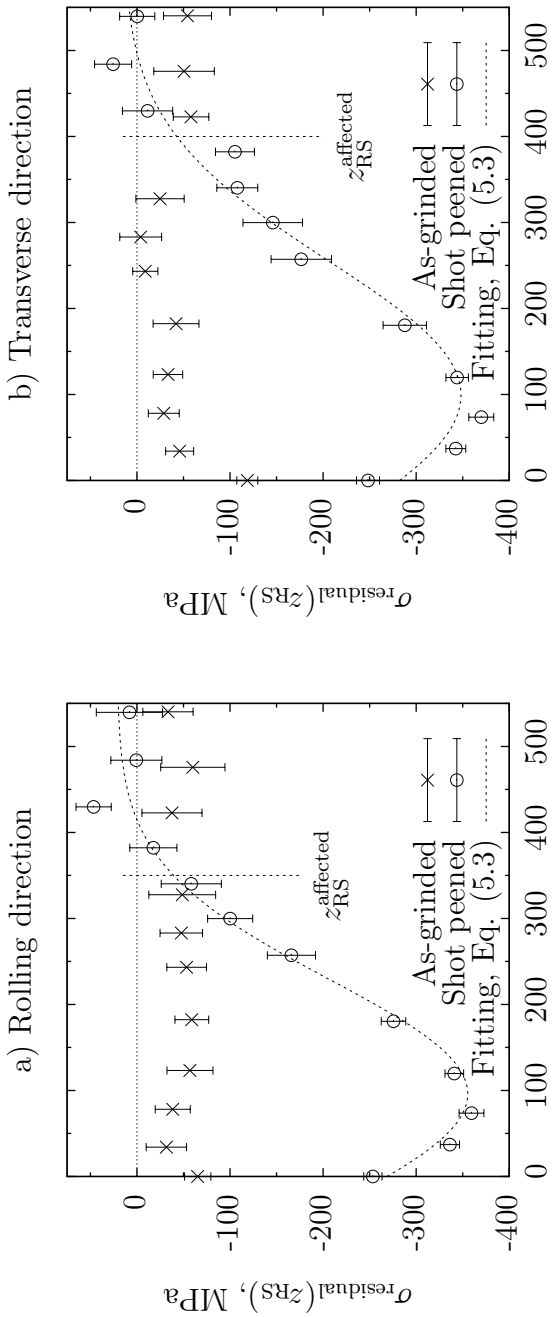

Figure 5.4 Experimentally determined residual stress profiles for as-grinded and shot peened AA2024-T351 specimens.

Quantification of the residual stress heterogeneity using numerical simulation

Vöhringer (1987) reported that, in addition to the residual stress gradient through the thickness, shot peening generates a non-uniform residual stress field in the plane parallel to the surface. To characterize this heterogeneous effect, he determined the residual stress state in shot peened steel at different locations on the surface with a X-ray beam diameter ($\varnothing$0.23 mm) similar to the diameter of a single impact dimple. To achieve such results, measuring time was increased to 5 h per value; for comparison purpose, each data point in the current study had an acquisition time around 15 min.

In the present work, the large grain size in the samples made performing local measurements impossible. Finite element simulations were therefore used as a means to complement the experimental data. Shot peening was simulated using `ABAQUS Explicit` with a dynamic impact model where shot impact locations and diameters were randomly defined to represent the stochastic nature of shot peening. In order to reduce the calculation time, impacts were simulated only over a 0.6 mm $\times$ 0.6 mm area and the residual stress state was extracted in a 0.56 mm $\times$ 0.56 mm $\times$ 0.8 mm volume. The mesh size in the impacted volume was set to 20 μm. Gariépy *et al.* (2011) determined that this volume is representative of the actual process in terms of residual stresses since increasing the model dimensions did not significantly change the calculated stress profiles (when all other parameters were kept constant). The aluminium alloy was modelled as an isotropic material with combined isotropic-kinematic hardening behaviour (Gariépy *et al.*, 2011). In the current study, each analysis took 22 h on an IBM P690 Regatta computer using 8-processor parallelization and four analyses were performed with the same process parameters but different impact sequences.

The stress components in each element for the two in-plane directions were extracted from each analysis for interpretation. Since an isotropic average stress field is expected after shot peening of an isotropic material with an impact angle of 90° (Kim *et al.*, 2010), all data were merged into a single population for further analysis.

Average residual stress values were first determined for each element layer for comparison with the experimental data. The calculated average stress profile is compared to the experimentally determined values in Figure 5.5. It can be noted that the model provides a fairly good estimation of the residual stress profile in the material, although each of the four impact simulations involved an area much smaller (0.36 mm^2) than that of the experimental measurements (15 mm^2). Predicted values did not correlate well with experimental results at depths of 250 to 400 μm, which could be in part due to the curved electropolished surface (Figure 5.2(a)). Material closer to the surface and subjected to a larger compressive residual stress amplitude was included in the irradiated area and could have shifted the calculated stress slightly towards more compressive values.

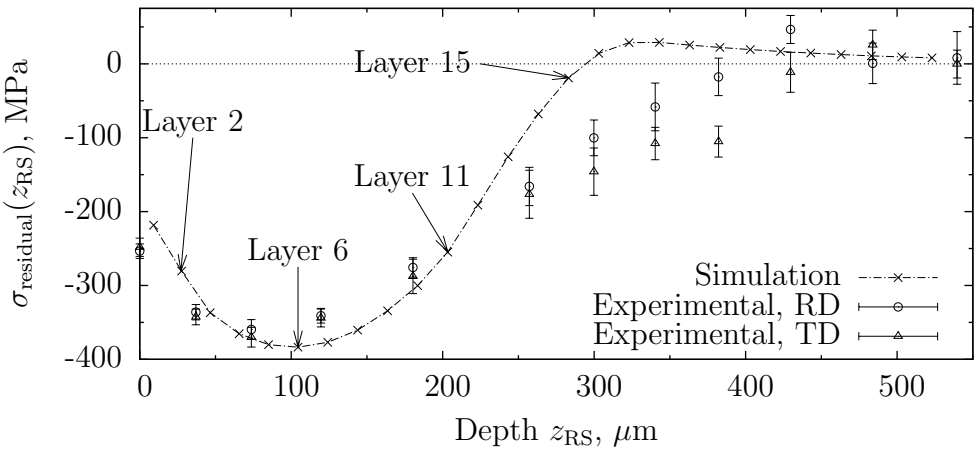

Figure 5.5 Comparison of numerically predicted residual stress profile with experimentally determined data.

In addition, the analyses provided the 3D spatial dispersion of residual stress for the 784 elements (28×28) in each layer. The residual stress heterogeneities were evaluated at different element layers (specified in Figure 5.5) from the results of the four simulations, as proposed by Meguid *et al.* (2007) and Larose *et al.* (2007). Figure 5.6 shows that there is a significant variation of calculated residual stresses from one element to another, especially near the surface. These variations occurred at a length scale of ≈ 100 μm. Simulation results suggest that tensile residual stresses could be present in some regions near the surface. Even though Kobayashi *et al.* (1998) observed such tensile residual stresses on a surface impacted by a large ball, the predicted extreme values could possibly be a numerical artefact not representative of the actual process. For comparison purposes, Vöhringer (1987) reported experimentally determined "local" surface residual stresses between -180 and -500 MPa over 11 measurement points while a value of -369 MPa was calculated for a much larger irradiated area. Further work is required to clarify whether experimental measurements did not reveal the most extreme values or numerical simulations overestimated the residual stress dispersion.

Considering the discrepancies between the experimentally determined average residual stress profiles along the RD and TD (Figure 5.4), it should be noted that an anisotropic material constitutive theory could improve the accuracy of the predicted residual stress fields.

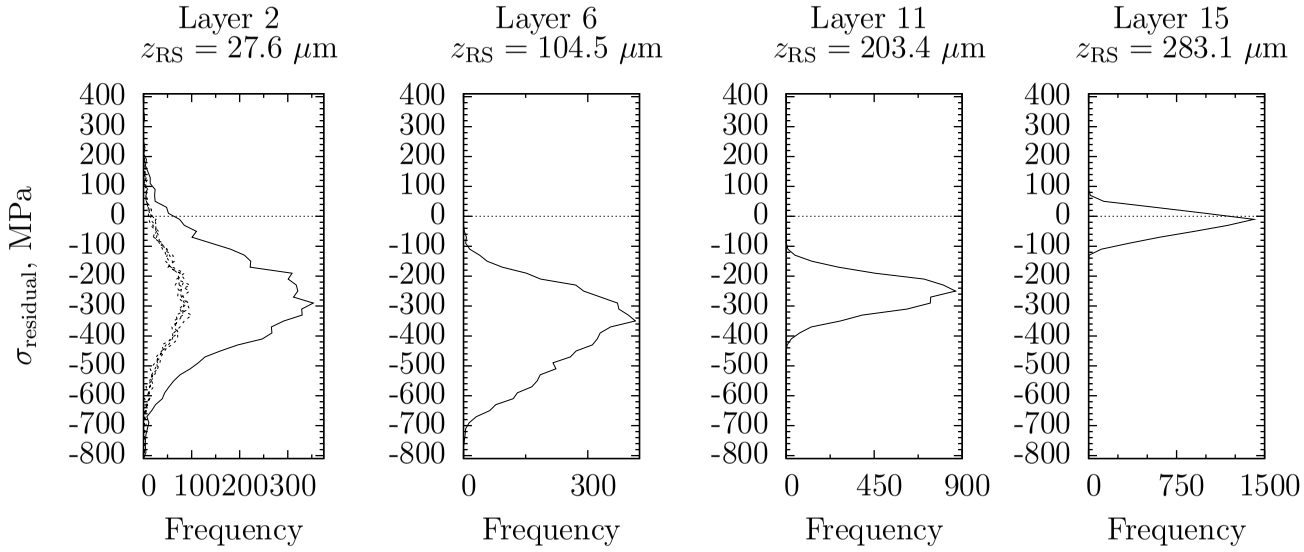

Figure 5.6 Dispersion of calculated residual stress values at different depths. Solid lines are the combined distributions from the four analyses and dashed lines are those from each of the four individual analyses. The total number of observations at each depth is 6272. This corresponds to twice the number of elements in each layer since stresses in both in-plane directions were considered.

5.4.2 Micro-indentation

Micro-indentation testing was also conducted to assess the uniformity (or lack thereof) of the as-polished and shot peened samples. The measured hardness values in the RD-TD plane displayed a significant scatter, both before and after shot peening (Figure 5.7). The dispersion observed before peening could be attributed to the presence of large constituent particles in the alloy as well as the relationship between the indentation and grain sizes. Average Vickers indentation diagonals were approximately 63 μm and 37 μm for 300 gf and 100 gf loads, respectively. These values are indeed smaller than the average grain size along the rolling direction and of the same order of magnitude as the grain size along the transverse direction near the surface (Figure 5.1). After shot peening, standard deviations of the measured hardness values increased by 93% and 65% for 300 gf and 100 gf loads, respectively, revealing the heterogeneous nature of the treatment effects.

Experimental observations using XRD suggest that this heterogeneity may be mostly related to local residual stress variations rather than to inhomogeneous dislocation density and strength (Vöhringer, 1987). However, XRD does not provide information on the kinematic hardening state, expressed as backstress tensors in material constitutive equations (Klemenz *et al.*, 2009). This factor could affect the indentation behaviour since this method generates plastic strains in the material. An heterogeneous kinematic hardening state could therefore contribute to the higher dispersion of measured hardness values after shot peening.

The measured Knoop hardness profile is illustrated in Figure 5.8. The maximum hardness is observed below the surface. Benedetti *et al.* (2009) observed this behaviour for a similar set of peening parameters and attributed the phenomenon to subsurface maximum shear stress due to Hertzian pressure during impact (Wolfhart, 1984). Considering the large plastic strains occurring in a relatively short time period during peening, a temperature rise near the surface may have contributed to lower the surface hardness values (Vöhringer, 1987). It should also be noted that although the recommendations of ASTM Standard E384 (2011) regarding minimum distances from free edges were respected, the decreased hardness near the surface may be related in part to edge effects due to the small distance between the indentations and the sample-mounting resin interface.

The data in Figure 5.8 can be fitted using an equation similar to Eq. (5.3):

$$\mathrm{HK}(z_{\mathrm{indent}}) = A \times \exp\left(-2 \times \frac{(z_{\mathrm{indent}} - B)^2}{C^2}\right) + D \tag{5.4}$$

with $A = 29.8$, $B = 71.2$, $C = 93.8$ and $D = 135.1$ for depths greater than 25 μm. Defining the affected depth as the depth for which the fitted hardness curve reaches 110% of the baseline value led to $z_{\mathrm{indent}}^{\mathrm{affected}} = 172$ μm. For comparison purposes, the affected depth in

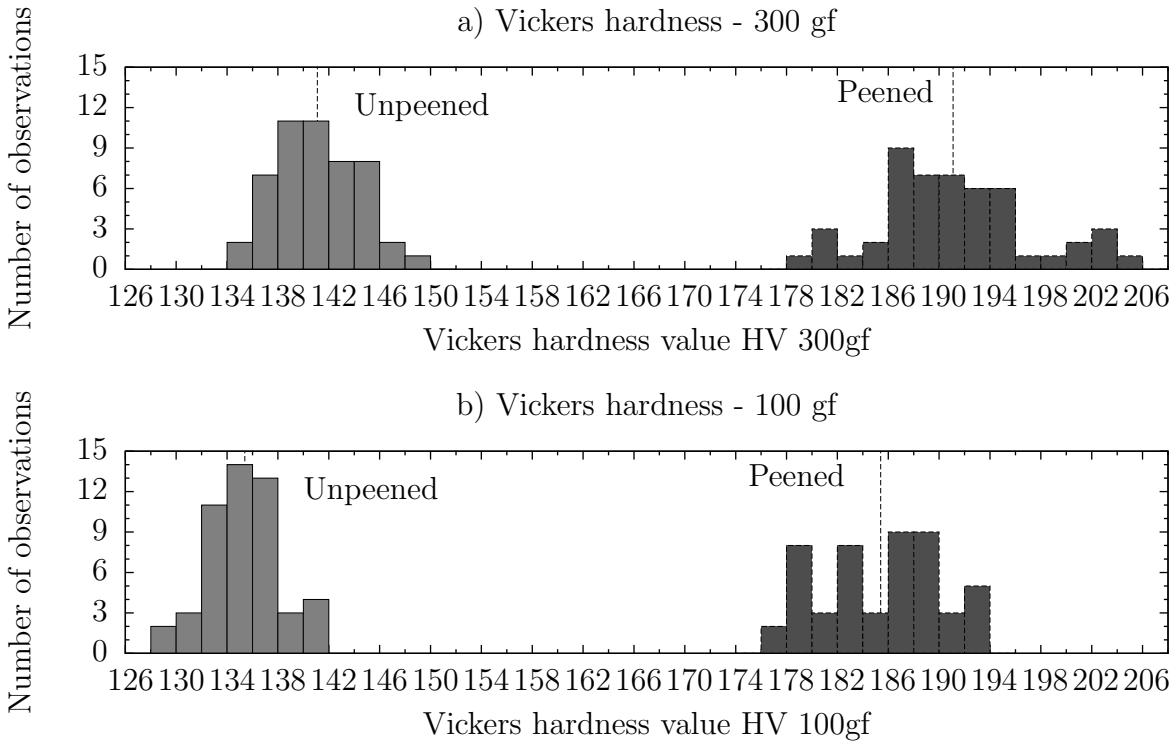

Figure 5.7 Distribution of measured Vickers hardness values before and after peening in the RD-TD plane. Vertical lines indicate average values.

terms of residual stresses was approximately 375 μm (Figure 5.4). This is consistent with the experimental observation by Child *et al.* (2011) that shot peening increased the grain orientation spread, an indicator of lattice rotation, up to a depth approximately half that affected by compressive residual stresses. It should be noted that the 110% threshold was selected arbitrarily: increasing this limit would yield a smaller affected depth.

The full width at half maximum (FWHM) of the measured X-ray diffraction peaks can also be used to assess work-hardening. A larger width indicates a greater dislocation density that can be correlated with a more work-hardened state and higher strength. Figure 5.9 shows the FWHM profiles for as-grinded and shot peened specimens. The depth for which the FWHM values are affected by the peening process $z_{\text{FWHM}}^{\text{affected}}$ is approximately 200 μm, which slightly larger than the depth $z_{\text{indent}}^{\text{affected}} = 172$ μm determined from micro-indentation testing. This is consistent with results presented by Vöhringer (1987). A significant difference between both techniques is that the Knoop peak hardness was observed below the surface whereas the maximum FWHM occurred at the surface. This phenomenon could be in part attributed to the dispersion of residual stresses in the material. Since the stress state in the

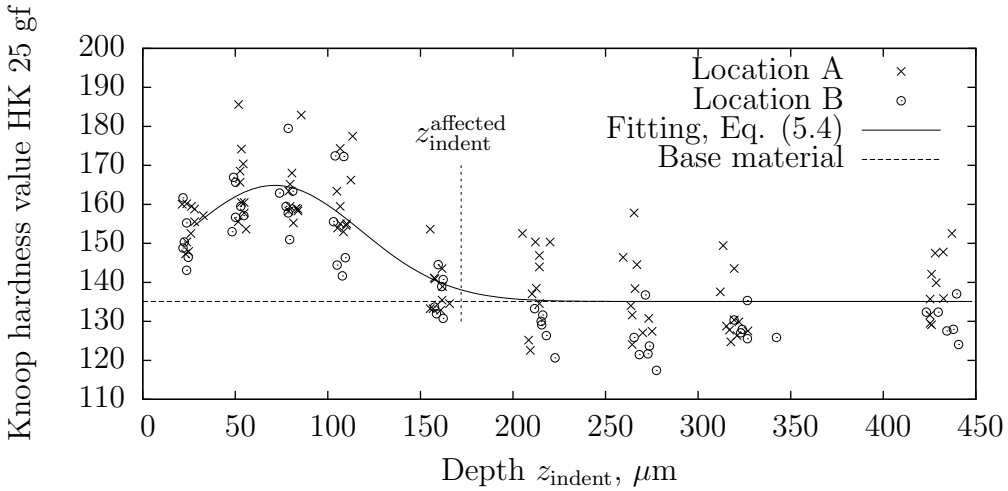

Figure 5.8 Through thickness Knoop hardness profile in shot peened samples.

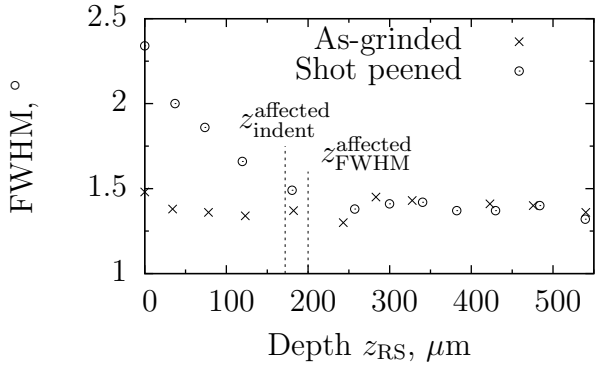

Figure 5.9 Average FWHM determined for X-ray diffraction peaks.

irradiated area is not uniform, the observed XRD peak is the summation of the contributions of small diffracting volumes subjected to different local residual stresses. Each individual volume therefore shifts its associated diffraction peak by a different value. This means that, in addition to the dislocation density and micro-stresses, a greater long-range stress heterogeneity contributes to a wider peak. Simulation results in Figure 5.6 suggest that the stress field is more scattered near the surface, which would contribute to the largest FWHM being observed at the surface.

It can be noted that shot peening increased the average measured hardness value by 36% in the RD-TD plane and by a maximum of 22% in the RD-ND cross-section (Figures 5.7 and 5.8, respectively). The latter value is consistent with the 20 to 25% hardness increase observed by Zupanc and Grum (2011) for AA7075-T651 peened with a similar intensity and

coverage. The large apparent differences between the RD-TD and RD-ND values may be attributed to the effect of the compressive residual stress state near the surface (Vöhringer, 1987; Tsui *et al.*, 1996; Zaroog *et al.*, 2011b): the Vickers indentations were made in a plane subjected to an approximately isotropic average residual stress field whereas large compressive stresses were only present along the long diagonal for the Knoop indentations. It therefore seems likely that the Vickers indentations were more significantly affected by the residual stress state. This also shows the complexity of dissociating the effects of residual stresses and intrinsic work-hardening when interpreting micro-indentations experiments (Child *et al.*, 2011).

The individual Vickers indentation topographies in the RD-TD plane also provide useful information regarding the material state after shot peening. Figure 5.10(a) shows that indentations on the unpeened material led to relatively uniform, square imprints even if some distortions were observed, possibly due to the presence of grain boundaries or large constituent particles. Indentations made after peening and polishing exhibit irregular imprints as well as pile-up and ripple-like features along their edges. Surface profilometry also confirmed higher pile-up around the indent edges after peening. Tsui *et al.* (1996) and Lee *et al.* (2004) reported that compressive residual stresses increase pile-up height, which can explain at least in part the observed behaviour. On the other hand, Bolshakov *et al.* (1996) and Cheng and Cheng (1998) concluded that a decreased work-hardening slope also leads to increased pile-up. The potential contributions from each phenomenon are however difficult to isolate.

Characterization of local material properties using numerical simulation

Numerical analyses follow the material state throughout multiple impacts and can indicate local yield strengths, plastic strains as well as the material kinematic hardening state. As for residual stresses, finite element modelling can therefore provide additional information on local mechanical properties. For instance, the accumulated equivalent plastic strain is often considered to assess work-hardening in numerical simulations (Bagherifard *et al.*, 2010; Zimmermann *et al.*, 2010). Figure 5.11 compares the predicted accumulated equivalent plastic strain profile with the micro-indentation testing results. Simulations correctly predicted the depth affected by peening but indicated a maximum accumulated plastic strain at the surface whereas indentation testing led to a sub-surface hardness peak. One possible hypothesis to explain this discrepancy would be the influence of the residual stress field on the measured hardness values. The largest compressive stresses occur at depths from 50 to 100 μm (Figure 5.4). The residual stress gradient would therefore generate a greater increase of hardness at these depths when compared to a depth of $\approx$ 25 μm. Further study is required on this topic.

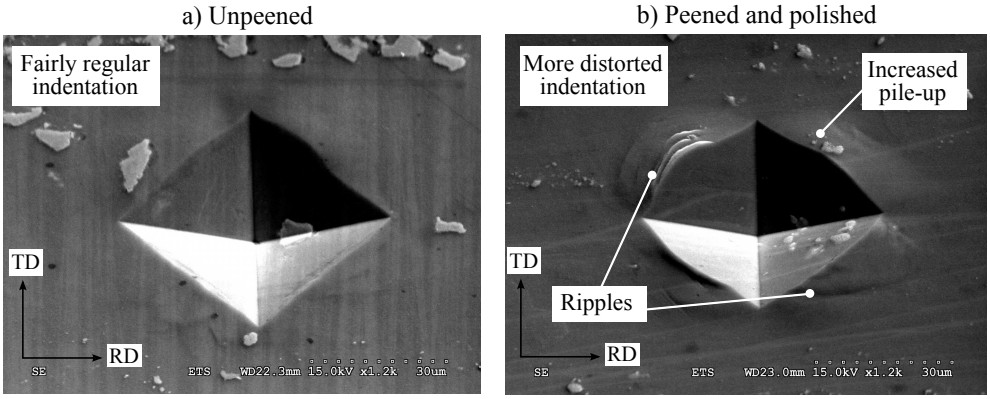

Figure 5.10 Typical indentations in (a) unpeened and (b) peened AA2024-T351. Samples were tilted around the horizontal axis at an angle of 40° to enhance contrast.

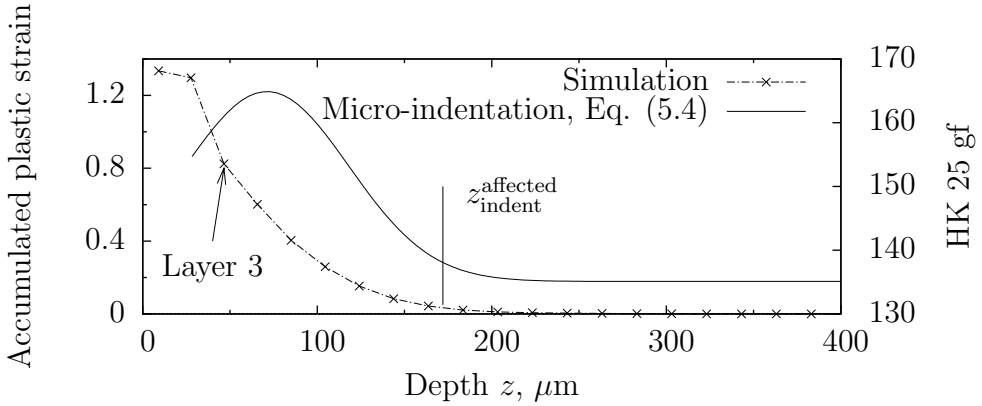

Figure 5.11 Comparison of the average accumulated plastic strains (PEEQ) profile with fitted micro-indentation testing results.

As for residual stresses, the dispersion of accumulated plastic strain was also studied and is presented in Figure 5.12. It can be seen that the distributions arising from the four different impact sequences were quite different whereas calculated residual stress distributions were quite uniform from one analysis to another (Figure 5.6). This phenomenon as well as the significant scatter can be explained by the stochastic nature of shot peening: since the impact sequence and shot diameters are random, some points are subjected to a greater number of impacts or impacts at higher energies and therefore accumulate larger plastic strains within the exposure time required to achieve full coverage (Zimmermann *et al.*, 2010). The mechanisms leading to the residual stress distribution being more uniform than that of the accumulated plastic strain shoud be studied further. One possible hypothesis could be that the length scale at which residual stresses equilibrate may be larger than that at which plastic deformation occurs.

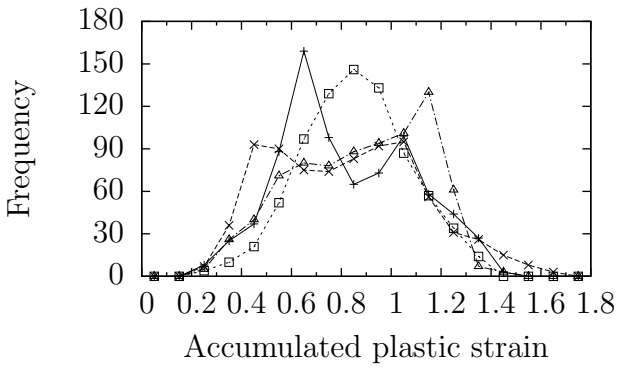

Figure 5.12 Distributions of accumulated equivalent plastic strain at a depth of 46.5 μm (third element layer). Each curve represents the distribution from one of the four different impact analyses.

The equivalent plastic strain does not however provide information on the kinematic hardening phenomenon. While the backstress tensor for each element was not readily available in `ABAQUS Explicit`, data processing could allow extracting this information. For materials exhibiting Bauschinger effect, kinematic hardening and the associated backstress tensor, which physically arise from short-range reversible interactions in the lattice, could play an important role in the material behaviour in service (Lillamand *et al.*, 2001). For instance, Holzapfel *et al.* (1998) reported that, due to in-plane plastic strains near the surface after shot peening, the Bauschinger effect affected the residual stress relaxation behaviour under compressive loading in quenched and tempered AISI 4140 steel.

5.4.3 Surface topography

Long-range roughness

Comparison of the roughness parameters calculated along the rolling and transverse directions showed no statistically significant differences. Clausen and Stangenberg (1999) also observed no dependence on measurement direction for shot peened samples. The measurement direction was therefore not taken into account in further interpretation.

Stress concentration factors K_t were evaluated for each of the 120 sampling lengths using Equations (5.1) and (5.2). Their distributions are illustrated in Figure 5.13. In Eq. (5.2), the root radius r was taken to be half the minimum shot diameter or 212.5 μm and tensile loading was assumed, leading to the constant $n = 2$. However, it should be noted that actual dimple radii of curvature may be larger than this value due to elastic recovery or smaller due to the presence of local damage. Average stress concentration factors based on

roughness parameters were 1.28 and 1.31 for Equations (5.1) and (5.2), respectively, which is slightly higher than the value of 1.26 determined by Miao *et al.* (2010) using 3D surface profilometry and Eq. (5.1). In addition, the scatter of local concentration factors is much larger for Eq. (5.1) due to the strong influence of the mean spacing between profile peaks S_{mi}. In this case, local K_t over 2.5 mm sampling lengths could be as high as 1.4.

2D roughness measurement is based on the assumption of a grooved surface which may not be appropriate for the 3D random topography generated by shot peening (Clausen and Stangenberg, 1999). A surface average roughness of 4.58 μm was determined using 3D confocal microscopy. It was not possible to estimate maximum peak-to-valley parameters accurately due to the presence of unmapped points in the map arising from poor reflectivity on the rough and locally damaged surface. Considering that 2D profiles yielded an average roughness of 5.09 μm, roughness parameters determined over 2.5 mm sampling lengths may overestimate slightly the surface topography amplitude, which would lead to conservative predictions in Equations (5.1) and (5.2). It should however be noted that Miao *et al.* (2010) calculated a surface average roughness of approximately 5.2 μm over a 5 mm $\times$ 5 mm area with a 12.5 μm pitch for similar shot peening parameters. Further study is required to investigate potential effects of measurement lenght or area and pitch on the calculated roughness parameters.

Surface damage

Embedded shot fragments were observed on the peened surfaces (Figure 5.14), as confirmed by energy-dispersive spectroscopy (Zupanc and Grum, 2011). The largest fragments had average diameters around 40 μm, while the beads had a minimum diameter of 425 μm. SEM imaging also revealed sharp features dispersed on the surface after peening (Figure 5.15). They had faceted geometries with lengths as large as 200 μm and may originate from different phenomena:

1. Sharp, broken shot fragments could have incised the surface. Even though new media was added, the peening machine may have contained used shots from previous experiments or very small, unfiltered particles. In addition, since the nozzle was kept perpendicular to the target surface, impacts between incoming and rebounding shots are likely and could have projected fragments onto the aluminium surface. Finally, shots may have broken when hitting the sharp edges of steel retaining bolts and then impacted the aluminium surface;
2. Large cyclic plastic strains could lead to material damage and embrittlement (Sidhom *et al.*, 2005; Benedetti *et al.*, 2009). Further impacts could then break off weakened regions of the material. For instance, the feature indicated by an arrow in Figure 5.15 could be a precursor to larger surface damage.

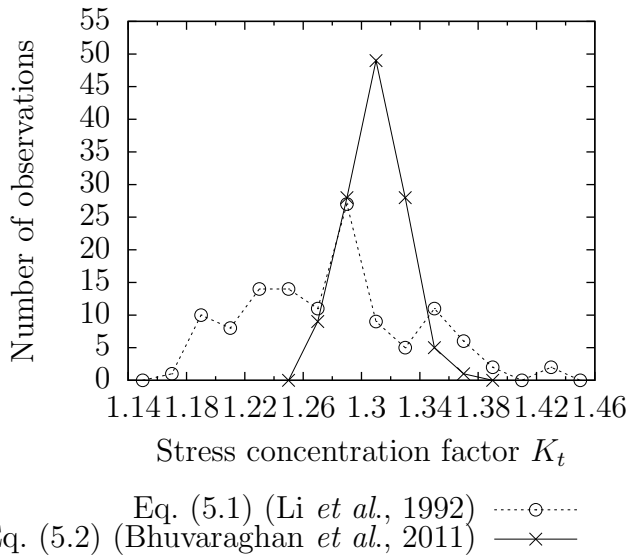

Figure 5.13 Calculated stress concentration factors based on Eq. (5.1) and Eq. (5.2).

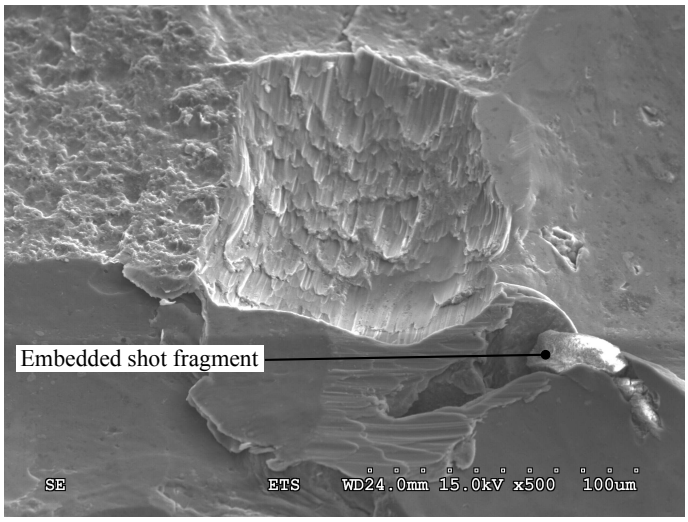

Figure 5.14 Example of embedded shot fragment.

Figure 5.15 also shows material overlap and scaling of the surface (Luong and Hill, 2010; Sidhom *et al.*, 2005). In addition, rounded pits with maximum diameters of approximately 50 μm were spotted on the peened surface (Figure 5.16). These may originate from impacts of broken but rounded shot fragments or from material chipping. No clear conclusions could be drawn between large constituent particles present in the alloy before peening and damage after peening: however, the influence of these particles should be investigated further. In addition, micro-crack were sometimes observed at the corners of sharp features and embedded

fragments. In the context of fatigue loading, all these defects would be potential crack nucleation sites (Fathallah *et al.*, 2004; Luong and Hill, 2010; Zupanc and Grum, 2011).

Numerical assessment of local stress concentration factors

Although more time-consuming than empirical relationships such as Equations (5.1) and (5.2), finite element modelling can be used to quantify local stress concentration factors more accurately as they allow second-order surface variations to be taken into account (Fathallah *et al.*, 2004). Three different 2.5 mm sampling lengths were arbitrarily chosen and their profiles were used as input data in `ABAQUS Standard`. For simplification, 2D profiles were considered and a plane strain condition was assumed; it should be noted that the actual surface topography is three-dimensional. Second-order reduced integration elements with a mesh dimension of 2 μm near the surface were used. The material was modelled as elastic with Young's modulus $E = 73.1$ GPa and Poisson's ratio $\nu = 0.33$ (Matweb, 2011). The effects of shot peening in terms of residual stresses and work-hardening were not taken into account in this simple analysis.

Figure 5.17 presents an example of the calculated results in terms of the von Mises stress σ_{VM} and hydrostatic pressure P, defined as $P = -(1/3)\ \mathrm{trace}(\sigma)$ (ABAQUS Analysis User's Manual, 2008). These two parameters are used in HCF predictive models such as the Crossland criterion (Fathallah *et al.*, 2003). Taking as a reference the von Mises stress calculated far from the surface $\sigma_{\mathrm{VM}}^{\mathrm{far\ field}} = 89.5$ MPa, the three different non-periodic profiles led to stress concentration factors close to 1.7-1.9 for σ_{VM}, which is higher than the values predicted by

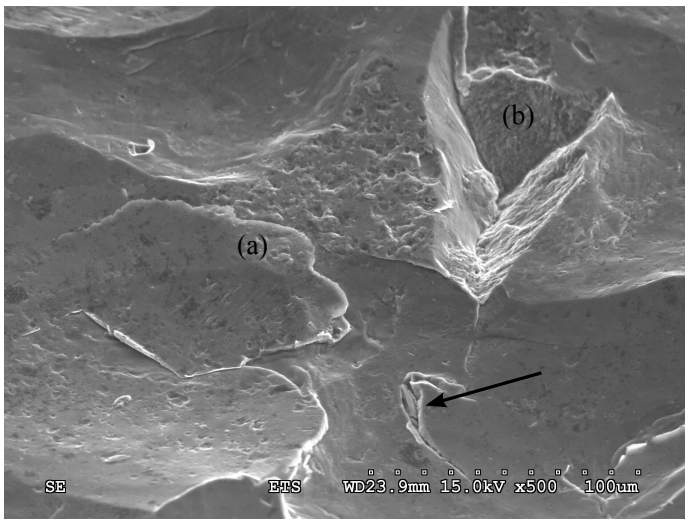

Figure 5.15 Examples of (a) folding and (b) sharp features on peened surface. The arrow indicates a possible precursor to larger damage such as (b).

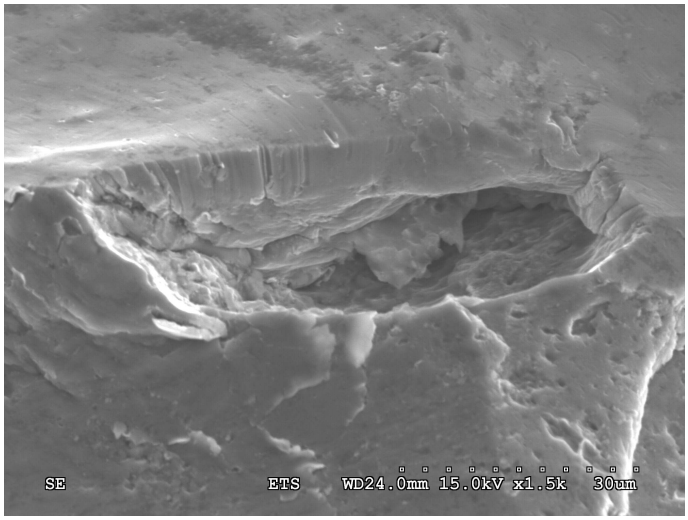

Figure 5.16 Example of rounded pit on peened surface.

Equations (5.1) and (5.2). As a result, the hydrostatic pressure $|P|$ also increased near the surface when compared to the value determined far from the surface, $|P^{\text{far field}}| = 42.5$ MPa. It should however be noted that such simulations can overestimate the stress concentrations near the sharp corners. Numerical results suggest that the most significant stress concentrations occur in deep valleys and in regions with small radii of curvature (*e.g.* damage). In addition, simulations indicate that their influence extends only approximately 20 μm through the thickness. This calculated stress concentration would therefore only be useful in the crack initiation stage. In the LCF regime with higher loads, plasticity becomes a significant factor and this type of analysis would have to consider the complete (and heterogeneous) work-hardening and residual stress states.

It should be noted that surface stress concentrations may have a limited effect since crack initiation can occur well below the surface in shot peened aluminium alloys subjected to low loading amplitudes (Benedetti *et al.*, 2009; Zupanc and Grum, 2011). Such initiation sites usually correspond to depths exposed to the tensile residual stresses present to balance the surface compressive residual stresses. Subsurface initiation is also sometimes associated with subsurface damage in the work-hardened layer.

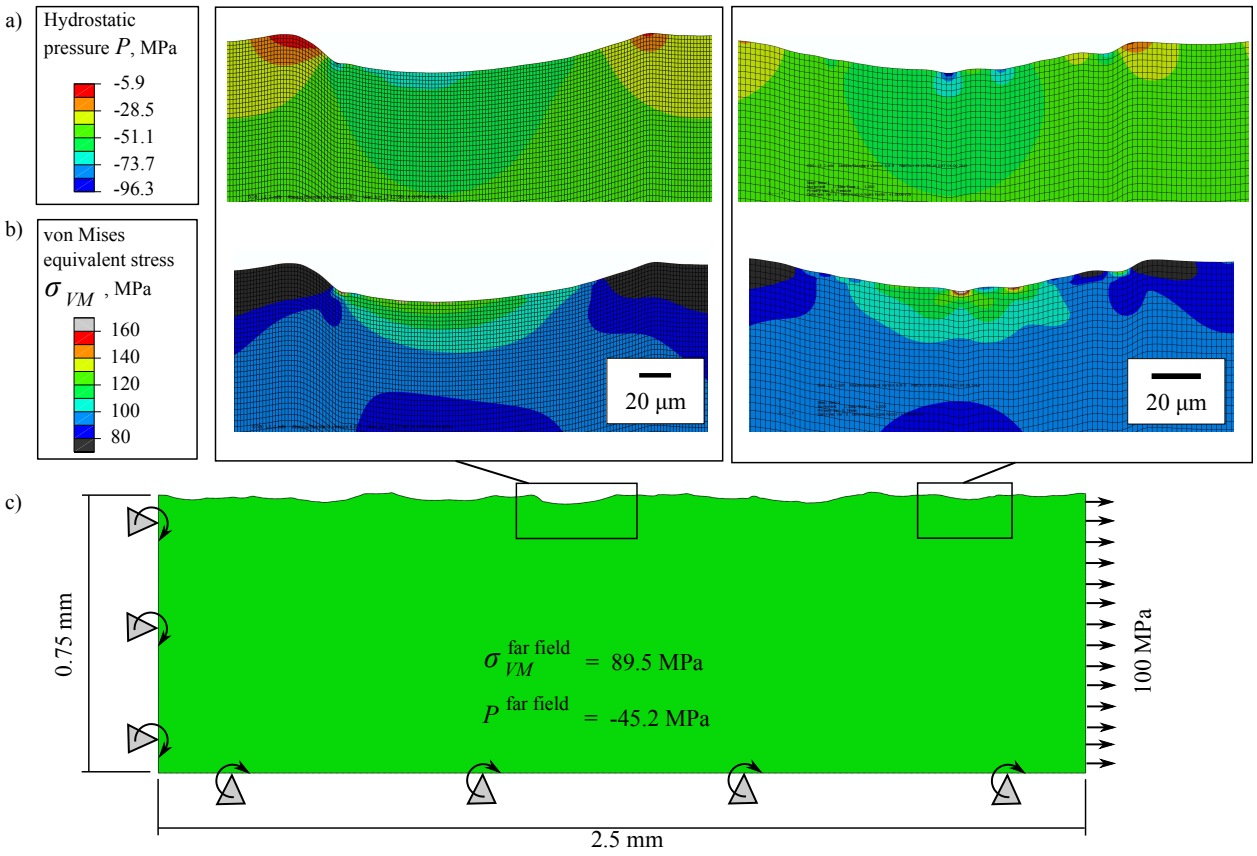

Figure 5.17 Example of the numerical calculation of stress concentration factors and the evaluation of stress concentration depth arising from roughness and local damage using a measured surface profile. The von Mises stress σ_{VM} is smaller than the applied stress and a negative pressure (*i.e.* tension) arises due to the plane strain assumption. Maximum K_t in terms of σ_{VM} is $\approx$ 1.8. For this specific sampling length, stress concentration factors calculated with Equations (5.1) and (5.2) were 1.23 and 1.34, respectively.

5.4.4 Microstructure characterization

While optical microscopy did not reveal significant microstructural modifications in terms of grain size, EBSD mapping provided rich information on the material state gradient after shot peening. Figure 5.18 illustrates the material crystallographic orientations with respect to the normal direction (Y) in a RD-ND cross-section. Four different zones can be identified:

1. A 5 to 20 μm thick layer near the surface with no indexed points. Although edge rounding certainly decreased the Kikuchi pattern quality in this region, it is likely that plastic straining contributed to this phenomenon. Wu *et al.* (2002) have shown that the deformation structure in an aluminium alloy can reach dimensions below 100 nm near the surface after severe plastic deformation by ultrasonic shot peening. While the current study investigated peening with much smaller impact energy, repeated impacts could still have refined the structure to a point where the interaction volume of the electrons became larger than the characteristic microstructural diffracting volume, resulting in no or poor Kikuchi diagrams (Child *et al.*, 2011).
2. A 50 to 75 μm thick layer with highly distorted grains and high internal misorientations. To complement the RD-ND cross-section, EBSD observations were also performed in the RD-TD plane in this region. Figure 5.19(a) presents the crystallographic orientations with respect to the normal direction observed after polishing to a depth of ≈ 20 μm (Section 5.3.2). It was noted that some grains appeared to be less deformed than others. This deformation heterogeneity can be related to two different phenomena:
   – The random impact sequence: for a given coverage, some points on the surface will be subjected to a greater number of impacts and thus higher plastic strains (Zimmermann *et al.*, 2010);
   – The original grain orientations: some combinations of crystallographic orientations and loading paths facilitate plastic deformation.
3. A layer one or two grains thick (≈ 30 μm) with small long-range distortions that follow the surface profile.
4. The parent, unaltered material.

The severely deformed zones 1 and 2 therefore extend to a depth much smaller than those of the increased hardness and the compressive residual stresses, as suggested by Lindemann *et al.* (2006). At the boundary between zones 1 and 2, EBSD data suggests that there could be some degree of grain refinement into subgrains. Low indexation percentages in this area however preclude accurate conclusions. Further study using TEM would be required to better understand the material state in zone 1 after conventional shot peening and its possible effects on fatigue life.

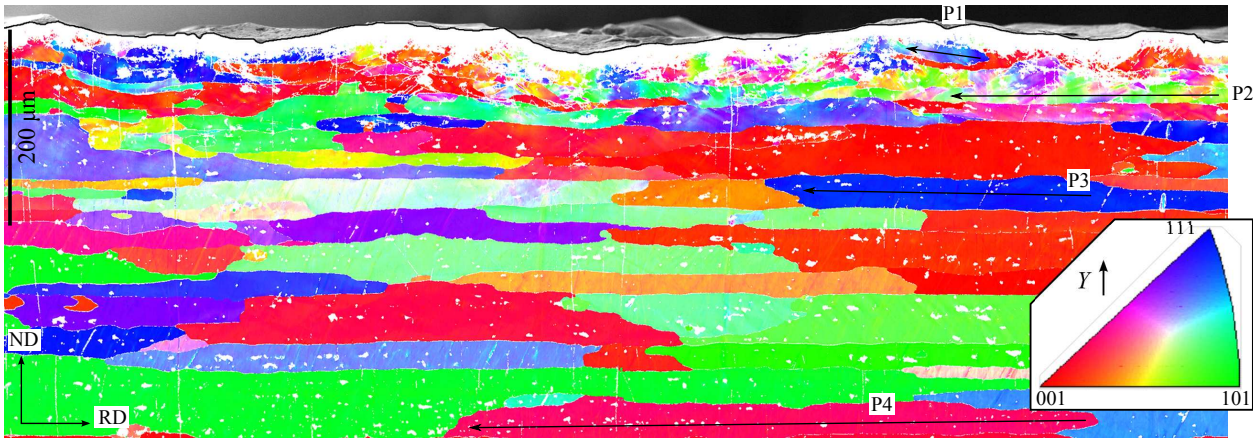

Figure 5.18 Composite image of the EBSD map and a secondary electron image of the near-surface region in the RD-ND cross-section. In the EBSD data, rounded unindexed spots correspond to constituent particles and vertical, elongated trails to polishing scratches. The images were lined up using the large constituent particles as references: this allowed a clear identification of the edge on the EBSD map. Cumulated misorientation profiles were extracted along paths P1 to P4, see Figure 5.20. Magnification: 200x, step size: 0.25 μm.

Study of the local misorientations between adjacent pixels provided some information on the deformation microstructure at the scale of a few micrometers. Local misorientations were determined between each point and its eight neighbours (3×3 filter) as shown in Figure 5.20. When comparing the observations in zone 2 (≈ 55 μm from the surface) to the parent material (zone 4), a more clearly defined structure with higher misorientations can be noted in zone 2. The curved shapes can be attributed to the tridimensional random strain paths generated during shot peening (Wu *et al.*, 2002). It is possible that this structure originated from the organisation of the dislocations generated by the intense plastic straining into dislocation walls. Greyscale level gradients in Figure 5.19(b) and (c) also suggest that at a fixed depth the dislocation density is not uniform throughout the material. It is interesting to note that the spacing between high misorientation lines is of the same order of magnitude as the microband width of 0.6 to 1 μm reported by Wu *et al.* (2002) using TEM for shot peened AA7075.

To assess the deformation state more accurately, misorientations profiles were traced within large grains at different depths. Figure 5.21 presents misorientation profiles extracted from four different paths (P1 to P4) chosen in Figure 5.18. Significant misorientations were found to develop close to the surface after peening. Paths P1 and P2 exhibited large, diffuse rotations over long distances rather than sharp subgrain boundaries. Such distortions could lead to long-range residual stress gradients within each grain. However, current experimental

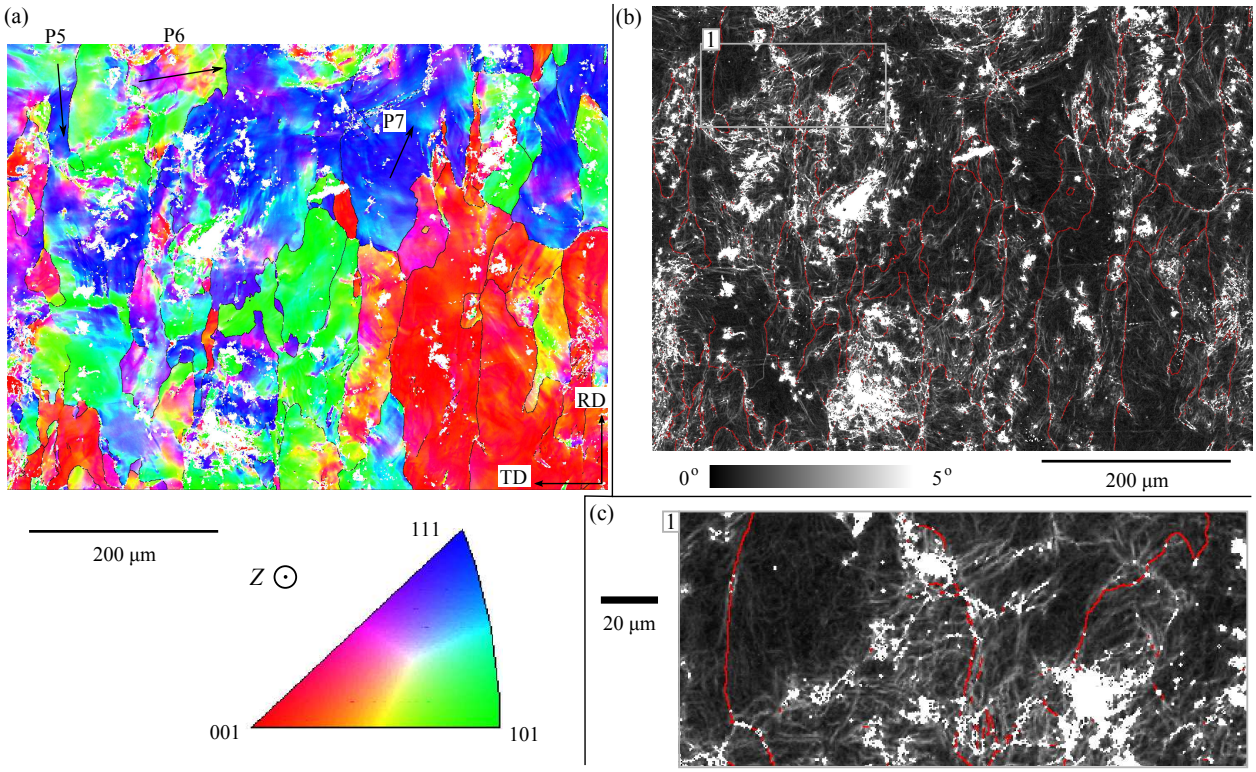

Figure 5.19 (a) EBSD crystallographic orientation map acquired in the RD-TD plane approximately 20 μm from the peened surface. Indexation percentage was 83%. Cumulated misorientation profiles were extracted along paths P5 to P7, see Figure 5.21. (b) Local misorientation map of the same area, using a 3×3 filter. (c) Magnified view of boxed area 1 in (b). Magnification: 200x, step size: 0.5 μm.

stress measurement methods cannot quantitatively describe this phenomenon. Finally, as the depth from the peened surface increased, misorientations decreased progressively down to values typical of the parent material.

The deformation heterogeneity was also quantified in the RD-TD plane at a depth of approximately 20 μm below the surface (P5 to P7 illustrated in Figure 5.19(a)). Figure 5.22 confirms that some areas were subjected to more significant lattice rotations over distances of a few tens of micrometers.

The average misorientation on a grain-by-grain basis or grain orientation spread (GOS) was also evaluated to assess the work-hardened depth, as proposed by Child *et al.* (2011) (Figure 5.23). While an increase of GOS was qualitatively noted near the surface, quantitative results could not be obtained due to the low indexation percentage at the surface, the grain size scatter, as well as the small sampled number of grains arising from the large grain size. When compared with the results by Child *et al.* (2011), larger GOS were observed in the

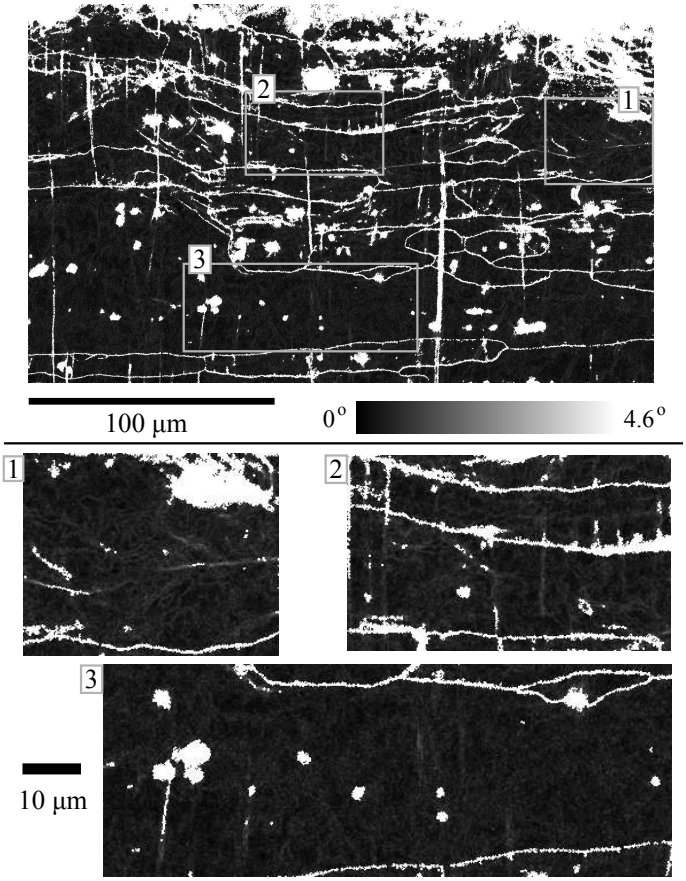

Figure 5.20 Local misorientation map using a 3 × 3 filter. This region corresponds to the left part in Figure 5.18. Magnification: 500x, step size: 0.2 μm.

current study, possibly due the large and elongated grains for which curvature after peening (as illustrated in Figure 5.21) contributes to increased orientation spread.

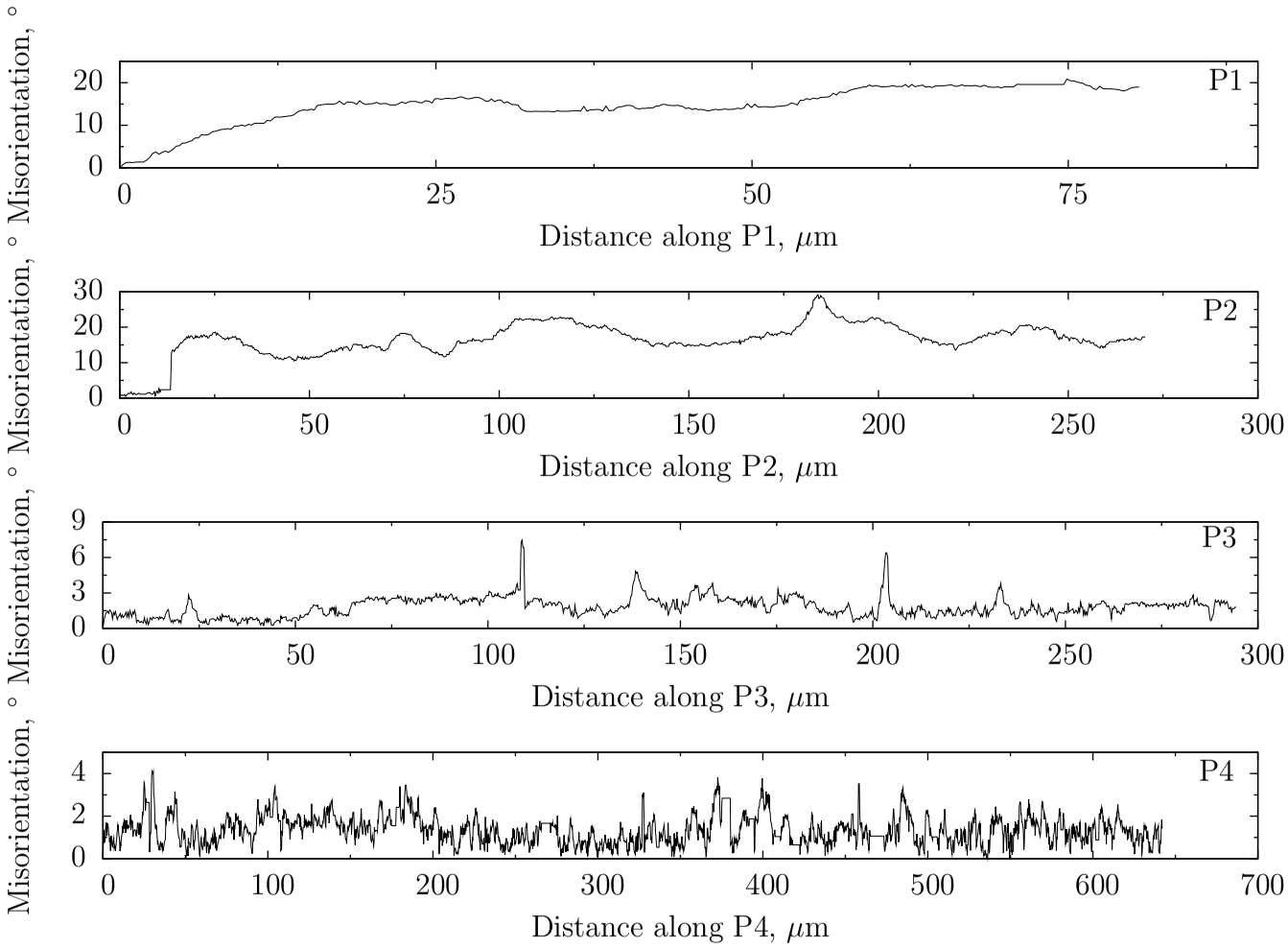

Figure 5.21 Cumulated misorientation profiles along paths located at different depths. Misorientations are relative to the first point of each path. Paths P1 to P4 are defined in Figure 5.18. Scales are different on each graph.

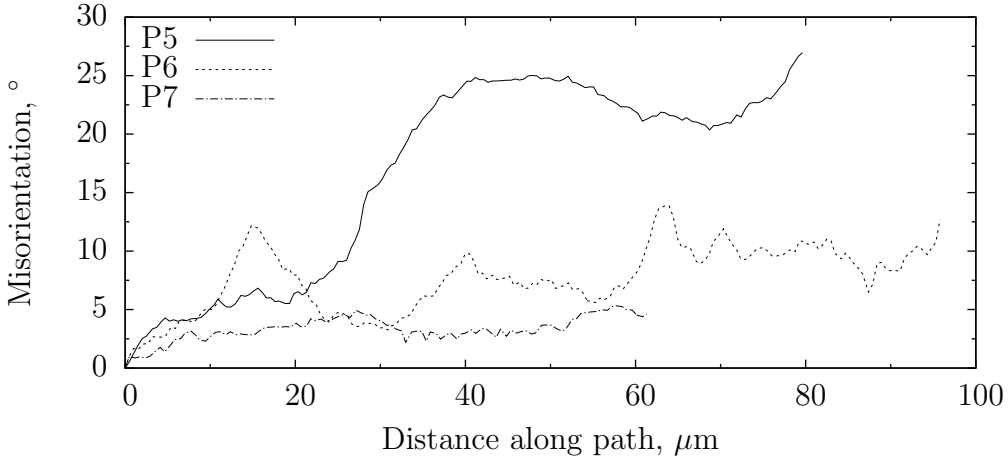

Figure 5.22 Cumulated misorientation profiles along different paths at a depth of ≈ 20 μm, illustrated in Figure 5.19(a). Misorientations are relative to the first point of each path.

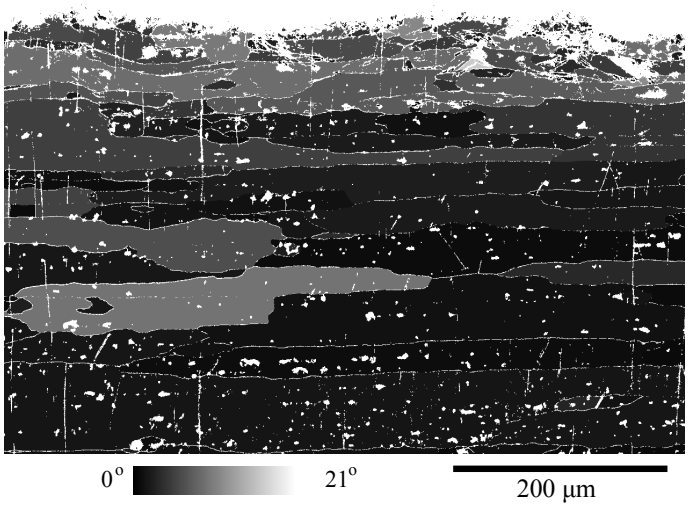

Figure 5.23 Grain orientation spread map for the left half of Figure 5.18. Magnification: 200x, step size: 0.25 μm.

5.4.5 Discussion

The proposed experimental and numerical characterization approach outlined the heterogeneities arising from the random impact sequence and revealed a significant effect of shot peening on the microstructure near the surface. These observations provide a basis for future studies that could lead to a more accurate understanding of the influence of peening on fatigue performance.

Most fatigue life prediction models assume that the material state is uniform in the plane parallel to the peened surface, *i.e.* it depends only upon the depth. Recently, Bouraoui *et al.* (2009) introduced a probabilistic model for the purpose of reliability assessment in the HCF regime. Using a Monte Carlo approach, their model takes into account the distributions of mechanical properties and loading amplitudes as well as the non-uniform effect of shot peening. They observed a significant influence of the variability of the residual stress amplitude on the calculated reliability. Arbitrary variations as large as 15% around the experimentally determined value were proposed. Impact analyses performed in the current study suggest that the actual variations may be much larger, especially near the surface (see Figure 5.6). This shows that an accurate description of the non-uniform material state after shot peening will lead to more accurate predictive models.

Within the context of fatigue life prediction, microstructure-based models take into account the presence of obstacles to microstructurally short crack growth, such as grain boundaries (de los Rios *et al.*, 2000; McDowell, 2007; Xue *et al.*, 2007). Using EBSD, it was found that shot peening of AA2024-T351 led to a structure of small local misorientations and to lattice rotations as large as 20° over distances of tens of micrometers. It could be interesting to evaluate the effect of these features through their contribution to the local increase of yield strength or as weak obstacles to short crack growth. In addition, the role of constituent particles and their behaviour during and after impact loading should be studied further (McDowell, 2007; Xue *et al.*, 2007).

Many fatigue life prediction models require the local mechanical properties as input data. Determining those properties is however a challenging task due to the interactions between residual stresses, work-hardening, and their distributions. For instance, for models that consider the FWHM to evaluate work-hardening or work-softening (Fathallah *et al.*, 2004; Bouraoui *et al.*, 2009), the contribution of residual stress heterogeneity to increased FWHM values may lead to an overestimated work-hardening or an underestimated work-softening effect (Section 5.4.2). Similarly, when determining local strength from indentation testing (de los Rios *et al.*, 2000; Benedetti *et al.*, 2009), compressive residual stresses induced by peening increase the apparent strength. It should be noted that, in both cases, these lead to overestimated strength and non-conservative fatigue life predictions.

Fatigue phenomena are often driven by the most detrimental conditions on a component, especially in the HCF regime (McDowell, 2007). In the current study, correlations between the distributions of residual stresses, dislocations densities, and stress concentration locations were not studied. When considering the significant dispersions experimentally and numerically outlined in this work, one important question that remains is the spatial correlation between the different factors. In other words, it would be useful to evaluate the probability of a crack initiating defect being located in a region of low compressive residual stress, a situation that is likely to be a limiting factor for fatigue life. Further work is required on this topic.

It is worth noting that the material cannot be considered as initially uniform at the scale of the impact dimple. Each impact occurs on a limited number of grains (Figure 5.1) and it is likely that the local crystallographic orientations could make the impact behaviour different from one shot to another. This adds another variable that makes the effect of shot peening heterogeneous.

Potential uses of numerical modelling

This work also investigated the possible uses of finite element (FE) modelling to complement experimental data when studying shot peening. Simulation has several advantages:

- Simulations allow evaluating individual effects that cannot be easily uncoupled in experiments. In the case of shot peening, this is especially useful to independently estimate the residual stress and work-hardening states that are inter-related in XRD and micro-indentation testing;
- It allows probing volumes much smaller than possible with typical experimental methods. In the case of residual stresses, simulations presented in Section 5.4.1 used a mesh size of 20 μm $\times$ 20 μm $\times$ 20 μm in the impacted volume and provided the local stress values at this scale. Experimental measurements yielded average values over a much larger volume since the XRD technique requires multiple grains with different crystallographic orientations to achieve reliable results. FE therefore made evaluating the 3D spatial distribution of residual stresses possible;
- When considering shot peening as a step in the service life of a component (Lillamand *et al.*, 2001), FE modelling provides the detailed history of material loading. This is extremely useful as experiments only characterize the resulting material state;
- While Equations (5.1) and (5.2) correlate stress concentrations with easily measured surface roughness parameters, FE analyses performed with actual surface profiles provided additional information on stress concentrations around damage sites as well as on the depth affected by such stress concentrations;

– Conducting simulations requires a good description of the material behaviour. This knowledge is also a key aspect for understanding and quantifying the fatigue life improvement by shot peening.

In this paper, numerical simulations assumed an isotropic material behaviour. Considering the initial large-grained microstructure (Figure 5.1), it would be interesting to investigate microstructure-based simulations, *e.g.* crystal plasticity. This could provide more information on lattice rotations as well as on the resulting grain-level micro-stresses, and eventually be used as input data in simulation-based fatigue life prediction models (McDowell, 2007).

While FE modelling yields useful information, it is not sufficient to fully characterize the material state after shot peening. One of its limitations is the prediction of local damage (Section 5.4.3) that play a significant role in fatigue life. Some numerical studies have already taken into account material integrity and included damage equations based on the loading state (Lillamand *et al.*, 2001; Frija *et al.*, 2006), but they did not predict features such as embedded shots, folding and microcracks. FE modelling should therefore be considered as a useful complement rather than a replacement for experimental data since simulations do not consider all aspects of the process yet and need to be validated through physical testing.

Case study: description of residual stress relaxation via numerical simulation

The heterogeneous material state after shot peening plays an important role in the residual stress relaxation phenomenon and should be taken into consideration. Benedetti *et al.* (2009) investigated stress relaxation in AA7075-T651 under reverse bending loading. Relaxation was more significant for larger bending loads and this phenomenon was attributed to a quasi-static behaviour. In this case, Holzapfel *et al.* (1998) defined the threshold for relaxation as the sum of the loading and residual stresses being larger than the local yield strength. The experimentally observed average stress relaxation may be affected by the distribution of local residual stresses. Considering the simulation results in Figure 5.7, it is likely that regions subjected to more compressive residual stresses will yield under a smaller external compressive load. This could shift the experimental XRD peak and lead to smaller average residual stress values. This hypothesis does not however explain residual stress relaxation in tension-tension cyclic loading (Rodopoulos *et al.*, 2004; Zaroog *et al.*, 2011b) unless a microstructure-based model is used. In this situation, the stress evolution arising from microplastic strains (Holzapfel *et al.*, 1998) is affected by the heterogeneous material state. Plastic straining will be facilitated in the regions with specific crystallographic orientations, local yield strengths, and local backstress states (Bauschinger effect). Numerical models will give the possibility to simulate such behaviour and validate the theories proposed to quantitatively describe the residual stress relaxation.

5.5 Conclusions

In this study, the potential of a combined experimental and numerical approach to characterize the thin layer of material affected by shot peening was presented. Experimental observations spanned multiple length scales, from the microstructure to the macroscopic residual stress state. The experimental data were complemented with simulation results. FE modelling was especially useful to evaluate the 3D distribution of residual stresses at a scale of a few hundreds of micrometers. Considering the challenges of decoupling significant phenomena in experimental testing (*e.g.* combined influence of work-hardening and residual stresses in micro-indentation), simulation could help dissociate the different effects of shot peening on the material.

For the specific material and peening parameters considered in this work, the plastic strain gradient associated with repeated impacts led to a layered structure with:

- Localized damage at the surface;
- Significant microstructural changes in the first 75 μm of material;
- A work-hardened layer about 175 to 200 μm thick;
- Compressive residual stresses extending to a depth of approximately 350 to 400 μm.

The microstructural effects of shot peening in AA2024-T351 were investigated with EBSD. An unindexable structure was found in the first few micrometers, suggesting large dislocation densities and very small dislocation substructures. For the large-grained microstructure under study, significant lattice rotations over distances of about 100 μm were also measured in a ≈ 70 μm thick layer near the surface. These microstructural changes and their effects on the short crack propagation behaviour should be studied further.

This work showed that the material state arising from shot peening is not uniform on the surface plane in terms of residual stresses, local mechanical properties, roughness, and surface damage. This feature is not considered in most current fatigue life prediction models. Future fatigue life prediction models should take into account the statistical nature of shot peening and the resulting distributions to quantify the fatigue properties improvement provided by this process.

Acknowledgements

The authors would like to thank the National Research Council Canada - Aerospace Manufacturing Technologies for providing the shot peening equipment and expertise. The help from C. Baillargeon at IREQ (confocal microscopy) as well as V. Savaria and M. Vals at ÉTS (residual stress corrections) and the continued support from R. Romanica and J.-G. Gagnon at ÉTS are also gratefully acknowledged. A. Gariépy would like to thank the

Natural Sciences and Engineering Research Council of Canada (NSERC), Rio Tinto Alcan and Fondation de Polytechnique for their financial support through scholarships.

CHAPTER 6

ARTICLE 3: ON THE EFFECT OF THE ORIENTATION OF SHEET ROLLING DIRECTION IN SHOT PEEN FORMING

A. Gariépy, S. Larose, C. Perron, P. Bocher, M. Lévesque. Submitted to *Journal of Materials Processing Technology* on July 9, 2012.

6.1 Abstract

Peen forming is commonly used in the aerospace industry to shape large and thin panels, such as wing skins. This manufacturing process uses shot peening to introduce unbalanced compressive stresses near the surface of the component. These stresses tend to bend the panel and, when optimized, lead to the desired contour. Sheet materials often exhibit both elastic and plastic anisotropy, which can alter the development of curvatures. Since peen forming relies on compressive stresses to upset equilibrium, resulting curvatures may also be affected by initial stresses in the part. In this work, the influence of the rolling direction orientation with respect to the sample was investigated experimentally and numerically for the first time for aluminium alloy 2024-T3 specimens. Although maximum deflections were only slightly dependent on the rolling direction orientation, it was found that radii of curvature varied by as much as 10% with respect to this parameter. Finite element simulations allowed quantification of the individual effects of non-equibiaxial initial stresses and elastic orthotropy. It was found that these factors can significantly influence curvature development. Comparison of experimental and numerical results suggested that plastic anisotropy should also be taken into account in future studies. The tools developed in this study show promises for the accurate prediction of peen forming process for large scale components.

6.2 Introduction

Shot peening is a surface treatment in which multiple small particles impact a ductile material. Each impact creates localized plastic strains that stretch the peened surface. Since only a thin layer is plastically deformed, compressive stresses are introduced near the surface. To balance the stresses induced by peening, the part bends and stretches, as schematically illustrated in Figure 6.1. For thick parts, such as gears, resulting macroscopic deflection is negligible; however, for thin parts the stresses induced by peening produce significant bending and stretching. Shot peen forming is a manufacturing process relying on the unbalanced

stresses generated by peening to accurately shape thin components. This versatile and cost-effective process is commonly used in the aerospace industry to shape wing and rocket skins (Baughman, 1984; Friese *et al.*, 2002).

The Almen test is commonly used to characterize peening treatments. It is a standardized procedure in which SAE 1070 steel strips of dimensions 76.2 × 19.1 mm, and specific thicknesses, are peened in a holder. The strips are subjected to the shot stream and their free deflection over a 31.75 × 15.87 mm area is measured with a dedicated instrument called an Almen gauge. The measured deflection is also known as the arc height. Figure 6.2 presents schematically the principle of the Almen test. The arc heights of a series of strips corresponding to different shot stream exposure times are measured. Then, these arc heights are plotted as a function of their respective peening durations. The saturation point is defined as the exposure time for which doubling the duration increases the arc height by 10%, while the Almen intensity a_h^S is the arc height corresponding to the saturation point. Due to its simplicity, the Almen intensity is a common process control variable in peening applications.

Shot peen forming of aluminium sheets and plates has been studied experimentally by many researchers and a few studies have considered the influence of the rolling direction orientation with respect to the sample on the forming results. Kulkarni *et al.* (1981) studied the effects of multiple process parameters by peening AA2024-T3 and AA7075-T6 samples of various geometries. It was observed that sample shape and the rolling direction of the sheet had an effect on resulting curvatures. Unconstrained, uniformly-peened rectangular specimens with an aspect ratio of four exhibited similar curvatures along the rolling and transverse directions while square samples developed a cylindrical contour. Wang *et al.* (2006) reported differences of Almen arc heights smaller than 5 % between AA5251-H22 strips cut along the rolling and transverse directions. Miao *et al.* (2010) peened 76.2×19.1 mm, 1.6 mm-thick AA2024-T3 strips held in Almen holders and observed that measured arc heights for strips cut along the rolling direction were larger than those for strips cut along the transverse

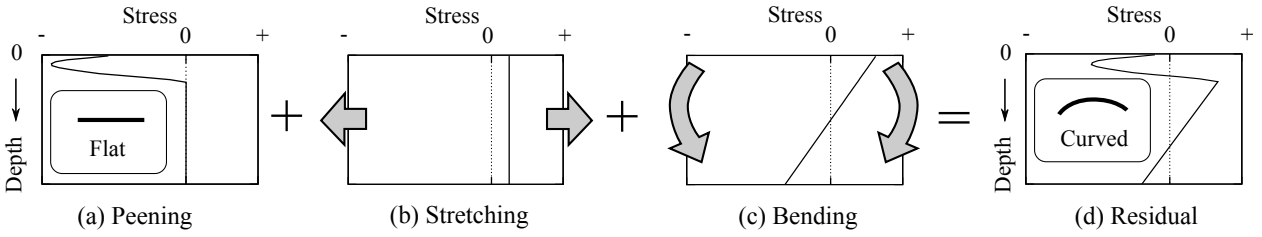

Figure 6.1 Balancing of (a) induced stresses through (b) elongation and (c) bending of the part to reach an equilibrated (d) residual stress profile.

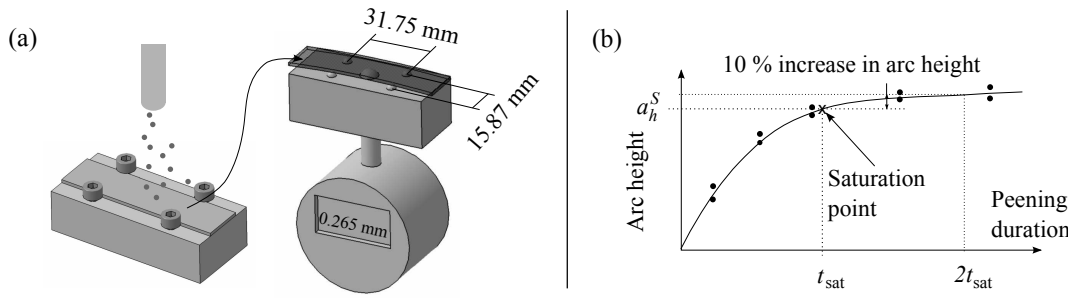

Figure 6.2 Principle of the Almen test. (a) An Almen strip is peened in a holder up to a predefined peening duration. It is then removed from the holder and its arc height is measured with an Almen gauge. (b) By peening strips at various peening times, the saturation curve is built.

direction.

While the influence of the rolling direction has been observed experimentally, the origins of this phenomenon have not been studied extensively. Miao *et al.* (2010) attributed their observations to the plastic anisotropy of the material. They also measured residual stress profiles in peened strips: the measurements showed unusually compressive stresses at mid-thickness, but this phenomenon was left unexplained. Kulkarni *et al.* (1981) noted the presence of surface residual stresses between 35 and 104 MPa (either tensile or compressive) in their aluminium alloy sheet samples prior to peening. Moreover, Feja *et al.* (1987) and Prime and Hill (2002) showed that initial stress profiles are not identical along the rolling and transverse directions of sheet and plate material (*i.e.* they are non-equibiaxial).

The objective of this article is therefore to investigate the possible influences of material anisotropy and initial stresses on the development of curvature during peen forming. Experiments were conducted to determine the combined effects of plastic and elastic anisotropy as well as initial stresses on resulting deflections and curvatures. Finite element simulations were run to assess independently the influences of initial stresses and elastic orthotropy. This article is divided into six sections. Section 6.3 presents the experimental procedure used to quantify the effect of the rolling direction on resulting arc heights. Section 6.4 discusses the potential effects of material anisotropy and initial stresses in the target material. Section 6.5 presents the finite element impact and forming models used in the current study. Section 6.6 discusses experimental and numerical results. Section 6.7 concludes this work and suggests topics for further studies.

6.3 Experimental procedure

6.3.1 Peen forming experiments

The influence of the rolling direction orientation with respect to the sample was quantified following the experimental procedure of Miao *et al.* (2010). The setup consisted of a Baiker air blast peening machine and a Motoman industrial robot arm. St-Gobain Zirpro Z425 ceramic shots having diameters ranging from 425 μm to 600 μm (Saint-Gobain, 2003) were fed at a mass flow rate of 0.4 kg/min. Strips with dimensions of 76.2×19.1 mm were sheared from a 1.6 mm-thick AA2024-T3 sheet. Samples were cut with the rolling direction aligned in either direction X and Y on the strip (Figure 6.3). Specimens were held in Almen holders during peening and the peening nozzle was kept perpendicular to the holder surface, as shown in Figure 6.2(a). The number of passes of the peening nozzle over the strip (at a constant robot travel velocity of 320 mm/s) was varied to adjust exposure time.

For the purpose of the current study, additional results were required since data from Miao *et al.* (2010) were not deemed to be statistically representative. Samples were peened with the parameters presented in Table 6.1. Miao *et al.* (2010) measured peening intensities of 0.127 mmA and 0.189 mmA for cases A and B, respectively; no standard Almen test was performed in the current study to evaluate the peening intensities. As the peening equipment did not include a recirculation or filtering apparatus, the shots were used only once. Strips were peened up to 2, 4, 7, 10, 16, and 24 passes. Four strips were peened for each condition to evaluate process variability. The experimental sequence was designed to reduce the effect of peening equipment drift: the four strips for each condition were peened on the same day but not sequentially. In order to take into account initial strip curvature, arc heights were measured before and after peening and initial deflections were substracted from the final deflections. It should be noted that some of the strips had significant initial arc heights: only strips with initial heights less than 0.012 mm were used in the experiments. Considering that SAE Standard J442 (2008) imposes a maximum initial arc height of 0.025 mm for steel Almen strips, this criterion was rather strict.

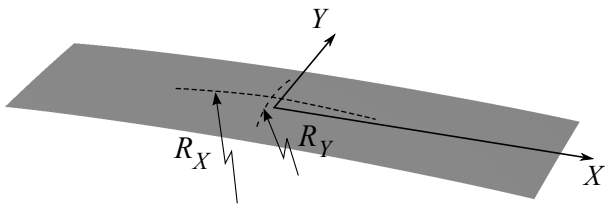

Figure 6.3 Coordinate system on the aluminium strip and definition of radii of curvature R_X and R_Y along X and Y, respectively.

To determine the saturation points, the experimental data were fitted with:

$$a_h(n) = \frac{C \times n_p}{D + n_p} \tag{6.1}$$

where a_h is the measured arc height, n_p is the number of passes and C and D are fitting parameters (Wang *et al.*, 2008). The number of passes at saturation, n_s, was calculated by solving:

$$1.1 \times a_h(n_s) = 1.1 \times \frac{C \times n_s}{D + n_s} = a_h(2 \times n_s) = \frac{C \times (2 \times n_s)}{D + (2 \times n_s)} \tag{6.2}$$

and the arc height at saturation was calculated as $a_h(n_s)$ (Miao *et al.*, 2010).

Radii of curvature were also determined near the center of the strips in order to gain a more accurate evaluation of the influence of the rolling direction. For cases A and B, surface profiles were measured for four strips peened up to ten passes using a Mitutoyo Formtracer profilometer with a 1 mm-diameter spherical tip and a step of 0.02 mm. Measurements were made on the peened surface over lengths of approximately 28 and 12 mm along directions X and Y of Figure 6.3, respectively. Radii were determined by fitting circular segments through the data.

Numerical simulations require knowledge of the impact velocity of the shots. This parameter was measured at the beginning, halfway through and at the end of the experiments with a Shotmeter^{TM} system. The average velocities are shown in Table 6.1; standard deviations were less than 1.5% of the average shot velocity. The measured velocities were approximately 3% lower than those measured by Miao *et al.* (2010). Factors such as nozzle wear could possibly explain this systematic difference.

Process stability

To evaluate process stability, experimental results of the arc height vs. the number of passes for strips cut along the rolling direction acquired in this study were first compared with those of Miao *et al.* (2010), as shown in Figure 6.4. Differences were generally less

Table 6.1 Experimental peening conditions

Case	Pressure (kPa)	Mass flow (kg/min)	Impact angle [a] (Degrees)	Shot velocity (m/s)	From Miao *et al.* (2010)	
					Shot velocity (m/s)	Almen intensity mmA
A	37.9	0.4	90	33.7	34.6	0.127
B	96.5	0.4	90	52.1	53.7	0.189

[a] Between the holder surface and the nozzle axis

than 2% of the average value for case A but average arc heights from the current work were as much as 7% higher than those from Miao *et al.* (2010) for case B. This discrepancy is difficult to explain since peening parameters and equipment were the same for both studies. Moreover, as lower velocities were measured in the current study, smaller arc heights would be expected. Since strips for cases A and B were peened alternatively, a variation due to shot batches seemed unlikely. Operator-related differences such as tightening torque on the holder bolts may be a source of variation. Another observation was that, for case A, experimental scatter was smaller for the current study. This may be related to the fact that all peening experiments were performed within a short time period.

6.3.2 Determination of initial residual stresses

Initial stresses in a 1.6 mm-thick AA2024-T3 sheet were determined along the rolling and transverse directions by the X-ray diffraction technique. Measurements were performed by Proto Manufacturing Ltd. using a cobalt target and considering the {331} aluminium crystallographic planes ($2\theta = 148.9°$). Corrections for stress gradient and material removal were calculated. Measurements were made at the surface and at ≈ 0.1 mm depth increments up to a depth of 0.8 mm, corresponding to half the sheet thickness. Initial stresses were determined on the side of the sheet that was subjected to shot peening and symmetry of the stress profiles about the mid-thickness was assumed.

6.4 Theoretical effects of material anisotropy and initial stresses in peen forming

Multiple factors can influence the development of curvature in peen formed sheets. Textured materials (*i.e.* with preferential crystallographic orientations) usually exhibit plastic and elastic anisotropy. Sheet manufacturing can also introduce significant internal stresses. A simplified analytical approach neglecting the incremental nature of the process is useful to understand the influence of each parameter. As shown in Figure 6.5(a) and (b), stress profiles induced by peening $\sigma^{\text{peening}}(z)$ are those existing in a fully constrained component after peening (VanLuchene *et al.*, 1995). Constraining moments M_r^{con} and M_t^{con} and axial forces F_r^{con} and F_t^{con}, where subscripts r and t refer respectively to the rolling and transverse directions, must be applied to prevent macroscopic bending and stretching. Constraining forces and moments can be calculated as (Guagliano, 2001; Miao *et al.*, 2009):

$$M_r^{\text{con}} = \int_0^h \sigma_r^{\text{peening}}(z) \left(z - \frac{h}{2} \right) \mathrm{d}z \tag{6.3a}$$

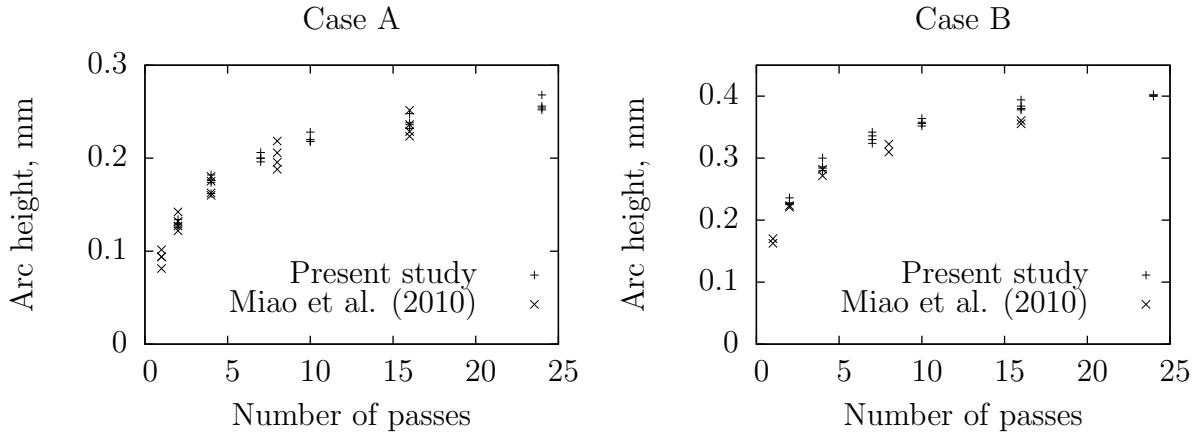

Figure 6.4 Comparison of experimental arc heights from this study and from Miao *et al.* (2010) for strips cut along the rolling direction. The same experimental setup was used. Peening parameters are presented in Table 6.1.

$$M_t^{\text{con}} = \int_0^h \sigma_t^{\text{peening}}(z) \left(z - \frac{h}{2} \right) \mathrm{d}z \tag{6.3b}$$

$$F_r^{\text{con}} = \int_0^h \sigma_r^{\text{peening}}(z) \mathrm{d}z \tag{6.3c}$$

$$F_t^{\text{con}} = \int_0^h \sigma_t^{\text{peening}}(z) \mathrm{d}z \tag{6.3d}$$

where h is the sheet thickness and z is the depth. For simplification, constraining forces were neglected in the following analytical study. Releasing the constraints is equivalent to applying opposite bending moments on a non-peened sheet:

$$M_r = -M_r^{\text{con}} \tag{6.4a}$$

$$M_t = -M_t^{\text{con}} \tag{6.4b}$$

The resulting deflections and curvatures can therefore be computed by considering the alternate problem illustrated in Figure 6.5(c). The relationships between bending moment and resulting curvatures along the rolling direction ($1/R_r$) and the transverse direction ($1/R_t$) for a sheet made of an elastically isotropic material are:

$$\frac{1}{R_r} = -\frac{12(M_r - \nu M_t)}{Eh^3} \tag{6.5a}$$

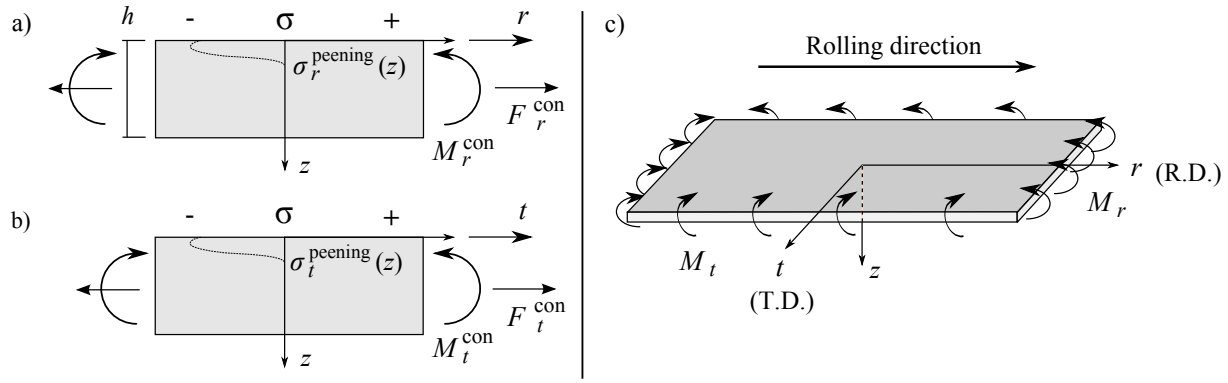

Figure 6.5 (a) and (b) Schematic representation of stress profiles generated by peening along the rolling (r) and transverse (t) directions, respectively. Constraining moments, M_r^{con} and M_t^{con}, and forces, F_r^{con} and F_t^{con}, required to prevent bending and stretching are also shown. (c) Equivalent problem used to evaluate the bending effect of shot peening on a sheet.

$$\frac{1}{R_t} = -\frac{12(M_t - \nu M_r)}{Eh^3} \tag{6.5b}$$

where R is the radius of curvature and ν and E are the material Poisson's ratio and Young's modulus, respectively.

The calculated radii of curvature can then be related to deflections. For illustration purposes, assuming that the total arc height h_{total} can be evaluated as the sum of deflections from two cylinders aligned along axes X and Y as illustrated in Figure 6.6, the total arc height would be:

$$h_{\text{total}} = h_X + h_Y \tag{6.6a}$$

$$= \frac{L_X^2}{8R_X} + \frac{L_Y^2}{8R_Y} \tag{6.6b}$$

6.4.1 Plastic anisotropy

Miao *et al.* (2010) noted that peened AA2024-T3 rectangular strips cut along the rolling direction exhibited larger arc heights than peened strips cut along the transverse direction. They performed monotonic tensile tests on samples cut along the rolling and transverse directions and observed that samples cut along the rolling direction had larger yield strength and ultimate strength. Based on the work of Wang *et al.* (1998), Miao et al. suggested that higher yield and ultimate strengths led to more compressive induced stresses along the rolling direction than along the transverse direction, $|\sigma_r^{\text{peening}}(z)| > |\sigma_t^{\text{peening}}(z)|$. Equations (6.3) and (6.4) indicate that more compressive stresses near the top surface yield a larger bending

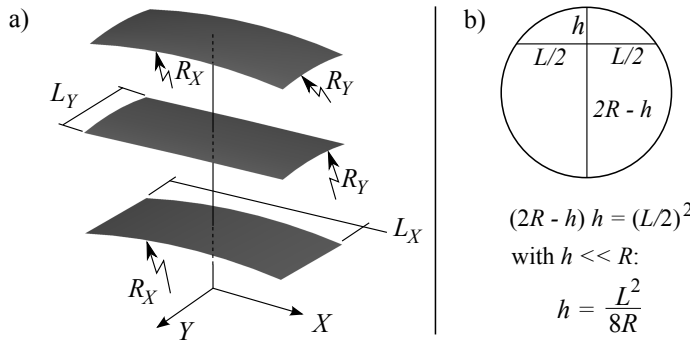

Figure 6.6 (a) The arc height over an $L_X \times L_Y$ area can be estimated by the summation of the deflections of two orthogonal cylinders having radii R_X and R_Y. (b) The intersecting chords theorem is used to determine the deflection h at the center of a cylinder.

moment, $|M_r| > |M_t|$. Based on Eq. (6.5), plastic anisotropy would therefore lead to a larger curvature along the rolling direction than along the transverse direction (Miao *et al.*, 2010).

An anisotropic yield criterion would be required to fully comprehend the impact process. Modelling plastic anisotropy is a complicated task since shot peening involves three-dimensional cyclic strains and stresses. For instance, studies such as those of Klemenz *et al.* (2009) and Zimmermann *et al.* (2010) suggest that stress profiles induced by peening are dependent on cyclic material properties. In addition, MIL-5H (1998) indicates that compressive yield stress is higher along the transverse direction than along the rolling direction for 1.6 mm-thick AA2024-T3.

This work therefore focuses on investigating the contributions from other simpler mechanisms that could affect the development of curvatures. Considering that peen forming is typically a surface plasticity process that leads to elastic deflections in the part, it seems likely that elastic phenomena could explain at least in part the global, experimentally observed effect of sheet anisotropy. In addition, the assessment of the elastic effects could help evaluate the significance of plastic anisotropy in peen forming.

6.4.2 Elastic anisotropy

Monotonic tensile stresses on AA2024-T3 by Miao *et al.* (2010) showed a 5% higher Young's elastic modulus along the rolling direction than along the transverse direction. For an elastically orthotropic material, the curvatures resulting from bending moments can be expressed as (Hwu, 2010):

$$\frac{1}{R_r} = -\frac{12\,(1 - \nu_{rt}\nu_{tr})\,(M_r - \nu_{rt}M_t)}{(E_r - \nu_{rt}^2 E_t)\,h^3} \tag{6.7a}$$

$$\frac{1}{R_t} = -\frac{12\,(1-\nu_{rt}\nu_{tr})\,(M_t - \nu_{tr}M_r)}{(E_t - \nu_{tr}^2 E_r)\,h^3} \tag{6.7b}$$

where E_r and E_t are the elastic moduli along the rolling and transverse directions, respectively, and $\nu_{rt} = -\varepsilon_t/\varepsilon_r$ is the Poisson's ratio when the material is uni-axially stressed along r. Similarly, $\nu_{tr} = -\varepsilon_r/\varepsilon_t$ is the Poisson's ratio when the material is stressed along t. Assuming that bending moments along the rolling and transverse directions are equal, $M_r = M_t = M$, and as $\nu_{rt}E_t = \nu_{tr}E_r$ for an orthotropic material, Equations (6.7) simplify to:

$$\frac{1}{R_r} = -\frac{12\,(1-\nu_{rt})\,M}{E_r h^3} \tag{6.8a}$$

$$\frac{1}{R_t} = -\frac{12\,(1-\nu_{tr})\,M}{E_t h^3} \tag{6.8b}$$

Since $E_r > E_t$, it follows that $\nu_{rt} > \nu_{tr}$ and according to Equations (6.8) the curvature along the rolling direction is smaller than the curvature along the transverse direction ($|1/R_r < 1/R_t|$). The anisotropy of monotonic elastic moduli would therefore lead to smaller curvatures along the rolling direction for equally applied bending moments.

6.4.3 Initial stresses

The effect of initial stresses on the development of curvature can be explained as follows. First, equilibrium requires that the initial stress profile $\sigma^{\text{initial}}(z)$ be balanced, that is:

$$M^{\text{initial}} = \int_0^h \sigma^{\text{initial}}(z)\left(z - \frac{h}{2}\right)\mathrm{d}z = 0 \tag{6.9}$$

When the material is peened without allowing macroscopic bending and stretching, compressive stresses $\sigma^{\text{peening}}(z)$ are created near the surface and initial stresses remain at greater depths, as illustrated in Figure 6.7. Experiments (Cao *et al.*, 1995) and simulations (Gariépy *et al.*, 2011) suggest that the stress profile generated by shot peening near the surface is not very sensitive to initial stresses. For simplification, it can be assumed that, when neglecting plastic anisotropy, $\sigma_r^{\text{peening}}(z) = \sigma_t^{\text{peening}}(z) = \sigma^{\text{peening}}(z)$. The equivalent bending moment along each direction can then be expressed with Eq. (6.3) and (6.4) as:

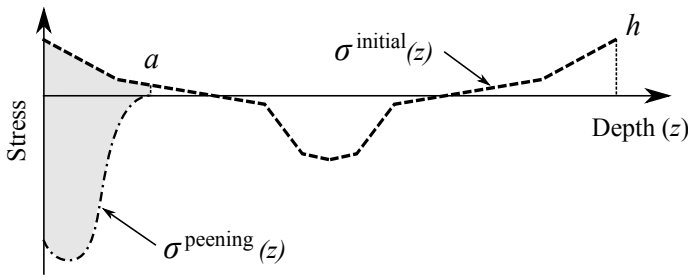

Figure 6.7 Schematic illustration of the effect of initial stresses in peen forming. The induced stress profile after shot peening consists of the stresses generated by peening $\sigma^{\text{peening}}(z)$ from the peened surface up to the affected depth a and the initial stresses $\sigma^{\text{initial}}(z)$ for $z > a$. In this simplified analysis, a is the depth where the stresses due to peening become zero in the absence of initial stresses. The resulting bending moment M, Eq. (6.10), is related to the greyed-out area.

$$
\begin{aligned}
M_r &= -\int_0^a \sigma_r^{\text{peening}}(z)\left(z-\frac{h}{2}\right)\mathrm{d}z - \int_a^h \sigma_r^{\text{initial}}(z)\left(z-\frac{h}{2}\right)\mathrm{d}z && \text{(6.10a)}\\
&= -\int_0^a \sigma^{\text{peening}}(z)\left(z-\frac{h}{2}\right)\mathrm{d}z \\
&\quad -\left(0-\int_0^a \sigma_r^{\text{initial}}(z)\left(z-\frac{h}{2}\right)\right)\mathrm{d}z \text{ (from Eq. (6.9))} && \text{(6.10b)}\\
&= \int_0^a \left(-\sigma^{\text{peening}}(z)+\sigma_r^{\text{initial}}(z)\right)\left(z-\frac{h}{2}\right)\mathrm{d}z && \text{(6.10c)}\\
M_t &= \int_0^a \left(-\sigma^{\text{peening}}(z)+\sigma_t^{\text{initial}}(z)\right)\left(z-\frac{h}{2}\right)\mathrm{d}z && \text{(6.10d)}
\end{aligned}
$$

where a is the depth affected by peening shown in Figure 6.7.

Initial tensile stresses near the peened surface increase $|M|$ since, in Eq. (6.10c), $\sigma^{\text{peening}}(z) < 0$ while $\sigma^{\text{initial}}(z) > 0$. From Eq. (6.5), increasing $|M|$ in one direction results in an increased curvature along this direction. When compressive surface stresses (such as those introduced by quenching) are present, the opposite effect will occur, inhibiting the development of curvature by reducing $|M|$. When the initial stress profiles are not equibiaxial (*i.e.* $\sigma_r^{\text{initial}}(z) \neq \sigma_t^{\text{initial}}(z)$), different curvatures are produced along the rolling and transverse directions.

6.4.4 Combined effect of sheet anisotropy phenomena

The observed effect of the rolling direction orientation with respect to the sample on the development of curvatures during peen forming is a complex phenomenon that involves material plastic and elastic anisotropy as well as the initial stress state in the component.

For instance, Sections 6.4.1 and 6.4.2 suggest that elastic and plastic anisotropy can have opposite effects: if the yield strength, ultimate strength and Young's modulus are larger along the rolling direction than along the transverse direction, plastic anisotropy may tend to increase curvature while elastic anisotropy may tend to decrease curvature along the rolling direction. Experiments typically give information on the combined effect of anisotropy and initial stresses. Experimental results can therefore show no effect from the orientation of the rolling direction when the three factors cancel each other. Uncoupling experimentally the effects of these phenomena is thus a challenging task.

6.5 Numerical simulations

Finite element (FE) peen forming simulations were performed to study the independent and combined effects of initial stresses and elastic orthotropy. The finite element approach of Gariépy *et al.* (2011) was applied. The first step consisted of using a three-dimensional dynamic impact model with cyclic material properties to calculate stresses induced by peening. The second step used the stress profiles obtained with the impact model for different peening exposure times to calculate the deformed shape of the strip with multiple incremental steps, taking into account progressive deflection.

6.5.1 Input data for initial residual stresses

Figure 6.8 shows the initial stress profiles in 1.6 mm-thick AA2024-T3 along the rolling and transverse directions, obtained by the X-ray diffraction method. Stress values are dependent on measurement direction. The main features of these profiles are:

1. At the surface, tensile stresses exist along the rolling direction while stresses along the transverse direction are negligible;
2. At depths between 0.1 and 0.6 mm, stresses in both directions are fairly similar;
3. Compressive stresses at mid-thickness are larger along the rolling direction than along the transverse direction to balance the near-surface stresses.

The results are quite consistent with the initial stress profile in a 3.0 mm-thick sheet of AA2024-T3 determined by Hospers and Vogelesang (1975) using successive chemical etching.

It should be noted that the measured stress profiles are not perfectly balanced axially when assuming symmetry. Equilibrium would require that -19.7 N/mm and -11.3 N/mm forces be applied on the edges along the rolling and transverse directions, respectively. There are many possible sources for this:

– The symmetry assumption may not be appropriate. Figure 6.9 illustrates an example of an asymmetric balanced initial stress profile ${}^{\text{asym}}_{\text{bal}}\sigma^{\text{initial}}(z)$ based on the experimental

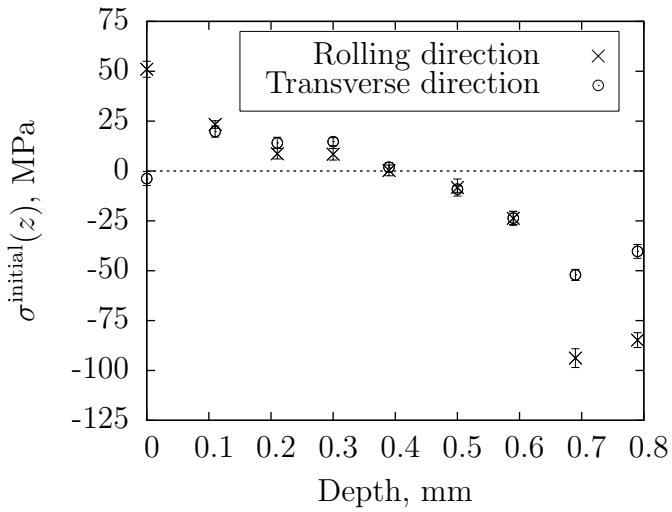

Figure 6.8 Experimentally determined initial (unpeened) stress profiles along the rolling and transverse directions in a 1.6 mm-thick AA2024-T3 sheet. Measurements were made on one side of the sheet from the surface to mid-thickness. Error bars indicate measurement uncertainty.

stress data obtained for half of the sheet thickness (Figure 6.8). However, considering the results by Prime and Hill (2002), a certain degree of symmetry would be expected;

– There could be a systematic error in the experimental measurements. Symmetric balanced initial stress profiles ${}^{\text{sym}}_{\text{bal}}\sigma^{\text{initial}}(z)$ could then be calculated as:

$$ {}^{\text{sym}}_{\text{bal}}\sigma_r^{\text{initial}}(z) = \sigma_r^{\text{initial}}(z) + 12 \text{ MPa} \tag{6.11a} $$

$$ {}^{\text{sym}}_{\text{bal}}\sigma_t^{\text{initial}}(z) = \sigma_t^{\text{initial}}(z) + 7 \text{ MPa} \tag{6.11b} $$

– The axial unbalance could be partly caused by local measurement inaccuracies. For instance, considering that the experimental stress values shown in Figure 6.8 were quite widely spaced through the thickness, it is possible that some of the corrections for the stress gradient were inaccurate (Prevey, 1991).

Sheet material is generally produced by multiple increments of hot and cold rolling combined with recrystallization treatments. According to ASM Handbook (1991) and Katgerman and Eskin (2003), the T3 heat treatment of aluminium alloys consists of solution heat treatment, cold working and natural aging to a substantially stable condition. Initial stresses in a sheet can therefore originate from many processes. One possible origin of initial stresses would be the quenching step during solution heat treatment. Due to the rapid cooling of

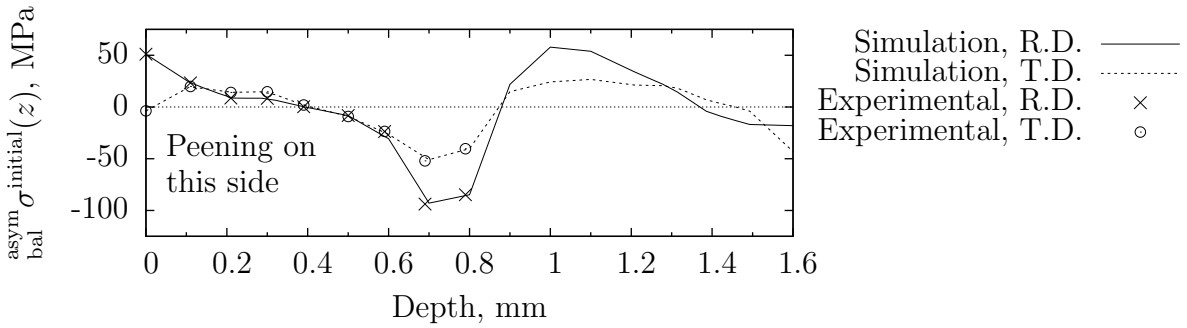

Figure 6.9 Example of possible asymmetric balanced initial stress profile $^{\text{asym}}_{\text{bal}}\sigma^{\text{initial}}(z)$ consistent with the experimentally determined stress values.

the surface when compared to the core of the sheet, quenching usually generates compressive stresses near the surface (Myer *et al.*, 1959). On the other hand, the experimental initial stress profiles in Figure 6.8 exhibit tensile or zero surface stresses and could therefore not be attributed to quenching of the sheet alone. While the exact history of samples is not known, ASM Handbook (1991) suggests that the cold-worked -T3 state is often achieved in aluminium sheets and plates by cold rolling. Myer *et al.* (1959) studied skin-pass rolling (with a low reduction) as a stress-relief method and showed that tensile residual stresses were created near the surfaces by the rolling operation. Feja *et al.* (1987) measured tensile stresses near the surface and compressive stresses at mid-thickness in a 1.0 mm-thick cold rolled steel sheet. Initial stresses amplitude was also found to be larger along the rolling direction than along the transverse direction, which is consistent with Figure 6.8. It therefore seems likely that cold rolling contributes to the initial stress state in AA2024-T3.

It is worth noting that, considering the relatively large initial stresses in the sheet material, these internal stresses may have affected the shape of the stress-strain curves and thus the yield strengths determined by Miao *et al.* (2010). During a tensile test, regions subjected to initial tensile stresses along the loading axis would yield before regions where compressive initial stresses are present. The stress-strain curve then shows the response of the structure rather than that of the material itself.

6.5.2 Dynamic impact modelling

In Gariépy *et al.* (2011), multiple shots with random coordinates and diameters within a prescribed range impacted a small target area. The stress state in the peened material was calculated using `ABAQUS Explicit` and was averaged over the representative area to obtain the stress profiles induced by peening $\sigma^{\text{peening}}(z)$. In order to compare numerical

predictions with the experimental results of Miao *et al.* (2010), it was calculated that one experimental peening pass corresponded to an impact density of 3.65 mg/mm^2. An isotropic-kinematic hardening material law was chosen to model cyclic hardening of AA2024-T351. It was assumed that the material properties of AA2024-T3 and AA2024-T351 were the same. Plastic and elastic anisotropy were not considered in the impact simulations. This model led to fairly good prediction of residual stresses for an impact velocity of 34.6 m/s but overestimated the residual stress amplitude for an impact velocity of 66.2 m/s. Predicted stresses for an impact velocity of 53.7 m/s were not validated due to lack of experimental data.

In the current study, simulations were run for the two measured impact velocities of cases A and B. Table 6.2 lists key model parameters. Mesh dimensions in the impacted area were determined from a convergence study (Gariépy *et al.*, 2011). Dimensions for the impacted and representative areas were scaled so as to keep the same number of elements in each region. For each case, four analyses were conducted and the calculated stress profiles $\sigma^{\text{peening}}(z)$ were then averaged to obtain $\bar{\sigma}^{\text{peening}}(z)$ for each case. Material properties were the same as those of Gariépy *et al.* (2011), except for Young's modulus $E = 73.1$ GPa (Matweb, 2011; MIL-5H, 1998). The small difference between tensile and compressive elastic moduli was not considered (MIL-5H, 1998). Each analysis required ≈ 20.5 h and ≈ 15.25 h for cases A and B, respectively, using 8-processor parallelization on an IBM P690 Regatta computer.

In Gariépy *et al.* (2011), an equibiaxial initial stress profile was assumed based on the results of Miao *et al.* (2010), but the authors noted that this hypothesis required further study. In the current work, symmetric non-equibiaxial initial stress profiles $\sigma^{\text{initial}}(z)$ based on experimental measurements were input as an initial condition, as shown in Figure 6.10. The axially-unbalanced initial stress data of Figure 6.8 were used in the impact simulations to avoid making an arbitrary correction (Section 6.5.1). Stress values were linearly interpolated from point to point from the experimental data shown in Figure 6.8. For comparison purposes, four additional impact simulations were run without initial stresses ($\sigma^{\text{initial}}(z) = 0$) for cases A and B.

Table 6.2 Model dimensions used for impact simulations; for more details, see Gariépy *et al.* (2011)

Case	Impact velocity (m/s)	Mesh size in impacted area (mm)	Impacted area		Representative area	
			Elements	mm	Elements	mm
A	33.7	0.015	30×30	0.45×0.45	28×28	0.42×0.42
B	52.1	0.020		0.60×0.60		0.56×0.56

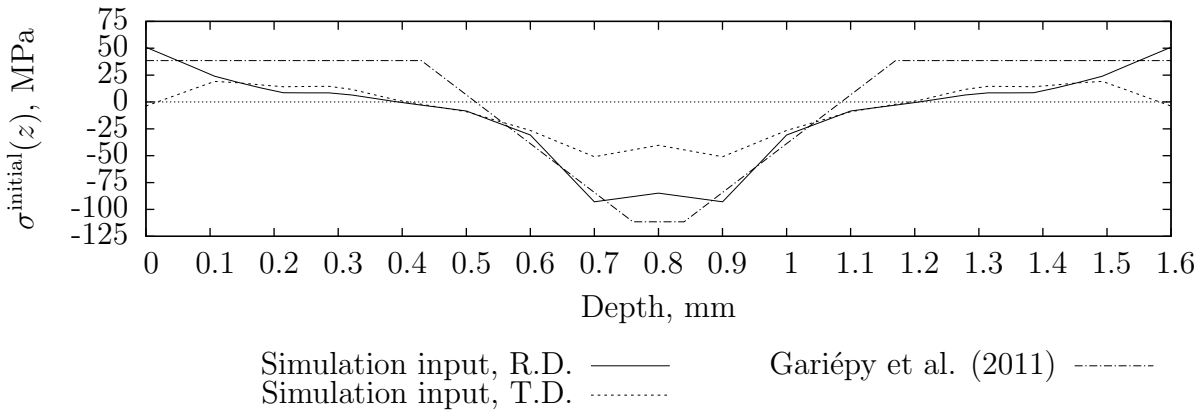

Figure 6.10 Initial stress profiles along the rolling (R.D.) and transverse (T.D.) directions input in impact and forming simulations. Linear interpolation was used between measured values and symmetry across the thickness was assumed. The assumed equibiaxial stress profile used by Gariépy *et al.* (2011) is also shown for comparison purposes.

6.5.3 Forming simulations

Gariépy *et al.* (2011) suggested a stress-based incremental forming simulation method to model the progressive strip deflection during peen forming observed by Cao *et al.* (1995). Using `ABAQUS Standard`, a shell element-based model was defined and in-plane stress values were input at section points (*i.e.* through the thickness at integration points). This capability was used to input into shell elements the induced stresses calculated with the impact model.

The modelled treatment was divided into calculation steps. One calculation step was used for each experimental peening pass. An approximate interpolation method was considered to take into account the effect of progressive peening. Based on numerical observations, it was assumed that "near-surface" induced stresses were not affected by initial stresses. Considering that peening affects only a thin layer near the surface, it was also assumed that stresses "far away from the surface" were not changed during peening when constraining forces and moments prevent balancing to reach equilibrium. This approach was similar to the hypothesis by Cao *et al.* (1995) in their analytical model. Gariépy *et al.* (2011) defined "near-surface" and "far away from the surface" based on the calculated stress profiles and determined interpolation functions S_p. As illustrated in Figure 6.11, a simple interpolation equation was proposed to calculate the new stresses $\sigma_x^{\text{unbalanced}}(p,n)$ at the beginning of each step n from the stresses induced by peening $\sigma_x^{\text{peening}}(p,n)$ at step n and balanced stresses

$\sigma_x^{\text{residual}}(p, n-1)$ from step $(n-1)$ at each section point:

$$\sigma_x^{\text{unbalanced}}(p, n) = S_p(p) \times \sigma_x^{\text{peening}}(p, n) + (1 - S_p(p)) \times \sigma_x^{\text{residual}}(p, n-1) \tag{6.12}$$

where p is the section point number and x subscripts refer to the stress direction; the same equation was used in the Y direction. The stresses induced by peening $\sigma_x^{\text{peening}}(p, n)$ for step n were extracted from the impact simulations for an effective impact density of $n \times 3.65$ mg/mm^2. For section points unaffected by peening, stress values remained unchanged. Shear stresses were not changed from one step to the next.

This approach allowed incremental peen forming to be modelled in a computationally-efficient manner since multiple costly impact simulations with variable initial stress states were not required. Impact analyses were run only with the initial stress profiles for a large number of impacts. The induced stress state was determined after each impact on the model. The stress profiles generated by peening $\sigma^{\text{peening}}(p)$ were therefore known throughout the peening treatment before forming simulations were conducted. Forming simulations then retrieved the stress profiles generated by peening corresponding to a given impact density $\sigma^{\text{peening}}(p, n)$ at each step n, for use in Eq. (6.12).

In the current study, the method was extended to include elastic orthotropic effects as well as non-equibiaxial initial stresses. Analyses were run as presented in Figure 6.12. First, dynamic impact simulations were run as described in Section 6.5.2. At the beginning of the first forming step, the non-equibiaxial initial rolling stresses presented in Figure 6.10 and the stresses corresponding to the first peening pass were introduced at the shell elements section points. Boundary conditions representing the Almen holder (Figure 6.2(a)) were applied. `ABAQUS Standard` was used to calculate the deformed shape and the balanced residual stress profiles in each element. At the beginning of step 2, the deformed geometry obtained in step 1 was imported and the new stress state in each element was calculated with Eq. (6.12) from the known residual stresses $\sigma^{\text{residual}}(p, 1)$ and the induced stresses calculated with the impact model for two passes $\sigma^{\text{peening}}(p, 2)$. Identical $S_p(p)$ functions were considered along both the rolling and transverse directions in Eq. (6.12) and their values were the same as those in Gariépy *et al.* (2011). Using the Almen holder boundary conditions, the new deformed shape and residual stress state were then calculated. This process was repeated until the desired number of peening passes N was reached. An additional step was introduced to remove the Almen holder constraints and calculate the free deformed shape. Arc heights corresponding to various numbers of passes were calculated and the data were used to plot a saturation curve. The numerical saturation points for cases A and B were calculated using Equations (6.1) and (6.2).

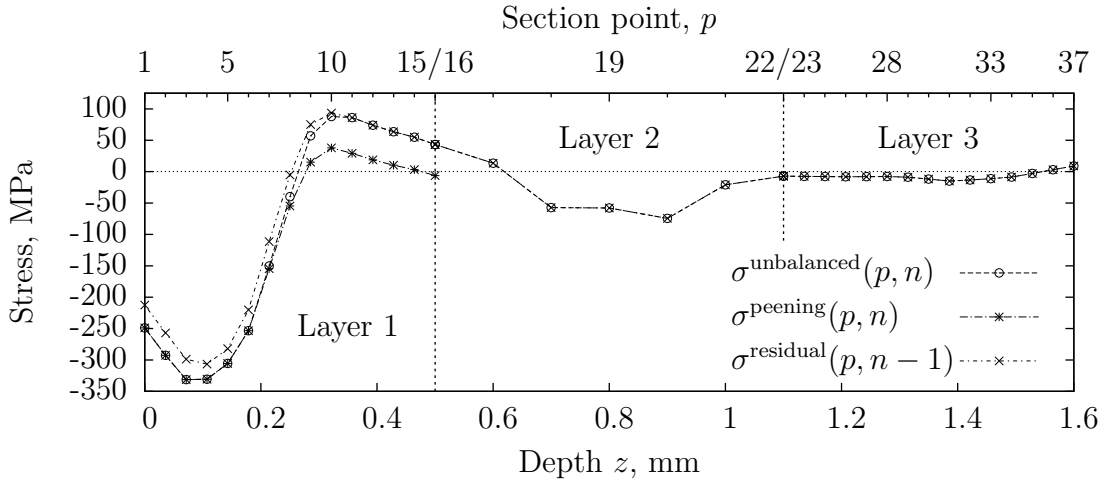

Figure 6.11 Example of unbalanced stress profile evaluation as described by Eq. (6.12) from step $(n-1)$ to step n. The shell elements consist of three layers: two 0.5 mm-thick outer layers and a 0.6 mm-thick inner layer. Section points 15 and 16 and 22 and 23 are coincident.

Forming simulations were run using averaged stress profiles $\bar{\sigma}^{\text{peening}}(z)$ to determine the average forming effect. In addition, scatter of numerical predictions was evaluated by running one forming analysis for each impact simulation. In other words, each forming simulation was based on the individual set of $\sigma^{\text{peening}}(z)$ predicted by a single impact analysis, as shown in Figure 6.12. For each case and the two orientations of the rolling direction, the four analyses led to different arc heights and radii of curvature from which average values and confidence intervals were derived.

In order to document the effects of various parameters on the resulting curvatures, forming simulations were performed as follows:

1. An elastically isotropic material having $E_r = E_t = 73.1$ GPa and $\nu_{rt} = \nu_{tr} = 0.33$, without initial stresses;
2. An elastically isotropic material with the initial stresses $\sigma^{\text{initial}}(z)$ from Figure 6.10;
3. An elastically orthotropic material with the initial stresses from Figure 6.10. Elastic orthotropy was taken into account in the forming simulations with the following parameters: $E_r = 73.1$ GPa, $E_t = E_r/1.05$, $\nu_{rt} = 0.33$ and $\nu_{tr} = \nu_{rt}/1.05$.

Due to the computational cost of the dynamic model, impact simulations were only run using isotropic elasticity and plasticity. It was assumed that small variations of the elastic moduli and Poisson's ratios had a negligible effect on the calculated induced stress profiles $\sigma^{\text{peening}}(p, n)$.

To evaluate the effect of the axial unbalance, additional forming simulations were con-

ducted for an elastically orthotropic material with the corrected initial stress profiles ${}^{\text{asym}}_{\text{bal}}\sigma^{\text{initial}}(z)$ from Figure 6.9 and ${}^{\text{sym}}_{\text{bal}}\sigma^{\text{initial}}(z)$ from Eq. (6.11). Induced stresses calculated with the initial stress profiles $\sigma^{\text{initial}}(z)$ were used as input data: it was assumed that the variation of the initial stress profiles did not significantly affect the calculated stresses $\sigma^{\text{peening}}(p, n)$.

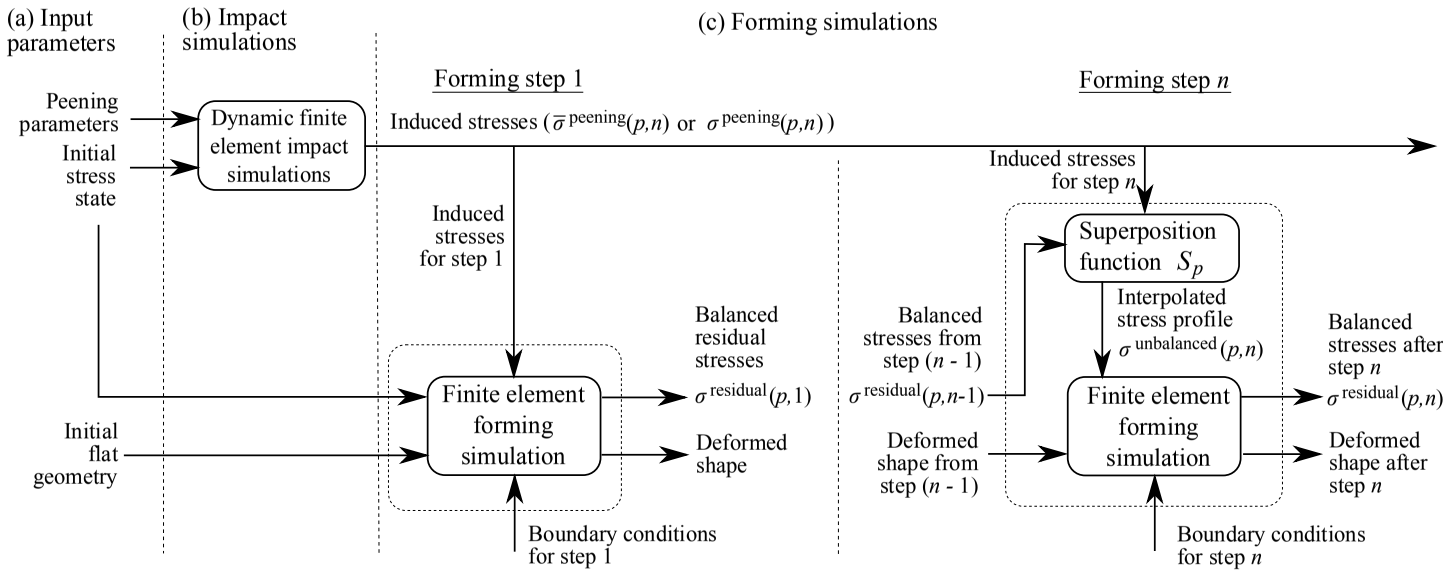

Figure 6.12 Summary of the finite element peen forming simulation method. Input parameters (a) are fed into both impact simulations (b) and forming simulations (c). Impact simulations are run first and calculated stress profiles are then used in forming analyses. Stresses induced by peening are input directly in forming step 1; interpolation with Eq. (6.12) is used to calculate unbalanced stresses for further steps. Boundary conditions corresponding to the Almen holder were maintained throughout the analysis, except for the final step where the free deformed shape was calculated.

6.6 Results and discussion

6.6.1 Experimental results

Arc heights

Figure 6.13 shows the experimental arc height vs. the number of passes curves obtained for cases A and B of the current study, for strips cut along the rolling and transverse directions. As observed by Miao *et al.* (2010), average arc heights tended to be slightly larger for strips cut along the rolling direction. For most data points, differences in average arc heights between strips cut in the rolling and transverse directions were smaller than 3% and were not statistically significant for a confidence level of 95%.

Based on this data, experimental saturation times and arc heights were determined for aluminium strips cut along the rolling and transverse directions of the sheet (Table 6.3). As observed by Miao *et al.* (2010), arc heights at saturation were higher when the rolling direction was aligned with the long side of the strip. The differences were however more significant in Miao *et al.* (2010). It should be noted that each study built the saturation curves with different sets of numbers of passes, which may in part explain this phenomenon.

Radii of curvature

Radii of curvature were determined to provide a more accurate evaluation of the rolling direction orientation effect. Radii were smaller along the rolling direction (*i.e.* curvatures were larger), as shown in Table 6.4. Differences between radii of curvature along X were almost 10%, which is much larger than the $\approx$ 3% variation observed with regards to arc height. Radii along Y were slightly less sensitive to the rolling direction orientation. It should be noted that the large difference between radii along X and Y is due to Almen holder constraints (Cao *et al.*, 1995; Gariépy *et al.*, 2011).

Arc height is a measurement of the "global" behaviour of the peened strip and is influenced by radii along both directions. From the data presented in Table 6.4, it can be seen that radius along X was smaller for a strip cut along the rolling direction than for a strip cut along the transverse direction. On the other hand, radius along Y was larger for a strip cut along the rolling direction than for one cut along the transverse direction. Inputting this data into Eq. (6.6), the contributions of deflections h_X and h_Y along the X and Y directions, respectively, to the total arc height h_{total} were calculated. The Almen gauge dimensions are $L_X = 31.75$ mm and $L_Y = 15.87$ mm (Figure 6.2(a)). Table 6.5 shows that for both cases, h_X is larger for a strip cut along the rolling direction than for a strip cut along the

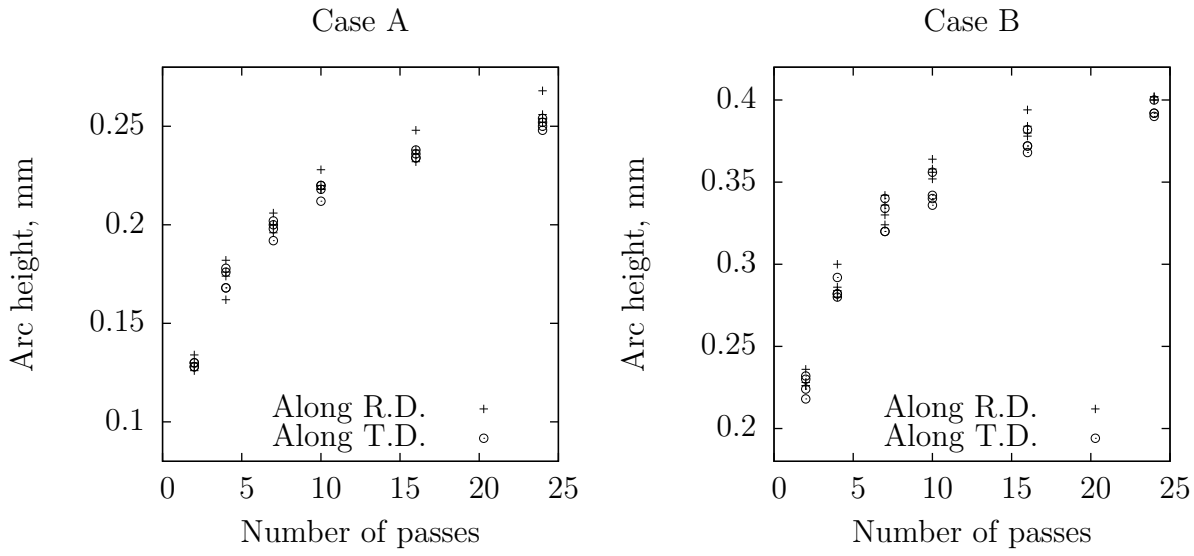

Figure 6.13 Experimental arc heights for strips cut along the rolling (R.D.) and transverse (T.D.) directions. Two sets of peening parameters were considered, as presented in Table 6.1.

transverse direction, that is $h_X^{\text{R.D.}} > h_X^{\text{T.D.}}$. On the other hand, h_Y is smaller for a sample cut along the rolling direction than for one cut along the transverse direction ($h_Y^{\text{R.D.}} < h_X^{\text{R.D.}}$). Since these differences tend to cancel each other, only measuring the maximum deflection at the center of the strip necessarily underestimates the effect of the rolling direction. The differences between the estimated h_{total} and the experimentally measured arc heights can be partly related to the complicated deformed shape resulting from the Almen holder boundary conditions. When considering a square plate with $L_X = L_Y = L$, Eq. (6.6) becomes:

$$h_{\text{total}} = \frac{L^2}{8R_X} + \frac{L^2}{8R_Y} \tag{6.13a}$$

$$= L^2 \left(\frac{R_X + R_Y}{8\ R_X\ R_Y} \right) \tag{6.13b}$$

Measuring only the maximum total deflection on a square surface hides the effect of the rolling direction orientation.

Table 6.3 Comparison of experimental saturation results for AA2024-T3 strips with numerically predicted values when both initial stresses and elastic orthotropy are taken into account.

a) Saturation times (numbers of passes)

	Case A		Case B	
Direction of strip	R.D. along X	T.D. along X	R.D. along X	T.D. along X
Experimental, current study	10.8	10.3	8.3	8.0
Experimental, Miao *et al.* (2010)	9.5	9.9	6.8	6.7
Predicted, current study	10.8	10.8	7.6	7.4
Difference with experimental (%)				
From current study	0.0	+4.9	-8.4	-7.5
From Miao *et al.* (2010)	+13.7	+9.1	+11.8	+10.5

b) Arc heights at saturation (mm)

	Case A		Case B	
Direction of strip	R.D. along X	T.D. along X	R.D. along X	T.D. along X
Experimental, current study	0.226	0.221	0.349	0.339
Experimental, Miao *et al.* (2010)	0.224	0.209	0.321	0.308
Predicted, current study	0.230	0.220	0.303	0.298
Difference with experimental (%)				
From current study	+1.8	-0.5	-13.2	-12.1
From Miao *et al.* (2010)	+2.7	+5.3	-5.6	-3.3

Table 6.4 Comparison of experimental and predicted radii of curvature at the center of strips peened up to ten peening passes. Process parameters for each case are presented in Table 6.1.

Case A

Strip orientation	Experimental radii (mm)		Simulated radii (mm)					
			1. Elastic isotropy No initial stresses		2. Initial stresses only		3. Initial stresses Elastic orthotropy	
	R_X^{exp}	R_Y^{exp}	R_X^{FE}	R_Y^{FE}	R_X^{FE}	R_Y^{FE}	R_X^{FE}	R_Y^{FE}
R.D. along X, average	785	551	845	580	734	561	732	529
N.C.I. 95 % [a]	±24	±21	±33	±11	±14	±22	±14	±20
$(R^{\text{FE}} - R^{\text{exp}})/R^{\text{exp}}$ (%)	-	-	+7.6	+5.3	-6.5	+1.9	-6.8	-3.9
T.D. along X. average	866	511	843	578	837	485	802	491
N.C.I. 95 % [a]	±21	±10	±20	±17	±31	±10	±30	±10
$(R^{\text{FE}} - R^{\text{exp}})/R^{\text{exp}}$ (%)	-	-	-2.6	+13.2	-3.4	-5.0	-7.3	-3.8
Difference between R.D along X vs T.D. along X (%)	9.8	7.5	0.2	0.2	13.1	14.5	9.2	7.4

Continued on next page

[a] Normalized confidence interval from four values with level of confidence of 95%, assuming a normal distribution.

Table 6.4 Comparison of experimental and predicted radii of curvature at the center of strips peened up to ten peening passes. Process parameters for each case are presented in Table 6.1. (*Continued from previous page*)

Case B

Strip orientation	Experimental radii (mm)		Simulated radii (mm)					
			1. Elastic isotropy No initial stresses		2. Initial stresses only		3. Initial stresses Elastic orthotropy	
	$R_X^{\exp}$	$R_Y^{\exp}$	R_X^{FE}	R_Y^{FE}	R_X^{FE}	R_Y^{FE}	R_X^{FE}	R_Y^{FE}
R.D. along X, average	518	285	595	366	540	345	538	326
N.C.I. 95 % [a]	±13	±9	±13	±7	±11	±1	±11	±1
$(R^{\mathrm{FE}} - R^{\exp})/R^{\exp}$ (%)	-	-	+14.8	+28.8	+4.2	+21.1	+3.8	+14.7
T.D. along X, average	569	274	590	370	567	322	545	326
N.C.I. 95 % [a]	±13	±20	±12	±10	±7	±9	±7	±9
$(R^{\mathrm{FE}} - R^{\exp})/R^{\exp}$ (%)	-	-	+3.8	+35.0	-0.3	+17.7	-4.2	+19.1
Difference between R.D along X vs T.D. along X (%)	9.3	3.8	0.8	0.9	4.9	6.6	1.3	0.0

[a] Normalized confidence interval from four values with level of confidence of 95%, assuming a normal distribution.

Table 6.5 Estimated deflections for strips cut along the rolling (R.D.) and transverse (T.D.) directions and peened up to ten passes, based on Eq. (6.6) and the experimental radii of curvature from Table 6.4.

	Case A		Case B	
Direction of strip	R.D. along X	T.D. along X	R.D. along X	T.D. along X
h_X (mm)	0.1605	0.1456	0.2433	0.2216
$h_X^{\text{R.D.}} - h_X^{\text{T.D.}}$	0.0150		0.0217	
h_Y (mm)	0.0572	0.0616	0.1106	0.1149
$h_Y^{\text{R.D.}} - h_Y^{\text{T.D.}}$	-0.0044		-0.0043	
h_{total} (mm)	0.2177	0.2072	0.3539	0.3365
Average experimental arc height (mm)	0.221	0.218	0.3575	0.3435

6.6.2 Numerical results

Arc heights

Figure 6.14 presents the numerically calculated saturation curves considering both initial stresses and elastic orthotropy. Simulations correctly predicted the larger arc heights for strips cut along the rolling direction. Differences of calculated average arc heights depending on the rolling direction orientation were approximately 5% and 1.5% for cases A and B, respectively. In most cases, these differences were not statistically significant considering the scatter observed in Figure 6.15. The scatter of simulation results was larger than the experimental scatter for low numbers of passes and decreased for higher numbers of passes. This may be related to the limited number of simulated impacts (≈ 3 per pass for case A, ≈ 5 for case B) on the modelled impacted region with an area less than 1 mm^2 (Table 6.2), when compared to the 1450 mm^2 area of the experimental samples. Although only four experiments and analyses were made, Figure 6.15 suggests that finite element simulations could possibly be used to evaluate peen forming variability in addition to the average shaping effect. Table 6.3 compares the predicted saturation points (when considering both initial stresses and elastic orthotropy) with the experimental results. Agreement between numerical and experimental results was fairly good, especially for case A.

Radii of curvature

The calculated influence of non-equibiaxial initial stresses and elastic orthotropy in terms of radii of curvature is presented in Table 6.4.

Results for an elastically isotropic material without initial stresses show a negligible influence from the model orientation. When averaging four analyses, the impact and forming models can therefore correctly predict the equibiaxial stress field after shot peening leading to curvatures independent from the orientation of the model, expected in this specific situation.

When considering the effect of initial stresses, predicted radii of curvature decreased by 10 to 16% along the rolling direction and by less than 6% along the transverse direction. The effect of initial stresses was more significant along the rolling direction because $|\sigma_r^{\text{initial}}(z)| \gtrsim |\sigma_t^{\text{initial}}(z)|$ for $0 \leq z \leq a$ (Figure 6.16). Based on Eq. (6.10), this leads to a larger variation of the equivalent bending moment M_r than M_t, which in turn results in a larger variation of the radius R_r along the rolling direction than R_t along the transverse direction. The relative difference (in %) of the radii of curvature between strips cut along the rolling and transverse directions was $\approx 14\%$ for case A and much smaller for case B. This behaviour is related to the depth of the calculated stress profiles induced by peening, which was larger for case B due to a higher impact velocity. Figure 6.16 shows that:

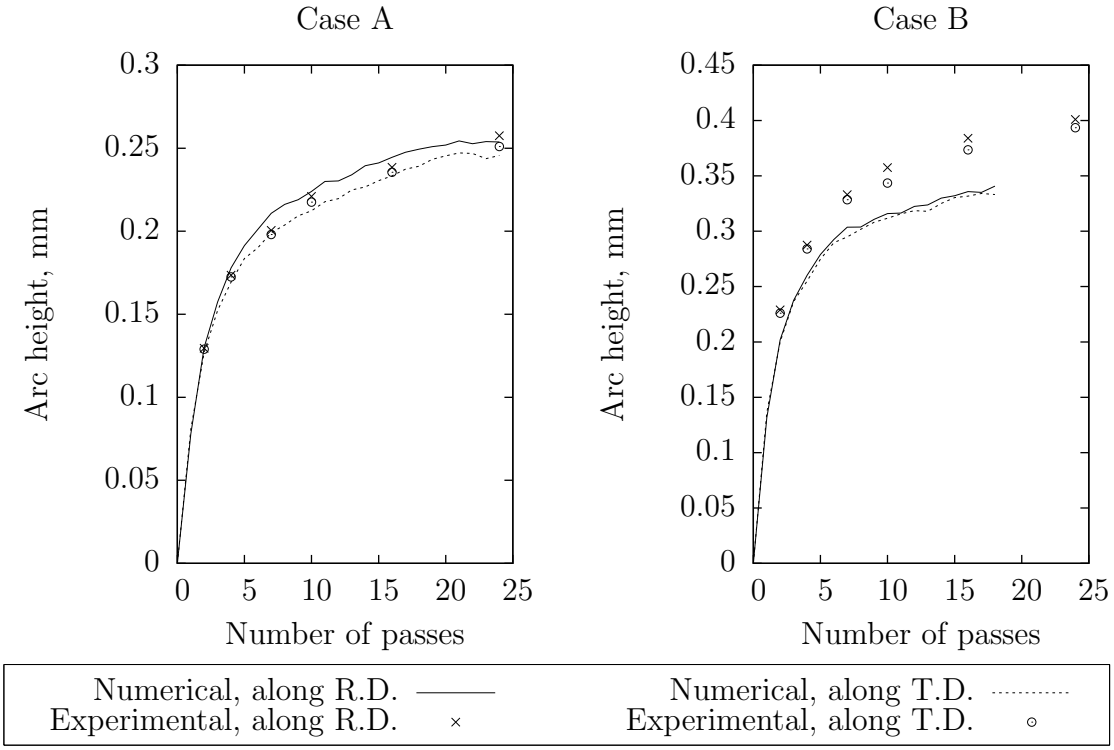

Figure 6.14 Comparison of numerically predicted average saturation curves with averaged experimental data. Both initial stresses and elastic anisotropy were modelled in the simulations.

1. The stress profiles generated by peening $\sigma^{\text{peening}}_{\{r,t\}}(z)$ extend deeper for case B than for case A, $a_A \approx 0.22 < a_B \approx 0.29$;
2. In the first 0.1 mm, $\sigma^{\text{initial}}_r(z) > \sigma^{\text{initial}}_t(z)$. This is the main driving force for the orientation dependence of curvatures;
3. For 0.1 mm $\leq z \leq$ 0.4 mm, $\sigma^{\text{initial}}_r(z) \lesssim \sigma^{\text{initial}}_t(z)$.

When comparing strips cut along the rolling and transverse directions, including elastic orthotropy partly counterbalances the effect of initial stresses by decreasing the radii (*i.e.* increasing the curvature) along the transverse direction since $E_t < E_r = E$, as explained in Section 6.4.2. Simulation results indicate that the combined effect of initial stresses and elastic anisotropy could explain the experimental observations for case A but not for case B. Plastic anisotropy may be a more significant factor for higher impact energy and should be studied further.

Table 6.6 presents predicted average radii of curvature for an elastically orthotropic material with different initial stress profiles. It can be seen that the initial stress state can have

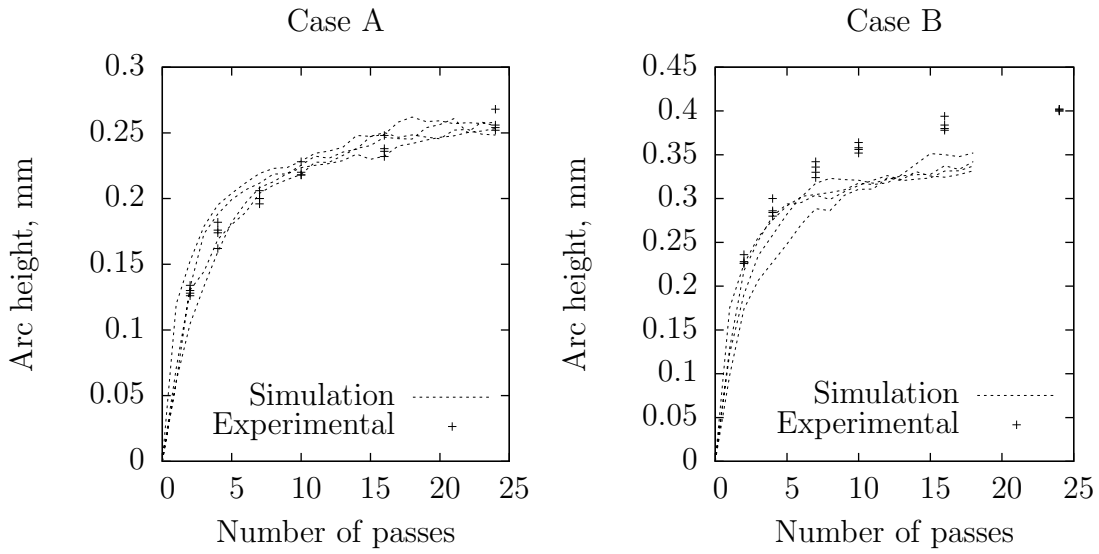

Figure 6.15 Comparison of experimental and predicted arc height scatter for both cases and for a strip cut along the rolling direction. Similar values were calculated for strips cut along the transverse direction.

a significant influence on the calculated curvatures and that the results for the $\sigma^{\text{initial}}(z)$ in Figure 6.10 lie between those for the asymmetric and symmetric balanced stress profiles. This can be attributed to a combination of the initial axial unbalance and the boundary conditions which allow stress redistribution throughout the analyses to establish axial equilibrium (especially along direction Y). Forming simulations performed with the symmetric balanced initial stress profiles ${}^{\text{sym}}_{\text{bal}}\sigma^{\text{initial}}(z)$ from Eq. (6.11) resulted in a decrease of the calculated radii of curvature. Based on Eq. (6.10), this is the expected behaviour since ${}^{\text{sym}}_{\text{bal}}\sigma^{\text{initial}}(z) > \sigma^{\text{initial}}(z)$ for $0 \leq z \leq a$ thus increasing the equivalent bending moments. The variations increased the effect of initial stresses on the development of non-uniform curvatures. Future studies should consider through-thickness stress measurements and more closely spaced measurements near the surface in order to determine the initial stress profile more accurately.

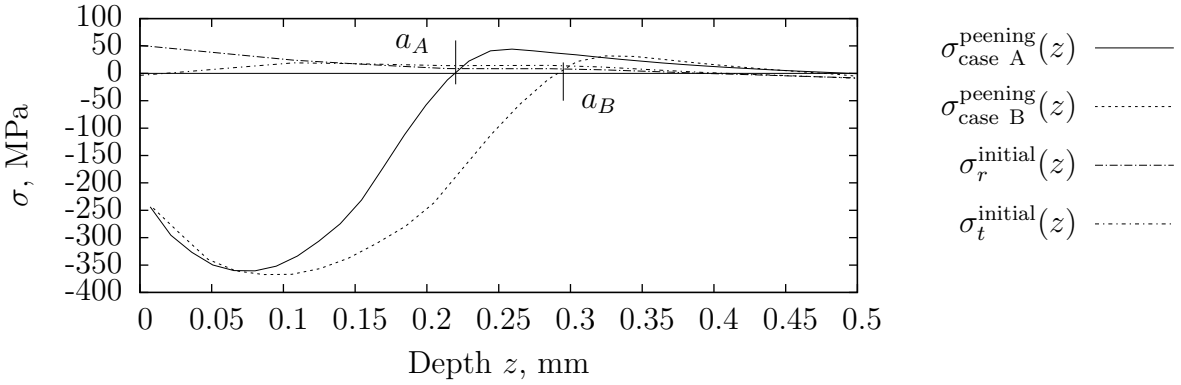

Figure 6.16 Comparison of the stress profiles induced by peening up to ten passes on a constrained component for cases A and B. Initial stress profiles are those from Figure 6.10. For each case, $\sigma^{\text{peening}}(z) = \sigma_r^{\text{peening}}(z, 10) \approx \sigma_t^{\text{peening}}(z, 10)$. a_A and a_B are the affected depths for cases A and B, respectively. As expected, a greater impact velocity produced a deeper affected layer (Miao *et al.*, 2010).

Table 6.6 Predicted average radii of curvature after peening up to ten passes for different initial stress profiles and an elastically orthrotropic material. Radii in mm.

Initial stress profiles	Case A				Case B			
	R.D. along X		T.D. along X		R.D. along X		T.D. along X	
	R_X^{FE}	R_Y^{FE}	R_X^{FE}	R_Y^{FE}	R_X^{FE}	R_Y^{FE}	R_X^{FE}	R_Y^{FE}
(a) Asymmetric balanced (Figure 6.9)	741	544	807	518	545	335	550	343
Difference vs. (b) (%)	+1.3	+2.8	+0.7	+5.4	+1.3	+2.6	+0.9	+5.1
(b) Symmetric unbalanced (Figure 6.10)	732	529	802	491	538	326	545	326
(c) Symmetric balanced (Eq. (6.11))	678	521	777	471	509	324	534	319
Difference vs. (b) (%)	-7.3	-1.5	-3.2	-4.1	-5.3	-0.7	-2.1	-2.4

6.6.3 Summary

Experimental results presented in Table 6.4 and Figure 6.13 show that:

1. Radii of curvature varied by as much as 10% depending on the orientation of the rolling direction with respect to the samples. This difference was statistically significant for three of the four profiles under study;
2. Radii along the rolling direction were systematically smaller than radii along the transverse direction. This observation is contrary to that of Kulkarni *et al.* (1981), who noted larger radii along the rolling direction when compared to the transverse direction in rectangular 4.6 mm-thick AA2024-T3 sheet. Sample size and boundary conditions were however different in their experiments;
3. Because of its "global" nature, arc height measurement underestimates the effect of rolling direction orientation. Radii of curvature are therefore a more suitable way to evaluate the shaping effect of peen forming.

Comparison of the experimental and finite element simulation results presented in Table 6.4 leads to the following observations:

1. Three different modelling parameters were studied:
   - An isotropic material without initial stresses;
   - An isotropic material with initial stresses;
   - An elastically orthotropic material with initial stresses.

   For case A, all three models led to predicted radii of curvature generally within 10% of the experimentally determined values. However, simulations conducted for an isotropic material without initial stresses did not capture the significant effect of the rolling direction orientation. Accuracy of the analyses was not as good for case B, especially along the short side of the strip. It should however be noted that experimentally determined residual stress profiles were not available to validate the calculated stress profiles induced by peening for case B;
2. For case A, modelling the combined effect of initial stresses and elastic anisotropy led to quantitatively good predictions of the radii of curvature. When comparing strips cut along the rolling and transverse directions, considering only the initial stresses overestimated the effect of the rolling direction orientation; adding elastic orthotropy partly cancelled the influence of initial stresses and correctly captured the effect of the rolling direction orientation. For this case, it may not be necessary to consider the effect of plastic anisotropy.
3. For case B, the effect of initial stresses on the predicted radii of curvature was much smaller. In addition, elastic orthotropy counteracted the influence of initial stresses and

reduced the predicted differences between strips cut along the rolling and transverse directions to almost zero. For this case, it would be necessary to consider plastic anisotropy in order to achieve accurate predictions.

4. For the cases studied here, the relative influence of material elastic orthotropy and initial stresses seems to be dependent on the peening parameters. Conclusions drawn from a specific case may therefore not be valid in all circumstances.

6.7 Conclusions

The main conclusions of this study are as follows:

1. Finite element simulations indicate that, in addition to material plastic anisotropy, elastic orthotropy and initial stresses can have a significant influence on curvature development during peen forming;
2. For the two cases studied, numerical simulations suggest that the initial stress state and material elastic orthotropy can explain in part the experimentally observed effect of the orientation of the rolling direction, but not entirely. The effect of rolling direction orientation would therefore arise from elastic and plastic anisotropy as well as initial stresses;
3. Knowledge of the material anisotropic elastic and plastic behaviour and of the initial stress state due to manufacturing (rolling, quenching, machining, etc.) could improve the accuracy of peen forming simulations;
4. Since the effects of material elastic and plastic anisotropy and initial stresses seem to be dependent on the peening parameters, it would be difficult to know *a priori* the influence of each factor. A study of all three factors may be required for each combination of target material and peening parameters.

Considering that non-equibiaxial initial stresses and elastic orthotropy can only partly account for variations caused by the orientation of the rolling direction, it seems necessary to consider plastic anisotropy in order to achieve more accurate shot peening and peen forming simulations. Moreover, plastic anisotropy may become a significant factor for actual peen forming applications that involve high energy impacts with larger and heavier shots. Future studies should therefore include plastic and elastic anisotropic effects in both impact and forming simulations and investigate their consequences on the development of curvatures. Since shot peening simulations require cyclic properties and high strain-rate data, the material constitutive theory will however become quite complex. The benefits gained from including an anisotropic yield criterion in impact simulations with respect to the related costs should be

evaluated. Future work could also study process and simulation variability, which were found to be quite significant. Finally, further work is also required to understand the combined effects of sample shape, peening patterns and the orientation of the rolling direction.

Acknowledgments

This research was made possible by a Natural Sciences and Engineering Research Council of Canada (NSERC) scholarship to A. Gariépy. A. Gariépy would also like to thank Rio Tinto Alcan and Fondation de Polytechnique for their financial support through scholarships. The authors would like to thank François Ménard at École Polytechnique de Montréal for his help in surface profile measurements.

CHAPTER 7

ARTICLE 4: ON THE EFFECT OF THE PEENING TRAJECTORY IN SHOT PEEN FORMING

A. Gariépy, S. Larose, C. Perron, P. Bocher, M. Lévesque. Submitted to *Finite Elements in Analysis and Design* on August 7, 2012.

7.1 Abstract

Peen forming is a manufacturing process commonly used in the aerospace industry to shape large and thin panels such as wing and fuselage skins and rocket panels. Due to the large size of the components, this process is generally performed by moving the parts through a peening enclosure or by moving peening equipment following a trajectory on the parts. Previous research on peen forming simulation has rarely considered the influence of the peening pattern on the resulting deformed shape. The purpose of this work was therefore to evaluate experimentally and numerically this effect using small scale tests. A simple model was proposed to simulate incremental deflections as the shot stream traveled over the samples. Model parameters were calibrated experimentally and then applied to a different geometry for validation. Finite element analyses correctly predicted the complex radius distribution arising from the peening path and the constraints applied to the sample during peening.

7.2 Introduction

Peen forming is a versatile manufacturing method that uses shot peening or laser peening to introduce compressive residual stresses at the surface of a component. This upsets the mechanical balance and alters the contour of the part. Large and thin panels like wing skins can be cost-effectively shaped using this process (Baughman, 1984). The forming mechanism can be explained as illustrated in Figure 7.1. Before peening, the component has an initial stress state σ^{initial} that has been imparted by previous manufacturing operations (*e.g.* rolling, heat treating or machining). After peening, unbalanced induced stresses σ^{induced} are generated when the component is perfectly constrained (VanLuchene *et al.*, 1995). Forces F and moments M must be applied to maintain the component in its original flat configuration. Releasing these constraints causes the part to bend and elongate to reach a new equilibrium that corresponds to a balanced residual stress field σ^{residual}. Complex shapes can be achieved in this manner by carefully controlling the peening treatments.

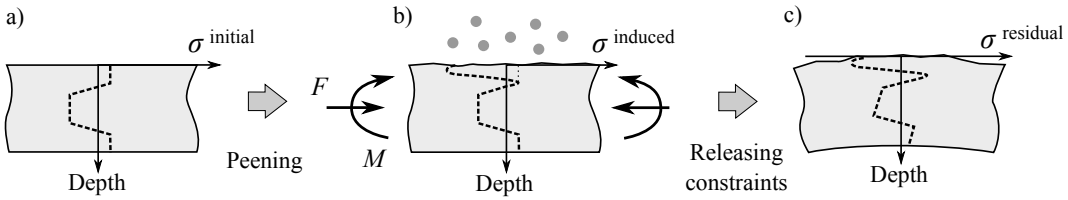

Figure 7.1 Schematic explanation of peen forming. A flat component with an initial stress state σ^{initial} (a) is subjected to shot peening. (b) If the constraining moment M and force F maintain the part in its original configuration, an unbalanced induced stress profile σ^{induced} is generated. (c) Upon releasing the constraints, the part bends and elongates. This leads to a new balanced residual stress state σ^{residual} in the component.

For long and relatively narrow parts such as wing panels, peening treatments often involve moving a part through a fixed peening enclosure (Burmeister, 1984). Peen forming can be achieved with one or more passes of the part through the peening enclosure (Kulkarni *et al.*, 1981; Harburn and Miller, 1982). Similarly, forming of rocket shells is done by controlling the trajectory of peening nozzles over the part (Friese *et al.*, 2002). Complex patterns are often required for tapered and integrally-stiffened components.

The Almen test is used to evaluate the energy, or intensity, of the peening treatments. This test consists of peening SAE 1070 steel strips held in a standardized holder called an Almen holder (Figure 7.2(a)). The Almen arc height of the free strip is then measured with a dedicated instrument, the Almen gauge (Figure 7.2(b)). Multiple strips are peened at different exposure times and a curve relating the Almen arc height to the exposure time of each strip is plotted (Figure 7.2(c)). The saturation point of the treatment is defined as the exposure time t_{sat} for which doubling the exposure time increases the arc height by exactly 10%. The intensity a_h^S is the Almen arc height at the saturation point.

In their study of the Almen test, Cao *et al.* (1995) have shown that peen forming is an incremental process: the part deforms progressively throughout peening. This observation suggests that the deformed shape after peen forming cannot be calculated as a single simulation step from the initial shape to the final state after the peen forming treatments. Instead, multiple incremental steps are required to capture the effect of previous peening on further deformation and predict the response of a component to peen forming.

Three finite element approaches have been suggested to simulate progressive build-up of curvature for uniformly peened parts. First, Grasty and Andrew (1996) used solid elements and applied pressure loads on surface elements to generate in-plane tensile plastic strains similar to those generated by shot peening. Similarly, Wang *et al.* (2006) introduced localized tensile plastic strains near the surface of shell elements by modelling a temperature gradient in constrained elements and then restoring the temperature to its original value. In

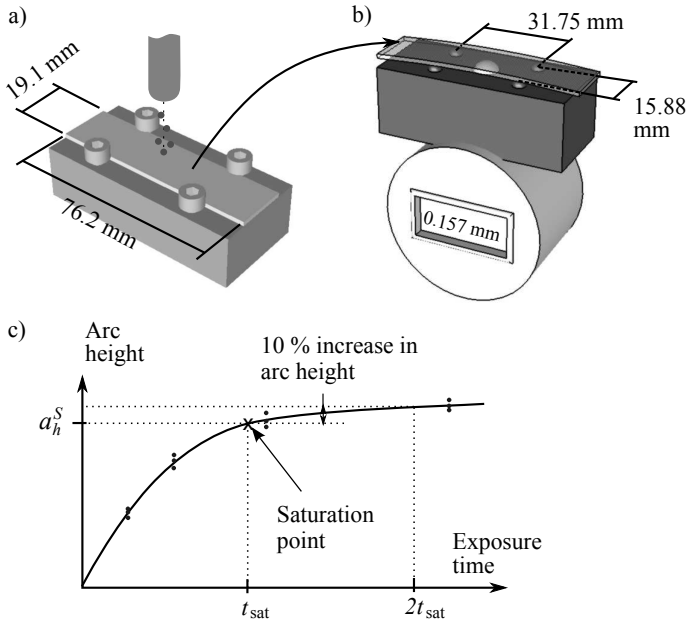

Figure 7.2 Description of the Almen test. (a) A SAE 1070 steel strip is held on an Almen holder and subjected to shot peening for a given exposure time. (b) The strip is removed from the holder and its deflection over a 31.75 mm $\times$15.88 mm area, labelled as the Almen arc height, is measured with an Almen gauge. (c) The saturation curve is plotted by peening multiple strips at different exposure times and is used to determine the saturation point.

the strain-based approaches of Grasty and Andrew (1996) and Wang *et al.* (2006), plastic strains created the unbalanced state leading to bending and elongation. In addition, multiple equivalent loading cycles were applied successively to model the incremental deflection phenomenon. Experimental calibration of the equivalent loads and relationships between peening time and number of loading cycles was required. The third method relies on induced stresses. Gariépy *et al.* (2011) suggested introducing numerically calculated induced stress profiles in shell elements. Based on numerical observations, an approximate method similar to that of Cao *et al.* (1995) and with a physical basis was developed to take into account the incremental build-up of curvature. Since induced stress profiles could be determined by finite element simulations, this stress-based approach required only the calibration of the relationship between peening time and number of loading steps. In the studies by Grasty and Andrew (1996), Wang *et al.* (2006) and Gariépy *et al.* (2011), peening was simulated uniformly on the surface in the model and incremental forming simulations only depended upon the exposure time.

In addition to exposure time, the peening trajectory should be taken into account when simulating a peen forming treatment performed in a single pass. This spatial feature was studied experimentally and numerically by Drouin (2006). Forming was modelled by intro-

ducing unbalanced induced stresses in the model through temperature or thermal expansion coefficient profiles. The trajectory of the peening equipment was simulated by inputting stresses progressively into the model using continuous functions depending on both location and time. The effects of curvature evolution on in-plane displacements and on the evolution of bending stiffnesses were discussed and simulations took into account these geometrical non-linearities. One shortcoming of this study was that the stress profiles considered to model forming had significantly larger amplitudes than experimentally measured values.

In their study of stress peen forming, Miao *et al.* (2010) performed an Almen-like test consisting of peening aluminium alloy (AA) 2024-T3 strips with dimensions 76.2 mm $\times$19.1 mm $\times$1.6 mm held in Almen holders. An "aluminium saturation point" was defined with the same definition as the Almen saturation point. It was also suggested that peening treatments can be considered equivalent if the ratio of the robot travel velocity v_r to the number of peening passes N_p by the robot over the pattern remains constant. Using the setup illustrated in Figure 7.3(a), this hypothesis was experimentally validated by maintaining the same overall exposure time and peening with multiples passes or a single pass. For a constant ratio v_r/N_p, peening with multiple passes at a fast pace or with a single pass at a slower pace yielded similar maximum deflections in the small aluminium strips. However, since peen forming is an incremental process, it is likely that, while the final maximum deflections are almost the same, different peening routes imply different shaping mechanisms, as illustrated in Figure 7.3(b).

The purpose of the present work was to further investigate the spatial dependence in single pass peen forming. The influences of peening trajectory and boundary conditions on the deformed shape were studied. This article is divided into five sections. Section 7.3 presents the experiments considered in the simulations. Section 7.4 summarizes the modelling approach proposed by Gariépy *et al.* (2011) and discusses its extension to the simulation of a single pass treatment. Section 7.5 compares experimental and numerical results. Section 7.6 concludes this work and suggests topics for future studies.

7.3 Experiments

The experiments performed in this work were based on the experimental setup and peening treatments studied by Miao *et al.* (2010). A Baiker air blast peening machine fed Z425 ceramic shots having diameters ranging from 425 to 600 μm (Saint-Gobain, 2003) to a 6 mm diameter nozzle mounted on a Motoman industrial robot. The stand-off distance between the peening nozzle and the test samples was 25 mm and the nozzle was kept perpendicular to the holder surface. Peening was performed in a single pass ($N_p = 1$) following a zig-zag pattern of

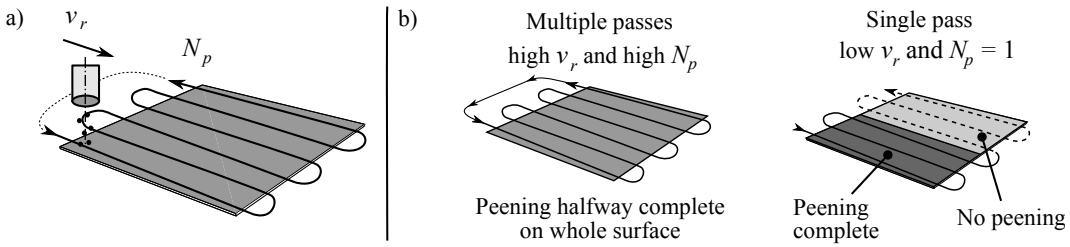

Figure 7.3 Comparison between single pass and multiple passes peening treatments. (a) Schematic view of the experimental setup by Miao *et al.* (2010). Peening nozzle followed a pre-defined zig-zag path over the part with travel velocity v_r. The nozzle ran over the path N_p times, where N_p is defined as the number of passes. (b) Comparison between single pass and multiple passes peening treatments halfway through processing. In the multiple passes treatment, progress depends only upon time and the whole plate has received half of its total exposure time. In the single pass treatment, the peening trajectory adds a spatial dependence and half of the plate is fully peened.

parallel lines with a step-over distance of 6 mm (Figure 7.4). The peening parameters are specified in Table 7.1. According to Miao *et al.* (2010), the corresponding Almen intensity was 0.127 mmA. The robot travel velocity v_r was set to achieve the "aluminium saturation" condition.

The samples were 76.2 mm ×19.1 mm rectangular strips and 76.2 mm ×76.2 mm sheets sheared from a 1.6 mm thick sheet of AA2024-T3. Clamping was applied at opposite ends of the samples, as illustrated in Figure 7.4(a). Miao *et al.* (2010) observed that the orientation of the rolling direction had an effect on deflections of AA2024-T3 strips after peen forming. This effect was taken into account in the present study by varying the orientation of the samples relative to the rolling direction, as shown in Figure 7.5.

The experiments were divided into two stages:

1. Calibration, to first determine an appropriate modelling strategy, using rectangular strips;
2. Validation, to test the modelling approach with a different geometry, using square sheets.

Table 7.1 "Aluminium saturation" peening parameters used in the experimental study of the single pass treatment

Pressure kPa	Mass flow $\dot{m}$ kg/min	Impact angle °	Stand-off distance mm	Step-over mm	Travel velocity v_r mm/s
37.9	0.4	90	25	6	28

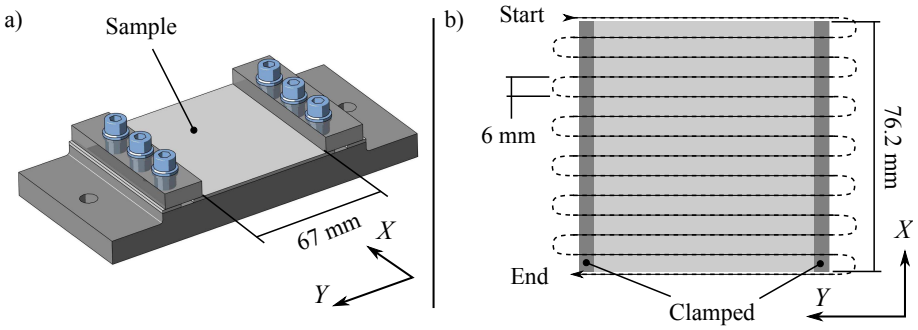

Figure 7.4 (a) Sample holder used in the current study (Miao *et al.*, 2010). When peening rectangular strips, four strips were installed side-by-side. The holder was positioned so that axis X was vertical during shot peening. (b) Schematic showing the peening nozzle trajectory over the 76.2 mm $\times$76.2 mm area of the sample(s). The step-over distance between two adjacent parallel lines was 6 mm.

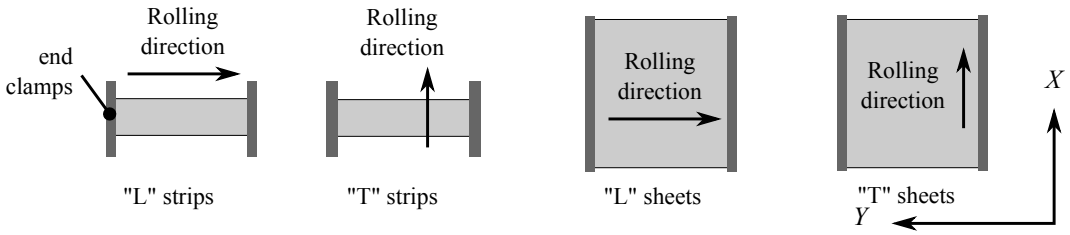

Figure 7.5 Orientation of the longitudinal (L) and transverse (T) samples with respect to the rolling direction and the constraints for the four types of samples used in the current study.

The Almen arc height (Figure 7.2(b)) of the formed strips was used as the measurand for calibrating the numerical simulations. Four longitudinal ("L") strips and four transverse ("T") strips were formed to determine the average shaping effect. Using an Almen gauge, arc heights were measured before and after peen forming for each sample and initial deflections were substracted from the final reading. For each set of four strips, standard deviation of the corrected Almen arc heights was less than 1% of the average value.

Although the arc height is simple and easy to measure, it does not provide detailed information about local curvatures. For this reason, surface contour and radii of curvature of the formed square sheets were considered in the validation experiments. Surface profiles were measured over 65 mm lengths centered on the formed "L" and "T" square sheets along directions X and Y, as presented in Figure 7.6. Measurements were made on the peened surface using a Mitutoyo Formtracer profilometer with a 1 mm diameter spherical tip and a step of 0.02 mm. Two "L" sheets and two "T" sheets were formed and measured. Radii of curvature were fitted through the measured profiles for five adjacent 13 mm segments to evaluate local curvatures, as schematically explained in Figure 7.6. Using shorter segments

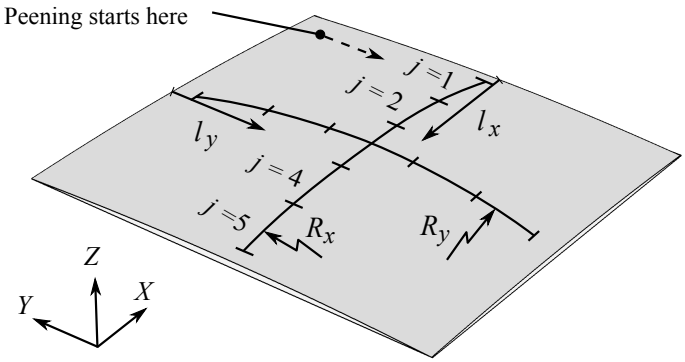

Figure 7.6 Determination of local curvatures on a shaped sheet. The measured surface profiles along directions X and Y at the center of the sheet were divided into five equal segments for which radii of curvature R_x along X and R_y along Y were obtained by fitting circular arc segments. l_x and l_y indicate distances from the starting edge of peening along directions X and Y, respectively.

resulted in scattered radius distributions, possibly due to the roughness of the measured surface.

7.3.1 Input data for simulations

Simulations required physical process parameters as input data. Shot velocities were measured with a ShotMeter$^{\text{TM}}$ system four times during the experiments and the average velocity was 33.7 m/s, with a standard deviation less than 2%. The total density of shot impacts I_D^{total} (by mass) on the target strips and sheets was estimated from:

$$I_D^{\text{total}} = \frac{\frac{L_p \times N_t \times \dot{m}}{v_r \times 60}}{A_{\text{target}}} \tag{7.1}$$

where the effective travel length of the peening robot along the Y direction L_p is 80 mm, the number of peening lines over the width of a rectangular strip N_t is 19.05 mm/6 mm, the mass flow rate $\dot{m}$ is 0.4 kg/min, the robot travel velocity v_r is 28 mm/s, and the target area A_{target} is 76.2×19.05 mm^2 (see Gariépy *et al.* (2011)). The calculated impact density for the treatment being studied was $I_D^{\text{total}} = 41.8$ mg/mm^2. This value was considered in the simulations for both the strips and the square sheets. It should be noted that Eq. (7.1) assumes that the whole surface is peened whereas in the current experiments two ends were covered by clamps over 4.6 mm. This represents a difference of less than 0.7% in terms of calculated impact density.

7.3.2 Shot stream characterization

The distribution of shots in the stream was characterized in order to define an appropriate shot stream model for the simulations. The setup consisted of a Nikon D60 camera, a 105 mm macro lens and a SB-900 flash (for details, see Gariépy *et al.* (2011)). Pictures were taken from the side and therefore showed a projection of the individual shots on the X-Z plane, as illustrated in Figure 7.7(a). Lighting was provided only by a flash: although the exposure time was 1/200 s, the flash duration was approximately 1/38500 s which allowed to "stop" the shots on the image. In addition, the elongated trails caused by the illumination duration provided information on the travel direction of each particle. Shot projections were traced back onto a plane corresponding to the stand-off distance between the nozzle and the peened component, located 25 mm from the nozzle, as shown in Figure 7.7(b). It should be noted that a stream without any interference was characterized; during shot peening, the distribution may be influenced by the interaction of the air flow with the peened surface.

This provided the shot distribution at the stand-off distance as a function of the distance from the peening axis x (Figure 7.7(b)). Assuming symmetry, the distribution was assessed based on the absolute positions $|x|$ using nine 1.0 mm high bins on the cross-section of the stream at the stand-off plane (Figure 7.8(a)). Using a greater number of smaller bins resulted in scattered distributions. The number of shots x_i in each bin i was determined for a sample of 373 shots. Figure 7.9(a) presents the frequency distribution of distances $|x|$ between the peening axis and the positions of the shots on the X-Z plane at the stand-off plane.

Further processing allowed the radial distribution of shots to be estimated. Assuming axisymmetry, the stream was divided into nine 1.0 mm wide concentric rings (Figure 7.8(a)). The number of shots per mm^2 in each ring j was labelled r_j. When the shot stream is viewed from the side, the number of shots observed between $x = h$ and $x = h + 1$ mm is the

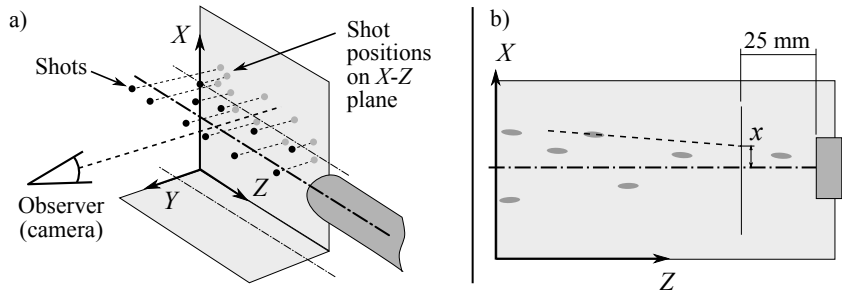

Figure 7.7 (a) High-speed photography pictures show a projection of the stream onto the X-Z plane and provide no information regarding the Y-Z plane. (b) Using shot locations and directions provided by the elongated shapes, shots were traced back to the stand-off plane, 25 mm from the nozzle. Distributions were evaluated at the stand-off distance.

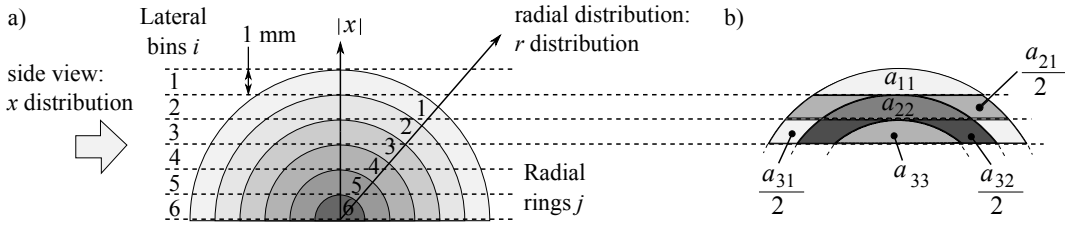

Figure 7.8 (a) Schematic illustration of the assumed axisymmetric cross-section of the shot stream used to determine the lateral shot distribution $|x|$ and the radial shot distribution r at the stand-off distance. In this study, nine 1.0 mm wide bins were used. (b) Definition of the partial cross-sectional areas a_{ij} used in Eq. (7.2).

summation of the contributions from multiple rings j. Partial cross-sectional areas a_{ij} were defined as the area of ring j contained in the lateral bin i, as shown in Figure 7.8(b). The total number of shots x_i observed in each lateral bin i (Figure 7.9(a)) can be related to the number of shots per mm^2 r_j in each ring j as:

$$x_i = \sum_{j=1}^{i} a_{ij} r_j \tag{7.2}$$

Using this relationship, the radial shot density in each ring r_j was evaluated successively starting with the outermost ring $j = 1$. The r_j distribution is presented in Figure 7.9(b). It should be noted that this method is very sensitive to the measurement of the number of shots in the outer lateral bins ($i = 1$) since errors in the shot densities r_j in the outer rings ($j = 1$) propagate in all subsequent calculations of r_j closer to the center (towards $j = 9$).

7.4 Forming simulation method

Section 7.4.1 first summarizes a methodology previously proposed by the current authors to simulate peen forming treatments performed uniformly over a surface. Incremental simulations were only a function of exposure time and this strategy was validated experimentally for peen forming treatments achieved with multiple passes at a fast pace. In Section 7.4.2, this methodology is then improved so as to take into account the effect of the peening trajectory for a treatment involving a single pass at a slow pace. In this case, peen forming is simulated as a function of both exposure time and location.

7.4.1 Spatially uniform forming simulations

In Gariépy *et al.* (2011), the current authors suggested a modelling approach in which unbalanced induced stress profiles were introduced at section points into shell elements. These

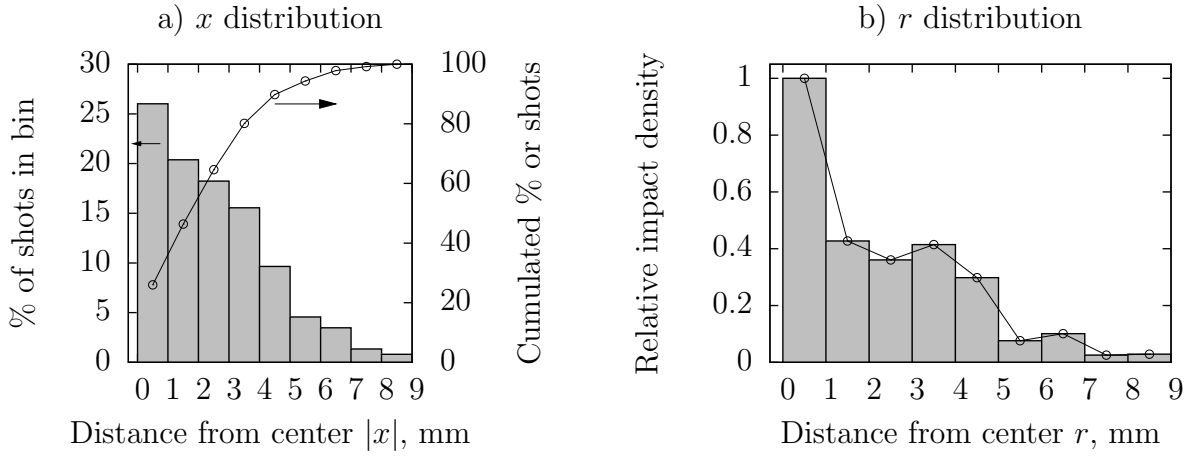

Figure 7.9 Shot distributions, assuming an axisymmetric stream. (a) Percentage of shots in each 1.0 mm high bin and cumulated percentage of shots vs. vertical ($|x|$) distance from the centerline. Total number of shots was 373. (b) Relative shot density vs. radial (X-Y plane) distance from the centerline. Data was normalized to the density in the central ring (in that case, a circle).

induced stress values were calculated using dynamic impact simulations as suggested by Han *et al.* (2002). Springback analyses were run with the commercial finite element code `ABAQUS/Standard` to determine the deformed shapes. Geometrical non-linearities were taken into account in the simulations.

As peen forming is an incremental process, forming treatments were modelled as multiple simulation steps. At the beginning of each step, new unbalanced induced stresses were introduced in the deformed geometry from the previous simulation step, resulting in additional displacements and a new residual stress state (Figure 7.10). Continuous displacements during processing led to stress redistributions to maintain equilibrium. To better understand the mechanics of peen forming, finite element impact analyses were performed with different initial stress profiles and number of impacts. It was observed that near-surface induced stresses were not significantly sensitive to the initial stress profile. In addition, impacts did not markedly alter the initial stress profiles underneath the plastically deformed layer. Miao *et al.* (2011) observed the same phenomenon in their numerical study of stress peen forming using different material constitutive equations. From these findings, Gariépy *et al.* (2011) suggested an approximate method to consider the incremental nature of peen forming. At the beginning of each simulation step n, new unbalanced stresses $\sigma_{\{x,y\}}^{\text{unbalanced}}(p,n)$ in each element were determined from the stresses induced by peening $\sigma_{\{x,y\}}^{\text{peening}}(p,n)$ calculated for this

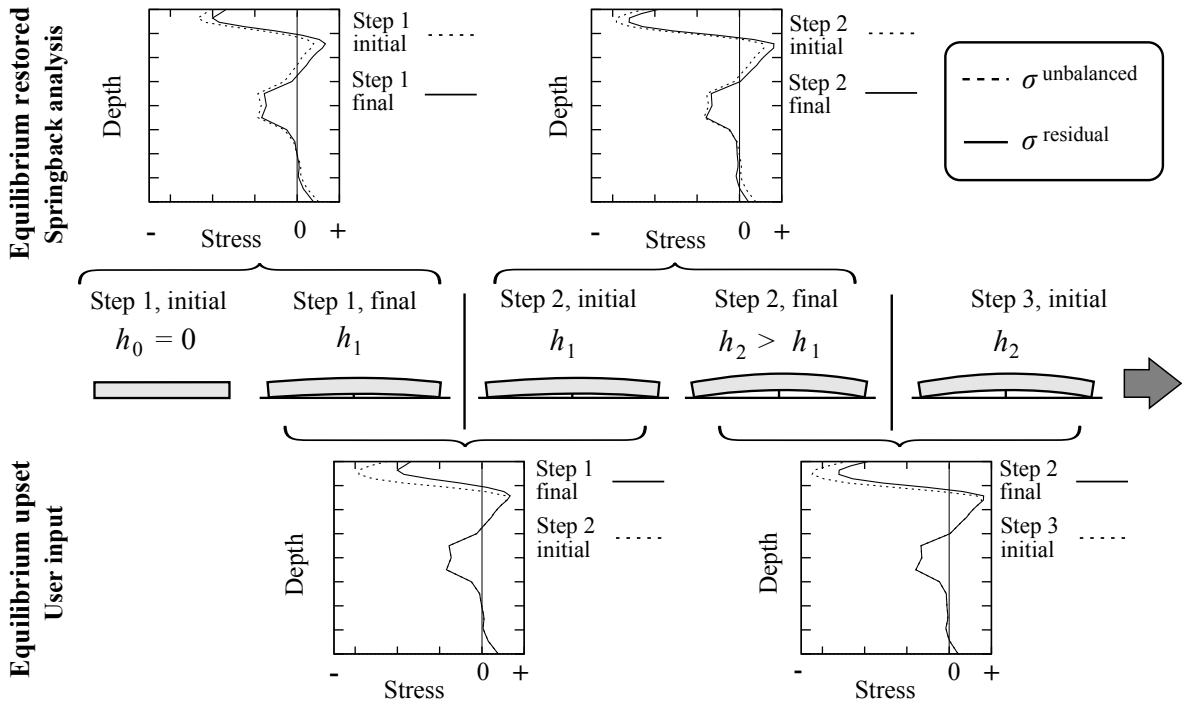

Figure 7.10 Schematic illustration of the incremental forming simulation method. At the beginning of each step, unbalanced stresses $\sigma^{\text{unbalanced}}$ are introduced into the previous geometrical configuration. During each step, a new deformed shape and balanced stress state σ^{residual} are calculated.

step and the residual stress state $\sigma^{\text{residual}}_{\{x,y\}}(p, n-1)$ from the previous step $(n-1)$:

$$\sigma^{\text{unbalanced}}_{\{x,y\}}(p,n) = S_p(p) \times \sigma^{\text{peening}}_{\{x,y\}}(p,n) + (1 - S_p(p)) \times \sigma^{\text{residual}}_{\{x,y\}}(p,n-1) \qquad (7.3)$$

where the x and y subscripts indicate the stress direction and p is the through thickness section point number. Shear stresses σ_{xy} were kept constant from one step to the next. $S_p(p)$ is a simple interpolation function used to connect the stresses induced by peening and the previous residual stresses at each section point (see Gariépy *et al.* (2011)).

The main advantage of this forming simulation method was that impact analyses were performed starting with the initial material state only, which greatly reduced the computational cost. In addition, since the stress state in the model was determined after each individual impact, each dynamic simulation provided a series of induced stress profiles $\sigma^{\text{peening}}(p)$ for different impact densities from zero to the target value. Forming simulations then only extracted the appropriate $\sigma^{\text{peening}}(p,n)$ from the impact analyses results for use in Eq. (7.3).

Peening treatments performed with multiple passes N_p and a low impact density per pass were simulated, which motivated the decision to neglect the influence of the peening pattern. In each step, the same stress profile induced by peening $\sigma^{\text{peening}}(p)$ was introduced

simultaneously in each element of the model using Eq. (7.3). One simulation step was performed for each experimental peening pass and each pass corresponded to an impact density of 3.65 mg/mm^2. The stress profile $\sigma^{\text{peening}}(p, n)$ for each simulation step n was therefore extracted from the impact analyses for an impact density of $n \times 3.65$ mg/mm^2 on the model.

7.4.2 Simulation of single pass treatment

As mentioned in Section 7.2, industrial peen forming applications generally involve moving peening equipment following trajectories, which means that all regions of the component are not simultaneously shot peened. Correspondingly, peen forming experiments described in Section 7.3 were performed with a single pass of the nozzle ($N_p = 1$) distributing a high impact density I_D^{total} over the surface. As peening progressed, some areas were completely peened while others had not been subjected to any peening yet, as illustrated in Figure 7.3(b). In the current work, the methodology presented in Section 7.4.1 was therefore improved to simulate the peening trajectory and its time and position dependencies.

Numerical simulation required the continuous shot stream to be discretized as a number of boxes N_i over its length L along the travel direction (Figure 7.11(a)). The number of boxes N_i is the number of times or increments for which unbalanced stresses have to be introduced at each point of the model in order to simulate the treatment accurately. In practice, N_i has to be calibrated through experimentation. Each peening increment k, with $k = [1, 2, \ldots, N_i]$, corresponded to a specific impact density and stress profile induced by peening. Given a total impacting mass density I_D^{total} on the component, increment k was assigned the profile $\sigma^{\text{peening}}(p, k)$ calculated for an impacting mass density I_k:

$$I_k = k \times \frac{I_D^{\text{total}}}{N_i} \tag{7.4}$$

In the current work, the stress profiles $\sigma^{\text{peening}}(p, k)$ were extracted from the impact simulations performed in Gariépy *et al.* (2012a).

The peening path was also divided into boxes with length (L/N_i) in which unbalanced stresses were introduced at selected simulation steps (Figure 7.11(b)). Since peening is a continuous process, the part deforms progressively as the shot stream advances. The shots projected onto the target at the trailing edge of the stream therefore interact with a component for which the curvature was affected by prior peening. The modelling approach for the shot stream travel is schematically illustrated in Figure 7.11(c). Simulations were run by moving the modelled shot stream following the peening path. Unbalanced stress profiles were introduced N_i times into each box on the peening path, starting with $k = 1$. In other words, stress profiles $\sigma^{\text{peening}}(p, k)$ associated with increments $k = 1, 2, \ldots, N_i$ were input in

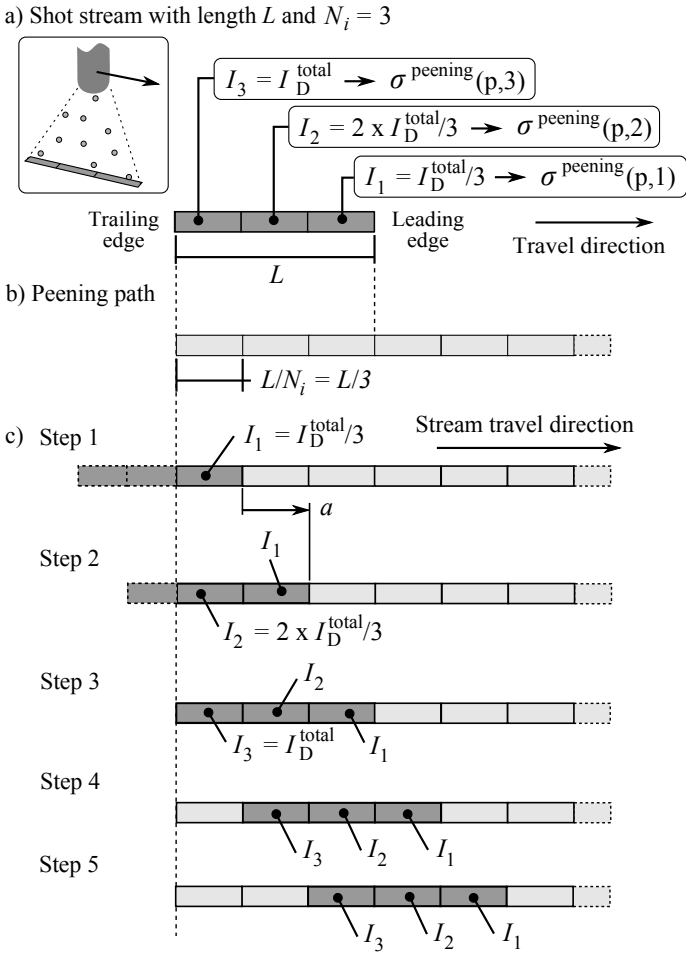

Figure 7.11 (a) A 2D schematic example with $N_i = 3$ increments. Each box and increment k corresponded to an impact density I_k and stress profile induced by peening $\sigma^{\text{peening}}(p, k)$. (b) Division of the peening path into discrete boxes. (c) The simulated shot stream travels following the peening path. In each box, stress profiles $\sigma^{\text{peening}}(p, 1)$, $\sigma^{\text{peening}}(p, 2)$ and $\sigma^{\text{peening}}(p, 3)$ are introduced in successive steps using Eq. (7.5).

successive calculation steps using:

$$\sigma_{\{x,y\}}^{\text{unbalanced}}(p, n) = S_p(p) \times \sigma_{\{x,y\}}^{\text{peening}}(p, k) + (1 - S_p(p)) \times \sigma_{\{x,y\}}^{\text{residual}}(p, n-1) \tag{7.5}$$

where p is the through thickness section point. The difference between Eq. (7.3) and Eq. (7.5) is that Eq. (7.3) was used to introduce the same stress profile generated by peening $\sigma^{\text{peening}}(p, n)$ in all elements at step n whereas, at step n, Eq. (7.5) inputs the appropriate $\sigma_{\{x,y\}}^{\text{peening}}(p, k)$ only in selected elements for which a peening increment k is simulated.

For illustration purposes, assume a shot stream with a number of increments $N_i = 3$. In the first step $n = 1$, the shot stream enters the peening path and the stress profile

$\sigma^{\text{peening}}(p, k = 1)$ corresponding to an impact density $I_1 = I_D^{\text{total}}/3$ is uniformly introduced at section points in the elements within the first box. A first springback analysis is then conducted to restore mechanical balance into the entire component and the residual stress profiles in each element $\sigma^{\text{residual}}_{\{x,y,xy\}}(p, n = 1)$ are calculated. In the second simulation step $n = 2$, the shot stream has traveled a distance $a = L/N_i$. In the first box, the impact density reaches $I_2 = 2 \times I_D^{\text{total}}/3$ and the stress profile generated by peening $\sigma^{\text{peening}}(p, k = 2)$ is inputted in the deformed geometry resulting from the first step. Since the stream has advanced, the second box of the model simultaneously receives an impact density I_1 and the corresponding stresses induced by peening. In each element of the first and second boxes, new unbalanced stresses are calculated with Eq. (7.5) using the appropriate $\sigma^{\text{peening}}_{\{x,y\}}(p, k)$. It is assumed that previous residual stresses in all other elements of the model were not affected by the local peening and remained unchanged until balancing occurred. The second simulation step is completed by running a second springback analysis starting from this new unbalanced stress state. In the third step $n = 3$, the first, second and third boxes reach cumulated impact densities of $I_3 = I_D^{\text{total}}$, I_2 and I_1, respectively. The corresponding stress profiles $\sigma^{\text{peening}}(p, k)$ are introduced in these boxes using Eq. (7.5) and a third springback simulation is performed. In the fourth step $n = 4$, only boxes 2 to 4 are subjected to peening and receive new unbalanced stresses since the modelled shot stream has left box 1. It should be noted that the modelled shot stream enters and leaves the peened surface progressively by varying the number of peened boxes at specific simulation steps, as illustrated in Figure 7.11(c).

Modelled path for peen forming experiments

In the present work, the length L of the peened area was set to 9.525 mm based on the shot distribution in the stream (Figure 7.9) as well as for compatibility with model and mesh dimensions. The length of the modelled stream was kept constant when changing the number of increments: each individual box therefore had a length of $(9.525/N_i)$ mm. The width of the modelled shot stream was set to 6.35 mm in the direction perpendicular to the travel (Figure 7.12(a)). Considering the 6 mm step-over distance between adjacent lines in the experimental peening trajectory (Figure 7.4), this approximated well the progression of peen forming along direction X on the strips and sheets. In addition, it allowed the peening treatment to be simulated as an integer number of peened lines of equal width over the strip and sheet models (Figure 7.12(b) and (c)). It should be noted that, with the simulated peening paths, the modelled stream entered and left the surface at the beginning and the end of each parallel line.

The main shortcoming of this approach is that overlap between adjacent lines was neglected. In the experiments, since the width of the shot stream was larger than the step-over

distance, impacts in a given area occurred as the peening nozzle traveled over several adjacent lines. Consider for instance point A in Figure 7.13(a): shots impacted at this location as the peening nozzle followed lines 2 and 3 (and, to a lesser extent, the subsequent line) so that the total impact density at this point was provided incrementally by multiple peening lines. For simplification, the overlap between experimental peening lines as well as the small variation of the total number of impacts with respect to position along X were neglected in the model. Instead, the impact density $I_D^{\text{total}} = 41.8$ mg/mm^2 was uniformly attributed to non-overlapping 6.35 mm wide peening lines. Each element in the model therefore received the same impact density I_D^{total} as the modelled stream traveled along a single peening line (Figure 7.13(b)). In other words, the experimental and modelled streams led to the same average impact density on the target; however, the accumulation of impacts as a function of time and location was different.

Boundary conditions for peen forming simulations of strips and sheets were as follows:

- All translational and rotational degrees of freedom were blocked for nodes covered by the end clamps. This corresponded to a length of 4.76 mm on each end of the model (Figure 7.12(b) and (c));
- A rigid plane was modelled underneath the deformable shell elements to represent the experimental setup. Contact between the bottom surface of the shell elements and this rigid plane allowed upward displacements but prevented downward displacements (Figure 7.4(a)).

In the last simulation step, constraints corresponding to the end clamps were removed. New boundary conditions preventing only rigid body motion were applied to obtain the free deformed shape.

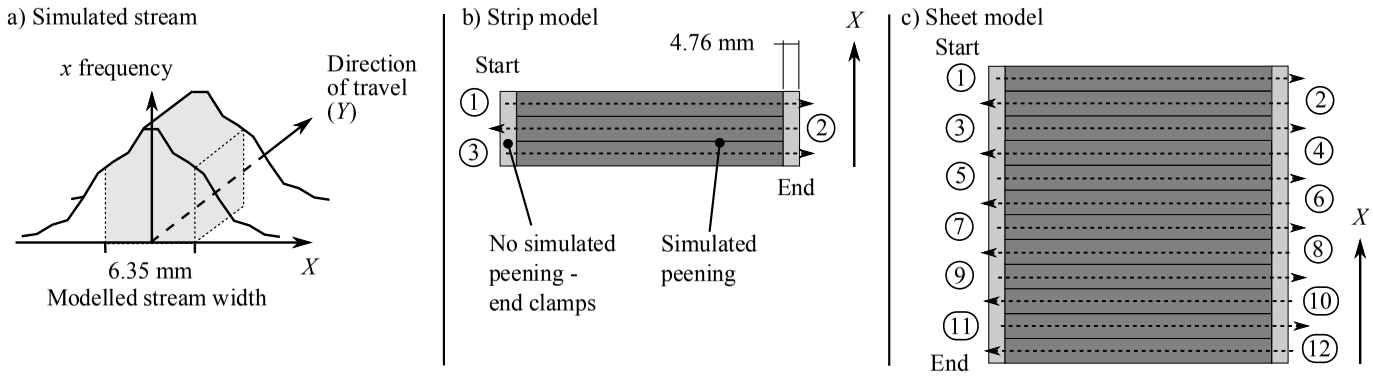

Figure 7.12 (a) Representation of the modelled stream width with respect to the experimentally determined shot distribution (Figure 7.9(a)). (b) and (c) Modelled peening lines over rectangular strips and square sheets. Each simulated peening line was 6.35 mm wide. Peening was simulated only on the center area since the ends were covered by clamps in the corresponding experiments.

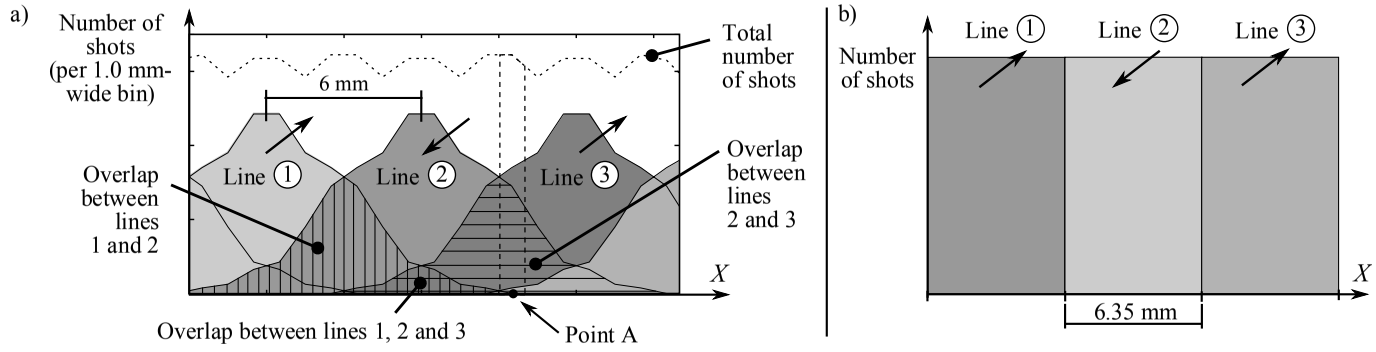

Figure 7.13 (a) In the experiments, the total impact density at a given point was the sum of the contributions from multiple adjacent overlapping peening lines. (b) In the modelled stream, the overlap between experimental peening lines was neglected and the total impact density I_D^{total} was provided during a single peening line.

Numerical calibration using rectangular strips

Numerical calibration of the treatment was performed by varying the number of increments N_i between 1 and 7 for 76.2 mm $\times$19.1 mm strips. As explained in Section 7.3, calibration was conducted based on the Almen arc height of the deformed strips. Simulations were run for both the "L" and "T" strips to account for material anisotropy, as described in Gariépy *et al.* (2012a). The orthotropic elastic properties and non-equibiaxial initial stress state for the 1.6 mm thick AA2024-T3 sheet were:

- $E^{\text{rolling}} = 73.1$ GPa, $E^{\text{transverse}} = E^{\text{rolling}}/1.05$, where E^{rolling} and $E^{\text{transverse}}$ are the elastic moduli along the rolling and transverse directions, respectively;
- $\nu_{rt} = 0.33$, $\nu_{tr} = \nu_{rt}/1.05$, where $\nu_{mn} = -\varepsilon_n/\varepsilon_m$ is the Poisson's ratio when the sheet is uniaxially stressed along direction m;
- Non-equibiaxial initial stresses, as illustrated in Figure 7.14.

Figure 7.15 shows that the calculated arc heights increased concomitantly with increasing number of increments N_i. A behaviour similar to the saturation curve (Figure 7.2(c)) was observed: the effect of increasing the number of increments became less significant as the number of increments increased. A larger N_i also required more steps to complete the treatment. Since the modelled shot stream advanced by $a = (9.525/N_i)$ mm at each simulation step, increasing N_i reduced the advance length a which in turn involved more steps to travel the fixed length of the peening trajectory.

Simulations correctly predicted the smaller arc heights of "T" strips when compared to "L" strips. However, the difference in terms of calculated arc heights between "L" and "T" strips was overestimated in the analyses when compared to the experimental results (Figure 7.15). A number of increments $N_i = 6$ was selected to model the peening treatment since this value led to the best compromise for predicting the deflections for both types of strips (Table 7.2).

The evolution of the stress profiles induced by peening $\sigma^{\text{peening}}(p, k)$ as a function of k for $N_i = 6$ and $I_D^{\text{total}} = 41.8$ mg/mm^2 is presented in Figure 7.16(a). For the first increment ($k = 1$), average induced stresses had a lower magnitude than those of subsequent increments.

Table 7.2 Relative differences between numerically predicted deflections for varying numbers of increments N_i and experimentally measured values for rectangular strips.

Strip Orientation	Experimental arc height mm	Difference between predicted deflection and experimental values for different N_i, %						
		1	2	3	4	5	6	7
"L" strips	0.240	−29.3	−10.6	−3.9	−1.0	+0.7	+1.9	+2.6
"T" strips	0.237	−32.4	−13.8	−7.5	−4.3	−2.7	−1.9	−1.1

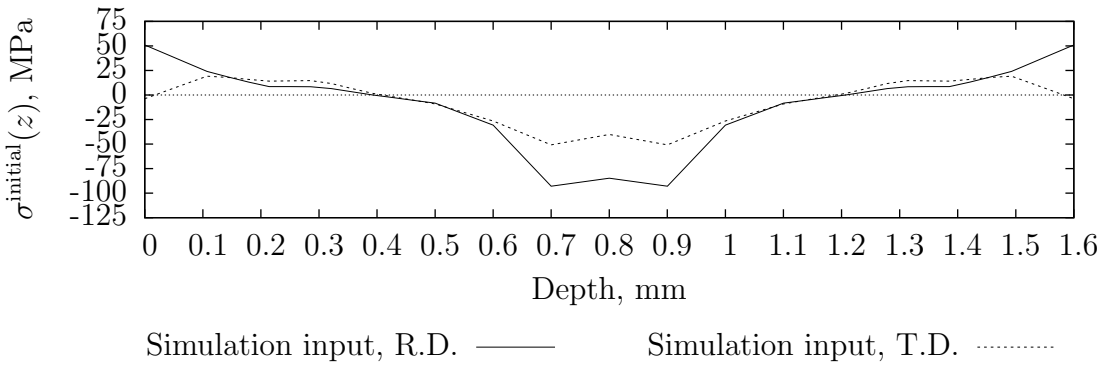

Figure 7.14 Initial stress profiles along the rolling (R.D.) and transverse (T.D.) directions in 1.6 mm thick AA2024-T3 used in impact and forming simulations (Gariépy *et al.*, 2012a).

As k increased from 1 to $N_i = 6$, the induced stress profile amplitude tended to stabilize. The depth subjected to compressive induced stresses did not increase significantly as k increased. Figure 7.16(b) shows that for a low impact density I_1 the calculated stress profiles generated by peening depended on the non-equibiaxial initial stress state. The higher as-received surface stress along the rolling direction (Figure 7.14) led to a higher surface induced stress along this direction when compared to the transverse direction. This result shows that near-surface induced stresses depend upon the previous stress field for very low impact densities ($k = 1$) and that the hypothesis upon which Equations (7.3) and (7.5) rely is not accurate in this case. As the impact density increased ($k > 1$), the differences between the stress profiles induced by peening $\sigma^{\text{peening}}_{\text{rolling}}(p,k)$ and $\sigma^{\text{peening}}_{\text{transverse}}(p,k)$ decreased to less than 10 MPa (Figure 7.16(c)).

The $S_p(p)$ of Eq. (7.5) was derived from the induced stress profiles illustrated in Figure 7.16 for the specific element definition using the criteria defined by Gariépy *et al.* (2011). Its values are given in Table 7.3 and were identical along directions X and Y and for all increments k.

With the calibrated $N_i = 6$, forming analyses required 142 calculation steps and approximately 2 hours using 4-processor parallelization on a desktop computer equipped with an Intel i7-920 CPU, 3.0 GB RAM and a 7200 rpm HDD.

Table 7.3 $S_p(p)$ function used in Eq. (7.5)

	Section point p					
	1 to 4	5	6	7	8	9 to 15
$S_p(p)$	1.0	0.9	0.7	0.3	0.1	0

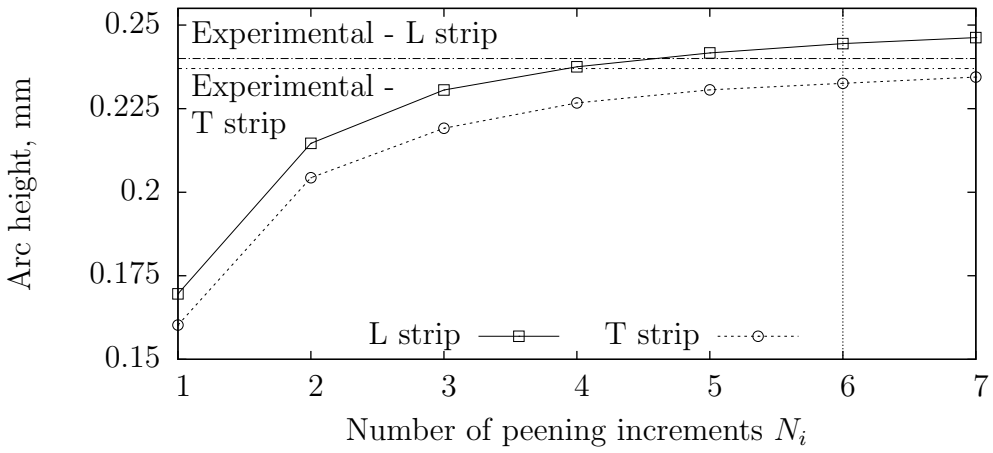

Figure 7.15 Effect of the number of peening increments on the calculated arc heights for rectangular strips.

Validation with square sheets

Peen forming of 76.2 mm ×76.2 mm AA2024-T3 sheets with equivalent boundary conditions was then simulated using the same methodology with $N_i = 6$. To evaluate the forming effect more accurately, radii of curvature were determined by fitting circular arc segments through the calculated contours. Local radii were obtained for five adjacent 13 mm segments along directions X and Y of the model, as well as for the experimental results (see Figure 7.6). Forming simulations had 565 steps and required approximately 17 hours on the computer described in Section 7.4.2.

All forming analyses took geometrical non-linearities into account by updating the stiffness matrix of the model as the strip or sheet deformed. In order to investigate the possible influence of this geometrical effect, some geometrically linear simulations were also run. In this case, the stiffness matrix used in the calculations was that of a flat sheet. It should however be noted that contact between the sheet and the rigid support was also modelled in the geometrically linear analyses: boundary non-linearities were therefore still present.

7.5 Results and discussion

7.5.1 Experimental results

Local radii of curvature determined from the measured surface profiles were not uniform over the sheets, as shown in Figure 7.17. Three different phenomena can be observed:

1. For a given direction X or Y on the sheets, radii of curvature were smaller along the

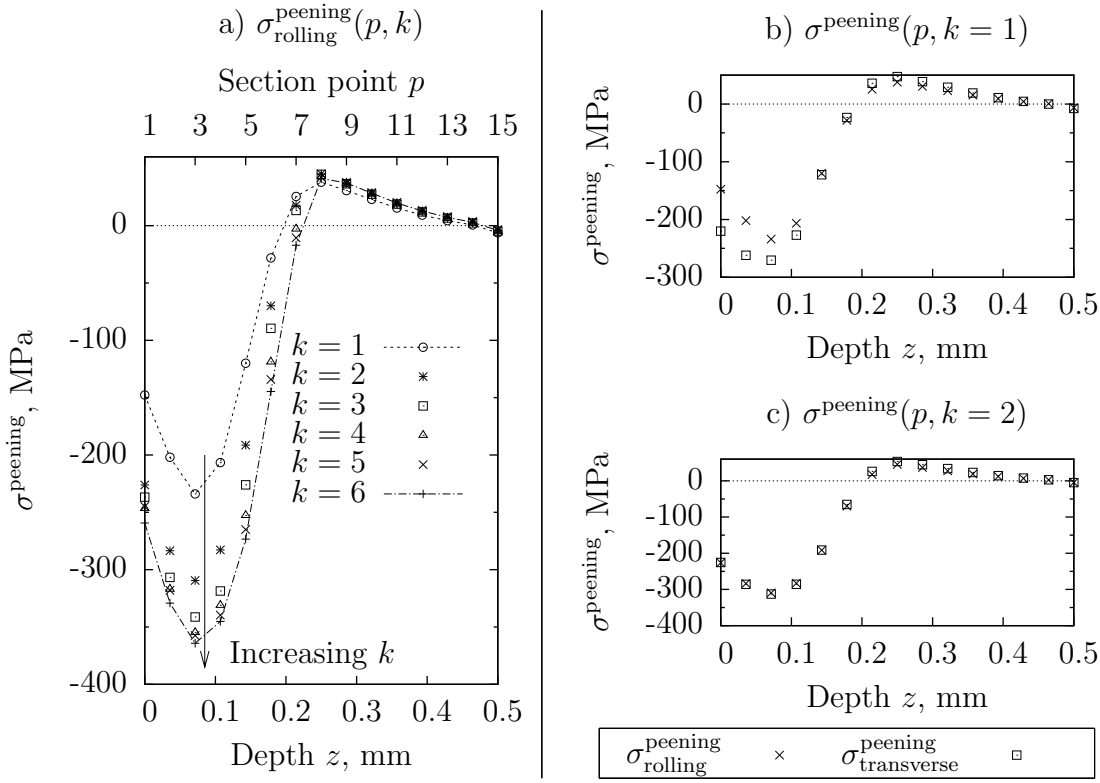

Figure 7.16 (a) Calculated stresses induced by peening σ^{peening} along the rolling direction used in forming simulations with $N_i = 6$. (b) For the first increment $k = 1$, the average induced stresses along the rolling and transverse directions were significantly different. (c) For subsequent increments $k = [2, \ldots, 6]$, differences between the rolling and transverse directions were much smaller.

rolling direction than along the transverse direction;

2. The distributions of radii of curvature along directions X and Y significantly differed. Along direction X, radii R_x were much smaller near the free edges, while along direction Y, radii R_y were larger near the clamp locations. This behaviour may be related to the constraints applied to the samples during processing. As a sheet deforms during peen forming, the end clamps create a bending moment around direction X, constraining bending along direction Y (Kondo *et al.*, 1981). On the other hand, the edges parallel to direction Y remain free throughout processing. In addition, the rigid support opposes deflections in the direction of the shot stream. The combination of these constraints creates a complex residual stress field that affects the response of the part to further peening.

   Drouin (2006) obtained similar results in his study of ultrasonic peen forming performed in a single pass although sample dimensions, constraints and peening trajectory in his

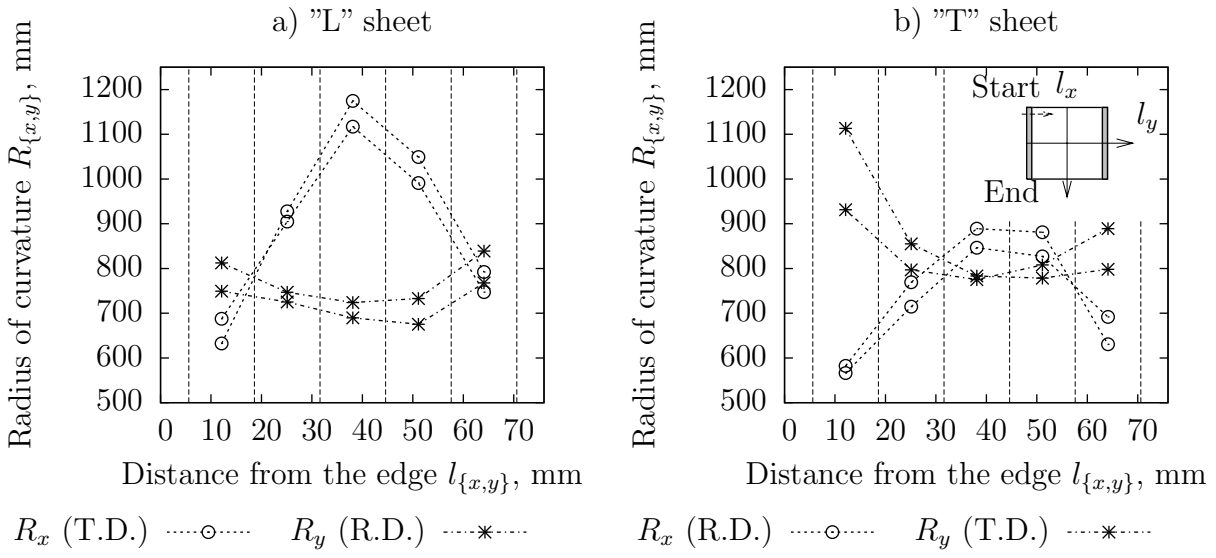

Figure 7.17 Experimentally determined radii of curvature for (a) "L" and (b) "T" sheets. Two samples were formed and measured for each case. Distances $l_{\{x,y\}}$ and radii R_x and R_y are defined in Figure 7.6. Radii were determined for five 13 mm segments in each direction.

study were significantly different from those of the current experiments. For AA7075-T6 square samples clamped at their corners, a behaviour similar to that along direction X in the current work was observed: radii of curvature were significantly larger near the center of the plate. Further study is required to better understand the combined effects of boundary conditions and peening pattern and investigate how to exploit these factors to achieve different contours.

3. Final radii of curvature differed between regions peened at the beginning and at the end of the treatment. When considering the radii distribution along direction X, radii were always smaller near the edge where peening began (Figure 7.17). This asymmetry suggests that the peening pattern is likely to affect the final shape. Average differences between opposite segments j (as defined in Figure 7.6) were around 14% but the scatter was quite significant (Table 7.4).

It should be noted that surface roughness of the measured profiles, as illustrated in Figure 7.18, may have had an influence when determining experimental radii of curvature by fitting circular arc segments. Future studies should consider measuring contours on an unpeened surface to avoid the possible influence of surface irregularities on calculated radii.

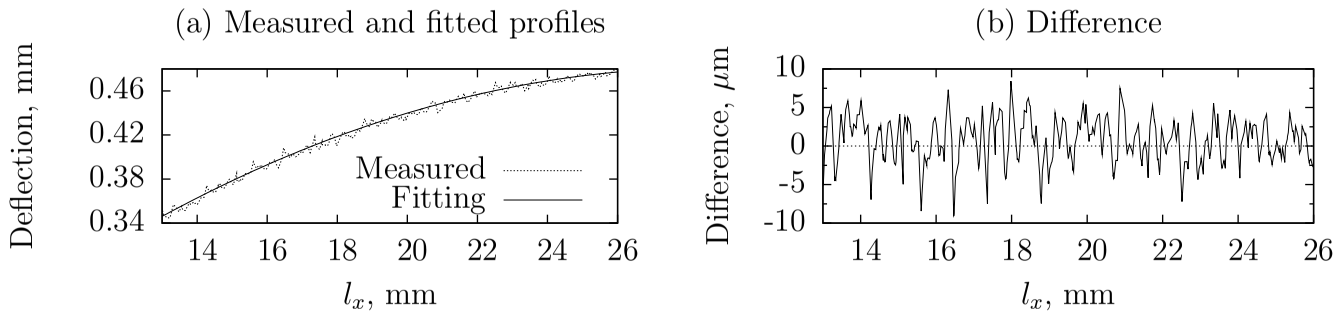

Figure 7.18 (a) Illustration of typical measured surface roughness along with the fitted circular arc segment ("L" sheet, sample 1, direction X, segment $j = 2$). (b) Difference between fitted and measured profiles in (a).

For comparison purposes, radii of curvature were determined over the complete 65 mm profiles. When comparing the global radii presented in Table 7.5 to the data from Figure 7.17, it can be noted that the global radii give a fairly good evaluation of the local radii along direction Y but not along direction X. Global radii can therefore be misleading: when studying complex peening treatments and boundary conditions, evaluation of local radii may be more appropriate than global radii.

7.5.2 Simulation results

Comparison of experimentally measured and numerically calculated profiles shows that simulations overestimated the sheet deflections by as much as 20% (Figure 7.19). For comparison purposes, the chosen calibration (Section 7.4.2) was a compromise that led to overestimated arc heights for "L" strips and underestimated arc heights for "T" strips by approximately 2%. Since the calibration was defined based on the arc heights of smaller rectangular samples, this indicates that the numerical representation of the actual treatment could be sensitive to the sample size and constraints. These factors have an influence on constrained deflection, which would in turn affect the free contour.

Calculated deformed shapes for the "L" and "T" sheets were used to determine local radii of curvature in five 13 mm segments (Figure 7.20). Finite element modelling correctly predicted the experimental trends described in Section 7.5.1: the influence of the rolling direction orientation, the differences between the radius distributions along directions X and Y, as well as the asymmetry of the radii along direction X. However, predicted radii of curvature were often smaller than the experimentally determined radii, which is consistent with the simulated deflections being larger than the measured values in Figure 7.19. Further work is required to achieve quantitatively accurate predictions since significant differences remained between the simulations and the experimental results.

Simulation results were used to further investigate the asymmetry of the curvature along

Table 7.4 Asymmetry of experimentally determined radii of curvature in opposite segments j along direction X. Surface profile segments j are illustrated in Figure 7.6.

Sheet type	Sample number	$\frac{R_X^{j=5}-R_X^{j=1}}{R_X^{j=1}}$	$\frac{R_X^{j=4}-R_X^{j=2}}{R_X^{j=2}}$
"L"	1	8.7%	9.5%
	2	25.2%	13.1%
"T"	1	8.3%	14.5%
	2	22.2%	15.7%

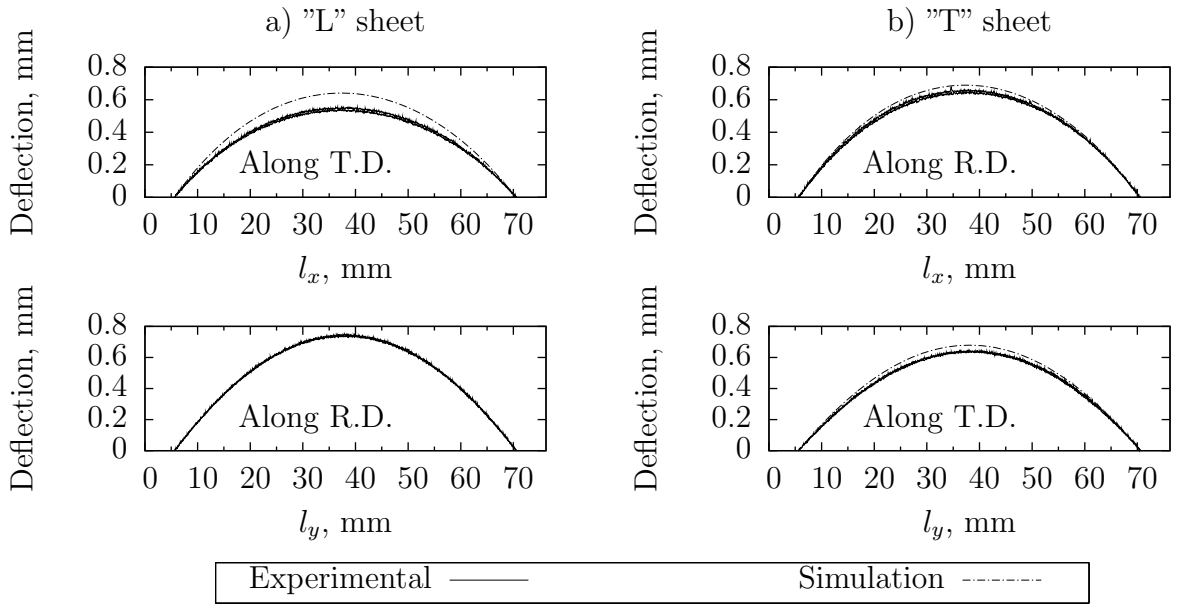

Figure 7.19 Comparison of experimentally measured and numerically calculated surface profiles for (a) "L" and (b) "T" sheets.

direction X. The deflections and stress state in the sheet were studied at three different stages of the simulated forming treatment (Figure 7.21). Due to progressive build-up of deflections, previous peening led to relatively large residual stresses in elements located near the boundary of the peened area. Since peening was then simulated onto those elements, the residual stress field affected the development of curvature. At the center of the upcoming peening lines, indicated by arrows in Figure 7.21(b), compressive surface stresses were observed along direction X (Figure 7.21(c)). Since stresses induced by peening are not much sensitive to the initial stress state, compressive surface stresses tend to decrease the equilibrium upset and the resulting curvature. The asymmetry in the radii of curvatures along X shown in

Table 7.5 Global radii determined over the full 65 mm profiles.

Sheet type	Sample number	R_x mm	R_y mm
"L"	1	1007.4	712.2
	2	979.2	706.2
"T"	1	832.3	825.3
	2	815.5	827.6

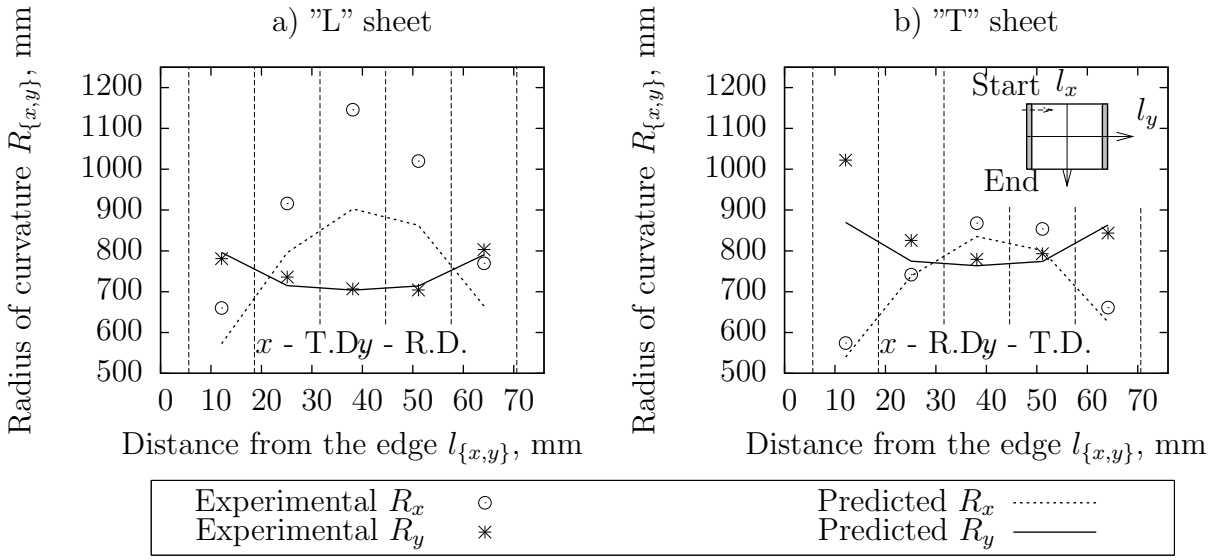

Figure 7.20 Comparison of predicted radii of curvature with average experimental data for modelled (a) “L” and (b) “T” sheets.

Figure 7.20 may be explained, at least in part, by the development of curvature and residual stresses as peening advances since:

1. Within the three stages under study, the largest compressive surface stresses along X were observed at step 282 (halfway through peening) while the smallest compressive stresses were noted at step 94 (at the early stage of peening);
2. Correspondingly, the largest radii along X occurred approximately halfway over the plate width while the smallest radii was found at the starting edge of peening.

This means that as the treatment proceeds some regions of the sheet become pre-stressed before peening occurs, which affects further development of curvature (Cao *et al.*, 1995; Miao *et al.*, 2010). Overlap between peening lines could play a significant role since this pre-stressing behaviour occurs mostly at the boundary between peening lines. While numerical simulations defined a sharp boundary between unpeened and peened areas, experiments led to a partially peened state in this boundary. Considering that the evolution of the residual stress state involves both the peening pattern and the boundary conditions, incremental finite element simulation could be a useful tool to better understand this complex phenomenon.

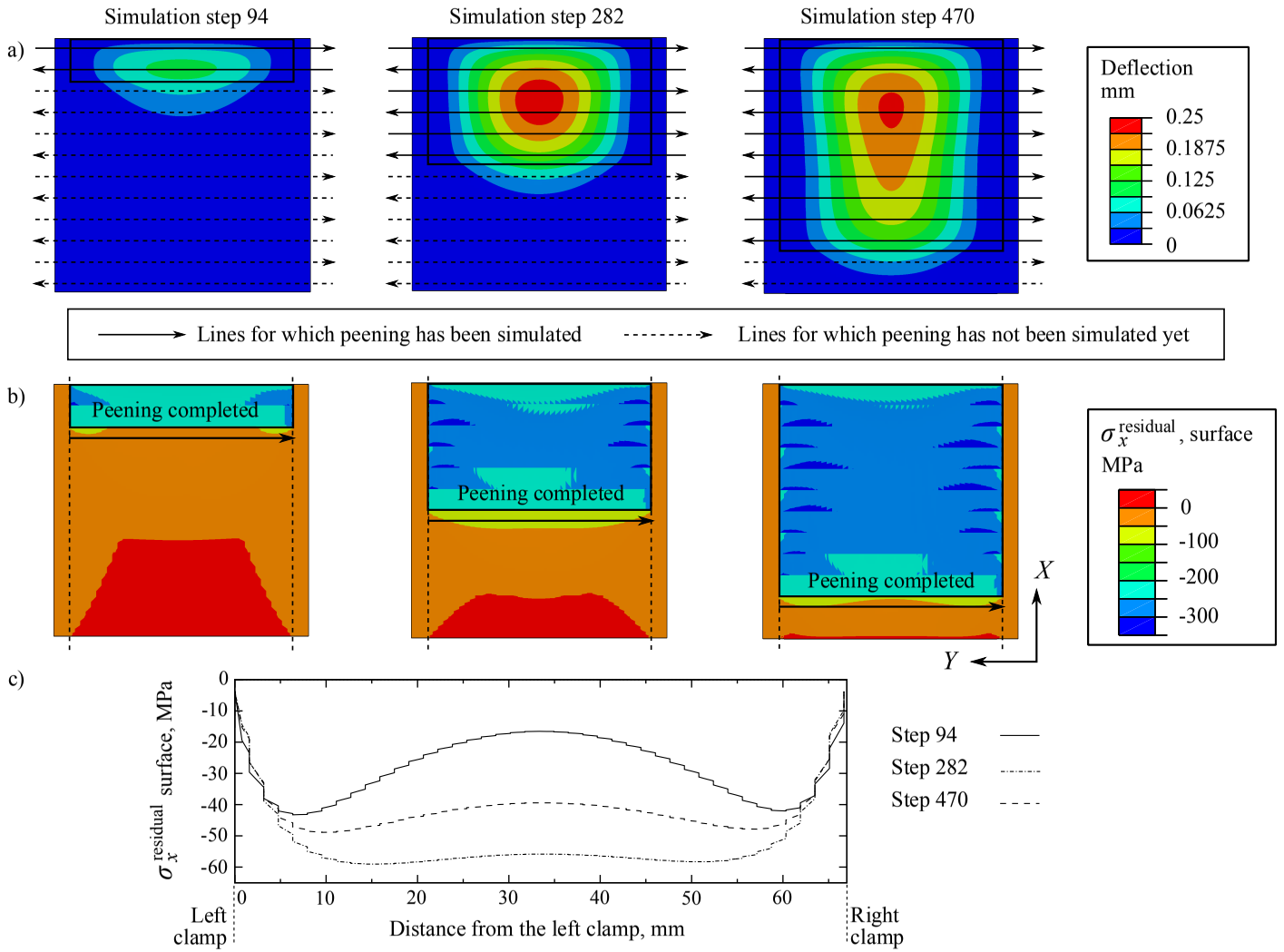

Figure 7.21 (a) Calculated sheet deflections at three different stages of peen forming for a "L" sheet. Due to the combined effects of previous peening and boundary conditions, further peening occurs on a deformed area with an initial curvature. (b) Development of curvature during peen forming generates residual stresses throughout the sheet. Regions closer to the peened area are more pronouncedly affected. Arrows indicate the next peening line at each stage. Further peening is conducted on a material with significant residual stresses. (c) Distributions of $\sigma_x^{\text{residual}}$ at the surface following the arrows indicated in (b).

Modelling peen forming with multiple passes using the same boundary conditions and total impact density would allow evaluating the individual influences of peening trajectory and boundary conditions. Simulations were attempted as described in Section 7.4.1. These analyses did not converge, most likely due to the complexity of the contact between the deformable sheet and the rigid plane. It was therefore not possible to numerically assess the specific effect of the peening path. This also shows that robustness of the forming simulation approach needs to be improved.

Effect of geometrical non-linearities

Forming simulations conducted in this study took geometrical non-linearities into account. Geometrically linear analyses were also run for square sheets and led to larger deflections and smaller radii (Figure 7.22). This behaviour can be explained by the lower bending stiffness of a flat sheet when compared to a curved sheet (Kulkarni *et al.*, 1981; Drouin, 2006). This stiffening effect of incremental curvature is neglected in geometrically linear analyses that consider the initial geometry to build the stiffness matrix.

Geometrical non-linearities improved the simulation accuracy and had a greater influence near the center of the sheet: differences between analysis types in terms of radius of curvature were as large as 12% at the center but less than 2% near the edges.

7.5.3 Summary

Incremental finite element simulations were performed to model peen forming experiments conducted with a single pass of a nozzle over different samples. A model was suggested to simulate the travel of a shot stream over a component. For simplification, the influence of overlapping peening lines was neglected. The numerical parameters of the modelled treatment were first calibrated from experimental data using the measured arc heights of small rectangular samples. These parameters were then applied to square samples with similar dimensions for which local radii of curvature were determined.

For the present sample dimensions and peening parameters, numerical simulations correctly predicted the trends experimentally observed for square sheets:

1. The radii depended on the anisotropic properties of the sheet;
2. The local radii varied according to the direction and position on the sample;
3. The radius distribution presented an asymmetry along direction X which is believed to arise from the peening trajectory.

Simulations, however, failed to accurately calculate some of the actual radii of curvature. These results suggest that, using simple calibration tests, finite element modelling may be

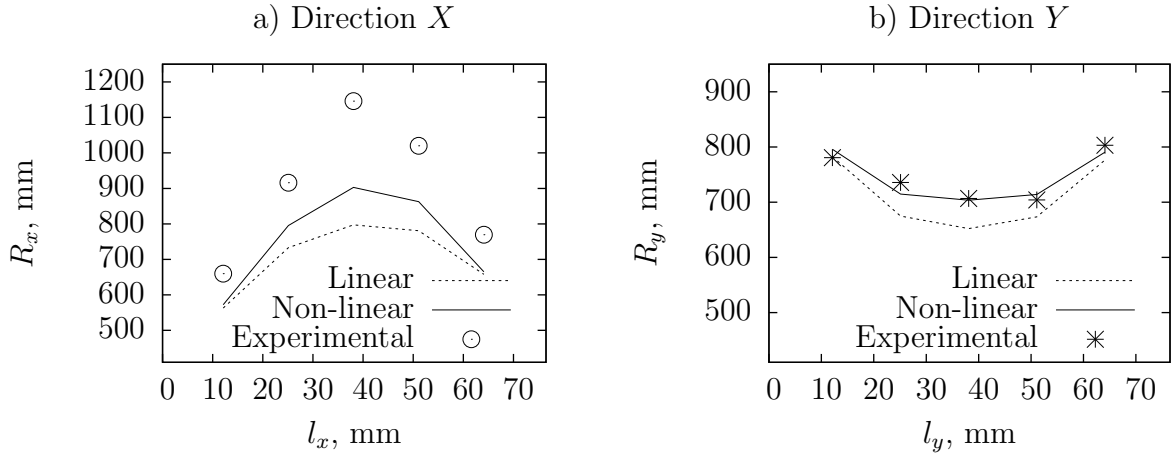

Figure 7.22 Comparison between calculated radii for a "L" sheet for geometrically linear and non-linear analyses.

used to predict at least qualitatively the shaping effect of peen forming treatments involving complex patterns and boundary conditions. Furthermore, simulation results provide a better understanding of the mechanisms leading to the final deformed shape.

It should be noted that the calibration and verification experiments involved the same boundary conditions. The compliance of the external constraints may possibly influence the development of curvature and the numerical calibration of a treatment by allowing smaller or greater constrained deflections. Further work is required to assess the effect of different boundary conditions on the numerical description of peen forming treatments.

In the current study, numerically predicted induced stress profiles were considered in the forming simulations. The impact model predicted an induced stress amplitude greater than experimentally measured data for the peening parameters investigated (Gariépy *et al.*, 2011): the calculated stress profiles σ^{peening} therefore led to an overestimated forming effect. It should be noted that this overestimation can be counteracted by a smaller number of peening increments N_i. In other words, different combinations of σ^{peening} and N_i may lead to similar results.

Simulations taking into account the peening pattern correctly predicted the asymmetry of the local radius distribution along direction X but required a large number of simulation steps and high computation time. In order to better assess the balance between the accuracy of the analyses and their computational cost, future studies should investigate experimentally and numerically the specific effects of peening trajectory and constraints on deformed shapes for different geometries.

7.6 Conclusions

The main conclusions of this work are as follows:

1. After numerical calibration of the treatment, incremental peen forming simulations can adequately predict the trends associated with peening patterns and boundary conditions as well as help explaining the phenomena leading to the final shape;
2. Geometrical non-linearities can have a significant effect on the deformed shape and should be considered in the simulations;

The main limitation of the current work is that calibration and validation tests were done with similar boundary conditions and sample sizes. This certainly contributed to the good agreement between experimental and predicted results in the validation stage. Future studies should consider different dimensions and constraints to evaluate their influence on numerical calibration of the treatments. Considering the high calculation time of the simulations conducted in this work, future studies should also investigate the accuracy gain from simulating the peening pattern with respect to the increased computational cost within the context of potential industrial applications.

Acknowledgements

A. Gariépy would like to thank the Natural Sciences and Engineering Research Council of Canada (NSERC), Rio Tinto Alcan and Fondation de Polytechnique for their financial support through scholarships. The authors would like to thank Christian Corbeil at the National Research Council Canada – Aerospace for setting up the stream photography experiments and François Ménard at École Polytechnique de Montréal for his help in surface profile measurements.

CHAPTER 8

ARTICLE 5: POTENTIAL APPLICATIONS OF PEEN FORMING FINITE ELEMENT MODELLING

A. Gariépy, J. Cyr, A. Levers, C. Perron, P. Bocher, M. Lévesque (2012). *Advances in Engineering Software* 52C, pp. 60-71.

8.1 Abstract

Peen forming is a versatile and flexible manufacturing process commonly used in the aerospace industry to shape wing skins and rockets panels. Development of peening parameters needed to obtain a specific component shape can be both costly and challenging due to the use of empirical methods which involve large quantities of physical experiments coupled with trial and error processing of prototype components. Many iterations are often required to get the desired shape with no guarantee that a specific component geometry can be achieved. Reliable numerical simulations could substantially reduce the time, cost and risk associated with process development. The purpose of this study is to further investigate the use of numerical tools to model the peen forming process. This work combines static and dynamic simulation techniques to predict the development of curvature on representative wing skin panels that include features such as integral stiffeners. This work illustrates the considerable potential of finite element simulations to determine the process parameters needed to produce a component design, and substantially reduce the dependence upon physical testing.

8.2 Introduction

Shot peening is a surface treatment performed by projecting numerous small particles at high velocity onto the surface of a metallic component. Each impacting shot plastically deforms the surface of the part. Repeated impacts lead to in-plane plastic stretching and compressive stress near the surface of the target component. The shot peening process can be separated into two distinct groups. The first, termed saturation peening, involves the complete obliteration of the surface of a component with impact dimples: this treatment is applied to improve the resistance of a component to fatigue and stress corrosion (Curtis *et al.*, 2003). The second group, peen forming, is performed at higher impact energy and lower surface coverage and is used to shape large and thin aluminium alloy components typically found in the aerospace industry, such as wing skins or rocket panels (Baughman,

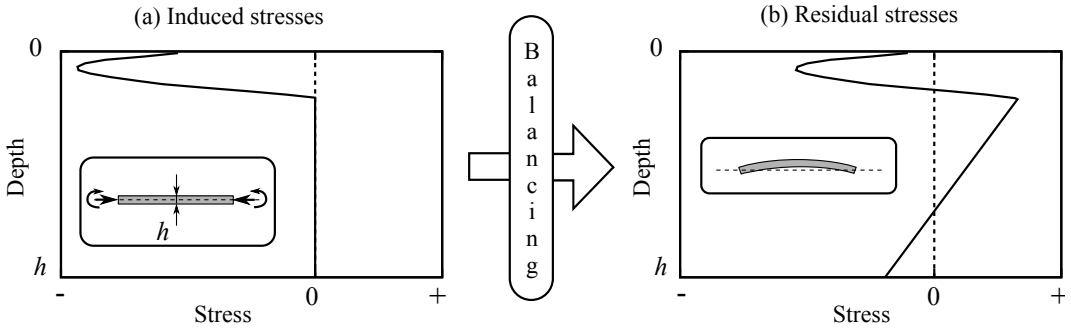

Figure 8.1 Relationship between (a) a typical induced stress profile in a constrained flat part of thickness h and (b) the resulting residual stress state in the deformed part. Scales are the same for both graphs. Inserts show part shape and constraints.

1984; Friese *et al.*, 2002), or to correct machining induced distortion of complex components such as ribs and spars (Tatton, 1986). The principle of peen forming can be explained as follows (Figure 8.1). When a component is perfectly constrained during peening, surface plastic strains generate an "induced stress" profile (VanLuchene *et al.*, 1995). This profile alters the mechanical equilibrium within the component. Upon removal of the constraints, the part bends and stretches. The final balanced stress profile is referred to as "residual stress". This balancing phenomenon allows thin parts that require relatively large formed radii to be produced by the shot peening process.

While shot peening of aluminium alloys is usually performed with small ceramic or steel shots, peen forming requires larger and heavier steel shots to achieve the shaping effect (Table 8.1). Peen forming is a flexible process since a wide variety of shapes can be attained by a simple variation of process parameters (*e.g.* shot size, type, velocity, exposure time, area of application, etc.). Peen forming can be considered to be dieless, unlike other metal forming processes that require dedicated – single purpose – tooling to produce a specific component geometry.

Typical applications for wing skin forming involve a sequence of treatments with different parameters (Moore, 1982; Burmeister, 1984; Ramati *et al.*, 1999; Yamada *et al.*, 2002). Panels are first saturation peened on all surfaces with small shots at relatively low impact velocity (energy) in order to introduce beneficial compressive stresses on all surfaces and improve fatigue life (Moore, 1982; Burmeister, 1984; Baughman, 1984; VanLuchene *et al.*, 1995; Ramati *et al.*, 1999). This operation also has the effect of elongating the part slightly, as shown in Figure 8.2(a). Further operations are then applied to induce three dimensional curvature in the component. Forming operations need to increase the induced stress amplitude and/or the depth subjected to compressive stresses in order to upset the bending equilibrium and induce curvature, as illustrated in Figure 8.2(b). This is usually done by projecting larger

shots onto the surface.

Forming operations are carried out in two stages (Moore, 1982; Burmeister, 1984; Baughman, 1984). The first stage is to induce a chordwise shape into the component, whilst further local peening is performed in the second stage to induce a spanwise contour through the creation of dihedral or anhedral breaks in the chordwise contour. When peening is conducted uniformly on an unconstrained plate made of an isotropic material, the part develops a spherical shape with uniform curvature in all directions; component contours are however much more complicated. Different techniques are therefore combined to achieve the required contours:

- Different peening parameters are used on different regions of the component due to the variable stiffness and target curvatures of the component (Harburn and Miller, 1982; Baughman, 1984; Yamada *et al.*, 2002);
- Spherical deformation can be inhibited by peening narrow strips to develop directional curvature (Baughman, 1984, 1987). Peening parallel strips along the span direction leads to a tighter curvature along the chord direction and a smaller curvature along the span direction;
- As shown in Figure 8.2(b), peening both sides of a plate tends to elongate the part. Elongating the edges of a curved component can reduce spherical deformation (Harburn and Miller, 1982; Baughman, 1984; VanLuchene *et al.*, 1995; Ramati *et al.*, 1999), whilst elongating the centre of a curved component can increase the spanwise curvature and shape a "hog back" contour.
- Integral stiffeners contribute to reducing spherical deformation by introducing a larger

Table 8.1 Examples of shot types used for saturation shot peening and peen forming aluminium alloy components (SAE Standard AMS-S-13165, 1997; SAE Standard AMS2431, 2010)

Application	Designation	Material	Density kg/m^3	xxx indicates...	Example Diameter (mm)
Saturation shot peening	Bxxx	Ceramic	3850	-	B120 0.063-0.125 (Saint-Gobain, 2012)
	Zxxx	Ceramic	3850	Minimum shot diameter, in μm	Z425 0.425 - 0.600Z425 (Saint-Gobain, 2003)
	Sxxx	Cast steel	7800	Nominal shot diameter, in 1/10000 of an inch	S660 $\approx$ 1.41 - 2.4
Peen forming					

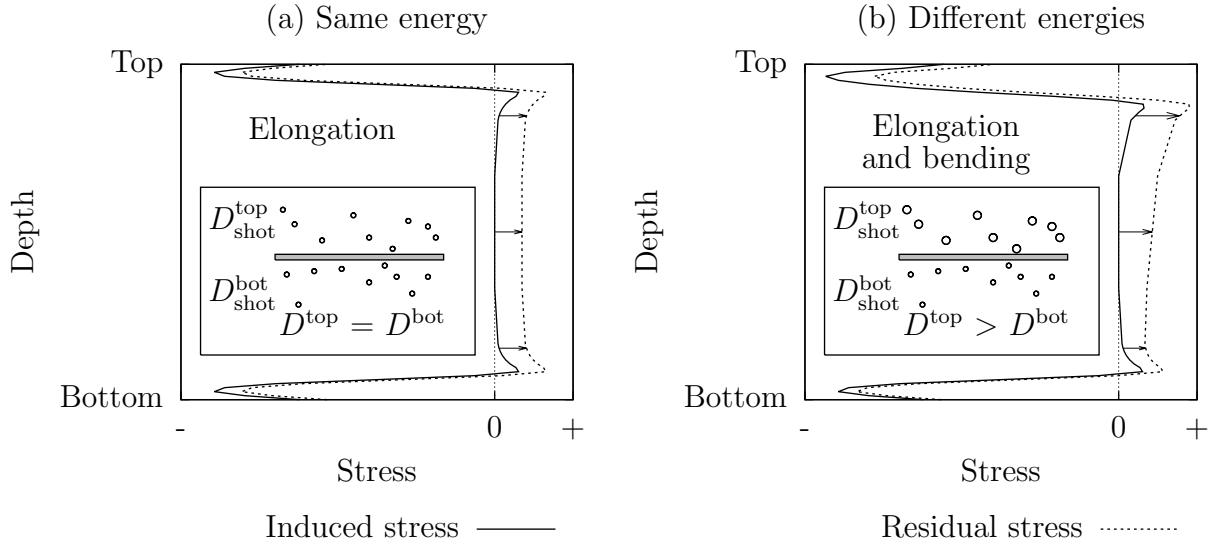

Figure 8.2 Effect of peening parameters on both sides of a part on resulting elongation and curvature. Inserts illustrate peening conditions. (a) Using the same energy (same shot type and diameter D_{shot}, impact velocity and impact density) on both sides, the component elongates and remains flat. (b) If the top surface is peened with a higher energy, *e.g.* larger shots with the same impact velocity, the part elongates and the top surface develops a convex curvature normal to the direction of peening.

bending stiffness along the span direction (Baughman, 1984; Yamada *et al.*, 2002). In addition, the surfaces of the integral stiffeners can be peened to obtain elongation and further mitigate spherical curvature or create dihedral curvatures along the span direction (saddle shape) (Ramati *et al.*, 1999; Yamada *et al.*, 2002; Kennerknecht and Cook, 2005; Wuestefeld *et al.*, 2007).

In addition to out-of-plane shaping, peen forming creates in-plane displacements in the component (Moore, 1982; Homer and VanLuchene, 1991). As shown in Figure 8.3, these phenomena are growth (elongation) and fanning (angular deformation). Even though typical growth and fanning displacements are relatively small, they must be considered for assembly of the shaped wing skin. For instance, the edges of heavily peened wing skin panels may have to be trimmed to restore the correct edge profiles and allow assembly. In addition, in extreme cases important feature locations such as spar and equipment – pumps, etc. – interfaces can move due to peening. Panel design must therefore take growth and fanning into account.

Simulating every shot impact needed to peen form a component is not practical due to the excessive calculation time (Grasty and Andrew, 1996). Impact simulations have shown that,

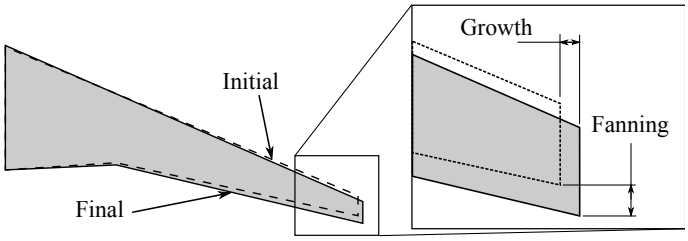

Figure 8.3 Growth and fanning in-plane displacements in a typical wing skin panel.

for a large number of impacts, shot peening tends to develop a relatively uniform induced stress and plastic strain state in the plane of the components surface (Grasty and Andrew, 1996; Wang *et al.*, 2002; Kang *et al.*, 2010). Three families of equivalent loading analogies have been developed to simulate the peen forming process based on the assumption that shot peening creates a state of stress and strain that depends only upon the distance from the surface. This assumption allows forming simulations to be performed at a reasonable computational cost. First, Grasty and Andrew (1996) suggested an equivalent pressure loading on solid elements to create plastic strains near the component surface. The second family uses thermal loading. Levers and Prior (1998) used temperature and thermal expansion coefficients to induce unbalanced stress profiles in shell elements. Wang *et al.* (2006) used thermal loading of fully constrained shell elements with non-uniform temperature distributions to create localized plastic strains near the surface. The third approach relies on induced stresses. Han *et al.* (2002) applied numerically calculated induced stresses to large continuum elements to model peen forming. Miao *et al.* (2011) presented a three-step combined analytical/numerical simulation for stress peen forming. Stress profiles computed with impact simulations were used to calculate equivalent bending moments and stretching forces. These moments and forces were then applied to the boundaries of shell element-based models to determine the deformed shape. Gariépy *et al.* (2011) proposed a method in which numerically calculated induced stresses were applied directly at section points of shell elements.

When modelling peen forming, it is important that the incremental nature of the process is reflected in the simulation method. Components deform progressively during peen forming according to the magnitude and location of the applied peening parameters (Cao *et al.*, 1995). The finite element methods proposed by Grasty and Andrew (1996), Wang *et al.* (2006) and Gariépy *et al.* (2011) considered this incremental deformation by applying successive loading steps. In each loading scheme the final deformed shape was calculated as the sum of multiple incremental displacements. In these studies, the relationship between peening time and the number of simulated loading steps was determined from experimental data. Once this calibration was performed, good correlation with experimental results was observed.

Despite the development of accurate peen forming simulation strategies since the late 1990s, forming parameters are still set based on experimentally derived databases and relationships, geometrical methods and trial-and-error (Harburn and Miller, 1982; Homer and VanLuchene, 1991; VanLuchene *et al.*, 1995; VanLuchene and Cramer, 1996). Many costly experimental tests are often necessary to achieve the required shape. In addition, a dedicated measurement fixture is generally required for each component which enables a degree a manual shot peening to achieve the desired component tolerance. In practical industrial situations, the inherent flexibility of the process is under exploited, due to the difficulties in relating the sequence and magnitude of the application of process parameters, to those required to produce a correctly shaped component. Reducing the physical tests and iterations with accurate finite element analyses to determine appropriate peening parameters will reduce manufacturing process development time and production cost. In addition, the availability of a process modelling system during early component design, where decisions such as how to discretise an aerodynamic surface into wing skin panels as well as the distribution of local thicknesses within a component or choice of structural material are made, would enable Design for Manufacture (DFM) analyses to be carried out leading to further reductions in production costs over the lifetime of the product.

This paper discusses the potential uses of a finite element based predictive methodology for industrial peen forming applications. The proposed methodology combines dynamic impact analyses with static forming simulations to predict the development of curvature. The method is first applied to calculate databases that relate process parameters to resulting curvatures. Finite element simulations are then conducted to predict the development of curvature in two realistic component configurations, typically found in wing skin applications on civil aircraft. This method reduces the dependence on experimental testing required to develop peen forming parameters. This article is divided into six sections. Section 8.3 summarizes the forming approach. Section 8.4 discusses the use of finite element simulations for calculating databases. Section 8.5 introduces the wing skin examples. Section 8.6 presents the simulation results and discusses potential uses of finite element simulations in peen forming. Section 8.7 concludes this work and suggests topics for further study.

8.3 Simulation method

In the current work, the simulation strategy presented in Gariépy *et al.* (2011) was applied to simulate realistic peen forming operations on AA2024-T351 aluminium alloy parts. AA2024 is a high-strength age-hardenable alloy with nominal composition 4.4% copper, 1.5% magnesium and 0.6% manganese. The -T351 designation indicates that the material was so-

lution heat treated, cold worked, naturally aged and finally stress relieved by stretching. This alloy is commonly used in aerospace applications that require damage tolerance.

The finite element simulation method is a multiscale strategy similar to that by Han *et al.* (2002) that incorporates:

1. A continuum element-based dynamic impact model to predict induced stress profiles in the material at a scale of a few dimple diameters;
2. A shell element-based forming model that uses the calculated stress profiles as input data to incrementally determine the deformed shapes at a scale of thousands of dimple diameters.

8.3.1 Impact simulations

In the dynamic impact analyses, a limited number of impacts were simulated on a small area (Figure 8.4). The induced stress state in the material was calculated with `ABAQUS Explicit` using eight-noded reduced integration brick elements. An isotropic-kinematic hardening law was used to represent the cyclic behaviour of AA2024-T351 aluminium alloy.

Dynamic impact analyses were run for S170 cast steel shots for saturation peening and for S330 and S550 shots for chordwise and spanwise forming (see Table 8.1). Model and mesh dimensions for each shot type are shown in Table 8.2. Shot diameters were assumed to vary following a uniform random distribution bounded by the lower and upper values presented in Table 8.2 (SAE Standard AMS-S-13165, 1997). Normal impacts (*i.e.* perpendicular to the surface) were studied. For the impact velocity of 40 m/s, the predicted dimple diameter (peak-to-peak) was approximately 0.41 times the shot diameter for the three shot types considered.

Four 70-impact simulations were performed for each shot type. Using 8-processor parallelization on an IBM P690 Regatta computer, analyses required 121 h, 33 h and 24 h each for S170, S330 and S550 shots, respectively. However, 70 impacts was a greater number than actually required by the forming simulations presented in this work. Since simulation time varies almost linearly with the number of simulated impacts given fixed model dimensions, the actual calculation time corresponding to the maximum simulated impact densities on the wing skin panel examples is significantly lower, at 39.8 h, 14.1 h and 14.4 h per analysis for S170, S330 and S550 shots, respectively. It should be noted that actual forming operations often require different impact velocities for a fixed shot type to achieve different peening intensities (Kulkarni *et al.*, 1981; Harburn and Miller, 1982; Ramati *et al.*, 1999). Additional simulations were not run with different shot velocities due to computational cost.

In the current study, it was not possible to use intensity or coverage to describe peening treatments. Since cyclic material properties for the SAE 1070 steel Almen strip were

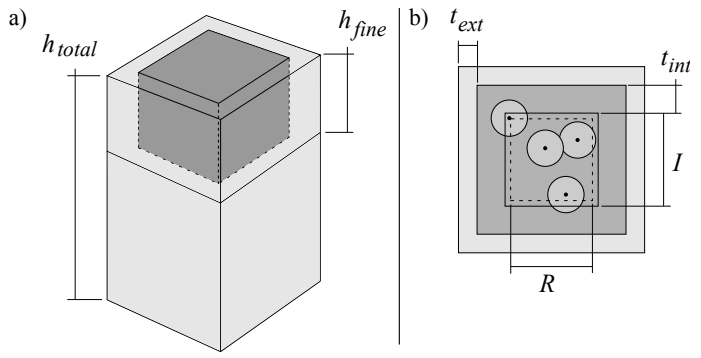

Figure 8.4 Schematic view of the dynamic impact model. (a) Isometric view. Dark grey indicates the volume with refined mesh. (b) Plan view of the model showing the impacted area (I) and representative area (R). The center of each shot was contained within the impacted area (I).

not available in literature, the Almen test could not be simulated. In addition, it was not possible to use coverage as a variable in the process model since plastic coverage predicted by the dynamic impact model does not correlate well with visual coverage (Wang *et al.*, 2002). Peening treatments were therefore described in terms of shot type, impact velocity and effective impact density, in mg/mm^2 (Kulkarni *et al.*, 1981).

Figure 8.5 presents examples of calculated average induced stress profiles $\sigma^{\text{peening}}(z_s)$ for the three shot types simulated. As expected, larger shots led to deeper induced stresses (Meguid *et al.*, 1999). Experimentally determined residual stress profiles indicate that maximum compressive stresses would be in the range of -250 to -360 MPa for AA2024-T351 under the simulated process parameters (Romero, 2002; Miao *et al.*, 2010). Impact simulations overestimate the amplitude of the induced stress profiles and therefore the forming effect for a given set of parameters.

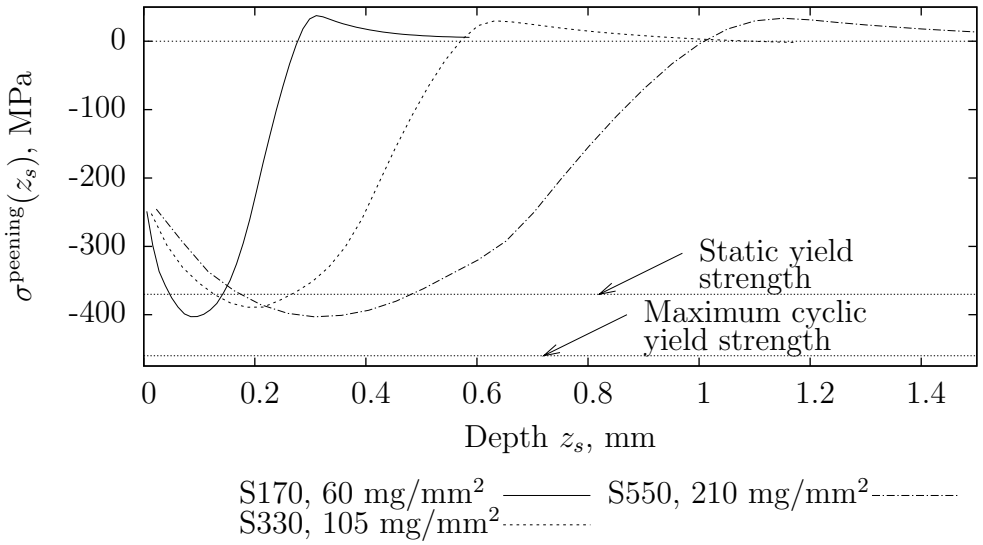

Figure 8.5 Examples of calculated induced stress profiles $\sigma^{\text{peening}}(z_s)$ for three types of steel shots impacting the AA2024-T351 target at 40 m/s.

Table 8.2 Mesh and model dimensions for impact simulations with S170, S330 and S550 shots

Shot type	Shot diameter (mm)		Impact velocity (m/s)	Refined mesh size (mm)	Model dimensions (see Figure 8.4)					
	Lower (mm)	Upper (mm)			I (mm)	R (mm)	t_{int} (mm)	t_{ext} (mm)	h_{total} (mm)	h_{fine} (mm)
S170	0.353	0.594	40	0.012	0.36	0.336	0.12	0.12	3.0	0.6
S330	0.706	1.191	40	0.030	0.90	0.84	0.30	0.30	4.8	1.2
S550	1.191	1.999	40	0.050	1.50	1.40	0.50	0.50	6.0	2.0

8.3.2 Transfer from impact to forming analyses

In the impact analyses, the material state was calculated using a very fine mesh of continuum elements to correctly capture the large stress and plastic strain gradients at the scale of the shot. As with other equivalent loading strategies, it was then assumed that shot peening generates a stress field that depends only upon depth. Average induced stress profiles $\sigma^{\text{peening}}(z_s)$, expressed only as a function of the distance from the impacted surface z_s, were therefore extracted from the four impact simulations.

Forming simulations used shell elements with a coarser through-thickness discretization. Each shell element had three layers through thickness (Figure 8.6). The outer layers were used to input calculated stress profiles induced by peening on both surfaces. Each outer layer had a constant thickness of 1.5 mm and 15 Simpson integration points through thickness (section points). This thickness was chosen based on the deepest induced stress profiles calculated with the impact model (Figure 8.5). Fifteen section points allowed an accurate discretization of the induced stress profiles. The inner layer had five section points and its thickness was adjusted to provide the appropriate plate thickness in each element. Induced stress profiles in the shell elements $\sigma^{\text{peening}}(z)$, where z indicates the through-thickness position, were interpolated from the profiles $\sigma^{\text{peening}}(z_s)$ obtained from impact simulations.

8.3.3 Forming simulations

In the forming model, numerically calculated induced stress values $\sigma^{\text{peening}}(z)$ were applied to the outer layers of large three and four-noded reduced integration shell elements as shown in Figure 8.6. Equilibrium calculations were performed with the commercial finite element code `ABAQUS Standard`. The final deformed shape was the result of multiple incremental steps in which new unbalanced stress profiles were successively introduced. The new stress profile $\sigma^{\text{unbalanced}}(z, n)$ at the beginning of step n was determined by interpolating between the induced stress profile calculated from dynamic impact simulations $\sigma^{\text{peening}}(z, n)$ and the previous balanced residual stress profile $\sigma^{\text{residual}}(z, n-1)$ as:

$$\sigma^{\text{unbalanced}}(z, n) = S_p(z) \times \sigma^{\text{peening}}(z, n) + (1 - S_p(z)) \times \sigma^{\text{residual}}(z, n-1) \qquad (8.1)$$

where n is the simulation step. Equation (8.1) was applied to each element for each step. The interpolation functions $S_p(z)$ were determined for each element and step using the criteria defined by Gariépy *et al.* (2011).

As noted by Wang *et al.* (2006) and Gariépy *et al.* (2011), a relationship between peening exposure time (or impact density) and the number of simulation steps is required to accurately model progressive deflection. Since no experimental data was available, the following

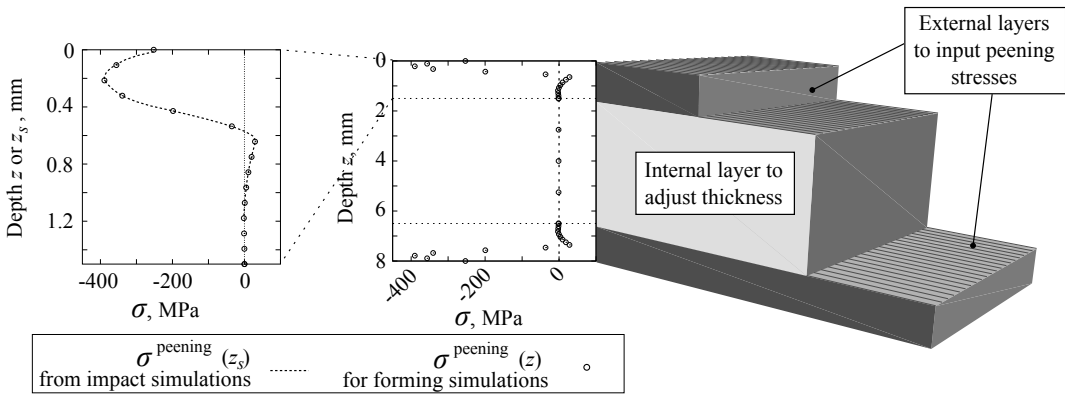

Figure 8.6 A typical stress profile in a three-layer composite shell element used for peen forming simulation.

calibration relationships were assumed:

- One simulation step for each 10 mg/mm^2 for S170 shots;
- One simulation step for each 15 mg/mm^2 for S330 shots;
- One simulation step for each 30 mg/mm^2 for S550 shots.

These relationships were selected so that the depth subjected to compressive induced stresses was stabilized after seven simulation steps. Each forming simulation step represented approximately 4 simulated impacts in the dynamic analyses for each shot type.

Due to computation time, it was not practical to model every combination of peening treatments with the dynamic impact model. Few studies have considered successive overlapping peening treatments. In their study of combined peening treatments for fatigue life improvement of AA7075-T651, Benedetti *et al.* (2009) peened tests specimens with Z425 ceramic shots (intensity 0.114 mmA and 100% coverage) and B120 ceramic beads (lower intensity of 0.114 mmN and 100% coverage). Residual stress measurements showed that peening with B120 beads led to compressive residual stresses at smaller depth than peening with Z425 shots only. When comparing a peening treatment with Z425 shots to a combined treatment using Z425 shots followed by B120 beads, it was observed that the combined treatment yielded approximately 10% more compressive residual stresses near the surface than the treatment relying only on Z425 shots. Even though the final treatment used a lower intensity, it still had the effect of increasing the residual stress amplitude. In the current study, a simplifying assumption was added to take into account such a phenomenon in areas subjected to multiple treatments. For section points where $S_p = 1$, it was decided not to allow the unbalanced stress $\sigma^{\text{unbalanced}}(n)$ to be higher (*i.e.* more tensile) than the previous

balanced residual stress $\sigma^{\text{residual}}(n-1)$ in Eq. (8.1). In other words,

$$\text{When } S_p(z)=1,\ \sigma^{\text{unbalanced}}(z,n) = \begin{cases} \sigma^{\text{peening}}(z,n) & \text{if } \sigma^{\text{peening}}(z,n) < \sigma^{\text{residual}}(z,n-1) \\ \sigma^{\text{residual}}(z,n-1) & \text{if } \sigma^{\text{peening}}(z,n) > \sigma^{\text{residual}}(z,n-1) \end{cases} \tag{8.2}$$

For illustration purposes, consider a case where six simulation steps with S170 shots were first performed and that an additional step with S330 shots was then simulated. Figure 8.7 shows that including Eq. (8.2) avoids an increase of the unbalanced stresses when compared to the previous balanced residual stresses, at any simulation step. However, this formulation does not capture the additive effect of combined treatments that would lead to more compressive induced stresses (Benedetti *et al.*, 2009): Eq. (8.2) therefore underestimates the forming effect. Further work is required to understand the interactions between successive peening treatments using different shot types and validate the use of Eq. (8.2) in practical situations.

The effect of gravity on the deformed shapes was not simulated in this work. Gravity could significantly affect the predicted contours for long and thin parts (VanLuchene and Cramer, 1996). Including gravitational loading throughout the forming simulations is left for future study.

Analysis automation

A GUI-based system was developed to facilitate the definition of complex models, peening parameters and sequence. A `Python` script and `ABAQUS` user subroutines `URDFIL` and `SIGINI` were programmed to automate the forming analyses. As in Levers and Prior (1998), the system is semi-automated: the information provided by the user is limited to the model geometry and peening treatments.

8.4 Databases

8.4.1 Process parameters vs. resulting curvature

An important use of finite element simulations could be predicting databases relating the bending and elongation of a specific material subjected to various combinations of shot size, impact density and plate thickness (Harburn and Miller, 1982). Comparing the results of such simulations obtained on a variety of alloys can generate useful data regarding the relative formability of potential structural materials in the early design cycle of a component. This type of comparison could also be made when considering a replacement structural material during a lifecycle update of an aircraft to understand the manufacturing consequences of a material change.

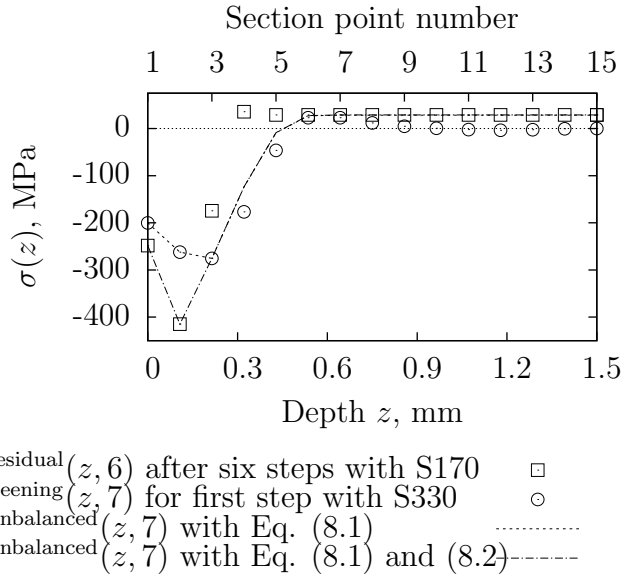

Figure 8.7 Effect of the application of Eq. (8.2). In this example, six steps with S170 shots were first simulated on both sides of a 6 mm-thick plate. At the seventh simulation step ($n = 7$), peening with S330 shot begins. The condition of Eq. (8.2) prevents the unbalanced induced stresses at simulation step $n = 7$ from being less compressive than the previous residual stresses.

Using the procedure described in Section 8.3 and a model of a 1×1 m plate with thicknesses ranging from 4 to 15 mm, two treatments were simulated successively as described in Table 8.3. Boundary conditions illustrated in Figure 8.8 were applied to prevent rigid body motion. Radii of curvature were determined by fitting circular segments through the deformed shapes, as shown in Figure 8.8. In this case study, the radii along directions X (r_X) and Y (r_Y) were identical, so $r_X = r_Y = r$. Figure 8.9 shows the calculated radii of curvature r for specific combinations of process and target parameters. As expected, for identical peening treatments, simulated curvatures decreased with increasing plate thickness. Increasing impact density was observed to increase curvature for a constant plate thickness.

Table 8.3 Peening treatments simulated to relate plate thickness and impact density to resulting radius of curvature.

Treatment	Surfaces	Shot type	Impact velocity (m/s)	Impact density (mg/mm^2)
1. Saturation peening	Simultaneously on both sides, all over model	S170	40	60
2. Peen forming	Top surface all over model	S330	40	60 to 210

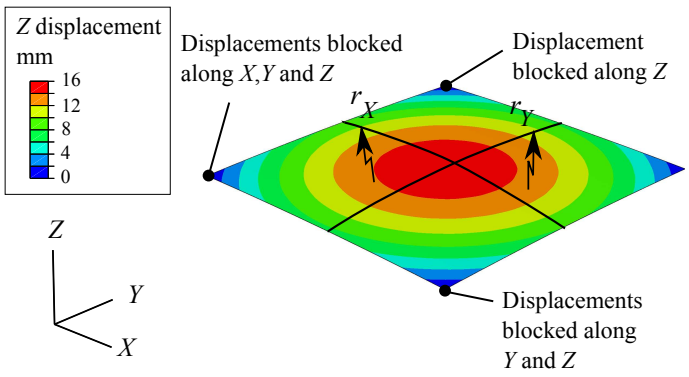

Figure 8.8 Example of deformed shape calculated for a 1 × 1 m, 8 mm-thick plate.

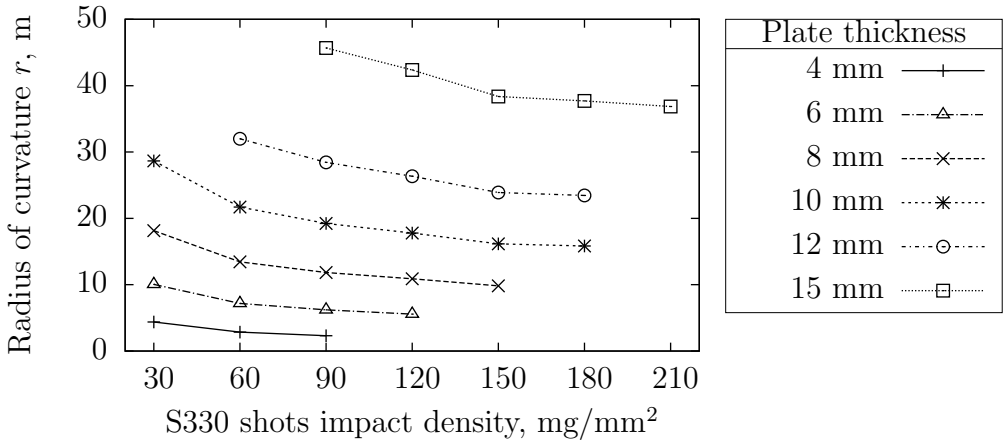

Figure 8.9 Predicted radii of curvature for an unconstrained plate peen formed with S330 shot impacting at 40 m/s at different impact densities, after saturation peening on both sides with S170 shots at 40 m/s and 60 mg/mm^2.

8.4.2 Peening of parallel strips

Finite element modelling could also be used to quantify the response of a part to more complex peen forming techniques such as peening narrow parallel strips (Section 8.2). This case study used a model of a 1×1 m, 8 mm-thick AA2024-T351 plate, as shown in Figure 8.10, and simulated the peening treatments defined in Table 8.4. Boundary conditions as shown in Figure 8.8 were applied.

A parametric study was performed to determine the effects of two parameters: the ratio of unpeened (l) to peened (L) areas $p = l/L$ and the number of peened strips s across the width of the plate. In this study, p took values of 0.0, 0.1, 0.25, 0.5 and 0.75 and the number of peened strips s was varied between 9 and 15. Deflections along X and Y axes from the middle

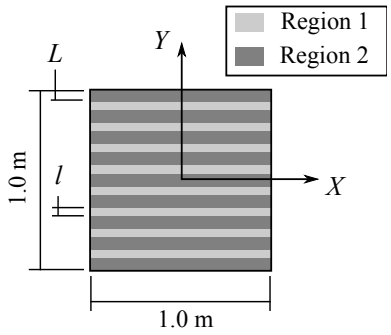

Figure 8.10 Geometry of the model with peened strips (plan view). Plate thickness was 8 mm. Saturation peening was modelled in regions 1 and 2. Peen forming with S330 shots was simulated in region 2.

of the plate were used to calculate radii of curvature r_X and r_Y, as illustrated in Figure 8.8. Figure 8.11 shows nearly linear relationships between the radii and parameter p within the range studied, with little influence from the number of strips. Since increasing p reduced the peened area, higher p values yielded smaller curvatures (*i.e.* larger radii) along both X and Y axes. The radii of curvature were larger along direction X (parallel to the peened strips) because region 1, which was not formed, opposed the bending effect of region 2 along this direction. Increasing s made the profile along Y smoother (Figure 8.12). This is due to the nearly flat unpeened areas in direction Y. Increasing s decreased both L and l (Figure 8.10): each flat spot was therefore shorter. For aerospace applications, profile smoothness is often an important factor.

Each analysis required 14 simulation steps: 6 for saturation peening and 8 for forming. Calculation time was approximately 20 min for each simulation using 4-processor parallelization on an Intel Core i7-920 desktop computer with 3.0 GB of RAM.

Table 8.4 Peening treatments simulated to study peening of parallel strips.

Treatment	Surfaces (see Figure 8.10)	Shot type	Impact velocity (m/s)	Impact density (mg/mm^2)
1. Saturation peening	Simultaneously on both sides of regions 1 and 2	S170	40	60
2. Peen forming	Top surface of region 2	S330	40	120

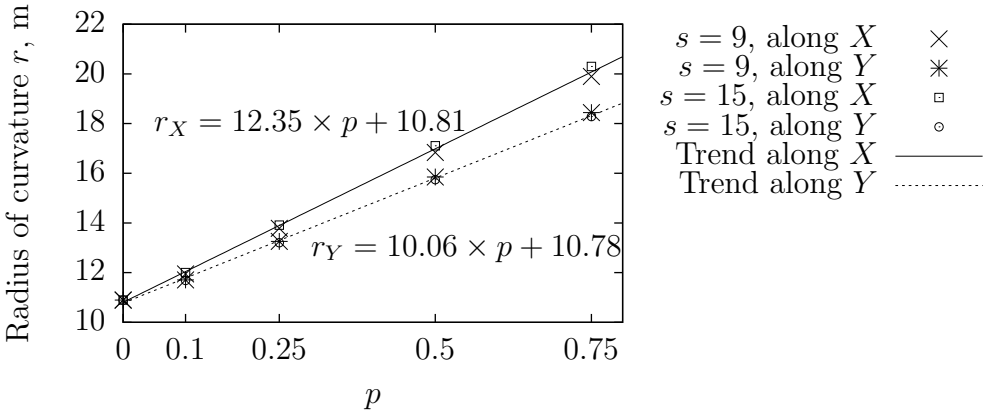

Figure 8.11 Effect of parameters p and s on the development of non-uniform curvatures by peening parallel strips.

8.5 Wing skin examples

8.5.1 Wing skin panel from Levers and Prior (1998)

The first case study is based on the wing skin panel presented by Levers and Prior (1998). In their work, two successive peening treatments using 0.5 mm-diameter shots at 100% coverage were simulated on different areas of the model using a thermal approach.

The model used in this study is illustrated in Figure 8.13. The skin panel is tapered along its length, with greater thicknesses towards the inboard end and trailing edge (Moore, 1982). The reference surface of the shell elements was taken to be the peen formed exterior surface. It was assumed that the panel is located on the lower wing surface between 0.3 and 0.7 of the chord length. The aerodynamic profile was assumed to be NACA 23012 (UIUC Applied aerodynamics group, 2012). Boundary conditions were chosen to prevent rigid body motion (Figure 8.13). The effect of gravity on the deformed shape was neglected: this represents a simplification of actual operations.

Multiple peening treatments were simulated as illustrated in Figure 8.14. Saturation peening was modelled first (treatment 1), followed by chordwise forming and spanwise forming. Using estimated chord lengths, the NACA 23012 profile was used to determine the required chordwise curvature at four sections (see Figure 8.15). For each section, curvature was calculated for the forward and aft regions of the panel. Using the databases presented in Section 8.4, combinations of panel thicknesses and peening parameters were then selected so as to approach the required chordwise curvature in each area. It should be noted that, in

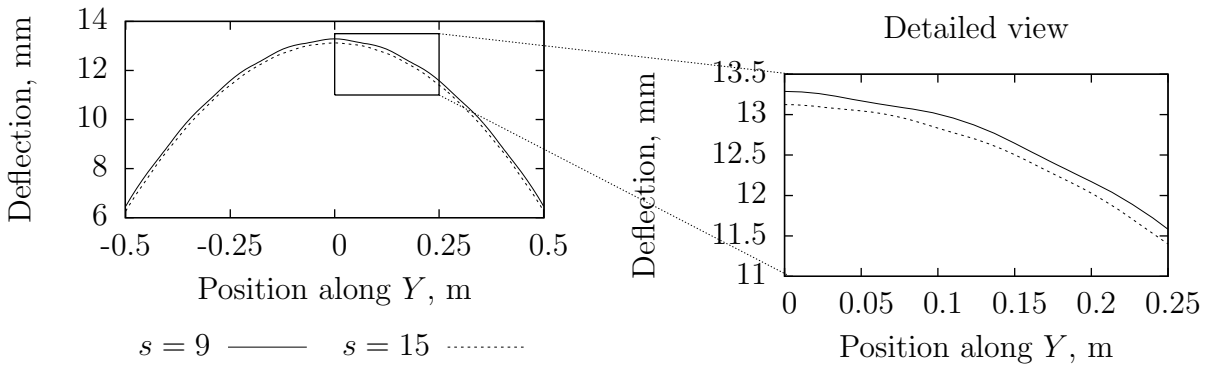

Figure 8.12 Deflections along Y from the middle of the plate for nine and fifteen peened strips over 1 m with $p = 0.75$. The detailed view shows that the profile is smoother for a larger number of strips s.

actual applications, panel thicknesses are prescribed from the wing design; only the peening parameters can be adjusted to yield the correct contour. Forming sequences with S330 and S550 shots were determined arbitrarily since no published data was available.

In this example, an attempt was made to mitigate spherical deformation of the panel. This was achieved by peening parallel strips in a specific direction (treatments 5 - 7) and attempting to elongate opposite edges of the panel (treatments 8 - 10). Elongation was obtained by peening with larger shots on both sides of specific zones of the panel. As can be seen in Figure 8.14, peening was modelled with a higher impact density (or energy) on the top surface in treatments 8 - 10 so as to achieve both elongation and curvature.

It should be noted that actual peen forming applications require a more refined definition of peen formed areas than considered here (Yamada *et al.*, 2002) and often use impact energy (Harburn and Miller, 1982; Kulkarni *et al.*, 1981), via the specification of dimple diameters for nominal shot sizes, as a control variable to achieve exact curvatures. The current work did not attempt to obtain a specific contour, a task that requires a great deal of investment and process knowledge. Determining peen forming parameters leading to a prescribed contour, within given tolerances (*e.g.* (Ramati *et al.*, 1999)), was not performed.

8.5.2 Integrally-stiffened wing skin panel

In the second case study, an integrally-stiffened and tapered upper wing skin panel was analysed. Component dimensions are shown in Figure 8.16 and were based on limited published data on the Gulfstream G280 wings (Gulfstream, 2011); integral stiffener (stringer)

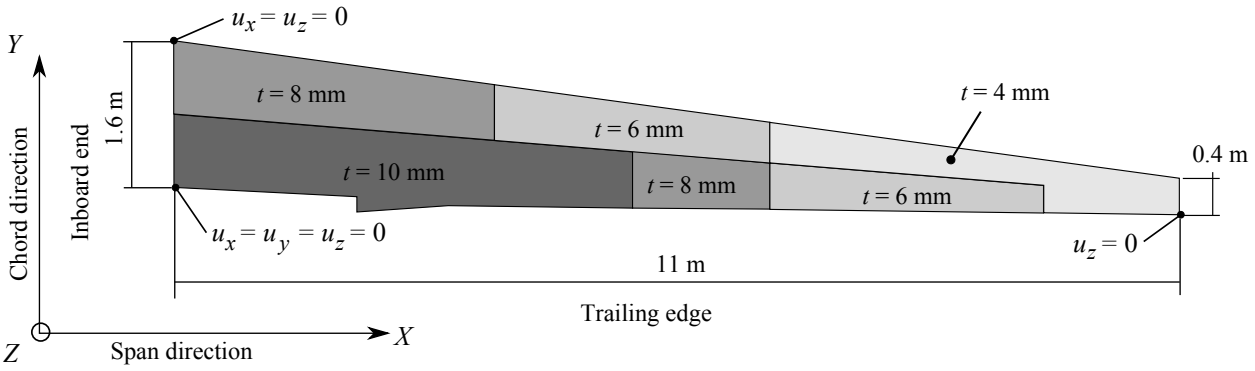

Figure 8.13 Geometry, dimensions, thicknesses and boundary conditions of the first wing skin panel. u_x, u_y and u_z indicate displacements along X, Y and Z, respectively.

dimensions and panel thicknesses were assumed due to lack of accurate published data. For simplification, blade stiffeners, as opposed to "I" or "J" sections, were modelled. It was also assumed that the wing skin was made from a single piece of aluminium (Ramati *et al.*, 1999) corresponding approximately to 0.3 - 0.9 of the chord length, with a NACA 23012 profile. Boundary conditions were applied to prevent rigid body motion (Figure 8.16).

`ABAQUS` offers options to define stiffeners analytically; the integral stiffeners were however modelled using shell elements in order to simulate peening on their webs (lateral surfaces). Peening was not modelled on the stringer crowns. Due to the stress gradient over the height of the integral stiffeners, a refined mesh with 14 elements along the height was selected following a convergence study, as illustrated in Figure 8.17(a). The reference surfaces of the shells elements were positioned so as to avoid unrealistic overlap of the modelled material, as shown in Figure 8.17(b).

Simulated peening parameters are illustrated in Figure 8.18. These parameters were chosen to approximate the chordwise radii of curvature prescribed by the NACA 23012 profile at three sections as explained in Section 8.5.1. In addition, spanwise forming (treatment 8) was achieved by peening selected stringer sections on both sides of the webs with equal energy to create elongation.

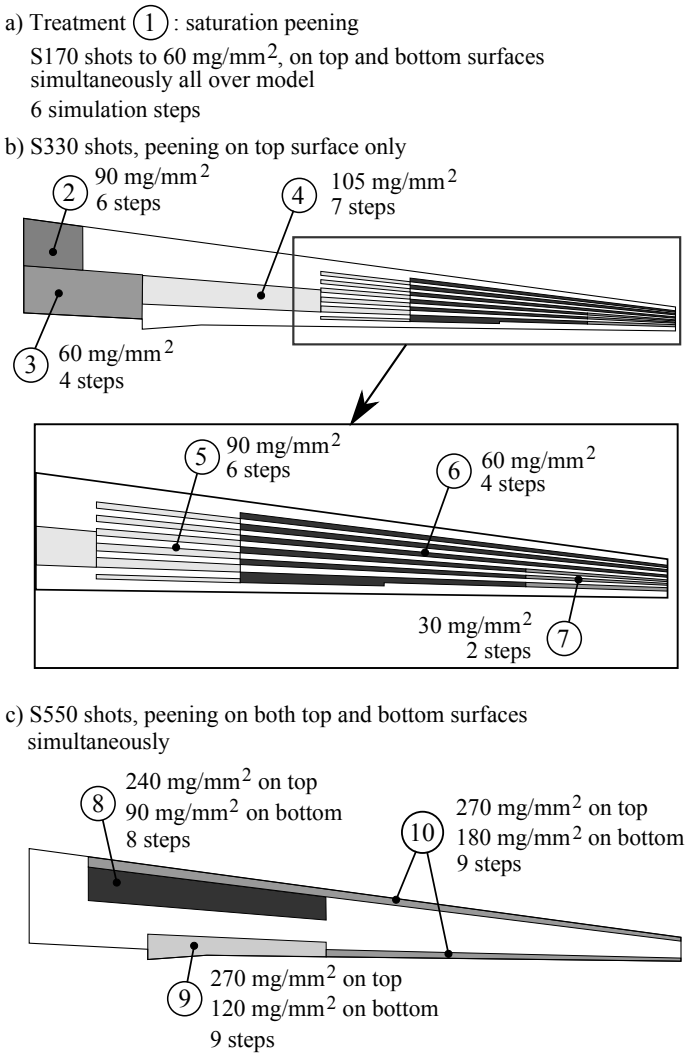

Figure 8.14 Peening treatments and sequence modelled for the first wing skin panel. The number of simulation steps needed for each treatment is also given. Panel is viewed from the top side.

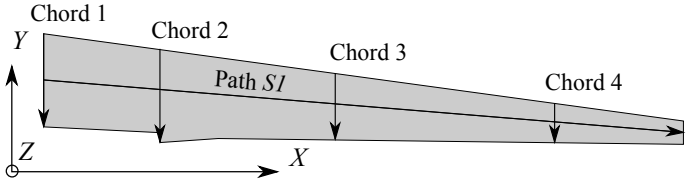

Figure 8.15 Paths on the wing panel used to assess required and predicted curvatures.

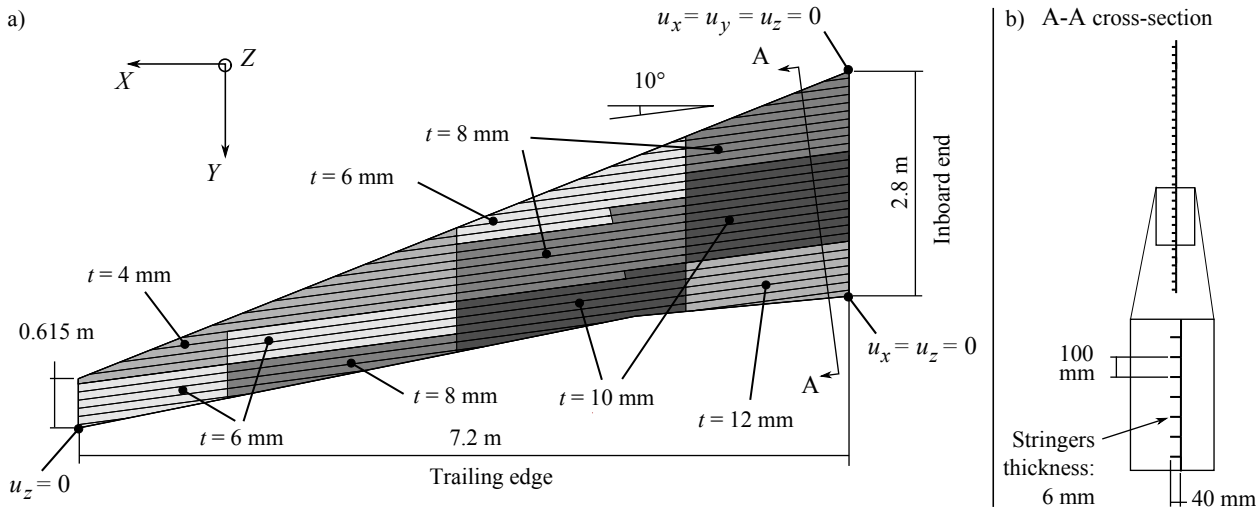

Figure 8.16 (a) Geometry, dimensions, thicknesses and boundary conditions for the integrally-stiffened wing skin panel. u_x, u_y and u_z indicate displacements along X, Y and Z, respectively. Panel is viewed from the bottom side. (b) Detail of stringers geometry.

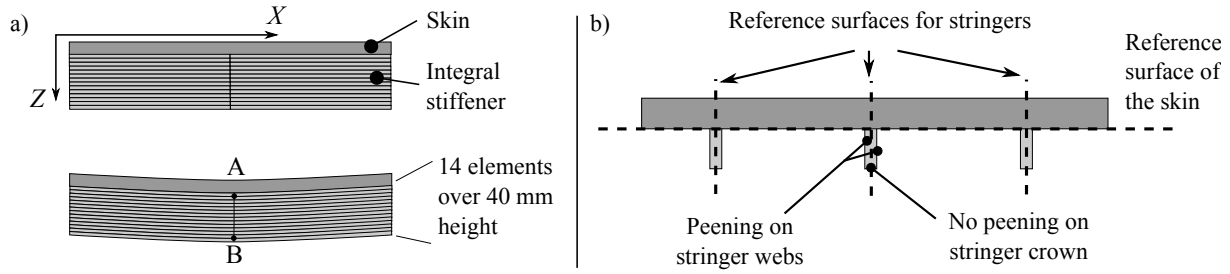

Figure 8.17 (a) Refined mesh along the height of the stringers to account for the gradient of σ_x along Z. In this example, $\sigma_x^{\text{PointA}} < \sigma_x^{\text{PointB}}$ due to bending. (b) Definition of the reference surfaces of shells elements to avoid overlap between the modelled skin and integral stiffeners.

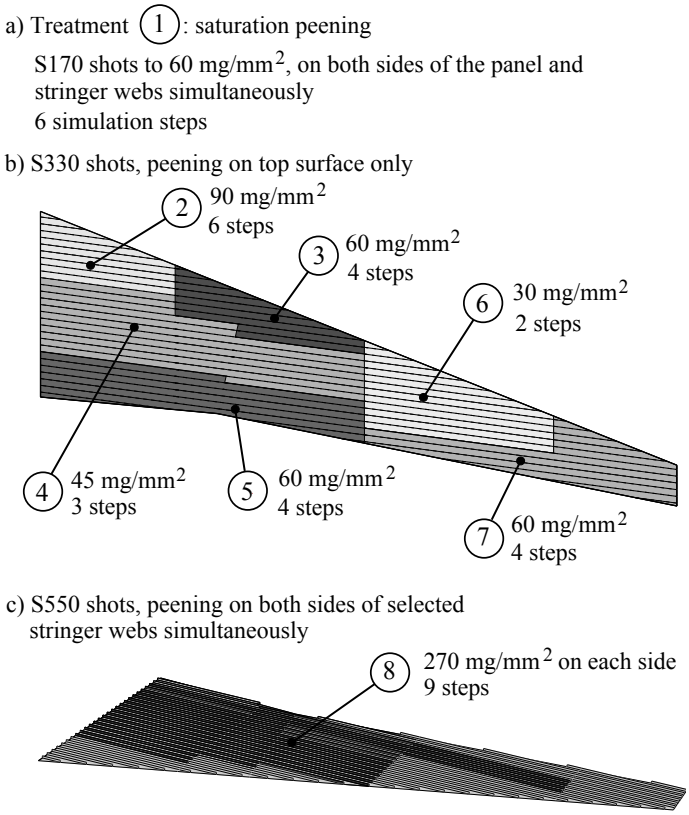

Figure 8.18 Peening treatments and sequence modelled for the integrally-stiffened wing skin panel.

8.6 Results and discussion

8.6.1 Wing skin panel from Levers and Prior (1998)

Figure 8.19 shows the deformed shape calculated for the wing skin panel example discussed in Section 8.5.1. Although it was attempted to reduce spanwise curvature, it can be seen that significant deflections still remain. Further reduction in the spanwise curvature would require optimisation of the applied peen forming parameters and is outside the scope of this study. It should also be noted that, in this example, gravity could have a significant effect on the formed shape due to the length and relatively low spanwise stiffness of the part. Assuming that the component lies horizontally on a checking fixture, the weight of the part would tend to decrease the spanwise curvature, which would in turn alter the chordwise curvatures slightly due to the Poisson effect.

The calculated displacements were used to assess the aerodynamic profiles. For simplification, the current study neglected the three-dimensional nature of the target contour. Instead, the local curvature profiles at specific Y-Z sections given in Figure 8.15 were assessed. As explained in Figure 8.20, each target profile was translated and rotated to match the general orientation of the corresponding calculated profile. This was achieved by making line C_i-D_i from the target profile coincident with line A_i-B_i from the calculated profile. This facilitates visual evaluation of curvatures but does not take into account the relative three-dimensional locations of the profiles, which is affected by phenomena such as spanwise curvature and twisting of the panel around the X axis. Results from this analysis are shown in Figure 8.21. The coarse selection of peening parameters certainly contributed to the discrepancies between the target and calculated profiles. For chords 2 and 3, the predicted shapes have slightly smaller curvatures than the target profiles. The peening sequence illustrated in Figure 8.14 may have had an influence in these cases. The databases in Section 8.4 were obtained for uniformly peened plates while peen forming is performed on a region-by-region basis in this case study, starting from the inboard edge and continuing towards the wing tip. As peening advances, adjacent undeformed material opposes bending, resulting in reduced curvatures

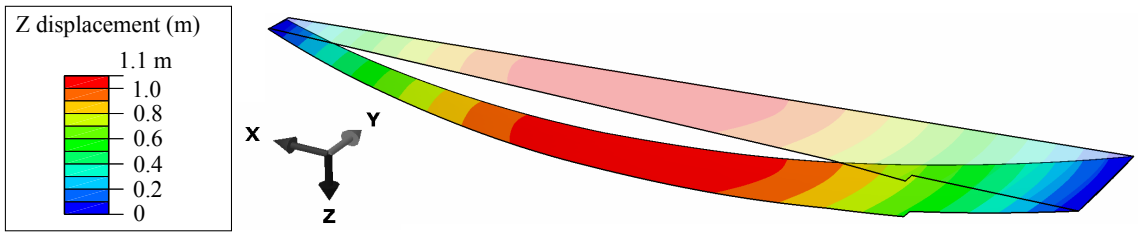

Figure 8.19 Deformed shape after all peening treatments.

when compared to fully unconstrained peen forming. This behaviour was first discussed by Homer and VanLuchene (Homer and VanLuchene, 1991). Further enhancements to the simulation method could be made if this behaviour were properly categorised with respect to its influence on the selection of peening parameters.

The finite element simulation predicted approximately 8.9 mm of growth and 24.0 mm of fanning towards the trailing edge at the wing tip (see Figure 8.3). The growth prediction of 0.8 mm/m was quite consistent with the typical growth factor of 0.42 mm/m suggested by Moore (1982). Finite element modelling could be used to establish the initial dimensions required to achieve the desired final shape and feature locations (VanLuchene *et al.*, 1995).

Figure 8.22 compares the deformed shapes along the span direction after peening treatments 9 and 10 from Figure 8.14. It was observed that peening treatment 10, which involved elongating the edges, resulted in increased deflections along the span. Observations from literature suggest that elongation of the edges should lead to a reduction of curvature along the span direction (Baughman, 1984; Ramati *et al.*, 1999). Numerical simulations did not predict this behaviour. One possible hypothesis for this discrepancy is that finite element simulations were run without considering non-linear geometrical effects (VanLuchene and Cramer, 1996). Initial attempts to include geometrical non-linearity led to lack of convergence; future studies will investigate this aspect. Another hypothesis is that the shot sizes investigated were not representative of industrial processes: U.S. Patent 4,329,862 suggests that shots with diameters up to 4.0 mm can be required for spanwise forming, which is nearly three times the diameter of the S550 shots modelled for this purpose. It should be noted that, depending on the support method, peening with very large and heavy shots may introduce more complex phenomena such as vibration of the part due to the large repeated impact forces.

This wing skin model had 41904 nodes and required 62 simulation steps. The analysis took approximately 6.5 h on a workstation equipped with Xeon 5620 processors, RAID 0, 7200 rpm hard disc drives and 48 GB of RAM.

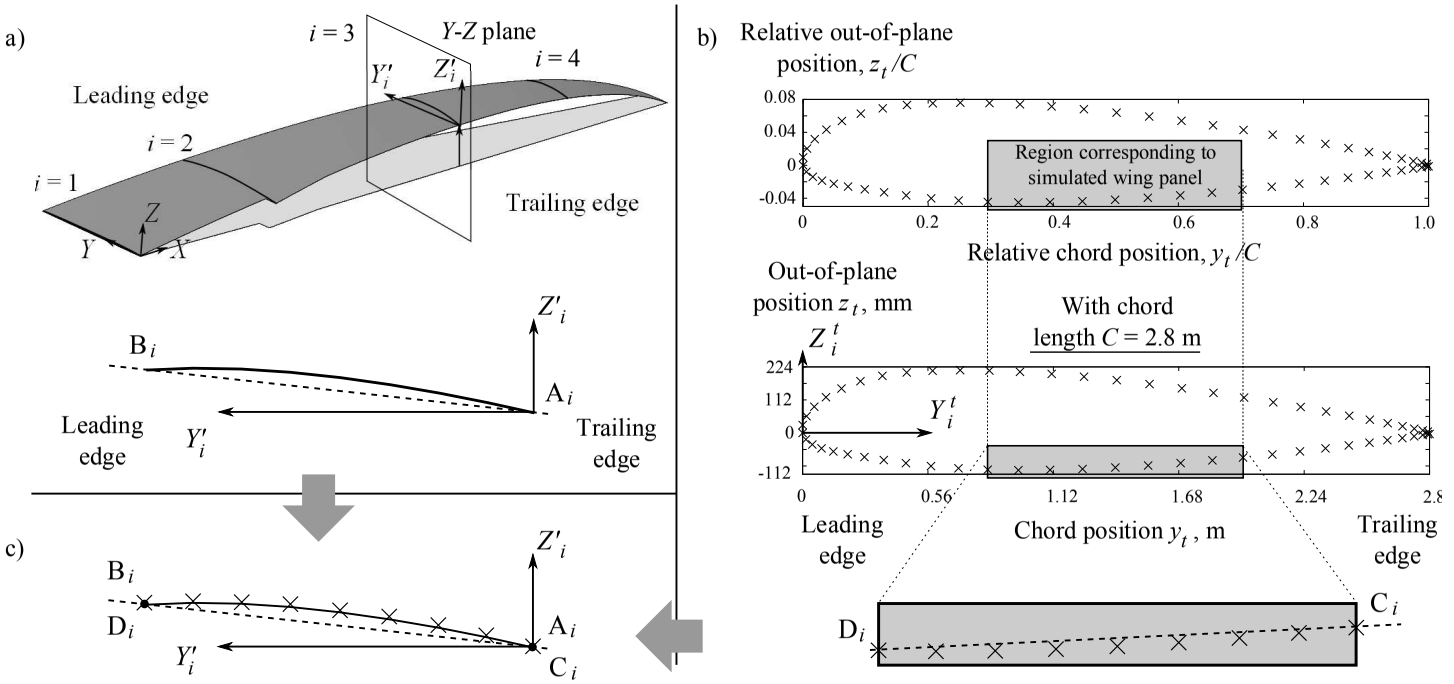

Figure 8.20 (a) The calculated profiles are given in the X-Y-Z coordinates system. For analysis purposes, each Y-Z section i was attributed a local coordinate system Y_i'-Z_i' in which the Y-Z axes are translated so that the origin becomes the trailing edge. (b) The target aerodynamic profile consists of a set of data points normalized to the chord length C (UIUC Applied aerodynamics group, 2012). The target profile at a given section i is calculated by multipying the data points by the local chord length C_i. These points are given in a different coordinate system Y_i^t-Z_i^t. (c) To facilitate visual assessment of curvatures, each target aerodynamic profile was translated and rotated so that the end points of the target profile, C_i and D_i, were coincident with the end points of the corresponding calculated profile, A_i and B_i.

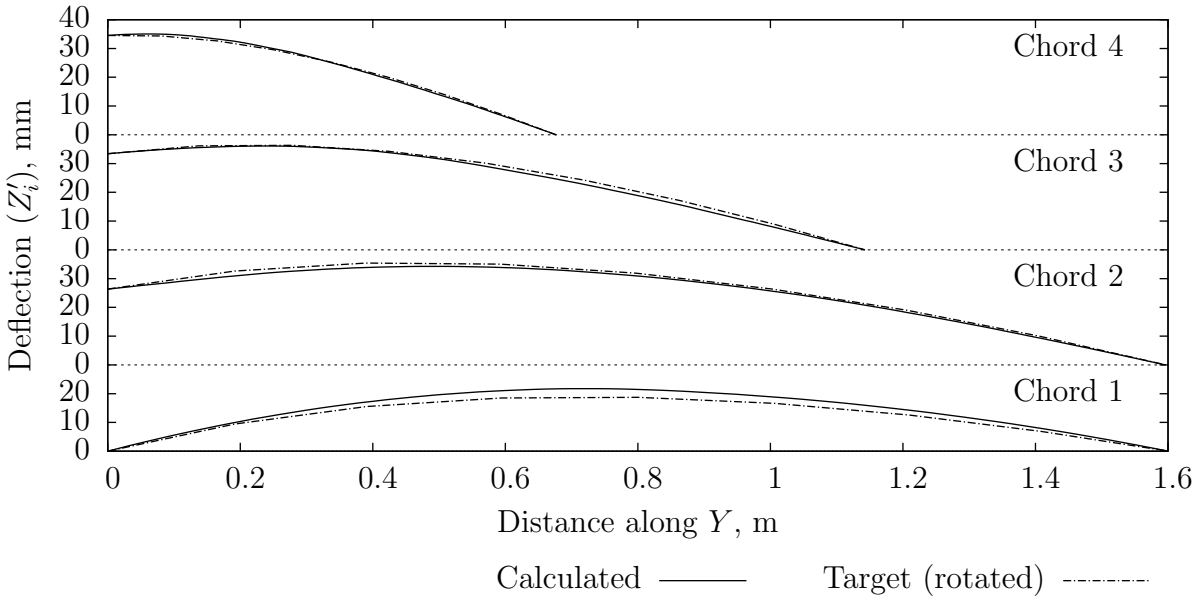

Figure 8.21 Calculated chordwise contours for the first wing skin panel example, after all 10 peening treaments. Each target profile was translated and rotated as explained in Figure 8.20. Deflections are shown in local Z_i' coordinate corresponding to each section. Paths are illustrated in Figure 8.15.

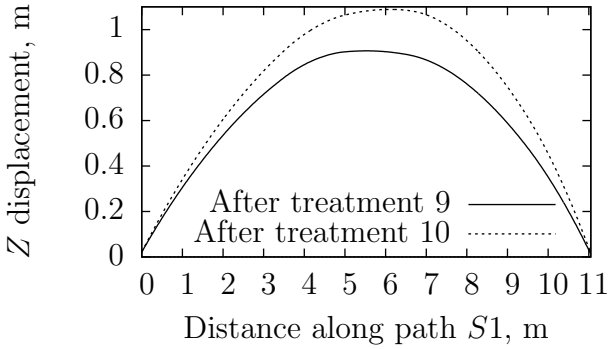

Figure 8.22 Calculated deflections along the span direction after peening treatments 9 and 10 from Figure 8.14. Measurement path is illustrated in Figure 8.15.

8.6.2 Integrally-stiffened wing skin panel

Figure 8.23 illustrates the deformed shape for the integrally-stiffened wing skin example presented in Section 8.5.2. A saddle shape with opposite curvatures along the chord and span directions was formed due to the elongation of the stringers. In addition, the panel exhibited significant twist (rotation about span direction) characterised by a rise of the leading edge towards the tip of the wing. This warping may have occurred due to poorly selected peening treatments. In this example, calculated growth and fanning were 2.1 mm (0.29 mm/m) and 4.7 mm towards the trailing edge, respectively, which is lower than the values predicted for the first example. This reduction could be related to factors such as the length and aspect ratio of the panel, the stiffening effect of the stringers or the lack of edge elongation.

This second example had 85745 nodes and required 39 simulation steps. The analysis took approximately 7.5 h on the workstation described in Section 8.6.1.

8.6.3 Discussion

This work has outlined a multiscale strategy that uses accurate material behaviour modelling to predict the outcome of realistic peen forming operations within a reasonable computating time on a typical workstation. An hypothesis was proposed to model successive treatments in a computationally-efficient manner, an important element for simulating representative forming operations. The forming simulation method was also programmed into an operational graphical package that could be used in an industrial context.

Although simulation results could not be validated experimentally, the results obtained from stringer peening simulations (on the integrally stiffened panel) as well as the peening of narrow parallel strips are consistent with the behaviours reported in literature. However, numerical analyses failed to predict the expected reduction of spanwise curvature following edge elongation, although it should be noted that the location, area and magnitude of the peening parameters applied could have been inadequate to achieve this effect. This is an important phenomenon that needs to be modelled accurately to predict the outcome of peen forming treatments. To do so, the possible influence of geometrical non-linearities needs to be investigated. The forming simulation method also requires experimental validation on a large-scale component (for which complete data is not publicly available). While finite element analyses can already provide useful trends for early component design, accurate predictions of deformed shape would allow further reductions in experimental testing throughout the component design cycle.

This study modelled successive peening treatments in a simplified manner. As shown in Figures 8.14 and 8.18, large regions of the panels were assumed to be peened uniformly and

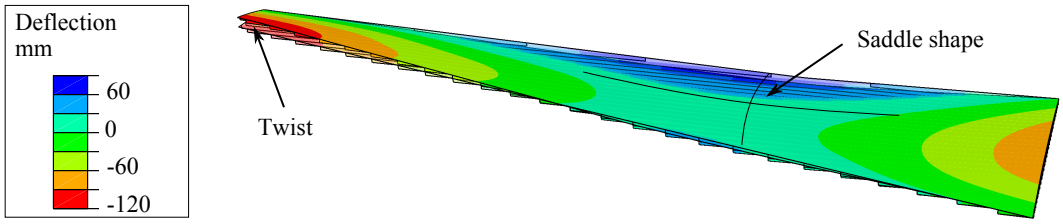

Figure 8.23 Deformed shape after all peening treatments.

induced stress profiles were input simultaneously over large areas at any given simulation step. Possible effects of peening path and feed direction were therefore neglected in the simulations. In actual operations, saturation peening and initial chordwise forming may be performed each with a single pass through the peening machines (Kulkarni *et al.*, 1981; Harburn and Miller, 1982). Assuming that the component travels through the machine along the span direction, in this case either the inboard edge or outboard tip of the component will be peened before regions at the opposite end. This processing approach could affect the development of curvature. Similarly, in Figure 8.18, it is not realistic to peen all the integral stiffeners simultaneously. In actual operations, a more practical solution is to peen stringers one at a time, travelling along their length. While this type of processing could be simulated, this would lead to a much larger number of simulation steps and higher computational cost. This clearly suggests that in certain industrial situations (*i.e.* where there is a requirement to produce fast analysis data) a compromise between accuracy and complexity may be needed. An example of this could be in the need to determine a processing sequence to correct component distortions in a reactive production support environment. Correspondingly, the balance between simulation accuracy and cost would be more biased towards accuracy if a simulation process were undertaken to define a component processing sequence prior to the start of production.

Relating numerical simulation results to actual process variables remains a challenging task. One of the main difficulties in this task is that the process control parameters used by industry are themselves analogies used to standardise the measurement process, that is they cannot be directly related to the effect on the component without supplementary empirical testing. Almen intensity and surface coverage are commonly used to describe peen forming treatments but could not be predicted for the sets of process parameters studied. As noted in Section 8.3.1, dynamic impact modelling could be improved to allow accurate predictions of these variables. Alternatively, new control parameters for the shot peen forming process could be implemented with the application of programmable automation to achieve a direct transfer of input parameters such as impact density between numerical simulation and its

application on the component. In addition, due to the incremental nature of peen forming, some experimental tests will always be necessary to establish a relationship between peening exposure time and the number of simulated forming steps.

One shortcoming of the proposed finite element approach is the high computational cost of the impact simulations. As noted in Section 8.3.1, this cost can be reduced by choosing appropriate numbers of impacts and is also lower when studying peen forming at low coverage (or impact densities). Moreover, dynamic impact analyses results can be stored for use in multiple, less-expensive forming simulations. Numerical simulations become more cost-effective when impact simulation data is used repeatedly in numerous forming simulations. In other words, once induced stress profiles are predicted and stored for a variety of process parameters, forming simulations become cheaper to perform than experimental tests.

8.7 Conclusion

The capability to produce the aerodynamic contours on aircraft wing skins is a core competence in the manufacture of metallic airframes. Shot peen forming has been used to shape metallic wing skins for over four decades, yet the detailed understanding required to deploy the process successfully and to take advantage of the considerable flexibility offered by the process remains confined to large aircraft manufacturers such as Boeing and Airbus as well as a small number of specialist subcontractors.

In this work, the potential uses of finite element modelling in the field of peen forming were investigated. Two numerical simulation tools acting at different process scales, dynamic finite element simulation of shot impacts and static peen forming modelling, were combined to simulate peen forming of representative wing skin panels in a computationally-efficient manner. It was found that FE simulation results correlated well with the experimentally observed behaviours related to peening of parallel strips and peening of integral stiffeners. It was also noted that incremental peen forming simulations could take into account the effect of sequential peen forming treatments. However, the method in its current form failed to predict the influence of edge elongation.

Although impact simulation remains time-consuming, forming simulations are believed to be much cheaper than experimental tests with full-size panels and represent a means of mitigating the risks associated with process development, as well as effectively reducing the time to market of the product. Numerical simulation also has the potential to be expanded to include other forming operations such as stress peen forming (Miao *et al.*, 2011), local press bending, trimming and sanding (VanLuchene *et al.*, 1995; Ramati *et al.*, 1999). In addition, the initial geometry used in the analyses could include residual stresses arising

from billet manufacturing and machining. Furthermore, the effects of drilling the formed component and riveting or bolting sub-assemblies such as stringers could also be modelled. It would then be possible to simulate complete forming and sub-assembly sequences. It seems possible that the combination of shot peening and forming simulations could complement or eventually replace some of the iterative experimental testing often required to obtain the desired contour in complex panels. Finite element simulations could then be used throughout component design and manufacturing as part of a global process design capability. In order to achieve accurate predictions, further studies are still required to better understand and model the complex mechanics of peen forming. Most importantly, the methodology outlined in this work needs to be validated with actual full-scale applications.

Acknowledgements

This research was made possible by a Natural Sciences and Engineering Research Council of Canada (NSERC) scholarship to A. Gariépy. A. Gariépy would also like to thank Rio Tinto Alcan and Fondation de Polytechnique for their financial support through scholarships. The authors would like to thank Simon Larose at NRC for his insightful suggestions and the anonymous reviewers who contributed to improving this paper through their comments.

CHAPTER 9

GENERAL DISCUSSION

9.1 Clarifications on Chapter 4

Following the jury's comments, this section aims to provide further information and explanations on the article presented in Chapter 4.

9.1.1 Impact modelling

Throughout this project, impact simulations were conducted with all degrees of freedom fixed for the nodes of the bottom surface (*i.e.* opposite to the impacted surface, see Figure 4.5). This selection of boundary condition is not completely realistic and should be studied further. Considering that these nodes are located far from the plastically deformed region and that the lateral boundary conditions also constrain in-plane displacements, it seems possible that the influence of the lower boundary condition would be small.

9.1.2 Material properties

This section describes the method used to identify the parameters of the material constitutive theory based on experimental uniaxial test data (see Section 4.4.2). The cyclic hardening behaviour of AA2024-T351, *i.e.* the increase of the yield stress under reversed loading, was first evaluated from experimental cyclic testing results (Figure 4.12 and Table 4.3). The isotropic hardening component was modelled using the data presented in Table 9.1. This data as well as the approximate uniaxial tensile true stress-true strain curve determined by Miao *et al.* (2010) were then input in `ABAQUS`. Built-in options were used to identify the non-linear kinematic hardening parameters C and γ provided in Section 4.4.2.

This is a very simplified approach to determining the material parameters. For simplification, it was assumed that the material reached a stabilized behaviour during repeated impacts. This assumption needs to be revised. It can also be noted that both the isotropic

Table 9.1 Modelled evolution of yield stress as a function of equivalent plastic strain.

Equivalent plastic strain	0	0.05	0.20	0.40
Yield stress (MPa)	370	410	420	460

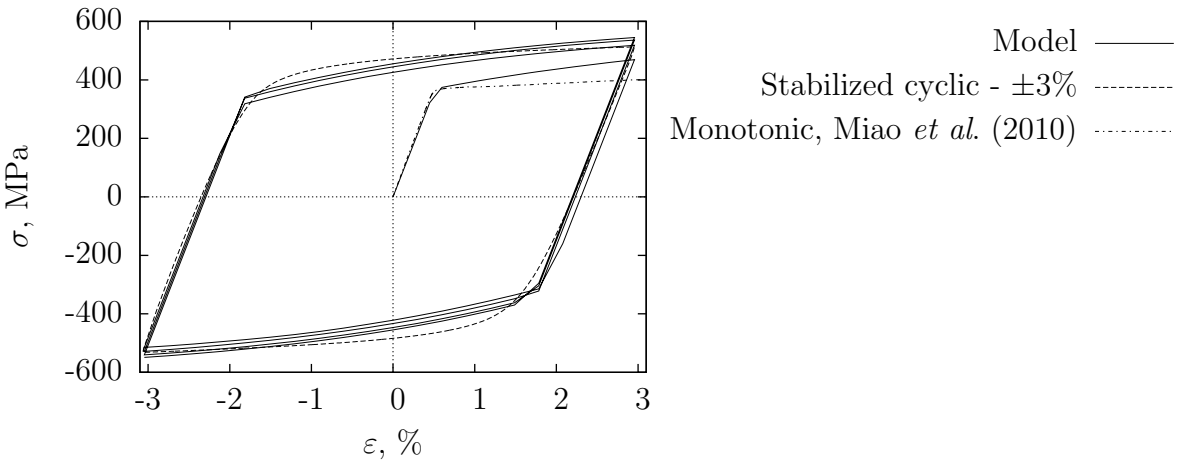

Figure 9.1 Comparison of modelled material behaviour with stabilized cyclic experimental data and uniaxial tensile data from Miao *et al.* (2010).

and kinematic hardening components contributed to strain-hardening for equivalent plastic strains between 0 and 0.40 while strain-hardening was only controlled by kinematic hardening for larger equivalent plastic strains. As a result, the simulated initial material behaviour did not correlate well with monotonic tensile test data, as illustrated in Figure 9.1. The limitations of the chosen material law are further discussed in Section 9.2.

9.1.3 Forming simulations

In Section 4.4.3, the first description of the novel sequence-sensitive forming simulation method referred to numerically calculated stresses induced by peening being "added" to the previous balanced residual stress state. This wording is not appropriate and was improved in the subsequent articles. A more accurate description of the method is that, at each simulation step, the previous balanced residual stress state is replaced by a new unbalanced one calculated with Eq. (4.9) using stresses induced by peening for the given step and the residual stresses at the end of the previous step.

9.2 Material behaviour during shot peening

A relatively simple material constitutive theory was chosen to represent the cyclic behaviour of AA2024-T351 (Section 4.4.2). When compared to the more complete material laws by Klemenz *et al.* (2009) and Zimmermann *et al.* (2010) summarized in Table 1.3, this approach required less experimental testing (thus lower investments) and did not require pro-

gramming a user-defined material law for the FE software. While the surface residual stress and the depth subjected to compressive residual stresses were correctly predicted for saturation conditions, the material law may have contributed to the notably overestimated residual stress amplitude at intermediate depths of 0.1 to 0.2 mm (Figure 4.22). Similarly, for full coverage peening, the calculated surface and maximum compressive residual stresses were in good agreement with experimentally determined values, but the underestimated depth subjected to compressive stress could be explained in part by the material model (Figure 5.4). Significant improvements are possible and desirable to better represent the impact behaviour over a wide range of peening conditions.

9.2.1 Cyclic behaviour

A non-linear combined isotropic-kinematic hardening constitutive theory was selected (ABAQUS Theory Manual, 2008). This material law takes into account the Bauschinger effect as well as the evolution of the cyclic yield strength with accumulated plastic strain. This evolution is however independent from the loading history. Experimental stress-strain curves presented in Figure 4.12 indicate that the uniaxial yield stress is strongly dependent upon the strain amplitude for AA2024-T351. Considering that shot peening generates a plastic strain gradient, material located at the edge of the plastically deformed layer experiences smaller strain amplitudes and should therefore reach a smaller cyclic yield stress than the material closer to the surface (assuming a cyclic hardening behaviour). In Klemenz *et al.* (2009), this strain memory phenomenon was taken into account using Equations (1.10) and (1.11). This type of model is not readily available in `ABAQUS` and requires programming a custom material constitutive theory. This endeavour was outside the scope of the current project.

When considering the results in Figure 4.22, it seems likely that neglecting the strain memory effect could have contributed to the discrepancies between the experimental and predicted data. Previous studies have shown that the residual stress amplitude increases concomitantly with increasing yield strength (Wang *et al.*, 1998; Hong *et al.*, 2008b). Building on the results from Figure 4.22, Figure 9.2 shows that at intermediate depths between 0.1 and 0.2 mm, the local yield stress increases with respect to its monotonic value due to the accumulation of plastic strain. However, the accumulated equivalent plastic strain (PEEQ or $\bar{\varepsilon}_p$) reaches values below 30% over ≈ 65 simulated impacts. This means that the average equivalent plastic strain experienced during each impact is less than 0.5%; this is of course a lower bound since impacts located far enough from a given element do not plastically deform this element. Considering the relatively low strain amplitudes expected in this region, the local yield stress increase may not be realistic and would overestimate the local compressive residual stress amplitude. Similarly, it has been shown that the depth subjected to compres-

sive residual stress decreases with increasing yield stress (Schiffner and Droste gen. Helling, 1999; Hong *et al.*, 2008b). The overestimated strength at intermediate depths could also explain in part the fact that numerical simulations underestimated the depth subjected to compressive stress for full coverage peening in Figure 5.4.

Comparison with isotropic hardening

Additional impact analyses involving the same impact sequence were conducted for two material constitutive theories (Gariépy *et al.*, 2012b):

1. The isotropic-kinematic hardening law described in Section 4.4.2;
2. The Johnson-Cook isotropic hardening law, without strain-rate and temperature dependencies, expressed as:

$$\sigma_0 = 265 + 426\bar{\varepsilon}_p^{0.34} \tag{9.1}$$

where σ_0 is the yield stress (in MPa) and $\bar{\varepsilon}_p$ is the equivalent plastic strain (Lesuer, 1999).

Simulations were conducted for an impact velocity of 33.7 m/s and an impact density of 34.3 mg/mm^2 (experimental "aluminium saturation"). Figure 9.3(a) presents the calculated results as well as the corresponding experimentally determined residual stress profile from Miao *et al.* (2010). The isotropic hardening law overestimated the residual stress amplitude more significantly than the isotropic-kinematic law. Unlike the isotropic-kinematic hardening law, the isotropic hardening model of Eq. (9.1) does not limit the yield stress: as plastic strain accumulates, the yield stress keeps increasing. This can lead to overestimated local yield stress and residual stress amplitude near the surface. An isotropic-kinematic hardening behaviour therefore represents more accurately the reversed loading phenomena involved in shot peening.

Klemenz *et al.* (2007) observed a similar phenomenon when comparing residual stress profiles predicted with isotropic-kinematic and isotropic hardening material models against experimental data for AISI 4140 steel. The difference for this material was even more significant than that illustrated in Figure 9.3(a) since AISI 4140 exhibited a cyclic softening behaviour that reduced the cyclic yield stress whereas the yield stress of AA2024-T351 increased during cyclic loading (Figure 4.12).

Experimental testing

The experimental uniaxial cyclic tests were performed with constant, fully reversed strains with a maximum strain amplitude of $\pm 3\%$. Although this methodology is common for shot

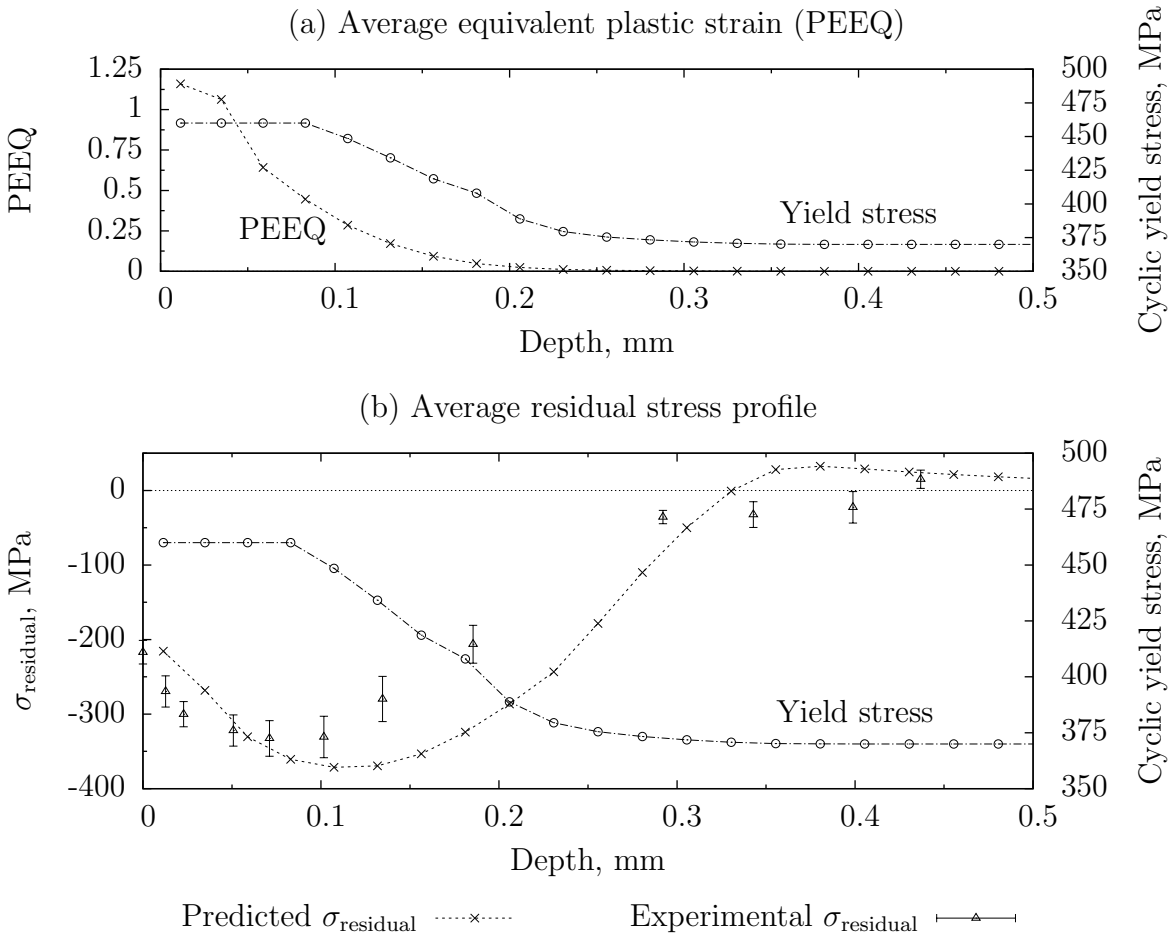

Figure 9.2 (a) Average equivalent plastic strain profile calculated for the simulations presented in Figure 4.22 for an impact velocity of 66.2 m/s. The resulting local cyclic yield stress based on the equations defined in Section 4.4.2 is also shown. (b) Comparison of the numerically predicted residual stress profiles and the corresponding experimental data from Miao *et al.* (2010).

peening modelling (Klemenz *et al.*, 2009; Zimmermann *et al.*, 2010), it is not representative of shot peening since the actual process:

1. Produces random tridimensional load paths at each point;
2. Requires accumulation of net compressive plastic strain normal to the surface and tensile plastic strain in the plane of the surface (on average) to achieve a compressive residual stress state;
3. Can induce calculated equivalent plastic strains in excess of 20% during a single impact for the experimental peening parameters considered in this study. Plastic strains could

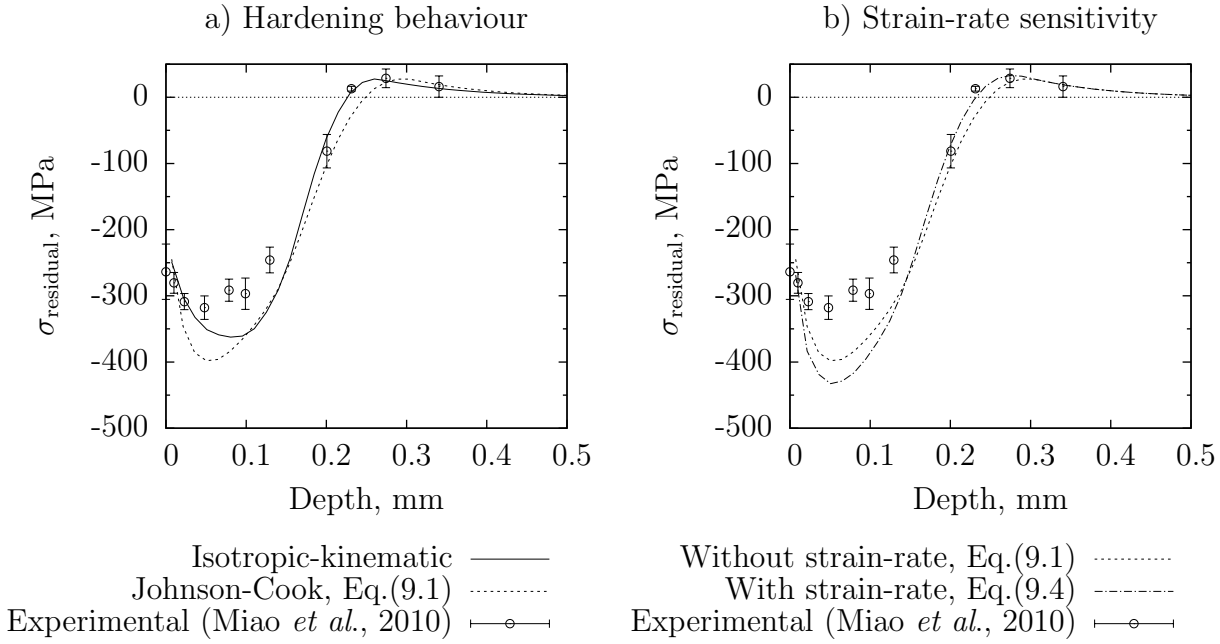

Figure 9.3 (a) Effect of the hardening behaviour on the calculated residual stress profile. (b) Effect of strain-rate sensitivity on the predicted residual stress profile. Impact velocity was 33.7 m/s the impact density at saturation was 34.3 mg/mm^2. All simulations were performed using the same impact sequence.

be even larger for peen forming applications requiring larger Almen intensities.

The cyclic testing methodology therefore requires improvements. The main difficulty remains buckling (Section 4.3.2). According to ASTM Standard E9 (2000), the critical buckling stress S_{cr} in the plastic regime can be determined as:

$$S_{cr} = C_e \pi^2 E_{\text{tangent}} / (L_c/\rho_{\min})^2 \tag{9.2}$$

with the minimum radius of gyration of the cross-section $\rho_{\min}$:

$$\rho_{\min} = \sqrt{\frac{I_{\min}}{A_{\text{CS}}}} \tag{9.3}$$

where C_e is the end-fixity coefficient, $E_{tangent}$ is the tangent modulus at the critical buckling stress, L_c is the column length, $I_{\min}$ is the minimum moment of inertia about the centroidal axis, and A_{CS} is the cross-section area. For a column with both ends fixed, $C_e = 4$. The maximum strain amplitude of $\pm 3\%$ was controlled by the thickness of the available plate

material, which prescribes $\rho_{\min}$.

Obviously, increasing the minimum radius of gyration $\rho_{\min}$ by using thicker material would allow reaching larger compressive stresses. However, the forces applied to the sample described in Figure 4.4 for a strain amplitude of ±3% were already 85 kN, which is quite close to the 100 kN limit of the available hydraulic grips. Another option for sheet and plate specimens would be to use a guiding fixture such as that presented by Cao *et al.* (2009).

9.2.2 Strain-rate sensitivity

The simulations neglected the effect of strain-rate on material strength. Since peen forming is inherently a dynamic process, strain-rate sensitivity should also be taken into account in future simulations (Section 1.4.2). It should be noted that shot peening can deform the material at rates as high as 10^6 s^{-1} (Meguid *et al.*, 2007), which is larger than the values generally achievable with equipment such as split Hopkinson pressure bars. It would be interesting to compare the performance of empirical relationships such as the Johnson-Cook and Cowper-Symonds equations to physically-based equations, such as Eq. (1.9), when extrapolating experimental data to even higher strain-rates.

For comparison purposes, an additional simulation was performed using the Johnson-Cook law with strain-rate dependence, formulated as:

$$\sigma_0 = \left[265 + 426 \times \bar{\varepsilon}_p^{0.34}\right] \left[1 + 0.015 \ln\left(\dot{\bar{\varepsilon}}_p^*\right)\right] \tag{9.4}$$

where $\dot{\bar{\varepsilon}}_p^*$ is the normalized equivalent plastic strain rate (Lesuer, 1999). The second term on the right of Eq. (9.4) indicates that the yield stress increases when the strain-rate increases. Figure 9.3(b) shows that including the strain-rate sensitivity increased the residual stress amplitude (as observed by Meguid *et al.* (2002)) and reduced the depth subjected to compressive residual stresses (Gariépy *et al.*, 2012b). These two phenomena are consistent with the increased transient yield stress of the material during the impact, as discussed in Section 9.2.1.

Experimental testing

It is worth noting that Klemenz *et al.* (2009) performed low temperature testing with relatively low strain-rate instead of high strain-rate testing at room temperature. This approach was motivated by the relationship between the temperature T and strain-rate $\dot{\varepsilon}$ terms in Eq. (1.9). Combining low temperature and high strain-rate could possibly provide useful information on the material behaviour at the very high strain-rates encountered during shot peening.

9.2.3 Thermal effects

Considering that most plastic strain energy is dissipated as heat, the large plastic strains accumulated during a short time period during shot peening could lead to a significant temperature increase at the surface. Rouquette *et al.* (2009) noted transient temperature increases as large as 180°C for a single impact of a steel shot on a steel target. Assuming that thermal and mechanical properties were independent from the temperature, thermal expansion effects led to a significant decrease of the residual stress amplitude between the surface and the depth of maximum compressive stress.

Thermal effects could be even more significant for low melting point materials such as aluminium alloys since the temperature increase could also affect their local mechanical properties. In addition, multiple impact simulations are likely to yield even larger temperature increases. Further study is required on this topic.

When considering the two peening strategies illustrated in Figure 7.3(b), *i.e.* multiple passes at a fast pace or a single pass at a slow pace, the latter could generate a larger maximum temperature increase since all impacts occur in quick succession at a given location, whereas in the former approach heat could be in part dissipated between passes.

9.2.4 Hydrostatic pressure

When studying damping of stress oscillations in the impact model (Figure 4.7), it was noted that the predicted hydrostatic stress reached values in excess of -1 GPa (for less than 1 μs) for the experimental peening parameters under study. Classical metal plasticity as used in this project relies on the deviatoric stress tensor and neglects the effect of hydrostatic stress on the yield locus. However, studies such as those of Bulatov *et al.* (1999) and Wilson (2002) have shown that the hydrostatic stress can affect the plastic behaviour of aluminium alloys. The transient strengthening effect of large hydrostatic pressure during shot peening could be the subject of future studies.

9.2.5 Plastic anisotropy

The differences between experimentally determined residual stress profiles acquired along the rolling and transverse direction (Figure 5.4) suggest that the material behaviour post-yielding is not always isotropic. This is consistent with the observations in Section 6.6 that elastic anisotropy and non-equibiaxial initial stresses cannot explain by themselves the development of non-uniform curvatures when peen forming small AA2024-T3 samples. However, based on the development presented in Section 6.4 and the results of Figure 5.4, plastic anisotropy may lead to smaller radii of curvature along the TD than along the RD whereas

observed radii are actually smaller along the rolling direction. It should be noted that the stress profiles in Figure 5.4 were acquired for 12.9 mm thick AA2024-T351 plates while peen forming experiments used 1.6 mm thick AA2024-T3 sheets and that those stress profiles should be validated with repeated measurements on a different sample.

While peen forming can be simulated using the plane stress assumption, impact loading during shot peening involves tridimensional loads. Considering the complexity and the number of parameters of successful material constitutive theories for shot peening modelling (Section 1.4.2), developing a tridimensional yield locus will require an excellent grasp of solid mechanics and extensive experimental testing.

9.2.6 Modelling approach

As for most numerical studies on shot peening, this project followed a methodology in which material properties were as much as possible determined from independent experiments rather than from calibration against experimentally determined residual stress profiles. While this approach requires more mechanical testing, it also provides a more accurate insight on the material behaviour. Considering the numerous factors affecting the material response during impacts, independent experiments allow identifying their individual contributions.

Even then, it is possible that two (or more) misestimated factors could lead to opposite errors. For instance, cyclic testing (Section 4.3.2) was limited to a strain amplitude of $\pm 3\%$. As a result, it was attempted to extrapolate the available experimental data for higher strain amplitudes typical of shot peening and a maximum cyclic yield stress of 460 MPa was assumed (Section 4.4.2). The data presented by Rodopoulos *et al.* (2004) indicate that the yield stress of AA2024-T351 should be in the range of 420 to 450 MPa, although the corresponding strain amplitude was not specified. The selected material constitutive theory may therefore have overestimated the cyclic yield stress, but the resulting overestimation of the residual stress values could have been cancelled out by the fact that strain-rate sensitivity was neglected in the simulations (Figure 9.3(b)).

A single material constitutive theory capable of describing the material behaviour over wide range of impact energies is certainly desirable. For a given aluminium alloy, the theory should be able to predict the response to peening parameters typical of fatigue life improvement as well as to higher energy parameters encountered in shot peen forming since the mechanisms involved are the same, albeit at different scales. Validating the model for the lower and upper bounds as well as the mid-range impact energies would then provide confidence in the model and avoid repeated and costly experimental validation for multiple set of peening parameters.

9.3 Peen forming modelling

9.3.1 Comments on the influence of initial stresses

The computational efficiency of the proposed methodology relies on the numerical observation that for a large number of impacts, initial stresses do not significantly affect further development of induced stresses near the surface.

While the mechanisms leading to the predicted phenomenon are complex, studying the basic principles can help to understand the observed trend. Consider an equibiaxial initial stress state $\boldsymbol{\sigma}_{\text{initial}}$ in a cartesian coordinate system with an in-plane stress $\sigma_{\text{plane}}^{\text{initial}}$ expressed as:

$$\boldsymbol{\sigma}^{\text{initial}} = \begin{bmatrix} \sigma_{\text{plane}}^{\text{initial}} & 0 & 0 \\ 0 & \sigma_{\text{plane}}^{\text{initial}} & 0 \\ 0 & 0 & 0 \end{bmatrix} \tag{9.5}$$

Impact loading initially imposes a compressive stress $-\sigma^{\text{pressure}} < 0$ perpendicular to the surface:

$$\boldsymbol{\sigma}^{\text{pressure}} = \begin{bmatrix} \sigma_{\text{plane}}^{\text{initial}} & 0 & 0 \\ 0 & \sigma_{\text{plane}}^{\text{initial}} & 0 \\ 0 & 0 & -\sigma^{\text{pressure}} \end{bmatrix} \tag{9.6}$$

This idealized stress state $\boldsymbol{\sigma}^{\text{pressure}}$ is instantly modified since a compressive strain perpendicular to the surface generates tensile strains parallel to the surface. Due to the constraint from the adjacent material, this develops an additional compressive stress $-\Delta\sigma_{\text{plane}}^{\text{reaction}} < 0$ parallel to the surface:

$$\boldsymbol{\sigma}^{\text{reaction}} = \begin{bmatrix} \sigma_{\text{plane}}^{\text{initial}} - \Delta\sigma_{\text{plane}}^{\text{reaction}} & \tau_{xy} & \tau_{xz} \\ \tau_{xy} & \sigma_{\text{plane}}^{\text{initial}} - \Delta\sigma_{\text{plane}}^{\text{reaction}} & \tau_{yz} \\ \tau_{xz} & \tau_{yz} & -\sigma^{\text{pressure}} \end{bmatrix} \tag{9.7}$$

It should be noted that the following analysis uses a highly simplified representation of the impact process since the actual stresses in the material are functions of both time and position and include tridimensional shear stresses τ. In addition, the development of stresses at a given location is a function of the constraints provided by the surrounding material. This introduces a complex relationship between $\sigma_{\text{plane}}^{\text{initial}}$ and $\Delta\sigma_{\text{plane}}^{\text{reaction}}$ that cannot be easily described in the plastic regime.

In the context of pressure-independent plasticity, yielding is controlled by the deviatoric

stress tensor $\mathbf{s}$ calculated as:

$$\mathbf{s} = \boldsymbol{\sigma} - \frac{\mathbf{I}}{3}\,\mathrm{trace}(\boldsymbol{\sigma}) \tag{9.8a}$$

$$= \boldsymbol{\sigma} - \frac{\mathbf{I}}{3}\,(2\sigma_{\mathrm{plane}}^{\mathrm{initial}} - 2\Delta\sigma_{\mathrm{plane}}^{\mathrm{reaction}} - \sigma^{\mathrm{pressure}}) \tag{9.8b}$$

where $\mathbf{I}$ is the identity matrix (ABAQUS Theory Manual, 2008). Equation (9.8) suggests that a compressive initial stress state $\sigma_{\mathrm{plane}}^{\mathrm{initial}} < 0$ tends to algebraically increase the hydrostatic pressure P and the diagonal components of the deviatoric stress tensor. Since the three terms on the diagonal of $\boldsymbol{\sigma}$ become compressive during the impact, this decreases the absolute values of the deviatoric stress components. A compressive initial state would therefore inhibit plastic flow. As a result, a greater portion of the fixed kinetic energy of the impacting shot will be stored as elastic deformation and then released, thus reducing the amount of kinetic energy converted into plastic strains. Oppositely, a tensile initial stress state $\sigma_{\mathrm{plane}}^{\mathrm{initial}} > 0$ would facilitate plastic deformation of the material.

When compared to the stress-free case, the decreased plastic deformation in presence of compressive initial stresses would reduce plastic stretching of the surface. The variation of the resulting compressive elastic in-plane strain and residual stress $\Delta\sigma^{\mathrm{impact}}$ state due to impact would be less significant for the compressively pre-stressed material, as schematically illustrated in Figure 9.4. While this variation certainly does not exactly cancel the difference in terms of initial stresses, it tends to reduce the difference between the final residual stress states of the stress-free and pre-stressed cases $|\Delta\sigma^{\mathrm{final}}|$ below the initial stress amplitude $|\sigma^{\mathrm{initial}}|$. As the number of impact increases, the residual stress states near the surface for stress-free and pre-stressed materials would therefore converge. Oppositely, tensile initial stresses would increase plastic stretching, leading to a greater residual stress variation that would partly cancel the higher initial stresses (Figure 9.4(c)).

Single impact simulations were performed for a 600 μm diameter shot with a velocity of 66.2 m/s. Model dimensions, as defined in Figure 4.5, are presented in Table 9.2. Three initial stress states were considered: an equibiaxial compression of -100 MPa, stress-free and an equibiaxial tension of 100 MPa. The energy dissipated through plastic strains was evaluated for each case. It was found that the compressive stress state decreased the dissipated energy by 2.4% and that the tensile stress state increased the plastic strain energy by 5.3% with respect to the stress-free state, which supports the hypothesis discussed herein.

Similarly, in the case of a non-equibiaxial stress state such as that presented in Figure 6.8, larger plastic strains would be forced in the direction with the algebraically larger stress, thus tending to reduce the difference between the induced stress profiles along each direction.

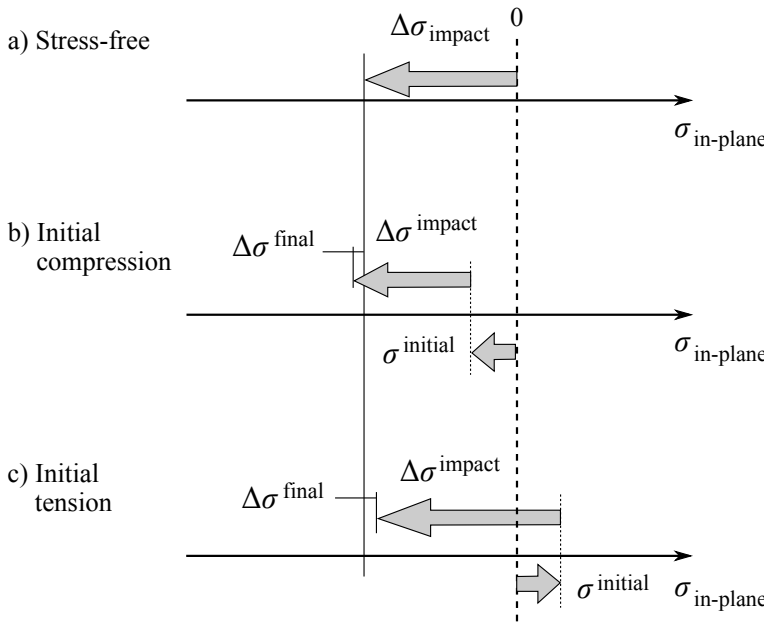

Figure 9.4 Schematic explanation of the influence of initial stresses σ^{initial} on the residual stress variation due to impacts $\Delta\sigma^{\text{impact}}$. The stress-free case (a) is compared to compressively (b) and tensilely (c) pre-stressed cases.

9.3.2 Choice of a stress-based methodology

When compared to strain-based methods such as that of Wang *et al.* (2006), the novel approach introduced in this project reduced the required calibration by relying on accurate impact simulations to provide the stress profiles induced by shot peening. It is worth noting that developing a numerical strain-based approach would be quite challenging since the predicted average in-plane plastic strain was found to be dependent upon the model size (Figure 4.8). As the impacted area became smaller relative to the total model area (*i.e.* increasing t_{ext}), plastic strain profiles reached higher values due to the greater compliance of the unimpacted region. It would therefore be difficult to determine appropriate dimensions for the impact model and exploit the calculated plastic strain profiles.

Relying on calculated induced stress profiles also has shortcomings: forming simulations can fail to adequately predict the response of a component when the predicted induced stresses

Table 9.2 Model dimensions used to study the influence of initial stresses during a single impact.

t_{ext}	t_{int}	I	Mesh size	Thickness
0.25 mm	0.15 mm	0.75 mm	25 μm	1.6 mm

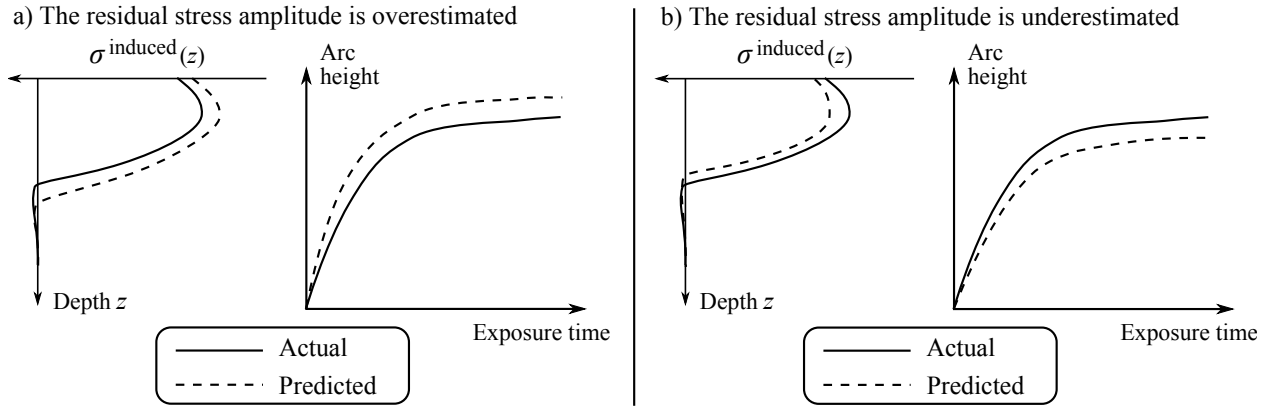

Figure 9.5 Influence of (a) overestimated and (b) underestimated residual stress amplitude and/or depth on the resulting saturation curves.

are incorrect. For illustration purposes, consider the two possible situations and their effects on calculated saturation curves (Figure 1.2):

1. FE simulations overestimate the induced stress amplitude and/or depth:
   In this case, the predicted arc heights will also be overestimated (Section 1.1.2), as illustrated in Figure 9.5(a).
2. FE simulations underestimate the induced stress amplitude and/or depth:
   The predicted arc heights will also be underestimated, as shown in Figure 9.5(b). This behaviour was observed for case B in Table 6.1 and Figure 6.14. As a result, it was chosen not to study and model this set of shot peening conditions in the following investigation of the influence of the peening trajectory (Chapter 7) since predicted arc heights near "aluminium saturation" were systematically underestimated.

The novel incremental stress-based approach could predict with good accuracy the complex curvatures resulting from boundary conditions, material orthotropy and peening trajectory. Previous research had not attempted to model these phenomena. It is believed that the promising results achieved in this project justify further work to improve both the impact and forming simulation models.

9.3.3 Calibration

Although it was attempted to remove the need for experimental calibration in the proposed peen forming simulation methodology, this objective could not be fully achieved. Experimental data (albeit limited) is still necessary to establish the relationship between the exposure time and the number of simulation steps (Chapters 4, 6 and 8) or the number of

peening increments (Chapter 7).

As presented in Figure 4.20 and schematically described in Figure 9.6, altering the relationship between the exposure time (or number of passes or impact density) and the number of simulation steps tends to compress or extend the saturation curve horizontally. In addition, following the hypothesis by Cao *et al.* (1995) that peening always restores the same induced stress profile, all curves would tend to the same saturated arc height corresponding to that calculated after an infinite number of simulation steps. It should be noted that FE simulations conducted in the present work suggest that the induced stress profiles does not fully stabilize, as shown in Figure 7.16. This behaviour may however be caused by an inadequate material constitutive theory.

Small errors in the predicted induced stress profiles may be cancelled by altering the relationship between the exposure time and the number of simulation steps, especially if the induced stress amplitude and/or depth is overestimated. In this situation, using a smaller number of steps for a fixed exposure time would stretch the curve horizontally, thus improving the correlation between the experimental and predicted data (Figure 9.7). On the other hand, if the induced stress amplitude is underestimated, some corrections are still possible for low exposure time (or coverage), but could not lead to accurate predictions for higher exposure times since the calculated saturation curve tends towards too low a value (Figure 9.5(b)). It should be kept in mind that such corrections may provide accurate predictions within a specific range of exposure times, but could lead to inaccurate values in other ranges. Accurate induced stress predictions are therefore always desirable.

9.3.4 Experimental results by Kulkarni et al. (1981)

As mentioned in Section 1.3, the experimental research by Kulkarni *et al.* (1981) contains a wealth of information that could be used as a basis for future modelling works. Their results describe and quantify significant phenomena that the simulation methodology developed in this project cannot predict yet, such as:

1. Rectangular samples with a length-to-width ratio of 4 exhibited essentially the same curvatures along both directions whereas square samples developed almost cylindrical contours (*i.e.* very large radius along one direction);
2. Sheet thickness can affect the development of curvature beyond the behaviour described by Eq. (1.4). For a rectangular sample with a relatively small thickness peened to a high impact density, the radius of curvature along the long direction increased significantly while the radius along the short direction decreased, leading to a nearly cylindrical contour;

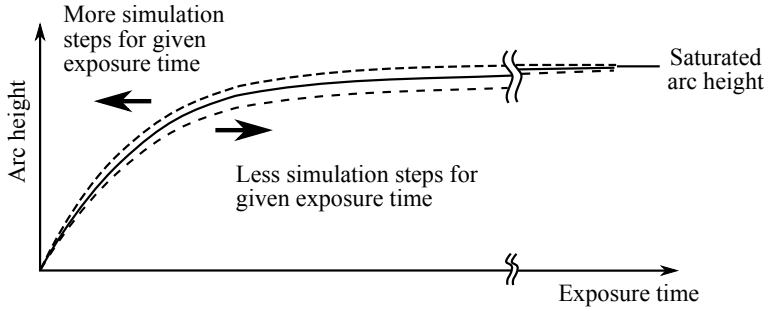

Figure 9.6 Schematic illustration of the influence of the relationship between the exposure time and the number of simulation steps.

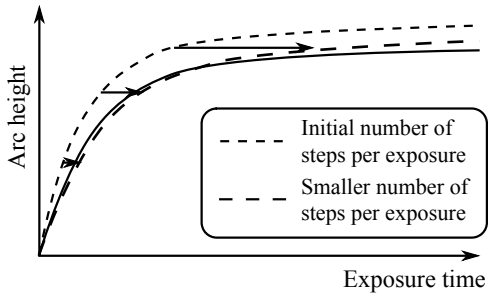

Figure 9.7 Possible correction of the influence of overestimated induced stress profiles through the relationship between the exposure time and the number of simulation steps.

It should be noted that their experiments were conducted with unconstrained samples. This could possibly explain the difference their observations and the results presented in Chapter 7, which involved constrained square specimens.

Further work is required to correctly simulate the influence of component thickness on the development of curvature. Based on the definition of "relative thickness" by Kulkarni *et al.* (1981), the experiments conducted in the present work used "relatively thick" samples. On the other hand, Kulkarni *et al.* (1981) performed large-scale trials and observed an almost cylindrical contour for peen formed 2.44 m × 0.61 m, 4.6 mm thick ("relatively thin") AA2024-T3 plate. Considering that these dimensions are quite representative of aerospace components such as wing skin panels (Moore, 1982; VanLuchene *et al.*, 1995), the experimentally observed behaviour should be successfully modelled in order to achieve useful predictions for industrial applications.

9.4 Towards industrial peen forming simulations

In the article presented in Chapter 8, the potential applications of peen forming simulations in an industrial context were discussed. However, the examples presented used many

simplifying assumptions when compared to the actual operations described in Section 1.6.

1. The material was assumed to be isotropic. This assumption may not be true for rolled sheets and plates, as presented in Chapter 6. While the experimental testing required to accurately describe the anisotropic material state can be quite costly, especially for initial stresses and plastic anisotropy (Section 9.2), such testing may be required in order to achieve quantitatively accurate predictions. For integrally stiffened components where a considerable quantity of material is machined away, initial stresses could also have an effect since such components can develop significant curvatures following machining due to internal stress redistribution.

   Investments required for complete material characterization would be more useful when peen forming a relatively large series of parts such as wing skin panels. This is especially true if multiple panels are manufactured starting from the same alloy and plate thickness. The relatively high cost of mechanical testing may not be justified when shaping or performing distortion correction on a small number of parts.

2. Peen forming large components generally involves moving the peening equipment (nozzles or wheels) over the surfaces. This can lead to unreasonable computational cost for industrial purposes. In Chapter 7, including the actual peening trajectory in the forming simulations led to a computation time of 2 to 17 h for small strips and sheets while similar spatially uniform simulations in Chapters 4 and 6 were completed in less than 10 minutes. Considering that simulations for realistic components in Section 8.5 already took as much as 7.5 h without taking into account the peening trajectory, it seems likely that peening trajectories will have to be simulated in a simplified manner for actual components. It should be noted that the computational cost of forming simulations (*i.e.* excluding impact simulations) could also be reduced with more efficient data management.

CONCLUSION

This thesis investigated and refined the potential applications of finite element modelling in the fields of shot peening and peen forming. These complex processes involve multiple concurrent mechanisms and numerical simulation can provide very useful insights regarding their importance and interactions. The purpose was to achieve quantitatively accurate predictions and demonstrate their potential for both scientific inquiry and industrial applications.

An improved dynamic impact model was first proposed. The random nature of shot peening as well as the cyclic behaviour of AA2024-T351 were taken into account. This led to fairly good predictions in terms of residual stresses, even though the selected material constitutive theory remained relatively simple, when compared to recent simulations works. These results showed the interest of combining stochastic impact simulations with a material law suitable for the reversed loading paths encountered in shot peening.

The potential of such a model to complement physical data was illustrated through a combined experimental and numerical characterization of AA2024-T351 shot peened with parameters typical of fatigue life improvement applications. Special attention was also given to the heterogeneous nature of the shot peened material, an important aspect that most current fatigue life prediction models neglect and that could be effectively investigated with numerical simulation. This study also revealed significant microstructural changes near the peened surface for the specific material and peening parameters studied.

A novel multiscale strategy for modelling the peen forming process was introduced. The approach combined the advantages of existing methods and relied on the unbalanced induced stress profiles predicted by the impact analyses to simulate the shaping effect associated with shot peening. To model the incremental build-up of curvature during peen forming, these unbalanced stress profiles were input repeatedly into shell elements using a computationally-efficient interpolation method. Validation with small-scale experiments using AA2024-T3 samples showed that this strategy correctly predicted the development of non-uniform curvatures arising from the boundary conditions of the Almen holder.

The potential effects of sheet rolling direction orientation on the curvatures generated by peen forming were then studied. The effects of elastic and plastic orthotropy, as well as initial residual stresses, were qualitatively discussed. The novel forming simulation approach provided a quantitative assessment of the influences of elastic orthotropy and initial stresses. Comparison with experimental data showed that plastic orthotropy may have to be taken into account in some cases to obtain accurate peen forming predictions.

The methodology was also improved so as to represent more realistically the peening

equipment trajectory, a potentially significant factor when shot peening is conducted as a single pass at a slow pace. The experimental shot stream was characterized and a simplified model was suggested. Simulations qualitatively predicted the non-uniform local radii of curvature originating from the boundary conditions as well as the asymmetry that is believed to arise from the peening trajectory.

The potential applications of peen forming simulation in an industrial context were illustrated using representative wing skin panels. Finite element modelling provided the versatility required to simulate features such as variable thicknesses and integral stiffeners as well as the complex peening treatments involved in actual procedures.

In conclusion, the main contribution of this thesis is the development and validation of accurate and computationally-efficient finite element models for predicting the response of AA2024-T351 subjected to both shot peening and peen forming. Although the novel peen forming simulation strategy was not validated with a full-scale component, this project put in place some of the important building blocks required to achieve accurate yet efficient peen forming simulations in an industrial context. This has the potential to lead to significant costs and time savings related to the forming of wing panels.

Limitations and future studies

Several important questions have been raised throughout this project and require further research.

Shot peening modelling

First, the material law used in this project is certainly incomplete and needs to be improved. The first step would be to conduct an extensive material characterization campaign involving at least asymmetric uniaxial cyclic testing up to higher strain amplitudes and high strain-rate testing. With this data, the cyclic behaviour, the strain memory phenomenon as well as the strain-rate sensitivity could be assessed. Considering the possible influence of increased temperatures during shot peening, it could also be useful to perform high-temperature testing, especially on low melting point materials such as aluminium alloys. The experimental data could then be used to choose and program an appropriate material constitutive theory and determine its parameters. The effect of temperature rise during repeated impacts, both in terms of thermal expansion and mechanical properties variations, should be included in this material law. In addition, pressure-dependent yield criteria could be investigated. The validity of the impact model dimensions should also be confirmed for the new material constitutive theory. Obviously, such a campaign will have to be repeated for each material under

study. It will then be interesting to evaluate the relative importance of each behaviour for similar alloys (*e.g.* aluminium alloys 2xxx and 7xxx) and for different types of materials (*e.g.* steel, titanium, nickel alloys).

A useful complement to conventional mechanical testing would be instrumented indentation. By continuously recording the indentation force and depth, the local mechanical properties could be estimated at different shot peening exposure times. The evolution of mechanical properties throughout peening would then be known. The response of the already impacted material to further impacts could therefore be better understood, instead of relying only on the measured properties of the virgin material subjected to simplified load cases.

The importance of plastic anisotropy should be studied further through the determination of residual stress profiles along different directions in rolled, cast and forged components. If it is deemed significant, once a reliable material constitutive theory is validated for an isotropic material, it should be extended to a tridimensionally anisotropic material. The contribution of plastic anisotropy to the development of non-uniform curvatures could then be quantified.

Another modelling option is microstructure-based models. The development of crystal plasticity laws including cyclic, high strain-rate, thermal and high-pressure behaviour would lead to a more fundamental understanding of the impact process based on basic microstructural mechanisms such as dislocation glide on slip planes. The effects of grain size and crystallographic texture on the resulting material state could also be evaluated. The first step in this direction would be to conduct single impact experiments on single crystals with different crystallographic orientations to explore the deformation mechanisms with EBSD or TEM. Additional impacts could then be added to investigate the interactions between adjacent impacts.

Preliminary impact simulation results suggest that the current random impact model overestimates surface roughness and coverage accumulation rate. Although a more accurate material constitutive theory could improve those predictions, these aspects need to be investigated since:

- Roughness is an important factor contributing to the overall fatigue life improvement by shot peening. The ability to accurately predict the surface topography would allow correlations between predicted roughness, residual stresses and work-hardening state to be made;
- Optical coverage is a key method used in industry to monitor shot peening and peen forming treatments. Accurate coverage predictions would facilitate correlations between experimental and numerical data. This will require a more philosophical approach in order to understand how the human eye (or automated evaluation methods) perceives impact dimples.

Finally, once accurate and reliable models are established, FE modelling results, either from isotropic or anisotropic material or from microstructure-based simulations, could be a driving force towards the development of new fatigue life prediction models taking into account the heterogeneity of the material state after shot peening. Numerical simulation indeed provides information difficult to obtain with experimental methods. One interesting approach would be to model crack propagation in the predicted material state or microstructure with methods such as the virtual crack closure technique. It should be noted that experimental testing will remain a key aspect of material characterization after shot peening since it still provide and most likely will continue to provide unique data on complex phenomena such as surface damage.

Peen forming modelling

First, additional controlled forming experiments are required to comprehend the influence of sample aspect ratio and relative thickness. Based on previous research, experiments should be conducted with larger samples (on the order of hundreds of millimetres) with varying aspects ratios and a wide range of thicknesses. The resulting radii of curvature should be assessed to identify the development of cylindrical contours in some cases. The simulation method then needs to be improved so as to adequately capture these significant phenomena. Factors such as gravitational loads due to the weight of the component, bending under impact loading and vibration should be investigated. This will be a key aspect towards modelling large-scale and relatively thin industrial components.

Different boundary conditions should be considered in future experiments. In this project, two types of constraints were used when peen forming small samples. This allowed evaluating their influence on resulting curvatures and represented an interesting and successful test of modelling capabilities. However, industrial applications of peen forming (with the exception of stress peen forming) generally involve unconstrained specimens and this situation needs to be investigated further.

Further work is required towards simulating peen forming of industrial components. First, gravity was neglected in all simulations. This is certainly not realistic for long and thin parts such as wing skins, where the weight of the part can induce significant bending depending on the support jig. In addition, the interactions between different peen forming treatments on a given area were not thoroughly studied. The proposed hypothesis neglected the possible additive effect of successive peening with different parameters and needs to be refined and validated through additional numerical and experimental investigation. The meaning and the validity of predicted average induced stress profiles at low impact densities, where impacts are mostly separated, should also be examined in more details in the perspective of simulating

peen forming treatments performed at low coverage. Finally, validation with actual aerospace components is required to demonstrate the potential of numerical simulation in this field and determine the possible shortcomings that need to be addressed.

This project only considered convex peen forming without preloads. Considering the industrial applications stress peen forming, where elastic prestresses are applied, and concave forming, which involves much larger impact energies, these related processes need to be examined in more details. It would be interesting to verify the applicability of the proposed impact and forming models to those cases. This could lead to a powerful, complete simulation tool that encompasses all peen forming methods.

Another interesting industrial application of the general methodology outlined in this project would be to better correlate physical process parameters with the associated Almen intensity. This work outlined the shortcomings associated with neglecting the incremental nature of peen forming, an assumption often used to relate the induced stress profiles to the resulting arc heights. Unlike previous studies, the proposed methodology simultaneously leads to fairly accurate predictions of residual stress profiles and peen formed contours.

REFERENCES

ABAQUS Analysis User's Manual (2008). *ABAQUS Analysis User's Manual, version 6.8*. Dassault Systemes.

ABAQUS Theory Manual (2008). *ABAQUS Theory Manual, version 6.8*. Dassault Systemes.

AL-HASSANI, S. (1984). An engineering approach to shot peening mechanics. *Proc. 2nd conf. shot peening (ICSP2)*. Chicago, USA, 275–282.

ARUN PRAKASH, N., GNANAMOORTHY, R. and KAMARAJ, M. (2010). Microstructural evolution and mechanical properties of oil jet peened aluminium alloy, AA6063-T6. *Mater. and Design*, 31, 4066–4075.

ASM Handbook (1991). *ASM Handbook, Volume 4, Heat Treating*, ASM International Heat Treating of Nonferrous Alloys. In ASM Handbooks Online, http://www.asmmaterials.info ASM International, 2002.

ASTM Standard E384 (2011). *ASTM Standard E384 - Standard test method for Knoop and Vickers hardness of materials*. ASTM International, West Conshohocken, PA, USA.

ASTM STANDARD E606 (1992). *Standard Practice for Strain-Controlled Fatigue Testing*. ASTM International.

ASTM Standard E837 (2008). *ASTM Standard E837 - 08e1 - Standard test method for determining residual stresses by the hole-drilling strain-gage method*. ASTM International, West Conshohocken, PA, USA.

ASTM STANDARD E9 (2000). *Standard Test Methods of Compression Testing of Metallic Materials at Room Temperature*. ASTM International.

BAGHERIFARD, S., GHELICHI, R. and GUAGLIANO, M. (2010). A numerical model of severe shot peening (SSP) to predict the generation of a nanostructured surface layer of material. *Surf. Coat. Technol.*, 204, 4081–4090.

BARRETT, C. F. (1984). *Tool and manufacturing engineers handbook*, SME Peen forming.

BAUGHMAN, D. L. (1984). An overview of peen forming technology. *Proc. 2nd conf. shot peening (ICSP2)*. Chicago, IL, USA, 28–32.

BAUGHMAN, D. L. (1987). U.S. Patent No. 4,694,672 - Method and apparatus for imparting a simple contour to a workpiece. U.S. Patent and Trademark Office.

BENEDETTI, M., FONTANARI, V., SCARDI, P., RICARDO, C. L. A. and BANDINI, M. (2009). Reverse bending fatigue of shot peened 7075-T651 aluminium alloy: The role of residual stress relaxation. *Int. J. Fatigue*, 31, 1225–1236.

BHUVARAGHAN, B., SRINIVASAN, S. M., MAFFEO, B., MCCLAIN, R. D. and POTDAR, Y. (2010). Shot peening simulation using discrete and finite element methods. *Adv. Eng. Softw.*, 41, 1266–1276.

BHUVARAGHAN, B., SRINIVASAN, S. M., MAFFEO, B. and PRAKASH, O. (2011). Constrained probabilistic multi-objective optimization of shot peening process. *Eng. Optim.*, 43, 657–673.

BOLSHAKOV, A., OLIVER, W. C. and PHARR, G. M. (1996). Influences of stress on the measurement of mechanical properties using nanoindentation: Part II. Finite element simulations. *J. Mater. Res.*, 11, 760–768.

BOURAOUI, C., BEN SGHAIER, R. and FATHALLAH, R. (2009). An engineering predictive design approach of high cycle fatigue reliability of shot peened metallic parts. *Mater. and Design*, 30, 475–486.

BROWN, W. F. J., MINDLIN, H. and HO, C. Y., éditors (1996). *Aerospace structural metals handbook*, CINDAS/UASF CRDA handbooks operation, Purdue University, vol. 3.

BULATOV, V. V., RICHMOND, O. and GLAZOV, M. V. (1999). An atomistic dislocation mechanism of pressure-dependent plastic flow in aluminum. *Acta Mater.*, 47, 3507–3514.

BURMEISTER, T. J. (1984). Peen forming of airfoil shapes for aircraft wing sections. *Proc.* 2^{nd} *conf. shot peening (ICSP2)*. Chicago, IL, USA, 1–5.

CAO, J., LEE, W., CHENG, H. S., SENIW, M., WANG, H.-P. and CHUNG, K. (2009). Experimental and numerical investigation of combined isotropic-kinematic hardening behavior of sheet metals. *Int. J. Plasticity*, 25, 942–972.

CAO, W., FATHALLAH, R. and CASTEX, L. (1995). Correlation of Almen arc height with residual stresses in shot peening process. *Mater. Sci. Technol.*, 11, 967–973.

CHENG, Y.-T. and CHENG, C.-M. (1998). The effects of 'sinking in' and 'piling up' on estimating the contact area under load in indentation. *Philos. Magazin. Lett.*, 78, 115–120.

CHILD, D. J., WEST, G. D. and THOMSON, R. C. (2011). Assessment of surface hardening effects from shot peening on a Ni-based alloy using electron backscatter diffraction techniques. *Acta Mater.*, 59, 4825–4834.

CLAUSEN, R. and STANGENBERG, J. (1999). Roughness of shot-peened surfaces – definition and measurement. *Proc.* 7^{th} *conf. shot peening (ICSP7)*. Warsaw, Poland, 69–77.

COCHENNEC, F., ROUHAUD, E., ROUCOULES, L. and FLAN, B. (2009). Numerical and experimental investigation on shot-peening induced deformation. Application to sheet metal forming. *Adv. X-ray Analysis*, 52, 511–518.

CURTIS, S., DE LOS RIOS, E. R., RODOPOULOS, C. A. and LEVERS, A. (2003). Analysis of the effects of controlled shot peening on fatigue damage of high strength aluminium alloys. *Int. J. Fatigue*, 25, 59–66.

DAI, K. and SHAW, L. (2007). Comparison between shot peening and surface nanocrystallization and hardening processes. *Mater. Sci. and Eng. A*, 463, 46–53.

DE LOS RIOS, E. R., TRULL, M. and LEVERS, A. (2000). Modelling fatigue crack growth in shot-peened components of Al 2024-T351. *Fatigue Fract. Eng. Mater. Struct.*, 23, 709–716.

DROUIN, P. (2006). *Simulation d'un procédé de mise en forme par grenaillage aux ultrasons avec billes*, Ecole Polytechnique de Montréal.

EBENAU, A., O., V. and MACHERAUCH, E. (1987). Influence of the shot peening angle on the condition of near-surface layers in materials. *Proc.* 3^{rd} *conf. shot peening (ICSP3).* Garmisch-Partenkirchen, Germany, 253–260.

ELTOBGY, M. S., NG, E. and ELBESTAWI, M. A. (2004). Three-dimensional elastoplastic finite element model for residual stresses in the shot peening process. *Proc. Inst. Mech. Eng. Part B: J. Engineering Manufacture*, 218, 1471–1481.

EVANS, R. W. (2002). Shot peening process: Modelling, verification, and optimisation. *Mater. Sci. Technol.*, 18, 831–839.

FATHALLAH, R., INGLEBERT, G. and CASTEX, L. (1996). Modelling of shot peening residual stresses and plastic deformation induced in metallic parts. *Proc.* 6^{th} *conf. shot peening (ICSP6).* San Francisco, CA, USA, 464–473.

FATHALLAH, R., LAAMOURI, A., SIDHOM, H. and BRAHAM, C. (2004). High cycle fatigue behavior prediction of shot-peened parts. *Int. J. Fatigue*, 26, 1053–1067.

FATHALLAH, R., SIDHOM, H., BRAHAM, C. and CASTEX, L. (2003). Effect of surface properties on high cycle fatigue behaviour of shot peened ductile steel. *Mater. Sci. Technol.*, 19, 1050–1056.

FEJA, K., HAUK, V., KRUG, W. K. and PINTSCHOVIUS, L. (1987). Residual stress evaluation of a cold-rolled steel strip using X-rays and a layer removal technique. *Mater. Sci. Eng.*, 92, 13–21.

FERREIRA, J. A. M., BORREGO, L. F. P. and COSTA, J. D. M. (1996). Effects of surface treatments on the fatigue of notched bend specimens. *Fatigue Fract. Eng. Mater. Struct.*, 195, 111–117.

FRANCHIM, A. S., DE CAMPOS, V. S., TRAVESSA, D. N. and DE MOURA NETO, C. (2009). Analytical modelling for residual stresses produced by shot peening. *Mater. Design*, 30, 1556–1560.

FRIBOURG, G. (2009). *Couplage entre précipitation et plasticité dans un alliage d'aluminium 7xxx : application à des traitements thermomécaniques de réduction des distorsions dans des composants aéronautiques*, Institut Polytechnique de Grenoble.

FRIESE, A., LOHMAR, J. and WÜSTEFELD, F. (2002). Current applications of advanced peen forming implementation. *Proc. 8th conf. shot peening (ICSP8)*. Garmisch-Partenkirchen, Germany, 53–61.

FRIJA, M., HASSINE, T., FATHALLAH, R., BOURAOUI, C. and DOGUI, A. (2006). Finite element modelling of shot peening process: Prediction of the compressive residual stresses, the plastic deformations and the surface integrity. *Mater. Sci. Eng. A*, 426, 173–180.

GARDINER, T. S. and PLATTS, M. J. (1999). Towards peen forming process optimisation. *Proc. 7th conf. shot peening (ICSP7)*. Warsaw, Poland, 235–243.

GARIÉPY, A., LAROSE, S., PERRON, C., BOCHER, P. and LÉVESQUE, M. (2012a). On the effect of the orientation of sheet rolling direction in shot peen forming. *Submitted to J. Mater. Process. Technol. on July 9, 2012.*

GARIÉPY, A., LAROSE, S., PERRON, C. and LÉVESQUE, M. (2011). Shot peening and peen forming finite element modelling - towards a quantitative method. *Int. J. Solids Struct.*, 48, 2859–2877.

GARIÉPY, A., PERRON, C., BOCHER, P. and LÉVESQUE, M. (2012b). Finite element simulation of shot peening: Prediction of residual stresses and surface roughness. *International Conference on Aluminium Alloys (ICAA13)*. Pittsburgh, PA, USA.

GRASTY, L. V. and ANDREW, C. (1996). Shot peen forming sheet metal: finite element prediction of deformed shape. *Proc. Inst. Mech. Eng. Part B: J. Engineering Manufacture*, 210, 361–366.

GUAGLIANO, M. (2001). Relating Almen intensity to residual stresses induced by shot peening: a numerical approach. *J. Mater. Process. Technol.*, 110, 277–286.

GUECHICHI, H. and CASTEX, L. (2006). Fatigue limits prediction of surface treated materials. *J. Mater. Process. Technol.*, 172, 381–387.

GULFSTREAM (2011). Gulfstream G280. Specifications sheet available at: http://www.gulfstream.com.

HAN, K., OWEN, D. R. J. and PERIC, D. (2002). Combined finite/discrete element and explicit/implicit simulations of peen forming process. *Eng. Comput.*, 19, 92–118.

HAN, K., PERIC, D., CROOK, A. J. L. and OWEN, D. R. J. (2000a). A combined finite/discrete element simulation of shot peening processes - Part I: studies on 2D interaction laws. *Eng. Comput.*, 17, 593–619.

HAN, K., PERIC, D., OWEN, D. R. J. and YU, J. (2000b). A combined finite/discrete element simulation of shot peening processes - Part II: 3D interaction laws. *Eng. Comput.*, 17, 680–702.

HARBURN, B. and MILLER, J. C. (1982). U.S. patent No. 4,329,862 - Shot peen forming of compound contours. U.S. Patent and Trademark Office.

HERZOG, R., ZINN, W., SCHOLTES, B. and WOHLFAHRT, H. (1996). The significance of Almen intensity for the generation of shot peening residual stresses. *Proc.* 6^{th} *conf. shot peening (ICSP6)*. San Francisco, CA, USA, 270–281.

HIRAI, N., TOSHA, K. and ROUHAUD, E. (2005). Finite element analysis of shot peening - on the form of a single dent. *Proc.* 9^{th} *conf. shot peening (ICSP9)*. Marne-la-Vallée, France, 82–87.

HOLZAPFEL, H., SCHULZE, V., VÖHRINGER, O. and MACHERAUCH, E. (1998). Residual stress relaxation in an AISI 4140 steel due to quasistatic and cyclic loading at higher temperature. *Mater. Sci. Eng. A*, 248, 9–18.

HOMER, S. E. and VANLUCHENE, R. D. (1991). Aircraft wing skin contouring by shot peening. *J. Mater. Shaping Technol.*, 9, 89–101.

HONDA, T., RAMULU, M. and KOBAYASHI, A. S. (2005). Effect of shot peening on fatigue crack growth in 7075-T7351. *J. ASTM Int.*, 2, 33–46.

HONG, T., OOI, J. Y. and SHAW, B. (2008a). A numerical simulation to relate the shot peening parameters to the induced residual stresses. *Eng. Fail. Anal.*, 15, 1097–1110.

HONG, T., OOI, J. Y. and SHAW, B. (2008b). A numerical study of the residual stress pattern from single shot impacting on a metallic component. *Adv. Eng. Softw.*, 39, 743–756.

HOSPERS, F. and VOGELESANG, L. B. (1975). Determination of residual stresses in aluminum-alloy sheet material. *Exp. Mech.*, 15, 107–110.

HUANG, X., ZENG, Y. and LI, Z. (2006). Finite element simulation of peen forming process for the saddle shape. *Int. Technol. and Innov. conf. (ITIC2006)*. Hangzhou, China, 1240–1242.

HWU, C. (2010). *Anisotropic elastic plates*. Springer Science+Business Media, New York. ISBN 978-1-4419-5914-0.

KANG, X., WANG, T. and PLATTS, J. (2010). Multiple impact modelling for shot peening and peen forming. *Proc. Inst. Mech. Eng. Part B: J. Engineering Manufacture*, 224, 689–697.

KATGERMAN, L. and ESKIN, D. (2003). *Handbook of Aluminum*, CRC Press, vol. 1: Physical metallurgy and processes 5: Hardening, annealing, and aging.

KENNERKNECHT, S. and COOK, D. (2005). U.S. Patent No. 6,938,448 - Shaped metal panels and forming same by shot peening. U.S. Patent and Trademark Office.

KIM, T., LEE, J. H., LEE, H. and CHEONG, S.-K. (2010). An area-average approach to peening residual stress under multi-impacts using a three-dimensional symmetry-cell finite element model with plastic shots. *Mater. Design*, 31, 50–59.

KIM, W. J., CHUNG, C. S., MA, D. S., HONG, S. I. and KIM, H. K. (2003). Optimization of strength and ductility of Al2024 by equal channel angular pressing (ECAP) and post-ECAP aging. *Scripta Mater.*, 49, 333–338.

KLEMENZ, M., SCHULZE, V., , VÖRINGER, O. and LÖHE, D. (2006). Finite element simulation of the residual stress states after shot peening. *Mater. Sci. Forum*, 524-525, 349–354.

KLEMENZ, M., SCHULZE, V., ROHR, I. and LÖHE (2009). Application of the FEM for the prediction of the surface layer characteristics after shot peening. *J. Mater. Process. Technol.*, 209, 4093–4102.

KLEMENZ, M., ZIMMERMANN, M., SCHULZE, V. and LÖHE, D. (2007). Numerical prediction of the residual stress state after shot peening. *High performance computing in science and engineering 06*, 5, 437–448.

KOBAYASHI, M., MATSUI, T. and MURAKAMI, Y. (1998). Mechanisms of creation of compressive residual stress by shot peening. *Int. J. Fatigue*, 20, 351–357.

KONDO, K. (1984). Investigations on peen forming – 3rd report, applications for the improvement of shape accuracy. *Proc. 2nd conf. shot peening (ICSP2)*. Chicago, IL, USA, 22–27.

KONDO, K., MATSUZAKI, S., HIRAIWA, M. and OHGA, K. (1979). Investigations on peen forming – 1st report, on the basic features of this process. *Bull. JSME*, 22, 893–900.

KONDO, K., TSUZUKI, S. and KATO, A. (1981). Investigations on peen forming – 2nd report, on the forming mechanism. *Proc. 1st conf. shot peening (ICSP1)*. Paris, France, 565–571.

KOPP, R. and BALL, H. (1987). Recent developments in shot peen forming. *Proc. 3rd conf. shot peening (ICSP3)*. Garmisch-Partenkirchen, Germany, 297–308.

KOPP, R. and SCHULZ, J. (2002). Flexible sheet forming technology by double-sided simultaneous shot peen forming. *CIRP Annals - Manuf. Technol.*, 51, 195–198.

KULKARNI, K. M., SCHEY, J. A. and BADGER, D. V. (1981). Investigation of shot peening as a forming process for aircraft wing skins. *J. Applied Metalworking*, 1, 34–44.

KUMAR, B. (2006). Effects of residual stresses on crack growth in aluminum alloys. A. G. Youtsos, éditor, *Residual stress and its effects on fatigue and fracture*. Alexandropoulos, Greece, 189–200.

KYRIACOU, S. (1996). Shot-peenng mechanics, a theoretical study. *Proc. 6^{th} conf. shot peening (ICSP6)*. San Francisco, CA, USA, 505–516.

LAROSE, S., MIAO, H. Y. and PERRON, C. (2007). Evolution of shot peening induced surface roughness and residual stresses. *2007 SAE AeroTech Congress - Automated fastening/assembly and tooling*. Los Angeles, CA, USA.

LEE, Y.-H., TAKASHIMA, K., HIGO, Y. and KWON, D. (2004). Prediction of stress directionality from pile-up morphology around remnant indentation. *Scripta Mater.*, 51, 887–891.

LESUER, D. (1999). Experimental investigations of material models for Ti-6Al-4V and 2024-T3, Lawrence Livermore National Laboratory.

LEVERS, A. and PRIOR, A. (1998). Finite element analysis of shot peening. *J. Mater. Process. Technol.*, 80-81, 304–308.

LI, J. K., MEI, Y., DUO, W. and RENZHI, W. (1992). An analysis of stress concentrations caused by shot peening and its application in predicting fatigue strength. *Fatigue Fract. Eng. Mater. Struct.*, 15, 1271–1279.

LI, K. (1981). Using stress peen forming process for integrally stiffened wing panels. *Proc. 1^{st} conf. shot peening (ICSP1)*. Paris, France, 555–564.

LILLAMAND, I., BARRALLIER, L., LALANNE, B. and CASTEX, L. (2001). Cyclic modelling of the mechanical state produced by shot-peening. *Fatigue Fract. Eng. Mater. Struct.*, 24, 93–104.

LINDEMANN, J., BUQUE, C. and APPEL, F. (2006). Effect of shot peening on fatigue performance of a lamellar titanium aluminide alloy. *Acta Mater.*, 54, 1155–1164.

LUONG, H. and HILL, M. R. (2010). The effects of laser peening and shot peening on high cycle fatigue in 7050-T7451 aluminum alloy. *Mater. Sci. Eng. A*, 527, 699–707.

MAJZOOBI, G. H., AZIZI, R. and ALAVI NIA, A. (2005). A three-dimensional simulation of shot peening process using multiple shot impacts. *J. Mater. Process. Technol.*, 164-165, 1226–1234.

Matweb (2011). Aluminum 2024-T3.

MCDOWELL, D. L. (2007). Simulation-based strategies for microstructure-sensitive fatigue modeling. *Mater. Sci. Eng. A*, 468-470, 4–14.

MEGUID, S. A., SHAGAL, G. and STRANART, J. C. (2002). 3D FE analysis of peening of strain-rate sensitive materials using multiple impingement model. *Int. J. Impact Eng.*, 27, 119–134.

MEGUID, S. A., SHAGAL, G. and STRANART, J. C. (2007). Development and validation of novel models for 3D analysis of peening of strain-rate sensitive materials. *J. Eng. Mater. Technol.*, 129, 271–283.

MEGUID, S. A., SHAGAL, G., STRANART, J. C. and DALY, J. (1999). Three-dimensional dynamic finite element analysis of shot-peening induced residual stresses. *Finite Elem. Anal. Des.*, 31, 179–191.

MEO, M. and VIGNJEVIC, R. (2003). Finite element analysis of residual stress induced by shot peening process. *Adv. Eng. Softw.*, 34, 569–575.

MIAO, H. Y., DEMERS, D., LAROSE, S., PERRON, C. and LEVESQUE, M. (2010). Experimental study of shot peening and stress peen forming. *J. Mater. Process. Technol.*, 210, 2089–2102.

MIAO, H. Y., LAROSE, S., PERRON, C. and LÉVESQUE, M. (2009). On the potential applications of a 3D random finite element model for the simulation of shot peening. *Adv. Eng. Softw.*, 40, 1023–1038.

MIAO, H. Y., LAROSE, S., PERRON, C. and LÉVESQUE, M. (2011). Numerical simulation of the stress peen forming process and experimental validation. *Adv. Eng. Softw.*, 42, 963–975.

MIL-5H (1998). *MIL-HDBK-5H : Metallic Materials and Elements for Aerospace Vehicle Structures*. U.S. Department of Defense.

MOORE, D. (1982). *Shot peening for advanced aerospace design SP-528*, Society of Automotive Engineers, Warrendale, Pennsylvania The application of shot peen forming technology to commercial aircraft wing skins. 23–28.

MYER, R. T., KILPATRICK, S. A. and BACKUS, W. E. (1959). Stress-relief of aluminum for aircraft. *Metal Progress*, 75, 112–115 + 190.

MYLONAS, G. I. and LABEAS, G. (2011). Numerical modelling of shot peening process and corresponding products: Residual stress, surface roughness and cold work prediction. *Surf. Coat. Technol.*, 205, 4480–4494.

O'HARA, P. (2002). Peen-forming – A developing technique. *Proc. 8^{th} conf. shot peening (ICSP8)*. Garmisch-Partenkirchen, Germany, 217–226.

PARIENTE, I. F. and GUAGLIANO, M. (2009). Influence of shot peening process on contact fatigue behavior of gears. *Mater. Manuf. Process.*, 24, 1436–1441.

PEYRE, P., FABBRO, R., MERRIEN, P. and LIEURADE, H. P. (1996). Laser shock processing of aluminium alloys. Application to high cycle fatigue behaviour. *Mater. Sci. Eng. A*, 210, 102–113.

PREVEY, P. S. (1991). *ASM Handbook, Volume 10, Materials characterization*, ASM International X-Ray diffraction residual stress techniques. In ASM Handbooks Online, http://www.asmmaterials.info ASM International, 2002.

PRIME, M. B. and HILL, M. R. (2002). Residual stress, stress relief, and inhomogeneity in aluminum plate. *Scripta Mater.*, 46, 77–82.

RAMATI, S., LEVASSEUR, G. and KENNERKNECHT, S. (1999). Single piece wing skin utilization via advanced peen forming technology. *Proc. 7^{th} conf. shot peening (ICSP7)*. Warsaw, Poland.

RODOPOULOS, C., CURTIS, S., DE LOS RIOS, E. and SOLISROMERO, J. (2004). Optimisation of the fatigue resistance of 2024-t351 aluminum alloys by controlled shot peening–methodology, results and analysis. *Int. J. Fatigue*, 26, 849–856.

ROMERO, J. (2002). *The study of residual stresses due to shot peening on aluminium alloys 2024 and 7150*. University of Sheffield.

ROUQUETTE, S., ROUHAUD, E., FRANOŲIS, M., ROOS, A. and CHABOCHE, J.-L. (2009). Coupled thermo-mechanical simulations of shot impacts: Effects of the temperature on the residual stress field due to shot-peening. *J. Mater. Process. Technol.*, 209, 3879–3886.

RUUD, C. O. (1991). *ASM Handbook, Volume 8, Mechanical testing and evaluation*, ASM International Residual stress measurements. In ASM Handbooks Online, http://www.asmmaterials.info ASM International, 2002.

SAE Standard AMS-S-13165 (1997). *SAE Aerospace Material Specification AMS-S-13165 – Shot peening of metal parts*. SAE International.

SAE Standard AMS2431 (2010). *SAE Standard AMS2431 – Peening media*. SAE International.

SAE Standard J2277 (2009). *SAE Standard J2277 - Shot peening coverage determination*. SAE Surface Enhancement Division.

SAE Standard J442 (2008). *SAE Standard J442 - Test strip, holder, and gage for shot peening*. SAE Surface Enhancement Division.

SAE Standard J443 (2010). *SAE Standard J443 - Procedures for using standard shot peening test strip*. SAE Surface Enhancement Division.

SAINT-GOBAIN (2003). Zirshot ceramic beads.

SAINT-GOBAIN (2012). Microblast technical data sheet.

SAVARIA, V., BRIDIER, F. and BOCHER, P. (2012). Computational quantification and correction of the errors induced by layer removal for subsurface residual stress measurements. *Int. J. Mech. Sci.* DOI 10.1016/j.ijmecsci.2012.07.003.

SCHIFFNER, K. and DROSTE GEN. HELLING, C. (1999). Simulation of residual stresses by shot peening. *Comput. Struct.*, 72, 329–340.

SCHWARZER, J., SCHULZE, V. and VÖHRINGER, O. (2002). Finite element simulation of shot peening - a method to evaluate the influence of peening parameters on surface characteristics. *Proc.* 8^{th} *conf. shot peening (ICSP8).* Garmisch-Partenkirchen, Germany, 507–515.

SIDHOM, N., LAAMOURI, A., FATHALLAH, R., BRAHAM, C. and LIEURADE, H. P. (2005). Fatigue strength improvement of 5083 H11 Al-alloy T-welded joints by shot peening: experimental characterization and predictive approach. *Int. J. Fatigue*, 27, 729–745.

SURFPAK-SJ help (2004). *SURFPAK-SJ, v1.401 help contents.* Mitutoyo Corp. and MSTI inc.

TATTON, R. J. D. (1986). Shot peen-forming. *Impact surface treatment.* Bedford, England, 134–143.

TSUI, T. Y., OLIVER, W. C. and PHARR, G. M. (1996). Influences of stress on the measurement of mechanical properties using nanoindentation: Part I. Experiemental studies in an aluminum alloy. *J. Mater. Res.*, 11, 752–759.

TURSKI, M., CLITHEROE, S., EVANS, A. D., RODOPOULOS, C., HUGHES, D. J. and WITHERS, P. J. (2010). Engineering the residual stress state and microstructure of stainless steel with mechanical surface treatments. *Appl. Phys. A*, 99, 549–556.

UIUC Applied aerodynamics group (2012). UIUC airfoil coordinates database.

VANLUCHENE, R. D. and CRAMER, E. J. (1996). Numerical modeling of a wing skin peen forming process. *J. Mater. Eng. Perform.*, 5, 753–760.

VANLUCHENE, R. D., JOHNSON, J. and CARPENTER, R. G. (1995). Induced stress relationships for wing skin forming by shot peening. *J. Mater. Eng. Perform.*, 4, 283–290.

VÖHRINGER, O. (1987). Changes in the state of the material by shot peening. *Proc.* 3^{rd} *conf. shot peening (ICSP3).* Garmisch-Partenkirchen, Germany, 185–204.

WANG, S., LI, Y., YAO, M. and WANG, R. (1998). Compressive residual stress introduced by shot peening. *J. Mater. Process. Technol*, 73, 64–73.

WANG, S. C. and STARINK, M. J. (2005). Precipitates and intermetallic phases in precipitation hardening Al-Cu-Mg-(Li) based alloys. *Int. Mater. Reviews*, 50, 193–215.

WANG, T., PLATTS, J. and LEVERS, A. (2002). Finite element impact modelling for shot peen forming. *Proc. 8th conf. shot peening (ICSP8)*. Garmisch-Partenkirchen, Germany, 540–546.

WANG, T., PLATTS, M. J. and LEVERS, A. (2006). A process model for shot peen forming. *J. Mater. Process. Technol.*, 172, 159–162.

WANG, T., PLATTS, M. J. and WU, J. (2008). The optimisation of shot peen forming processes. *J. Mater. Process. Technol.*, 206, 78–82.

WILSON, C. D. (2002). A critical reexamination of classical metal plasticity. *J. Appl. Mech. Trans. ASME*, 69, 63–68.

WITHERS, P. J. and BHADESHIA, D. H. (2001). Residual stress Part 1: Measurement techniques. *Mater. Sci. Technol.*, 17, 355–365.

WOLFHART, H. (1984). The influence of peening conditions on the resulting distribution of residual stress. *Proc. 2nd conf. shot peening (ICSP2)*. Chicago, USA, 316–331.

WU, X., TAO, N., HONG, Y., XU, B., LU, J. and LU, K. (2002). Microstructure and evolution of mechanically-induced ultrafine grain in surface layer of Al-alloy subjected to USSP. *Acta Mater.*, 50, 2075–2084.

WUESTEFELD, F., LINNEMANN, W. and KITTEL, S. (2007). U.S. Patent No. 7,181,944 B2 - Method and device for shaping structural parts by shot blasting or peening. U.S. Patent and Trademark Office.

XUE, Y., MCDOWELL, D. L., HORSTEMEYER, M. F., DALE, M. H. and JORDON, J. B. (2007). Microstructure-based multistage fatigue modeling of aluminum alloy 7075-T651. *Eng. Fract. Mech.*, 74, 2810–2823.

YAMADA, T., TAKAHASHI, T., IKEDA, M., SUGIMOTO, S. and OHTA, T. (2002). Development of shot peening for wing integral skin for Continental business jets. *Mitsubishi Heavy Industries, Ltd. Technical Review*, 39, 689–697.

ZAROOG, O. S., ALI, A. and SAHARI, B. B. (2011a). Characterization of shot peened 2024-T351 aluminum alloy. *Key Eng. Mater.*, 462-463, 912–917.

ZAROOG, O. S., ALI, A., SAHARI, B. B. and ZAHARI, R. (2011b). Modeling of residual stress relaxation of fatigue in 2024-T351 aluminium alloy. *Int. J. Fatigue*, 33, 279–285.

ZENG, Y. (2002). Finite element simulation of shot peen forming. *Proc. 8th conf. shot peening (ICSP8)*. Garmisch-Partenkirchen, Germany, 554–561.

ZIMMERMANN, M., KLEMENZ, M., SCHULZE, V. and LÖHE, D. (2009). Numerical studies on the influence of thickness on the residual stress developement during shot peening. *High performance computing in science and engineering 08*, 7, 481–492.

ZIMMERMANN, M., SCHULZE, V. and HOFFMEISTER, J. (2010). Finite element modelling of coverage effects during shot peening of IN718. *Int. J. Mater. Res.*, 101, 951–962.

ZUPANC, U. and GRUM, J. (2011). Surface integrity of shot peened aluminium alloy 7075-T651. *J. Mech. Eng.*, 57, 379–384.